Tetradentate NHC/Thiolato and NHC/Alcoholato Hybrid Scaffolds – A Nickel(II) Complex as Bidentate Metalloligand in 3d Transition Metal Chemistry

Dissertation
for the award of the degree
"Doctor rerum naturalium"
of the Georg-August-Universität Göttingen

within the doctoral program of chemistry
of the Georg-August University School of Science (GAUSS)

submitted by
Giuseppe Lococciolo
from Brindisi, Italy

Göttingen
2022

Thesis committee

Prof. Dr. Franc Meyer
Institut für Anorganische Chemie, Georg-August-Universität Göttingen

Prof. Dr. Inke Siewert
Institut für Anorganische Chemie, Georg-August-Universität Göttingen

Dr. Carole Duboc
Département de Chimie Moléculaire, Université Grenoble Alpes

Members of the Examination Board

Reviewer: Prof. Dr. Franc Meyer
Institut für Anorganische Chemie, Georg-August-Universität Göttingen

Second Reviewer: Prof. Dr. Inke Siewert
Institut für Anorganische Chemie, Georg-August-Universität Göttingen

Further members of the Examination Board:

Jun.-Prof. Dr. Anna Krawczuk
Institut für Anorganische Chemie, Georg-August-Universität Göttingen

Jun.-Prof. Dr. Johannes C. L. Walker
Institute of Organic and Biomolecular Chemistry, Georg-August-Universität Göttingen

Dr. Lisa Vondung
Institut für Anorganische Chemie, Georg-August-Universität Göttingen

Dr. Matthias Otte
Institut für Anorganische Chemie, Georg-August-Universität Göttingen

Date of the oral examination: 19th December 2022

To me

Table of contents

1. Introduction

1.1. Global Energy Consumption

The consumption of global primary energy in the last 10 years has grown significantly. Of all the global primary energy, 87% is provided by fossil fuels and on the other hand, renewable sources contribute to reach only 10% of the supply. In the last years, nuclear energy´s impact has increased, but given the decommissioning of multiple reactors in Europe and the USA, this will not affect a general trend to a reduced relevance of this source. Still, nowadays oil represents the first energy source, of which 80% alone is used for the world transportation system.[1]

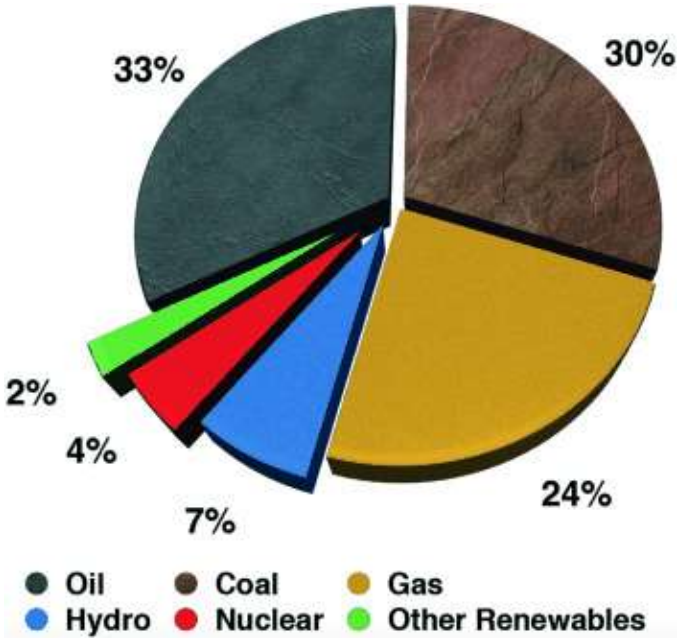

Figure 1 Global supply of commercially traded primary energy, from British Petroleum 2015.[1]

The challenge is now to change the primary energy sources, preferably long-lasting. Electricity and fuels are two different forms of energy that exhibit dissimilar properties but that are easily interconverted. Electricity is efficiently transported via wires, but it is hard to store on a large scale. In contrast, fuels have the possibility to be stored for a long period of time, but it is demanding to find a way for efficient transportation. Nowadays the general energy consumption is split into about 25% of electricity and 75% of fuels.

The global average temperature is increasing year by year, due to the release of anthropogenic greenhouse gases, like CO_2, and this makes it mandatory to widen the selection of sustainable and eco-friendly energy production.[2]

1.2. H_2 as fuel

Molecular Hydrogen can be obtained from the biggest supply reservoir on earth, water, and it is a form of fuel that upon reaction with O_2, does not produce carbon dioxide as a side product.[3]

In nature, hydrogen in the form of protons is utilized in different metabolic processes to vehicle energy in living organisms. More specifically, the combination of protons and electrons is key in the synthesis and transformation of the two molecules that are responsible for energy exchange and storage: ATP and NAD(P)H.[4,5]

H_2 exhibits the highest specific enthalpy of combustion among chemical fuels and it can be easily produced by electrolysis, and then converted to energy by fuel cells. An example of a common fuel cell is the proton exchange membrane (PEM), schematized in figure 2.[6]

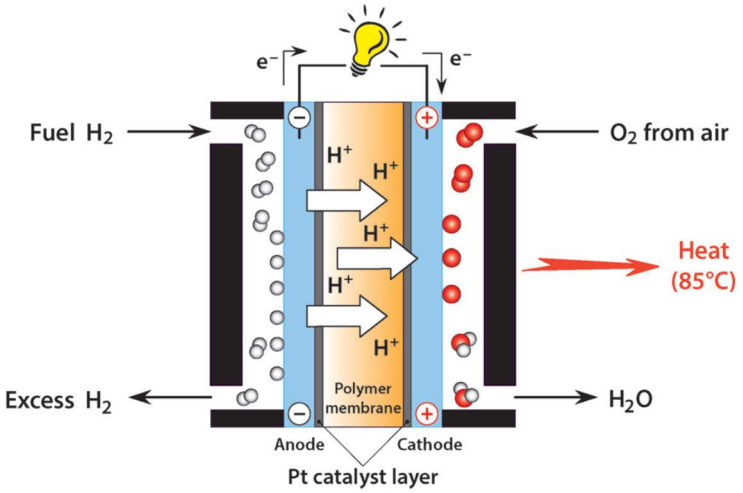

Figure 2 Working scheme of proton exchange membrane (PEM) fuel cell.[6]

At first hydrogen splitting happens with the assist of a Pt catalyst at the anode, to give out protons and electrons. Protons are allowed to migrate to the cathode by means of a polymer electrolyte membrane and the electrons travel to wires generating electricity. At the cathode, the recombination of proton and electrons with O_2 from air happens, also catalyzed by platinum, and generating water as a waste product.[6] Even though PEM cells are easily

operatable and have a high power density, they are expensive and fragile. In the last decades, the demand and price of Pt have indeed reached their maxima values (figure 3).[7]

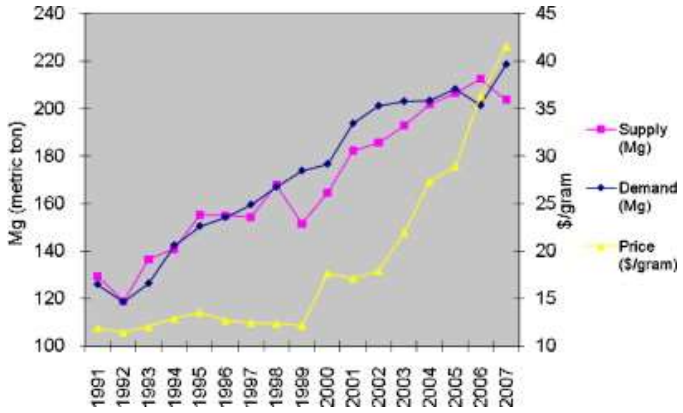

Figure 3 Pt supply (purple), demand (blue) and price (yellow).[7]

These trends will likely continue, leading to an imbalance that could escalate into a crisis. For this reason, it is mandatory to find alternative efficient catalysts to support hydrogen splitting, composed of abundant and inexpensive metals.

1.3. Hydrogen oxidation reaction (HOR) and hydrogen evolution reaction (HER)

Catalysis of hydrogen oxidation reaction (HOR) and hydrogen evolution reaction (HER) using earth-abundant metals has been one of the most important targets for research in recent times. HOR constitutes a critical process in sustainable energy production and conversion, however, the choices for anode catalysts remain still limited. In an alkaline medium, the reaction for HOR/HER is:

$$H_2 \rightleftarrows 2H^+ + 2e^-$$

Electrocatalysis in a basic medium has been already studied, highlighting the challenges in developing catalysts with high activity in an alkaline environment.[8] The pathway of HOR follows different steps. The first one is dissociative adsorption of H_2 without following electron transfer, described by the Tafel reaction[9]:

$$H_2 + 2 * \longrightarrow 2(* - H_{ad})$$

where * is the active site and H_{ad} is the adsorbed hydrogen atom. Subsequently, an electron transfer from H_2 to the catalyst occurs, a process represented in the Heyrovsky reaction[10]:

$$H_2 + OH^- + * \longrightarrow (* - H_{ad}) + H_2O + e^-$$

where the OH^- is in the proximity of the surface of the catalyst, which is assumed oxophilic.

The last step involves the release of the adsorbed hydrogen atom, and it is described by the Volmer reaction[11]:

$$(* - H_{ad}) + OH^- \longrightarrow * + H_2O + e^-$$

Non-noble metal catalysts have been explored for HOR in basic media, however, they still are far away from the activity of platinum-based catalysts.

Finding durable catalysts for the hydrogen evolution reaction (HER) is also a key point for the development of renewable energy sources and storage. Photoelectrochemical and electrochemical water splitting represent two strategies for the realization of solar to hydrogen energy conversion. The target of the research is then to engineer energy harvesting infrastructures with water splitting devices able to convert electricity obtained from green renewable sources, into H_2.[12]

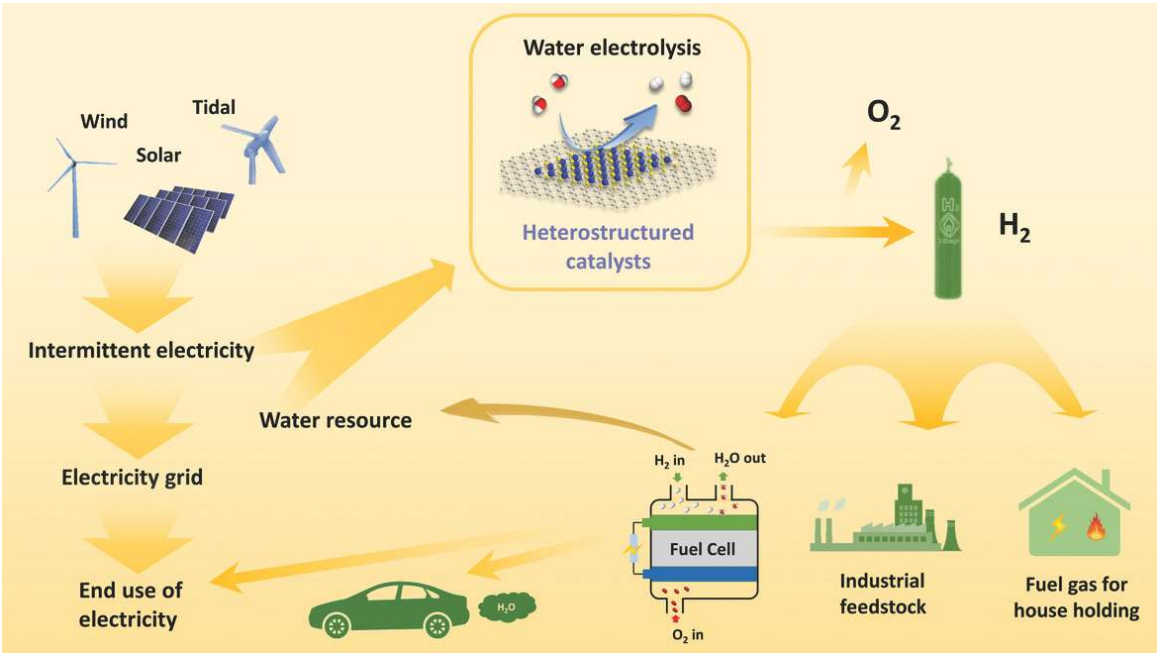

Figure 4 Sustainable pathway for the production and utilization of hydrogen energy.[12]

H_2 production via electrolysis is a CO_2-free process (figure 4) and requires water and electricity (produced by green renewable sources) only[13], whereas the steam reforming process, being

actually the principal industrial approach for H_2 production, involves fossil fuels consumption and CO_2 emission.[14]

In a typical water electrolysis process, H_2 is produced at the cathode by HER, but due to the high cost and low efficiency, it only contributes to 4% of H_2 supply worldwide.[15]

In terms of the pathway of the catalysis reaction, HER follows the inverted route already explained for HOR. In an acid media, the starting point is the H^+ adsorption on the catalyst surface and it is described by the Volmer reaction[11]:

$$H^+ + e^- \longrightarrow (* - H)$$

where * is again the active site on the surface of the catalyst. Following up, *-H combines with a H^+ and an electron to form H_2, as described by the Heyrovsky reaction[10]:

$$(* - H) + H^+ + e^- \longrightarrow H_2$$

Alternatively, H_2 can be produced by a chemical desorption step, which involves the combination of two hydrogen atoms adsorbed on the surface, as shown by the Tafel reaction[9]:

$$2(* - H) \longrightarrow H_2$$

The ideal catalyst for HER (and HOR) is one that is simultaneously cost-effective, efficient and durable. The cost of the catalyst is trivially connected to the elements/chemicals involved in the synthesis and the techniques used to prepare it. In this sense, abundant metals such as Ni, Fe are considered valid cheap candidates, in comparison to pricy noble metals like Pt and Pd.[16]

1.4. [NiFe]H_2ases

Nature already figured out how to store and use energy from sunlight in a chemical form, H_2, and the remarkable possibility to reversibly catalyze the reduction of protons to H_2 is attributable to hydrogenases.[17]

$$H_2 \rightleftarrows 2H^+ + 2e^-$$

Hydrogenases (H_2ases) are enzymes responsible for hydrogen metabolism in bacteria, and they are classified according to the active site.[18] Three types of H_2ases containing metals are defined: [FeFe] H_2ases , [Fe]H_2ases and [NiFe]H_2ases (figure 5).[19–21]

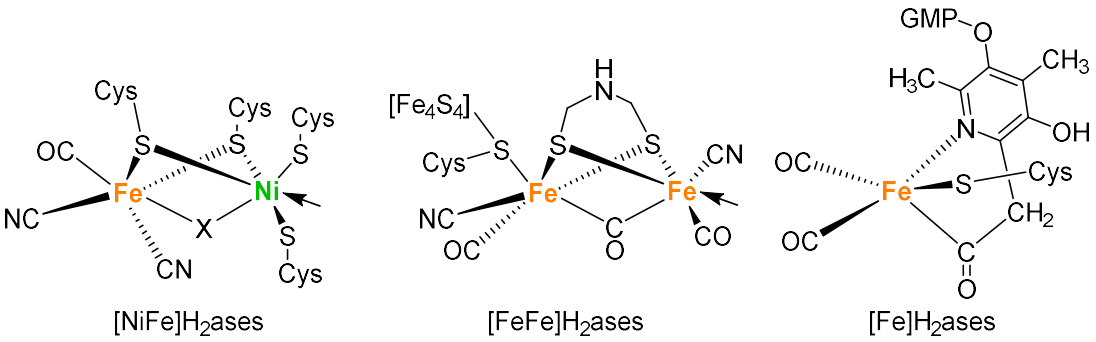

Figure 5 Chemical structures of the active sites are given; the arrows indicate the open metal coordination site.[22]

The structures of two [NiFe]H_2ases have been already published years ago, one from *Desulfovibrio gigas*[23] and the other from *Desulfovibrio vulgaris* Miyazaki.[24] The [NiFe]H_2ase from *D. gigas* consist of 28 kD and 60 kD subunits of a heterodimeric periplasmic protein and contains one [3Fe-4S] and two [4Fe-4S] clusters, responsible for the electron transport (ET) chain.[25,26] The two active sites are found in the large subunit, one being the [NiFe] located in the center of the molecule, and another assigned to a Mg ion located at the end of the large subunit.[17] The [NiFe] cluster is considered to be the catalytic site of the enzyme, and its similar in all [NiFe]H_2ases (figure 6).

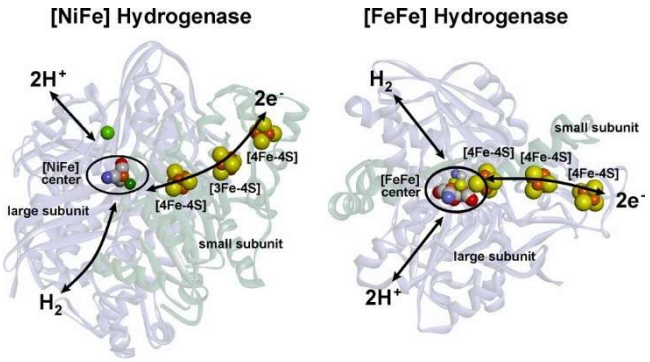

Figure 6 Structures of the [NiFe] hydrogenase and of the [FeFe] hydrogenase. Schematically indicated are the ET chain (via iron–sulfur centers), as well as pathways for the dihydrogen and the H^+ transfer.[22]

Four S from four cysteine residues are coordinated to the Ni, and two of them are bridging to the Fe center. The other two cysteine residues are bound to the Ni in a terminal fashion.[17] The low-spin (LS) Fe^{II} is 5-coordinated by the two bridging cysteine thiolates and three diatomic ligands, one CO and two CN^-, shown by FTIR spectroscopy studies.[27] The cyanides act as strong σ-donor ligands and can potentially form hydrogen bonds with the surrounding amino acids,

whereas the CO ligand may form only a very weak H-bond or not at all.[17] During the catalysis of H_2 oxidation, the enzyme passes through different intermediate states, and some of them have been characterized by X-ray diffraction, e.g. the reduced states Ni-C and Ni-R (figure 7).[24]

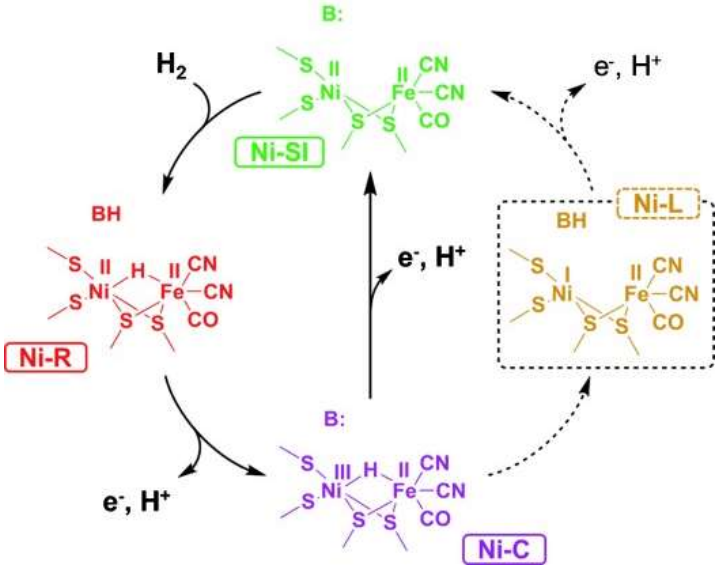

Figure 7 H_2 oxidation (black) and anaerobic inactivation (grey) of NiFe hydrogenase (generic proton acceptor depicted as B).[28]

To evaluate the active site of [NiFe] H_2ase redox states, IR spectroscopy and electrochemistry have been employed, due to the characteristic vibrational bands of CO and CN^- ligands, highly sensitive to a change in the electron density of the active site.[22] In the cycle in figure 7, H_2 is cleaved heterolytically and simultaneously reacts with the Ni-SI state, in presence of a proton acceptor B, forming the Ni-R state. Both Ni-SI and Ni-R states are EPR-silent, and the latter incorporates a bridging hydride. Long-range proton transfer channels have been identified as responsible for carrying the role of acceptor for the proton produced in the initial cleavage.[29] Removing this proton and one electron, leads to the Ni-C state, which is characterized by a formally oxidized Ni^{III} equipped with a bridging hydride to the Fe^{II} center.[30] Coupled transfer of one electron and one proton would be required to recover the Ni-SI state. A transient intermediate state is also considered, Ni-L, reported to appear only upon illumination at cryogenic temperatures. For the Ni-L state to be detectable, the electron transfer should have to be slower than the proton transfer. The conditions required for the formation of the Ni-L state have been considered irrelevant to the catalytic cycle.[31] The interconversion between

Ni-C and Ni-L state can be followed by EPR in function of pH and at different potentials applied (figure 8).

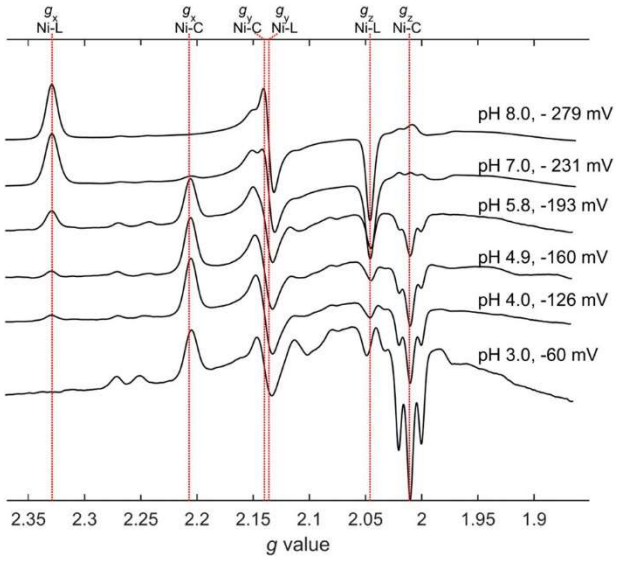

Figure 8 Relative proportions of Ni-C and Ni-L states change as a function of pH at different potentials. Conditions for measuring spectra: T = 60 K, microwave power = 2.0 mW, modulation amplitude 5.0 G.[32]

Different potentials are applied to maintain a maximum level of signals for both states. Overall, Ni-L interconverts into Ni-C lowering the pH. At pH 3.0 and -60 mV, the spectrum shows the full interconversion into Ni-C with $g_x = 2.21$, $g_y = 2.14$ and $g_z = 2.01$.

1.5. [NiFe]H_2ases mimics

A key challenge in synthetic biomimetic chemistry for many years has been the reproduction of the structure and function of the active site of [NiFe]H_2ase. The main downside of most active mimics is that the catalytic activity happens on the Fe^{II} center and not on the Ni^{II} site.[33] Relocation of the activity towards the Ni^{II} center can be obtained by design of ligands able to promote the redox flexibility of the Ni site while retaining stability towards the dinuclear system through various oxidation states. In this context, various [NiFe]H_2ase mimics were developed, one of the most popular being one based on a bipyridine-bisthiolate ligand reported by Brazzolotto et al. .[34] The nomenclature to identify the ligand used here adopts the "N2S2" acronym, in which the donor atom for complexation of the metal center are highlighted. The L^{N2S2} ligand is characterized by the ability to stabilize different oxidation states

of Ni (from I to III) and it is implemented in the synthesis of a [NiFe] complex with a {$Fe^{II}CpCO$} unit, that serves as a surrogate for the {$Fe^{II}CO(CN)_2$} moiety of the active site of the natural enzyme (figure 9).[35]

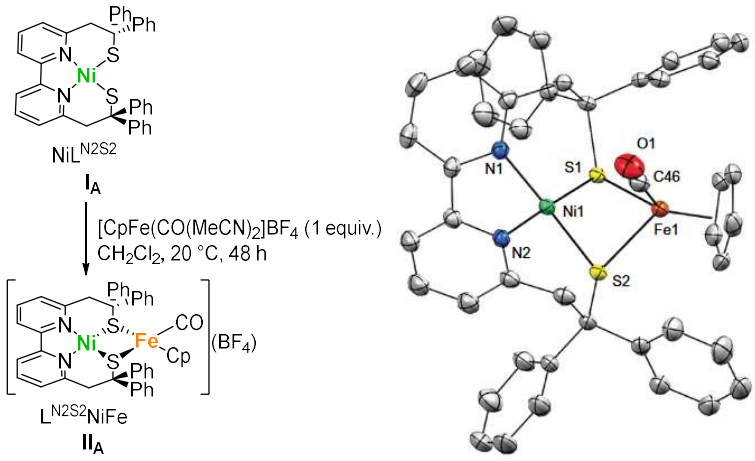

Figure 9 Synthesis and X-ray structure of $\mathbf{II_A}$. (left) Synthetic procedure for [L^{N2S2}NiFe]BF_4 (**II**). (right) ORTEP view of only one crystallographically independent unit of the $\mathbf{II_A}$ cation.[34]

Complex $\mathbf{II_A}$ mimics the Ni-SI state of the enzyme, having an identical core structure and also similar spectroscopic signatures. From EPR and NMR, $\mathbf{II_A}$ is confirmed to be diamagnetic with both metal centers in a low-spin (LS) configuration, as in the Ni-SI state. The cyclic voltammogram (CV) of complex $\mathbf{II_A}$ depicts an unprecedented feature in [NiFe]H_2ase mimics, having two reversible one-electron reduction processes, supported by structural reorganizations on the metal site(s). In presence of a proton source, complex $\mathbf{II_A}$ exhibit a catalytic process towards H_2 evolution, and the initially proposed mechanism is shown in figure 10.[34]

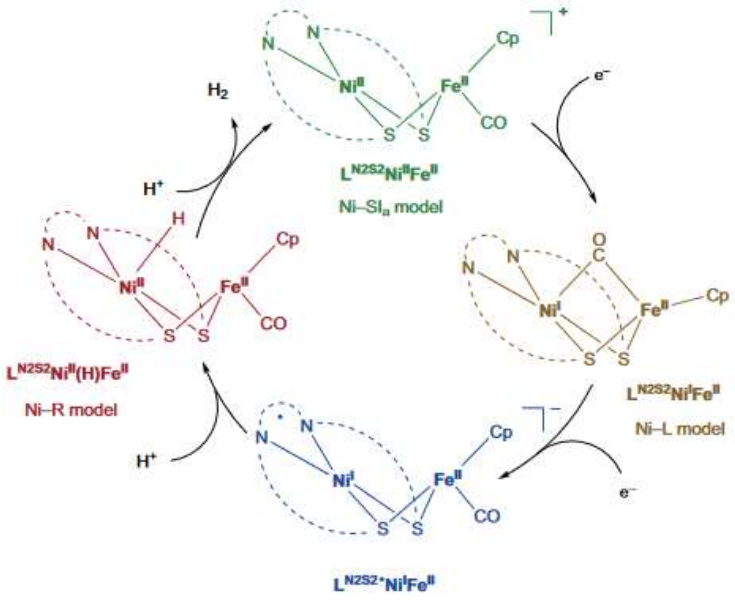

Figure 10 H_2 production catalytic cycle of $\mathbf{II_A}$.[34]

The catalytic cycle starts with a one-electron reduction of $\mathbf{II_A}$ to obtain the $Ni^{I}Fe^{II}$ complex as a mimic of the Ni-L state, which is further reduced to a ligand-radical $\{N2S2^{\bullet}\}Ni^{I}Fe^{II}$ complex. The radical complex reacts in presence of protons to form the $Ni^{II}(H)Fe^{II}$ complex, a mimic of the Ni-R state, which is further protonated to afford the release of H_2 and the recovery of the initial complex $\mathbf{II_A}$.[34] Complex $\mathbf{II_A}$ displays one of the best performances towards electrocatalytic H_2 production, even though overpotentials are quite high, it offers a new opening in the development of rationally designed [NiFe]H_2ase mimics.

Subsequent computational work has led to a refinement of the mechanism, which involves an E[CEEC] sequence (where E = electron transfer and C = chemical reaction), and suggests that the bridging thiolates serve as protons shuttles. To address this, the structure of **II** has been tuned by modification of the Fe site, replacing the Cp ligand with Cp* (complex **III**a*, figure 11).[36]

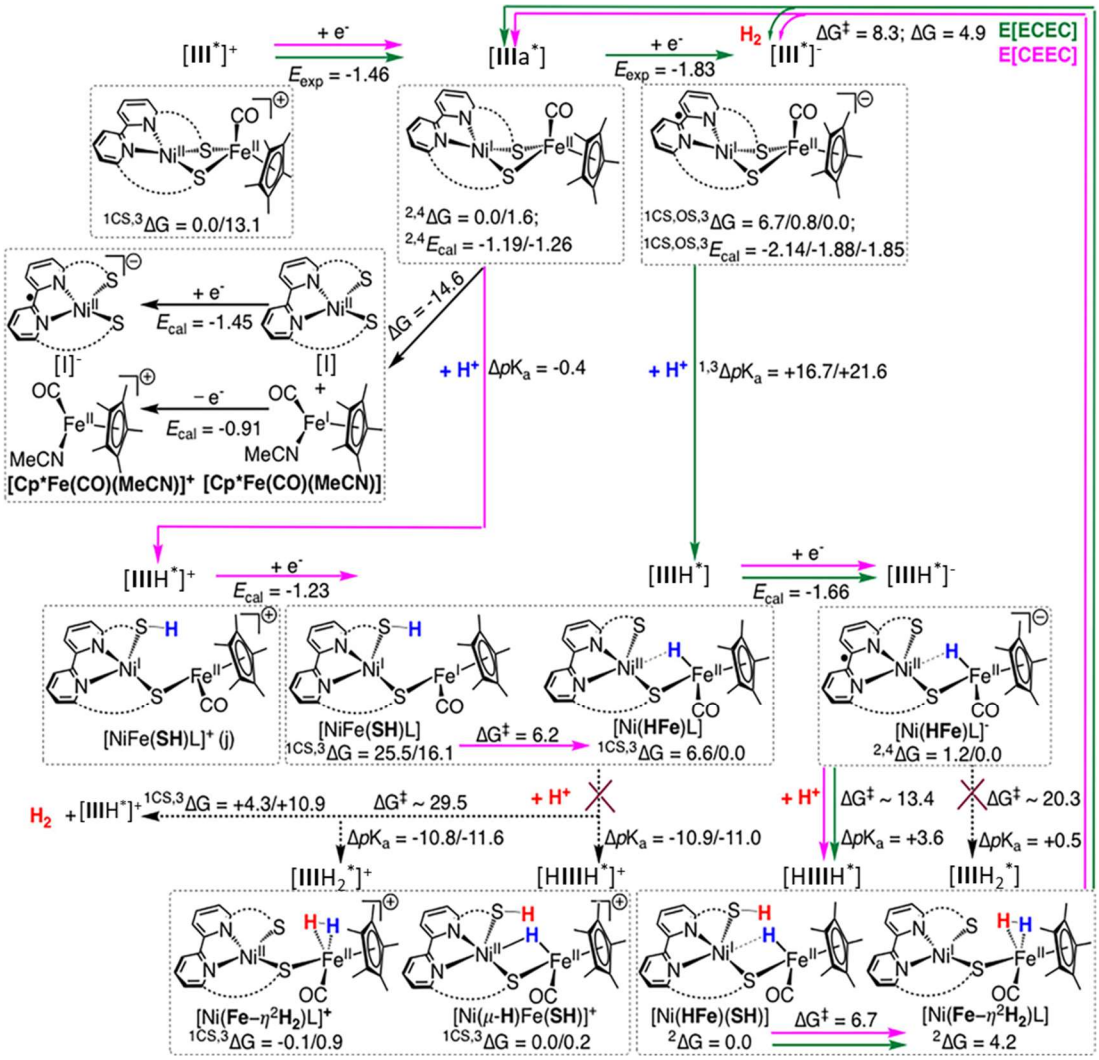

Figure 11 DFT(B3P86) Calculated H_2 Production Catalytic Cycle for **III**a*. The relative Gibbs free energies (ΔG) and barriers (ΔG‡) are given in kcal/mol. The reduction potentials (E° vs Fc+/0) are given in V. CS and OS indicate the closed-shell singlet and open-shell singlet states, respectively. The superscript numbers indicate the spin state. The relative acidities (ΔpKa = pKa(CatH) − pKa(Et_3NH^+)) are reported with reference to Et_3NH^+ in MeCN. The more positive ΔpKa values indicate that the protonation reaction is thermodynamically favourable, while the more negative ΔpKa values indicate that the protonation reaction is thermodynamically unfavourable. The green arrow indicates the E[ECEC] pathway, while the pink arrow indicates the E[CEEC] pathway.[36]

The predicted mechanism following the E[CEEC] pathway (pink arrows, figure 11) starts with the reduction of [**III***]$^+$ to give [**III**a*], in which the CO is terminally bound to the Fe unit. Compound [**III**a*] undergoes decomposition, leading to **I** and [FeCp*(CO)(MeCN)]. A second reduction of [**III**a*] is predicted to give out complex [**III***]$^-$, where the bipyridine moiety acts like an electron reservoir and the Ni center is in oxidation state (I). In presence of $[Et_3NH]^+$, the

protonation of [**III**a*] to [**III**H*]$^+$ is likely and the most stable isomer corresponds to the protonation of the bridging thiolate, leading to partial decoordination. Compound [**III**H*]$^+$ is then reduced to [**III**H*] at a predicted potential of $E_P^c = -1.23$ V, where neither the terminal thiolate nor the hydride are basic enough to be protonated to form the thiol hydride [H**III**H*]$^+$. A third one-electron-reduction process occurs, at the bipyridine ligand, to obtain [**III**H*]$^-$. Based on DFT calculations, the formation of [H**III**H*] is predicted to be kinetically and thermodynamically more favourable than [**III**H_2*]. Therefore, after protonation of [**III**H*]$^-$ to obtain [H**III**H*], the proton and the hydride react together to yield [**III**H_2*]. Finally, H_2 is released and the reduced species [**III**a*] is regenerated.[36]

A Co^{II} complex analogue to $\mathbf{I_A}$ was synthesized by Duboc´s group, following a similar synthetic pathway, in order to prepare a CoFe complex for comparison of its potential reactivity towards H_2 production with the NiFe variant.[37]

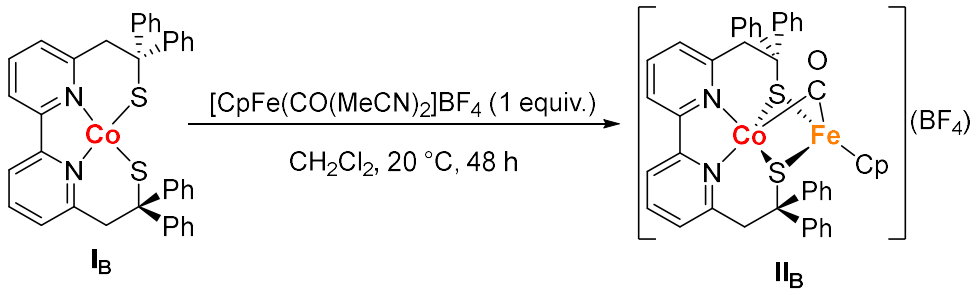

$\mathbf{I_B}$ $\mathbf{II_B}$

Scheme 1 Synthesis of Co^{II} complex $\mathbf{I_B}$ and bimetallic CoFe complex $\mathbf{II_B}$.[37]

Following the addition of Et_3NHB_4 as a proton source, an experiment for HER is conducted. However, in this case, there was no activity towards electrocatalytic H_2 production detected despite $\mathbf{II_B}$ being much easier to reduce ($E_P^c = -1.00$ V vs Fc$^+$/Fc, for the first one-electron reduction process) compared to $\mathbf{II_A}$ ($E_P^c = -1.99$ V vs Fc$^+$/Fc) (figure 12).[34,37]

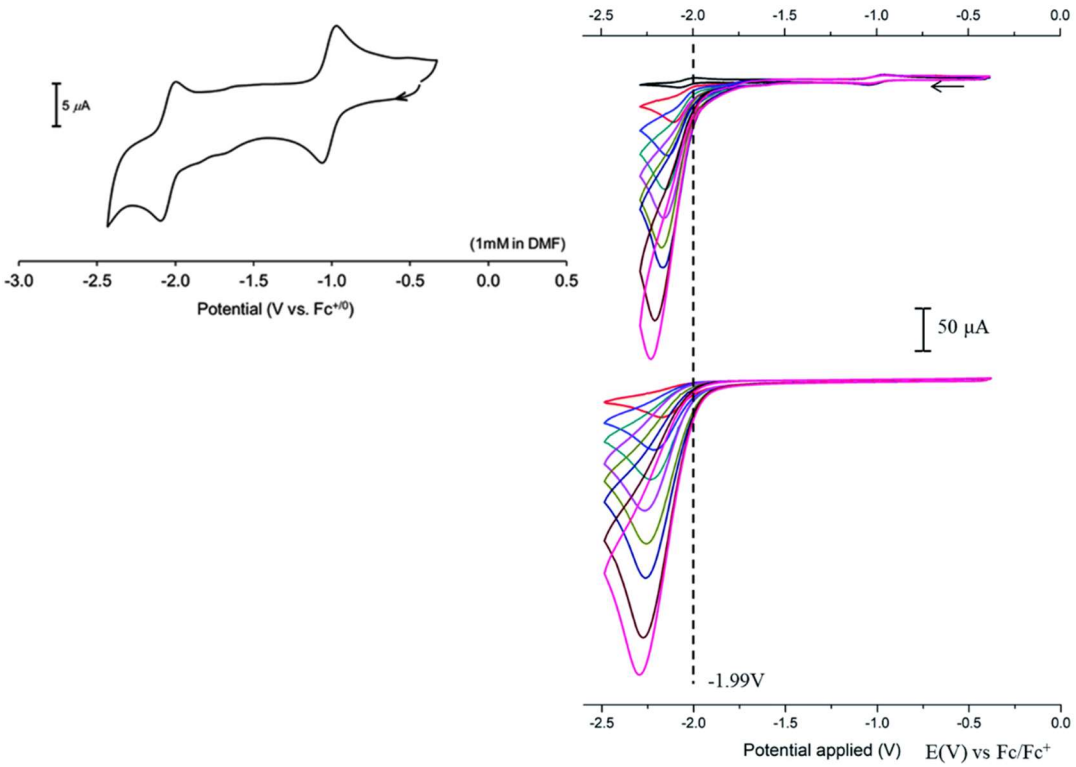

Figure 12 (Left) Cyclic voltammogram of a DMF solution of $\mathbf{II_B}$ (1 mM); electrolyte: 0.1 M $(Bu)_4NClO_4$; Ref: $Ag/AgNO_3$; CE: Pt wire; scan rate: 100 mVs^{-1}. (Right, top) CVs of $\mathbf{II_B}$ (0.73 mM, top, black) in the absence or presence of various amounts of Et_3NHBF_4 in DMF solution, 0.1 M *n*-Bu_4NClO_4, on a GC electrode at 100 mVs^{-1}: 5 equiv. (red); 10 equiv. (blue); 15 equiv. (cyan); 20 equiv. (pink); 25 equiv. (dark yellow); 30 equiv. (dark blue); 40 equiv. (deep red); 50 equiv. (magenta). (Right, bottom) CVs of the corresponding blank samples (no catalyst).[37]

1.6. NHCs-based ligands and complexes for catalysis

N-heterocyclic carbenes (NHCs) as ligands have a strong σ-donor and flexible π-acceptor character, where the extent of the π-bonding depends on the nature of the metal, its co-ligands and substituents on the backbone of the NHCs.[38] In this sense, NHCs are considered somewhat similar to organophosphanes (PR_3), but serving as stronger σ-donors and usually being more kinetically inert. Furthermore, they are usually considered to possess an innocent redox nature, capable to support metal-centered redox chemistry.[39] NHC-metal complexes have been in use in many catalytic processes, such as olefin hydrogenation[40], C-N cross coupling[41] and olefin metathesis[42]. In particular, nickel-based NHC complexes have been employed in different catalytic processes. A prominent example is given by Zhang et al. who were able to isolate the first NHC-nickel based complexes suitable for C-S coupling catalysis.[43]

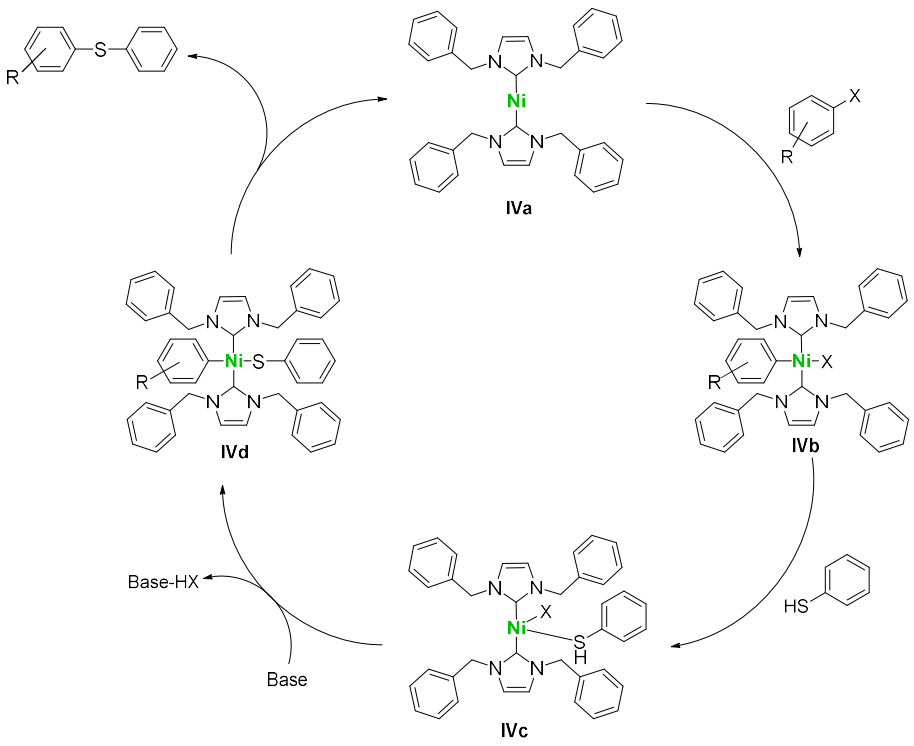

Figure 13 Scheme proposed for the catalysis of C-S coupling reaction.[43]

In the scheme in figure 13, it is assumed that the Ni-NHC catalyst undergoes a typical oxidative addition and reductive elimination cycle. The intrinsic steric hindrance of the ligand supports the reductive elimination step but slows down the oxidative addition. However, the strong electro-donating character of the NHC can balance this out by promoting oxidative addition.[43]

Another example is given by Vijaykuma et al. who reported the hydroheteroarylation of vinylarenes with an NHC-nickel complex, prepared using $Ni(COD)_2$, leading to 1-diarylethane products exclusively (figure 14).[44]

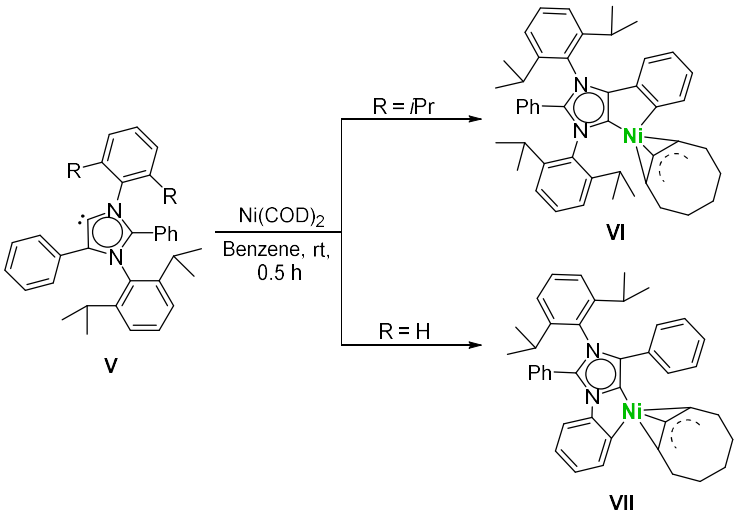

Figure 14 Synthesis of the Ni-NHCs complexes with $Ni(COD)_2$.[44]

The assumption made to explain the catalytic mechanism in the reaction for hydroheteroarylation is that the $Ni(COD)_2$ acts as a catalyst precursor generating a NHC-Ni(0) intermediate that undergoes oxidative addition to produce the Ni^{II} intermediate (see figure 14). In the following step, there is the coordination of the vinylarene to the nickel ion and subsequent regioselective insertion of the olefin into the Ni-H bond. The last step is a reductive elimination of the product to retrieve the catalyst (figure 15).[44]

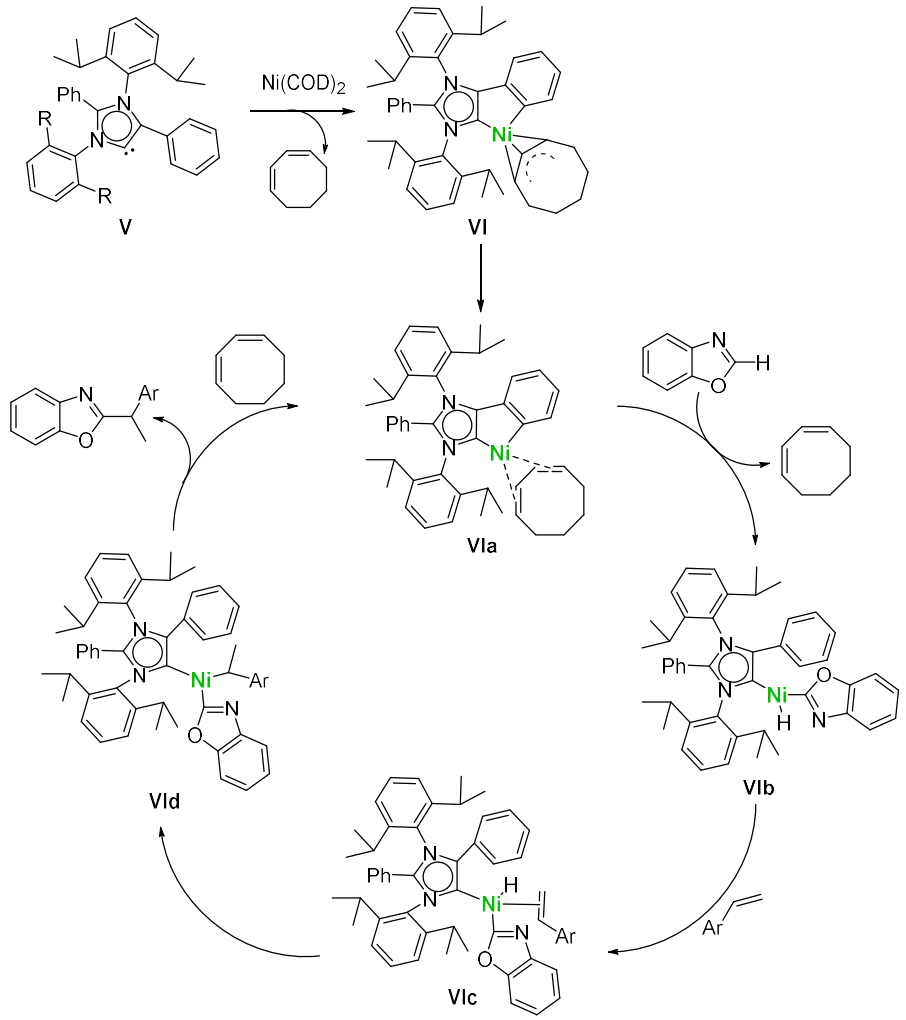

Figure 15 Possible mechanistic cycle for hydroheteroarylation.[44]

A modified class of NHCs that has been investigated in recent times is characterized by O-donors introduced as substituents on the imidazole.[45] In Ni^{II} chemistry, a wide range of heterobidentate NHCs have been prepared, offering coordination through neutral donors, like phosphines[46] or amines[47], but also by anionic donors, characterized by stronger interaction with the metal center.[48]

1.7. Ni^{II} complexes with alcoholate donor-NHCs

Anionic O-donors are able to stabilize oxophilic transition metals for catalytic applications[49] while offering the possibility to serve as hydrogen bond acceptor sites.[50] In this context, a prominent example is given by Bertini et al. with nickel-based NHCs complexes equipped with a O-donor sidearm (figure 16).[51]

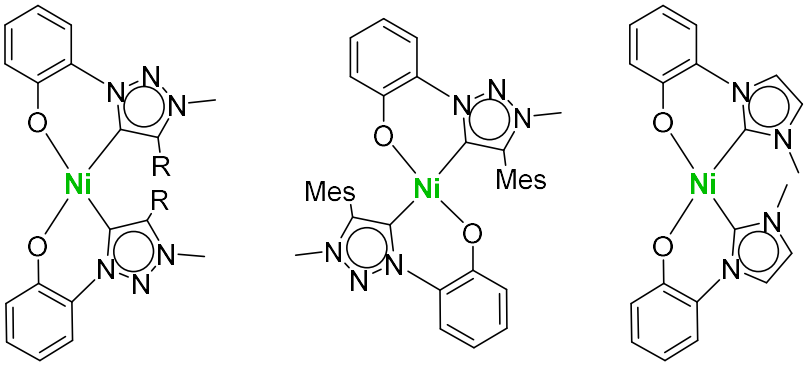

Figure 16 Oxygen-functionalized NHC Ni^{II} complexes.[51]

The series of complexes synthesized displays remarkable activity in the hydrosilylation of carbonyl groups (see figure 17).

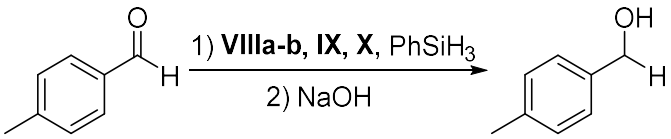

Figure 17 Hydrosilylation reaction of 4-methylbenzaldhehyde, catalyzed by compounds **VIIIa-b**, **IX**, **X**.

These findings provide guidelines for the design of novel O-donor substituted nickel-NHCs complexes, aimed at competing in the catalytic activity of noble metal catalysts and, more specifically to part of this thesis work, targeting new [NiFe]H_2ases mimics for the hydrogen evolution reaction (HER) and hydrogen oxidation reaction (HOR).

Another interesting example of O-donor substituted bidentate NHC ligands is given by Hameury et al., who reported a chelated Ni^{II} complex that has the interesting ability to bind additional metal ions via the O-donors (figure 18).[52]

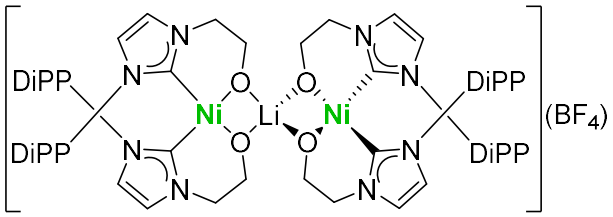

XI

Figure 18 Trimetallic alcoholate NHC nickel (II) complex.[52]

The trinuclear NiLiNi complex **XII** was tested as a catalyst towards oligomerization of ethylene, exploiting the functional sidearm that is prone to coordination to the metal center in the precatalyst or in the active species, preventing the reductive elimination of the ligand.[52]

With these blueprints in mind, this thesis work aims to build multimetallic complexes, by synthesizing a novel functionalized NHC ligand for the complexation of Ni^{II} and using the resulting complex as a neutral metalloligand unit for the complexation of various 3d metals. A multimetallic Fe^{II} complex will be introduced and it will be studied as a possible catalyst towards HER. The introduction of Co^{II} in the multimetallic system will lead to the first tetra-oxo ligated Co^{II}-based single ion magnet (SIM) ever reported.

1.8. Co^{II} single-ion magnets (SIM)

Much current research is focusing on molecular nanomagnets, in particular single molecule magnets (SMMs), which are molecules in which the slow relaxation of the magnetization is based purely on molecular origin. SMMs do not require intermolecular interactions, and this makes them particularly interesting in terms of application, e.g. in high density storage of data.[53] When SMMs contain only one metal center with significant magnetic anisotropy, they are referred to as single-ion-magnets (SIMs). To consider a molecule a decent SMM, it should show a large effective energy barrier against magnetization reversal U_{eff}, a high blocking temperature T_B, and a significant relaxation time τ. For these reasons, the goal in research is to increase U_{eff} and T_B as much as possible.[54] Given this, the great challenge is to prepare SMMs that exhibit slow relaxation of the magnetization (SRM) at readily accessible temperatures and to do so, it is crucial to understand magneto-structural correlations that govern magnetic anisotropy.

SMM behaviour is usually identified by:

1. the detection of maxima in the out-of-phase AC (alternating current) magnetic susceptibility χ_M'' versus the frequency ν;
2. the presence of hysteresis in the magnetization response with respect to an applied magnetic field.[55]

A very attractive class of SMMs is based on the 3d transition metal ion Co^{II}, and in recent years much research has been devoted to unravel the correlations between structural features, magnetic anisotropy and slow relaxation of magnetization.[53] A prominent example of a Co^{II} SIM is given by Rechkemer et al., with a complex that shows a high effective energy barrier and displays pronounced magnetic bistability. In their work, they used 1,2-bis(methanesulfonamido)benzene as a bidentate ligand resulting in the tetracoordinate Co^{II} compound shown in figure 19.[56]

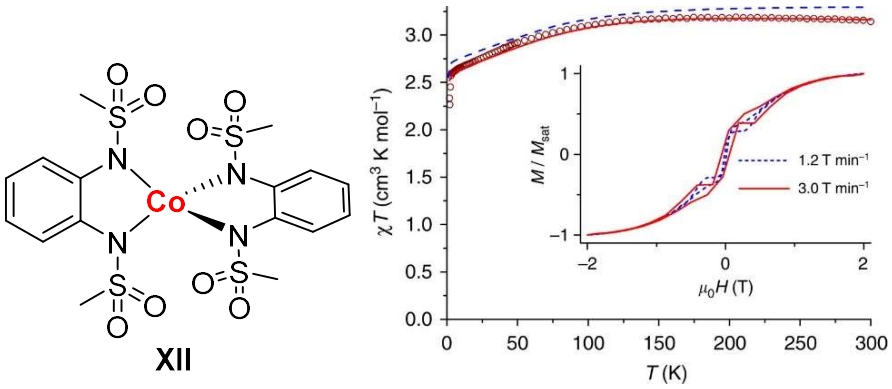

Figure 19 (Left) Structure of the Co^{II} complex **XII**; (Right) χT vs. T plots of 1 at 1000 Oe (T < 50 K) and 10,000 Oe (T > 40 K). The red line represents a spin Hamiltonian fit with D = –115 cm^{-1}, $g_{\perp}$ = 2.20, $g_{||}$= 3.03. The dashed blue line represents simulation. The inset shows magnetic hysteresis at T = 1.8 K.[56]

The coordination geometry adopted is a distorted tetrahedron with N-Co-N bite angles of 80.59° and 80.70°. The variable temperature DC magnetic susceptibility data showed χT = 3.14 cm^3Kmol^{-1} at room temperature, which is higher than the expected spin-only value for a system with S = 3/2 (χT = 1.875 cm^3mol^{-1} K). With decreasing temperature, χT stays relatively constant down to 130 K, then begins to drop, suddenly reaching a value near 2.50 cm^3Kmol^{-1} at low temperatures, which indicates a large anisotropy. The magnetization at 1.8 K is μ_B = 2.56, which is lower than the expected value for this system (3.90 μ_B), suggesting

the presence of pronounced zero-field splitting (ZFS).[53] Indeed analyses of the data fitted according to spin Hamiltonian yielded D = -115 cm^{-1}, $g_{\perp}$ = 2.20, $g_{||}$ = 3.03, which was one of the largest published values for tetracoordinate Co^{II} ion at the time, indicating large uniaxial anisotropy of complex **XII**. Investigation of the slow relaxation of magnetization via AC susceptibility shows that complex **XII** exhibits SMM behaviour, even in absence of a DC field (figure 20a). The Arrhenius plot constructed shows a linear regime of ln(τ) vs T^{-1} at high temperatures, where the relaxation undergoes via an Orbach process. At low temperatures, a curvature in the plot is created by QTM (quantum tunnelling of magnetization), Raman and direct processes (figure 20b).[56]

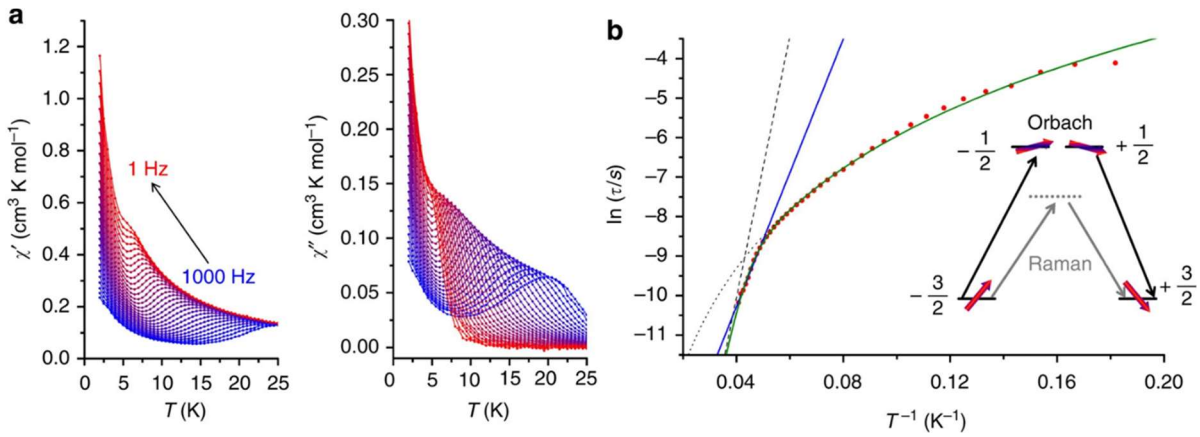

Figure 20 (a) In-phase χ_M′ and out-of-phase components χ_M″ of the ac susceptibility as a function of temperature recorded on a pressed powder sample of **XII** in zero dc field and at different frequencies of the ac magnetic field as indicated. (b) Natural logarithm of the relaxation time ln(τ) as a function of the inverse temperature T^{-1}. The straight blue line is a fit of the 10 points at highest temperatures to the Arrhenius law ln(τ) = ln(τ_0) + U_{eff}/k_BT with τ_0 = 3.89·10^{-8} s and U_{eff} = 118 cm^{-1}. The green line is the fit to the sum of Raman and Orbach processes τ^{-1} = CT^n + τ_0^{-1}exp(–U_{eff}/k_BT) with C = 0.087, n = 3.65, τ_0^{-1} = 1.31·10^{10} s^{-1} and U_{eff} = 230 cm^{-1} (fixed). The dashed and dotted grey lines are the Orbach and Raman contributions, respectively. The insert shows the energies of the m_S states as a function of the m_S quantum number and schematically displays the Orbach and Raman relaxation pathways. Horizontal lines correspond to energy levels and red arrows illustrate the magnetic moment.[56]

The linear regime of the Arrhenius law yielded values of U_{eff} = 170 K and τ_0 = 3.9·10^{-8} s, reported by the authors as the highest value of effective energy barrier amongst previously reported tetra-coordinated Co^{II} zero-field SMMs. Performing far-infrared transmission measurements, an apparent field-dependent absorption near 230 cm^{-1} was detected (figure

20), allowing to determine the energy barrier of spin reversal of U_{eff} = 230 K. Fixing this value in the fitting procedure of Orbach and Raman processes yielded the best fitted values C = 0.09, n = 3.65 and $\tau_0^{-1} = 9.1 \cdot 10^9$ s^{-1}.[56]

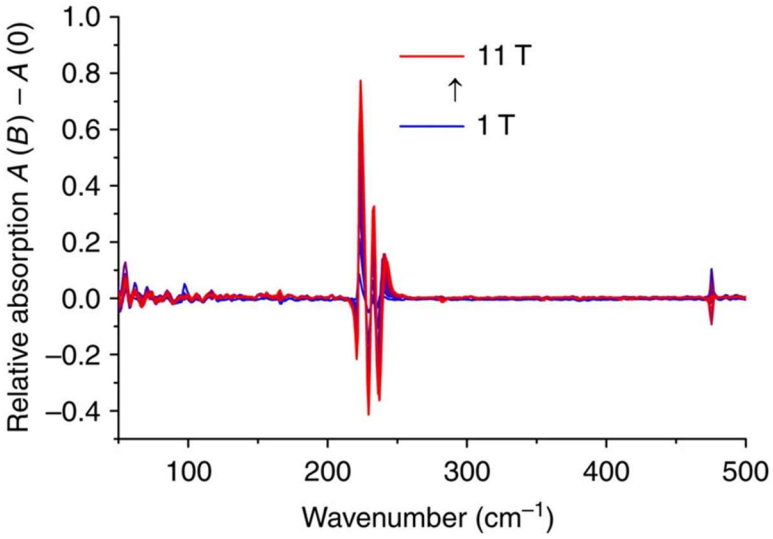

Figure 21 Normalized far-infrared absorption spectra recorded on a pressed powder sample of **XII** at T = 4 K, obtained by subtracting the zero-field absorption spectrum from absorption spectra at different fields.[56]

A series of tetrahedral Co^{II} SIMs with thiourea-based ligands (figure 22) has been studied in 2016 by Vaidya et al., using a rational design aimed to stabilize an Ising-type magnetic anisotropy (negative *D*).[57]

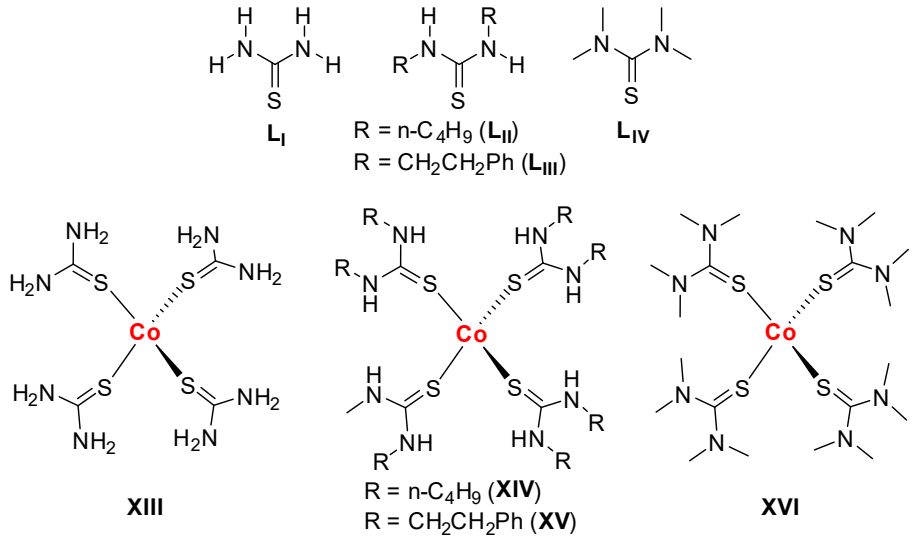

Figure 22 (Top) Sulfur-based ligands (L_I–L_{IV}) employed to isolate T_d Co^{II} complexes **XIII**-**XV** (bottom).

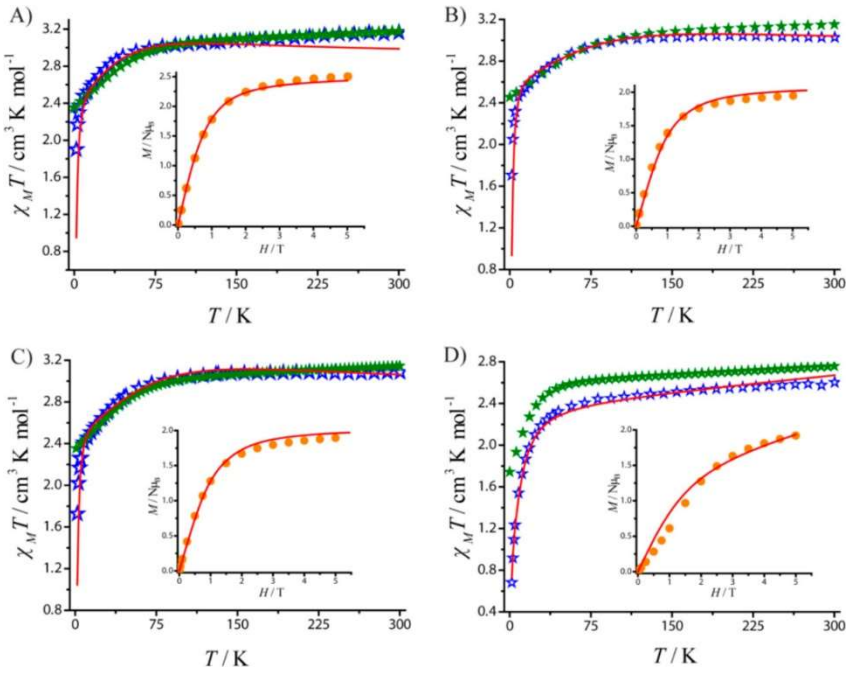

Figure 23 Temperature-dependent magnetic susceptibility plots, with measurements performed on polycrystalline samples of **XIII**-**XVI**, respectively (Hdc = 1.0 T). Open star symbols (blue) represent the experimental magnetic data, and filled star symbols (green) represent χ_MT computed from CASSCF calculations. Insets: Field-dependent magnetization data collected on polycrystalline samples of complexes **XIII**-**XVI** at 2 K. The solid red lines represent fits of the experimental magnetic data [χ_MT(T)] and the simulation of the magnetization data.[57]

Temperature-dependent dc magnetic susceptibility measurements were performed on the samples and the room temperature values for χ_MT of 3.10, 3.03, 3.08, and 2.60 cm^{3}Kmol^{-1} for complexes **XIII**-**XVI** are higher than the expected values for mononuclear Co^{II} complexes (χT = 1.875 cm^{3}mol^{-1} K). From the fitting, the extracted *D* values resulted consistent with literature reports.[58] Interestingly, it was shown that by increasing the number of soft donors atoms bound to the tetrahedral Co^{II} ion, the magnitude of (negative) *D* also increases (figure 23). Given the large anisotropy parameters, those complexes were finally tested for SIM behaviour via ac susceptibility measurements (figure 24).

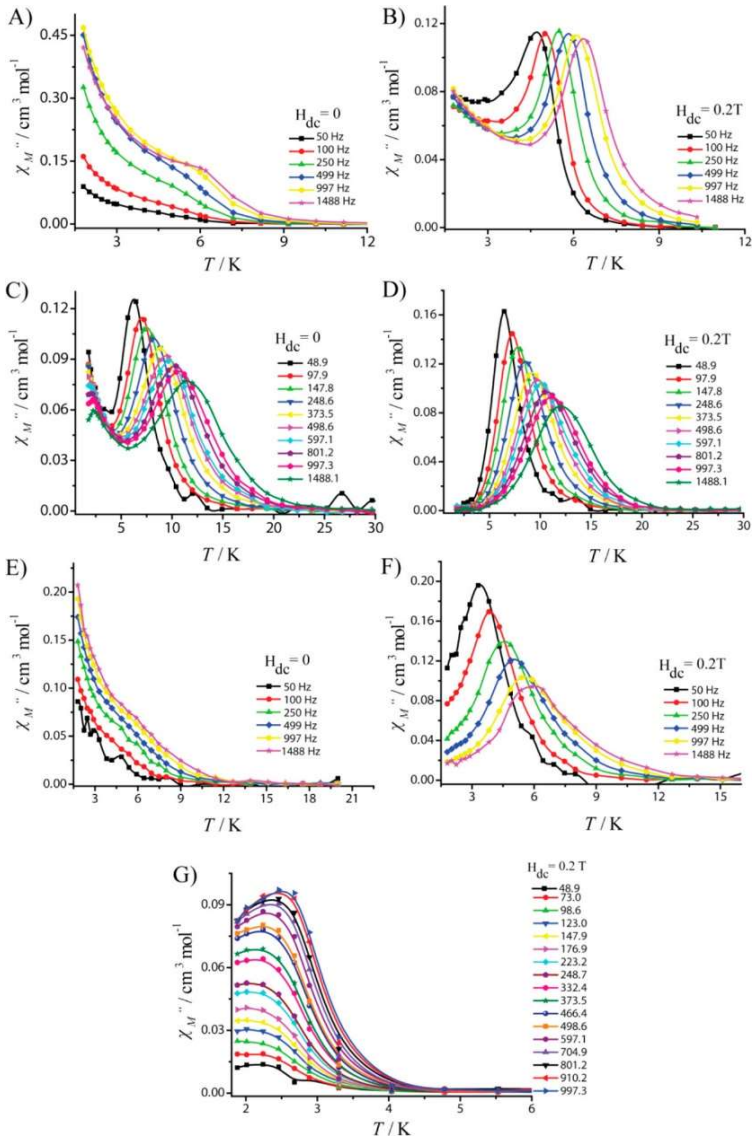

Figure 24 Frequency-dependent out-of-phase susceptibility signals for complexes **XIII**–**XV** in zero dc field (panels A, C, and E, respectively) and in the presence of 0.2 T of a dc bias field for complexes **XIII** –**XVI** (panels B, D, F, and G, respectively).[57]

These measurements showed SMM behaviour of compound **XIV** at zero field applied and of compound **XVI** as field-induced, proving the rational synthetic approach to lead to improved magnetic behaviour, offering enhanced *D* value to achieve new generations of tetrahedral Co^{II} SIMs.

2. Thesis outline

An efficient NiFe catalyst based on a bipyridine moiety has been published by Brazzolotto et al. in collaboration with the Meyer group in 2016, exhibiting ligand-based redox chemistry.[34] Part of this thesis work aims to develop a novel synthetic redox-innocent NiFe model by replacing the bipyridine with a bidentate N-heterocyclic carbene (NHC) moiety in the ligand scaffold. The strong σ-donor and flexible π-acceptor character of the NHC as well as its redox-innocent nature are potentially beneficial to impart high stability and to support metal-centered redox chemistry. The first goal of this thesis work is the development of a bis-NHC system equipped with two dangling thiolate groups, able to chelate the Ni^{II} ion, and potentially bridging two metal ions in close proximity, mimicking the active site of the [NiFe]H_2ase. Having the mechanism for electrocatalysis towards H_2 evolution using **II_A** proposed by Duboc´s group as blueprints, the synthesis of a bis-NHC functionalized with two alcoholate sidearms for comparison is proposed as a second goal of this thesis (figure 25).[36]

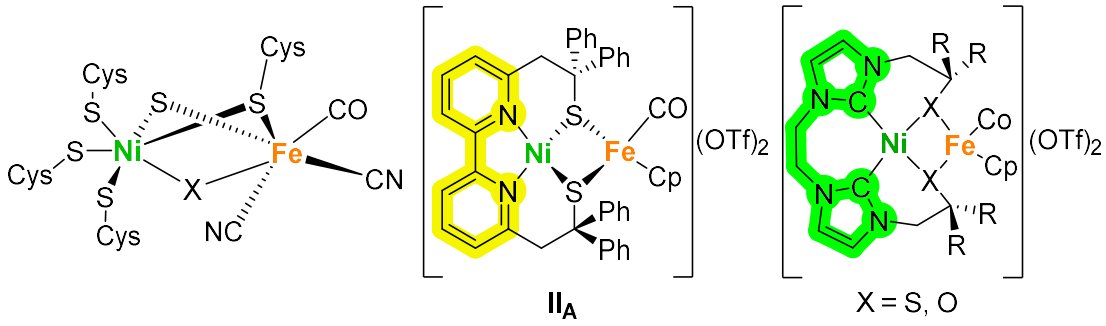

II_A X = S, O

Figure 25 Active site of [NiFe]H_2ase (left); [NiFe]H_2ase mimic complex **II_A** (middle); target H_2ase model analogues (right).

The first chapter focuses on the synthesis of the bis-imidazolinium dithiolate proligand $[L^SH_4](OTf)_2$ and its characterization. Several complexations attempts with different metal ions and following different synthetic pathways will be discussed.

In the second chapter, the synthesis of the $[L^OH_4](OTf)_2$ proligand is proposed, and a target Ni^{II} complex will be isolated and characterized (figure 26, left). The neutral $[L^ONi]$ unit will be used for the complexations of 3d metal ions, such as Fe^{II} and Co^{II}, to build target bimetallic systems (figure 26, middle), and the potential reactivity towards electrocatalytic H_2 production will be probed and discussed.

The neutral [L^{O}Ni] will be used, in the third chapter, to build up a series of trimetallic complexes of 3d metal ions, such as Fe^{II} and Co^{II}, targetting an unusual $\{O\}_4$-ligated metal system, where two units of [L^{O}Ni] are acting as metalloligands (figure 26, right).

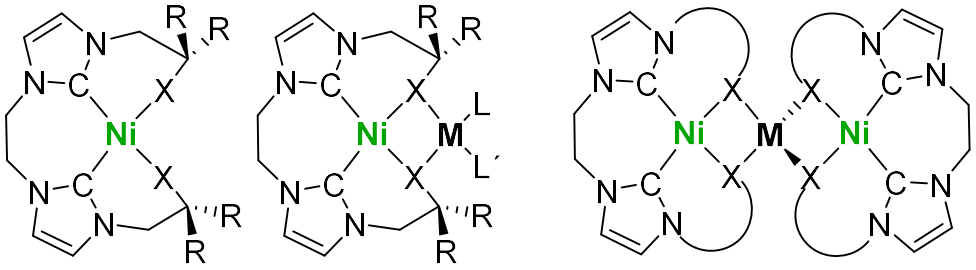

Figure 26 [L^{X}Ni] unit complex (X = S, O) (left); proposed structure of target binuclear (middle) and trinuclear (right) complexes (M = Fe^{II} or Co^{II}).

3. Synthesis of a potential $[L^SH_4](OTf)_2$ ligand and complexations attempts

3.1. Introduction

The first objective of this work is a new synthetic [NiFe]Hydrogenase model[59], featuring a novel ligand that is innocent towards redox processes. For this reason, the target ligand scaffold is constituted of two N-heterocyclic carbenes (NHC) moieties that provide a chelating site that cannot be affected by redox processes. The strong σ-donor and flexible π-acceptor character of the NHCs are potentially beneficial to impart high stability and to support metal-centered redox chemistry. To the two NHCs, sidearms equipped with thiolate functions are attached, in order to emulate the binding site of the cysteine present in the active site of the natural enzyme. The structural properties of the new carbene-thiolate ligand will be described in detail, focusing on NMR spectroscopy and X-Ray diffraction analysis.

With the new ligand, the synthesis of a Ni^{II} complex is going to be attempted and, after the full characterization, the synthesis of the [NiFe] hydrogenase model can be attempted. To that end, a precursory Fe^{II} complex is prepared following a published procedure[60], and then the coupling of the prepared precursor with the nickel complex is aimed. However, the synthesis of these complexes can be considered challenging, therefore in this chapter, multiple synthetic routes leading to complexation are discussed.

3.2. Synthesis of the tetradentate bis(imidazolinium)-dithiol proligand $[L^SH_4](OTf)_2$

The preparation of the ligand precursor **1** is a one-step synthetic procedure. First, a solution of imidazole in dry toluene was heated at the reflux temperature (111°C) to allow solubility, followed by a dropwise addition of a solution of isobutylene sulfide in dry toluene. The reaction involves the opening of a very reactive thiirane, with the driving force behind the ring opening residing in the presence of the two methyl groups on one of the carbons. The steric hindrance of one of the carbons allows the selective one-side opening of the thiirane resulting in the formation of only one final isomer. The precursor **1** was characterized via ^{1}H NMR spectroscopy and ESI(+) mass spectrometry (see appendix figure 1 and 2) and used for the second step of the synthesis, consisting of bridging two units of the precursor with 1,2-bis(trifuoromethylsulfonyloxyl)ethane; the latter was prepared according to the literature[61]. The S_N2 reaction gives the proligand **2** $[L^SH_4](OTf)_2$ quantitatively as a hygroscopic oil, that was then dried and re-crystallized, followed by anion exchange to yield **3** (Scheme 2).

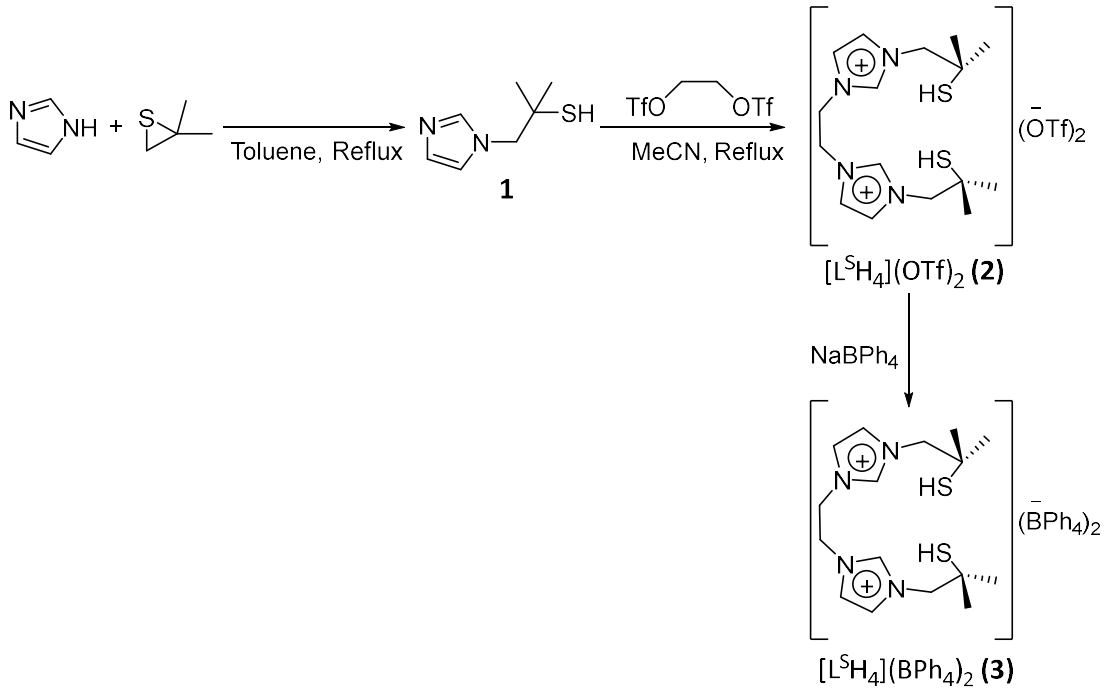

Scheme 2 Synthetic scheme for proligand [$\mathbf{L^SH_4}$].

The final product was analyzed via NMR spectroscopy, ESI-MS, and also X-Ray Diffraction.

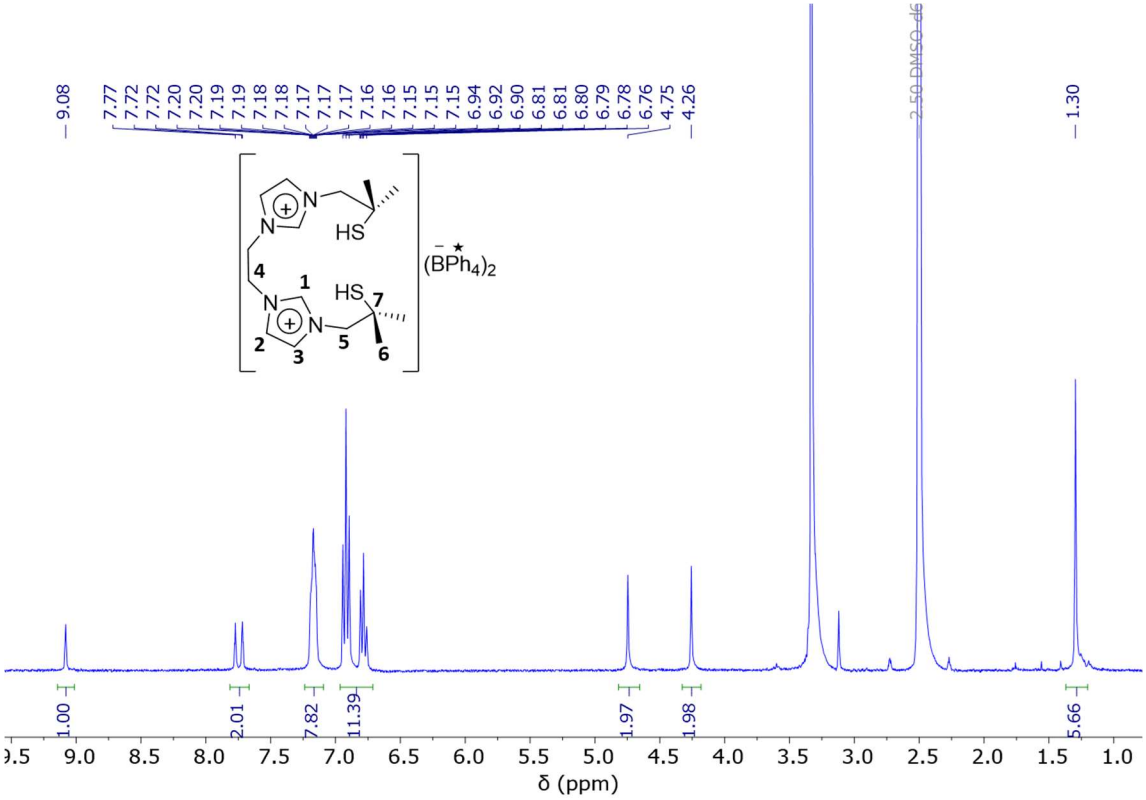

Figure 27 ^{1}H NMR of **3** in DMSO-d_6; solvent (DMSO) peak at 2.50 ppm, water peak at 3.33 ppm; the star-labelled signals belong to the BPh_4 counter-anions.

The ^{1}H NMR spectrum confirms the identity of the product. In solution, **3** has a two-fold symmetry so the two subunits are magnetically identical. The singlet at 9.08 ppm confirms the presence of a de-shielded H atom and this is in line with it being bound to an imidazolinium ion. The spectrum shows that there is only one set of imidazole signals and two sets of CH_2 protons, assigned to the sidearm and the bridging unit, while at high field there is the signal belonging to the 6 H from the methyl groups. In the aromatic region, the star-labelled signals belong to the counter-anion. The signal from the proton of the SH group is not present in the spectrum, due to fast exchange with the deuterated solvent.

The ESI(+) spectrum shows a peak at 489.13 m/z, belonging to the $[L^{S}H_4]^{2+}$ fragment (see appendix figure 8).

In addition, single crystals suitable for X-ray diffraction were obtained via diffusion of Et_2O in a solution of MeCN.

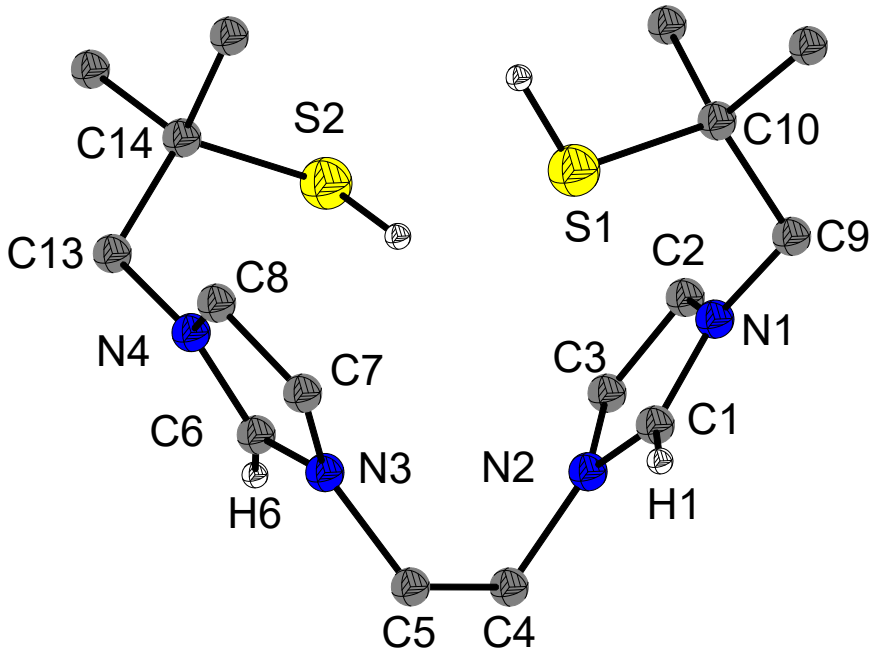

Figure 28 Molecular structure of **[L^SH_4]** determined by X-Ray diffraction; H atoms are omitted except the imidazolinium protons and thiol protons are shown. Counteranions are omitted.

The X-ray diffraction data showed that compound **3** crystallizes in the monoclinic space group Cc, with 4 molecules per unit cell. Significant bond lengths are reported in table 1.

Table 1 Relevant bond lengths for **3.**

Atoms	Bond lengths [Å]
S2-C14	1.810(12)
S1-C10	1.813(12)
N3-C6	1.336(12)
N3-C5	1.492(13)
N2-C1	1.327(12)
N2-C4	1.459(13)
C7-C8	1.381(15)
C2-C3	1.340(16)
N4-C13	1.488(12)
N1-C9	1.448(13)
N1-C1	1.327(13)
N4-C6	1.315(13)
C4-C5	1.510(15)

The S1-C10 and S2-C14 bond length are in accordance with the average C-S single bonds.[62] The bonds C8-C7 and C2-C3 are evidently shorter compared to the other C-C bonds, confirming the double bond character. In the {CH_2CH_2] bridge, the distance between C4 and C5 is 1.51 Å, typical for C-C single bonds.[63] In the imidazole ring, the distance between N3 and C6 (1.336 Å), as also between N4 and C6 (1.315 Å) is significantly lower than the standard C-N single bond distance[64], which can be attributed to a resonating double bond in the imidazole ring. The bond between C13 and N4 is longer and fits the average value of an N-C single bond[64]. Further details about other bond lengths and all the bond angles can be found in tables 1, 2 and 3 in the appendix.

3.3. Complexation attempts with $[L^SH_4](OTf)_2$

To avoid lowering the yield of the ligand synthesis by performing the anion exchange step, for subsequent complexation reactions, proligand $[L^SH_4](OTf)_2$ (**2**) was selected instead of proligand **3**. The primary goal was to obtain the Ni^{II} complex $[L^SNi]$ as a starting building block for a [NiFe]-Hydrogenase model. The first approach was to make an Ag or Cu complex, starting from their respective oxides, and then attempt a trans-metalation to get a Ni complex (Scheme 3).

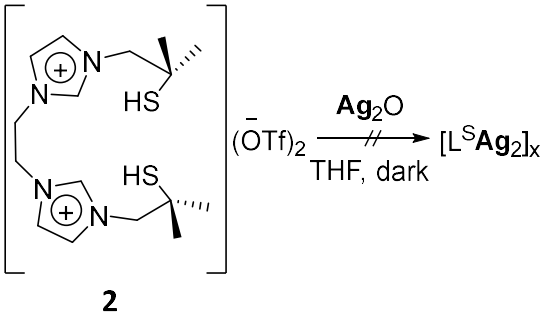

2

Scheme 3 Reaction of proligand **2** with Ag_2O.

The reaction was done with brown-glass glassware, because of the light sensitive Ag reagent. After the work-up, the solid obtained was analyzed by NMR spectroscopy and ESI(+) mass spectrometry. However, from the analysis obtained, the desired product could be identified.

A second reaction attempt was made to make a copper complex, with Cu_2O.

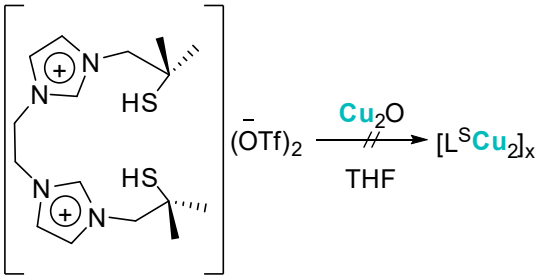

2

Scheme 4 Reaction of proligand **2** with Cu_2O.

In this case, ^1H NMR spectroscopy was not suitable for the analysis, given the paramagnetic nature of the crude product. By other techniques, such as Mass Spectrometry, it was not possible to reveal the presence of the desired product.

A second approach was the direct metalation of the ligand with different Ni salts.

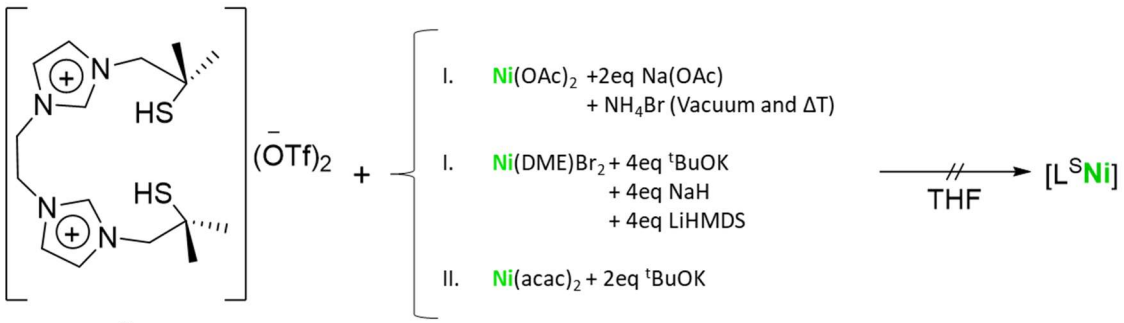

2

Figure 29 Reaction of proligand **2** with different Ni^{II} precursors.

Different types of nickel precursors were used, some containing an inner base, some with the addition of an external base in presence of the metal salt. Despite many attempts, the synthesis of the desired complex [L^SNi] could not be achieved.

To investigate the capability of proligand **2** towards complexation using other metal ions, a reaction with an Fe^{II} salt was prepared, to aim for a [L^SFe] complex.

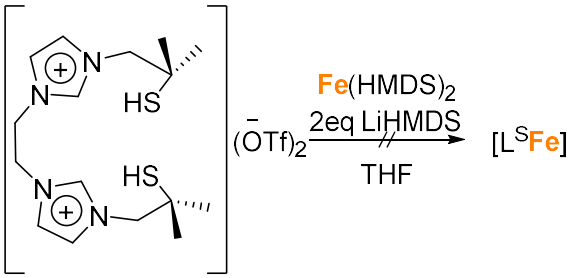

2

Scheme 5 Reaction of proligand **2** with an Fe^{II} precursor.

$Fe(HMDS)_2$ contains two equivalents of an internal base, therefore two additional equivalents of LiHMDS were added, in order to reach the proper stoichiometry. From the analysis of the crude mixture, it was not possible to identify the desired product, and only decomposition was observed.

In order to monitor the reaction using ^{1}H NMR spectroscopy due to the diamagnetic nature of the resulting products, the reaction of proligand **2** with a Pt^{II} salt has been followed.

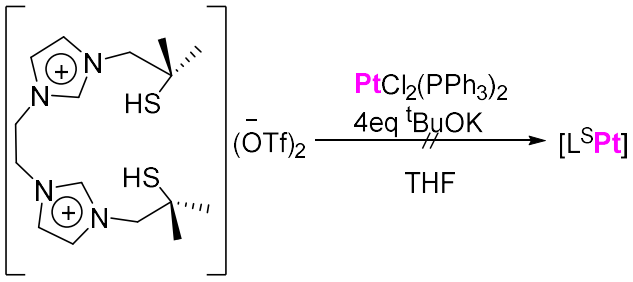

2

Scheme 6 Reaction of proligand **2** with Pt^{II} salt.

The Pt^{II} precursor is a pre-organized phosphine complex, chosen for its high solubility in organic media. Again, the desired product was not obtained, and from the NMR data, it was not possible to identify proton signals corresponding to the starting materials probably due to the immediate decomposition of the ligand in presence of a base. To investigate this, an attempt to isolate the free carbene from proligand **2** was made.

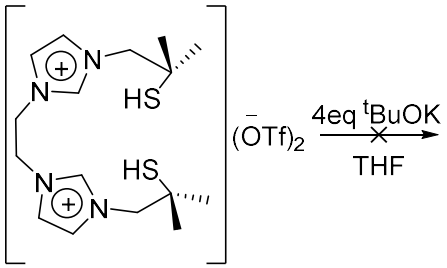

2

Scheme 7 Reaction of proligand **2** with a base.

Upon the addition of 4 equivalents of potassium tert-butoxide to proligand **2**, immediate decomposition of the starting material was noted. Due to the positive charge of the imidazolinium, it is possible that the de-protonation might cause the elimination of the sidearm, which is a good leaving group in this reaction. A scheme of the hypothetical mechanism is shown in figure 30:

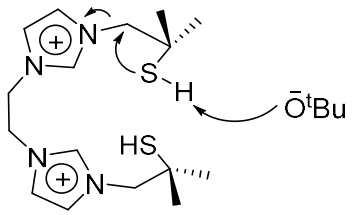

Figure 30 Possible mechanism for sidearm elimination.

The analysis of the crude mixture after the addition of the base did not lead to the identification of the predicted free carbene product.

Given the high instability of this ligand in presence of a base, a third approach for the complexation was used. In this case, no base was used, and the complexation was tested via oxidative addition to a Ni^0 precursor.

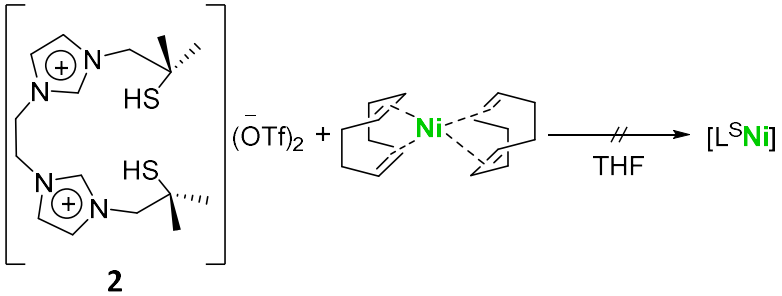

2

Scheme 8 Reaction of proligand **2** with $Ni(COD)_2$.

This reaction was performed in a glovebox, under Ar atmosphere, given the air sensitivity of the Ni^0 reagent. From the analysis of the crude mixture, the desired product was not identified.

3.4. Summary

The new bis-imidazolinium proligand $[L^SH_4](OTf)_2$ **2**, which was designed to serve as a tetradentate bis(NHC)-dithiolato ligand, was successfully synthesized. Its analogous (BPh_4) salt **3** has been fully characterized, focusing on NMR spectroscopy and X-ray diffraction analysis. Figure 29 summarizes all the complexation attempts made using proligand **2**.

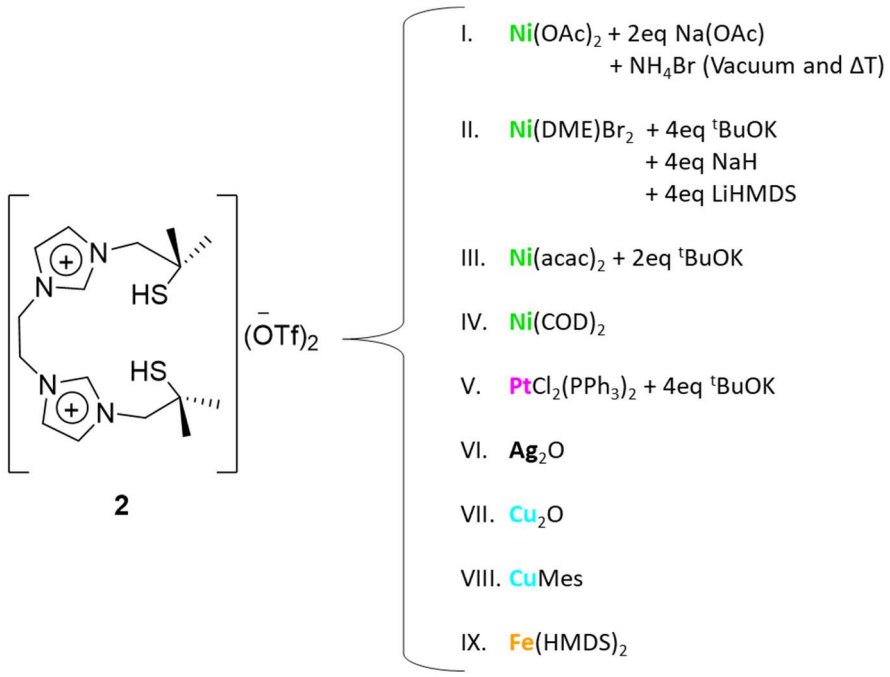

Figure 31 Summary of all reaction attempts for proligand **2**.

Despite the many attempts made, it has been proven impossible so far to synthesize any complex using proligand $[L^SH_4]$. Therefore, as described in the next chapter, a new ligand system was designed.

4. Synthesis of $[L^{O}H_4](OTf)_2$ proligand and bimetallic complexes

4.1. Introduction

A novel proligand $[L^{O}H_4](OTf)_2$ (**4**), structurally analogous to ligand **2,** has been designed bearing two NHCs moieties equipped with two alcoholate groups, with bulky phenyl substituents in α-position. In light of the reviewed mechanism for electrocatalytical H_2 production proposed by Duboc´s group (chapter 1.5., figure 11), highlighting the role of the bridging S-donor atom during the catalytic process, $[L^{O}H_4](OTf)_2$ (**4**) with its bridging O-atoms may be used for comparison. The structural properties of $[L^{O}H_4](OTf)_2$ will be described focusing on NMR spectroscopy and X-ray diffraction analysis.

The Ni^{II} complex $[L^{O}NiK(MeCN)(OTf)]$ (**5**) is isolated and its structural features are presented. Particular focus is given to the electrochemical properties of the complex, and its potential to serve as a catalyst for the hydrogen oxidation reaction (HOR) is investigated.

Exploiting the ability of the $L^{O}Ni$ unit to serve as an {O,O´}-chelating metalloligand, the bimetallic complexes containing Fe^{II} $[L^{O}NiFe](OTf)_2(acetone)_2$ (**8**) and Co^{II} $[L^{O}NiCo](MeCN)(I)_2$ (**9**) are prepared and characterized by different spectroscopic techniques.

Having insights into the electrochemical properties, an experiment to investigate the potential catalytic activity of the $[L^{O}NiFe](OTf)_2(acetone)_2$ complex towards hydrogen evolution reaction (HER) production will be discussed.

4.2. Synthesis of tetradentate bis-carbene dialcoholate ligand $[L^{O}H_4](OTf)_2$

The synthesis of $[L^{O}H_4](OTf)_2$ consists of two steps to get precursor **XVIII** following the reported literature procedure[65] and a final coupling step. Chloromethyltrimethylsilane is commercially available but in order to increase the yield of the reaction, the iodo analogue was prepared by conducting a Finkelstein reaction, with NaI in acetone, as described in literature.[66] Imidazole was dissolved and deprotonated with ^{n}BuLi, under Ar atmosphere, and then the freshly prepared Iodomethyltrimethylsilane was added giving compound **XVII**. Subsequent addition of a mixture of benzophenone and ^{t}BuOK, lead to the alcohol precursor **XVIII**. The last step of the reaction is analogous to the last step for the synthesis of **2** discussed in Chapter 3.2., consisting of the coupling of two substituted imidazole units with 1,2-bis(trifluoromethylsulfonyloxyl)ethane. The product was obtained as a clear oil and, after drying and recrystallization, as a white hygroscopic powder (Scheme 9).

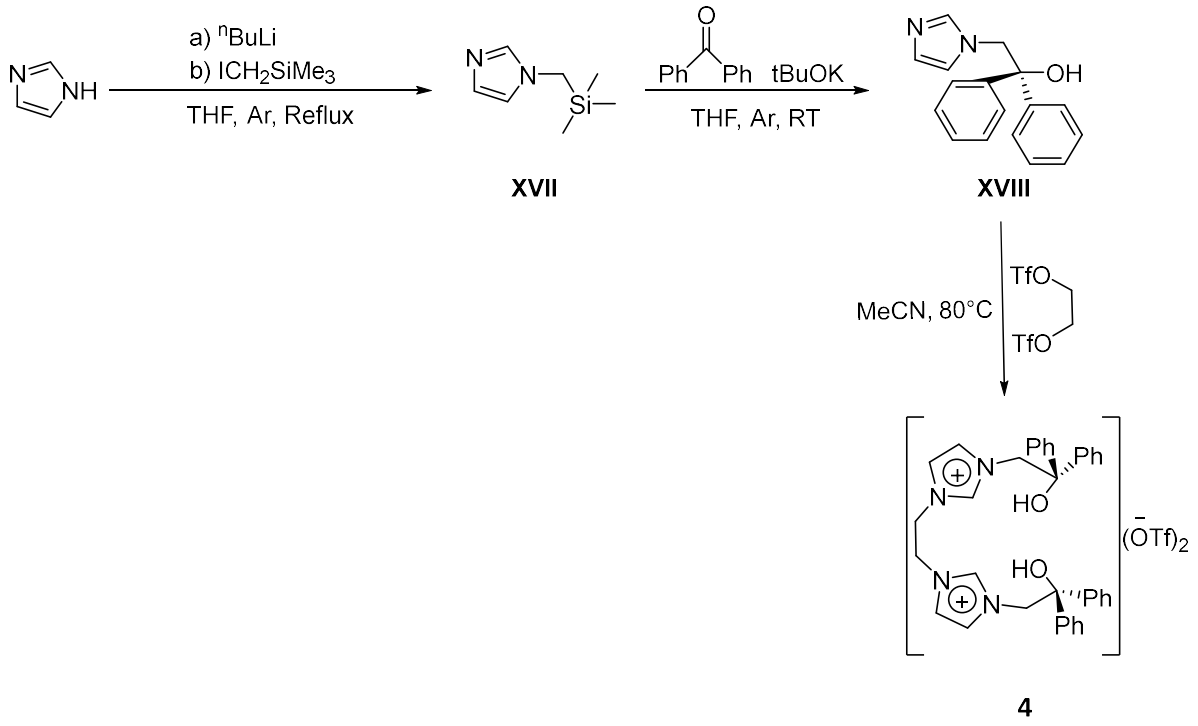

4

Scheme 9 Synthetic scheme for proligand $[L^{O}H_4](OTf)_2$ **4**.

The product was then characterized via NMR, ESI-MS and MALDI-MS.

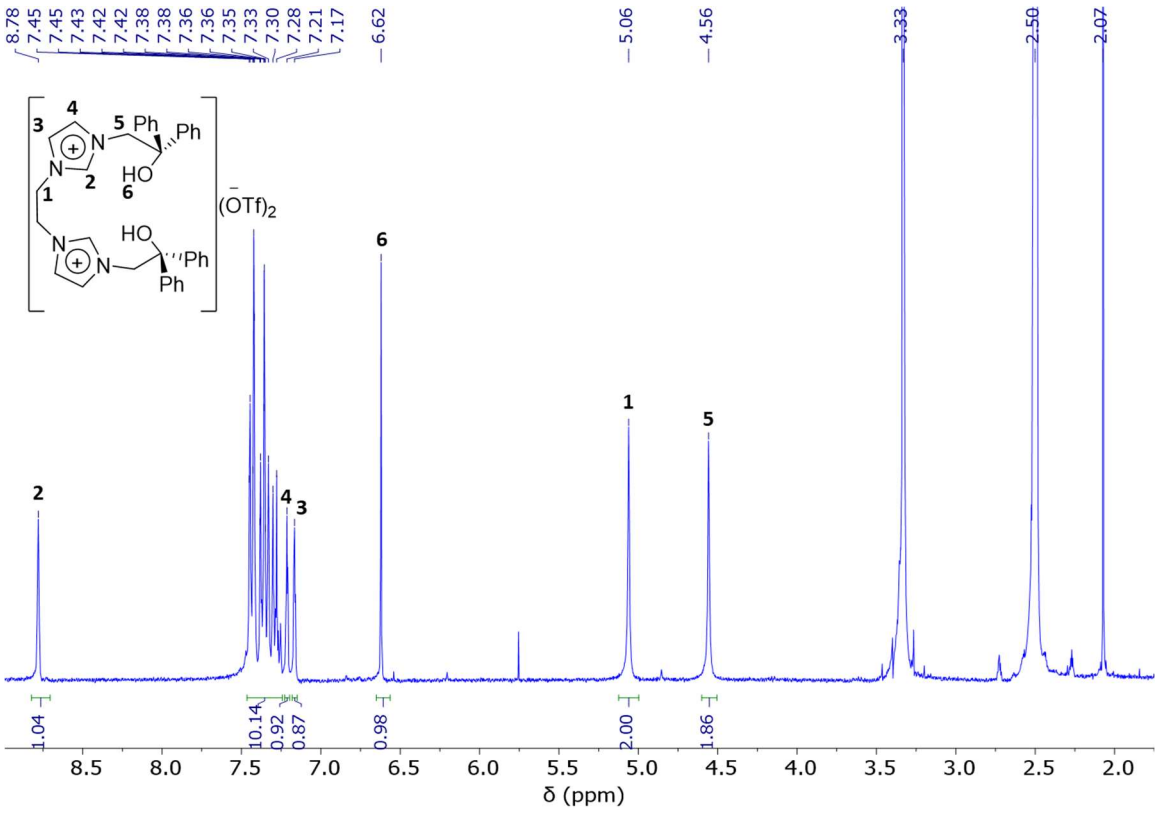

Figure 32 ^{1}H NMR spectrum of **4** in DMSO-d_6. DMSO peak at 2.50 ppm, acetone peak at 2.07 ppm and water peak at 3.33 ppm.

Similarly to **3**, the ^{1}H NMR spectrum of **4** also shows characteristic signals of the product, which shows two-fold symmetry. The imidazolinium proton resonates at low field (8.78 ppm) and the signals at 4.56 ppm and 5.06 ppm belong to the two sets of aliphatic protons 5 and 1 respectively. In contrast to the spectrum of **3** where, due to fast exchange with the solvent, the thiol proton could not be detected, in this case, the alcohol proton signal is present and resonates at 6.62 ppm. The signals from the proton of the imidazole backbone moiety, and all the signals from the phenyl rings adjacent to the OH group, can be identified in the region between 8.78-7.17 ppm.

From the MALDI-MS data, the peak at 705.4 m/z was assigned to the mass of the $[L^{O}H_4(OTf)]^{+}$ ion (Appendix figure 12).

All additional spectra for characterization of **4** are listed in the Appendix.

4.3. Synthesis of [L^{O}NiK(MeCN)(OTf)] complex

Proligand [L^{O}H$_4$](OTf)$_2$ (**4)** was used for the complexation of Ni^{II}. Analogously to ligand **2**, **4** in presence of base undergoes decomposition. Therefore, the de-protonation of the ligand must be performed in presence of the metal salt fully dissolved in the solution. The [L^{O}NiK](MeCN)(OTf) complex was synthesized by adding potassium tert-butoxide to a solution of [L^{O}H$_4$](OTf)$_2$ and Ni(DME)Br$_2$ in THF, exploiting the high solubility of the metal salt in organic media. Potassium tert-butoxide was chosen as a strong base for carbene generation and alcohol de-protonation. The product was obtained as a yellow solid and, by slow diffusion of Et$_2$O in a MeCN solution, single crystals suitable for analysis were obtained (Scheme 10).

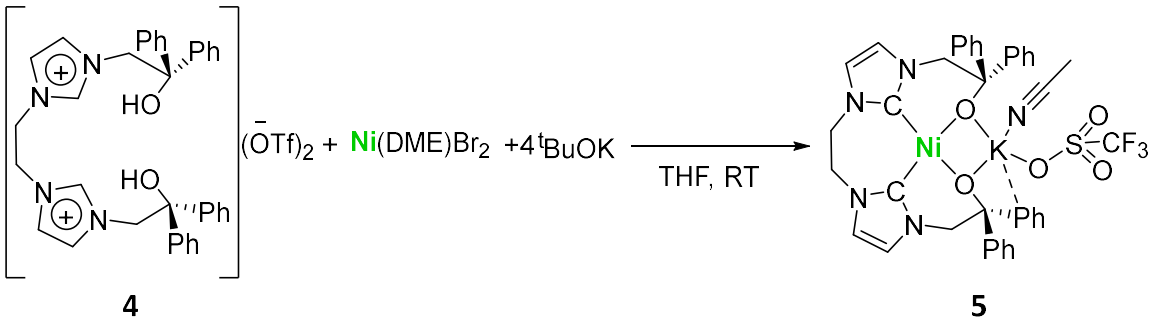

Scheme 10 Synthetic scheme of complex **5.**

Complex [L^{O}NiK](MeCN)(OTf) **5** was characterized by NMR spectroscopy, UV/Vis spectroscopy, ESI-MS spectrometry and X-ray diffraction.

Suitable single crystals of **5** were analyzed to obtain structural parameters.

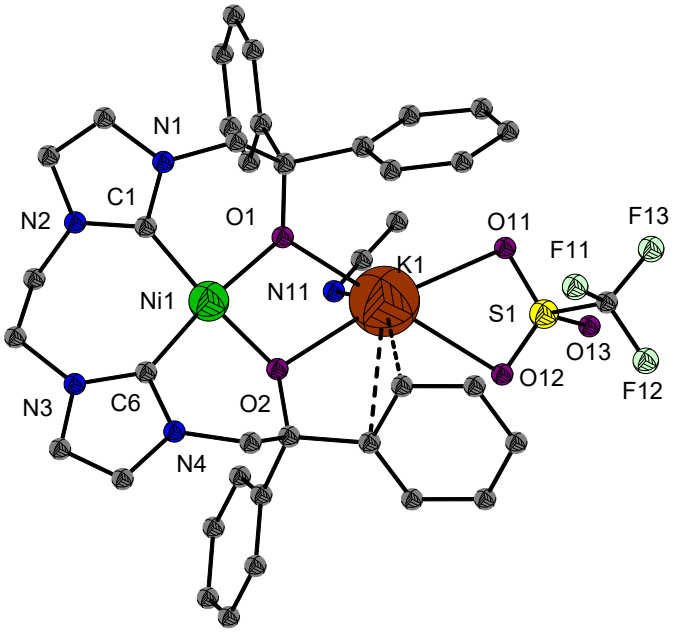

Figure 33 Molecular structure of [L^{O}NiK](MeCN)(OTf) complex **5**; hydrogen atoms are omitted for clarity.

The X-ray diffraction data show complex **5** crystallizes in the monoclinic space group $P2_1/c$, with 4 molecules per unit cell. Significant bonds and angles are reported in table 2.

Table 2 Relevant bond lengths [Å] and bond angles [°] for **5**.

Atoms	Bond lengths [Å]	Atoms	Bond angles [°]
Ni1-C1	1.8462(15)	C1-Ni1-O1	90.85
Ni1-O1	1.8733(11)	C1-Ni1-O2	170.56
Ni1-O2	1.8843(11)	O1-Ni1-O2	82.92
Ni1-C6	1.8862(16)	C1-Ni1-C6	95.38
Ni1-K1	3.6852(4)	O1-Ni1-C6	169.03
K1-O1	2.5967(11)	O2-Ni1-C6	91.93
K1-O2	2.6373(11)	C1-Ni1-K1	129.27
K1-N11	2.812(2)	O1-Ni1-K1	41.46
K1-O12	2.8306(14)	O2-Ni1-K1	42.89
K1-O11	2.9083(15)	C6-Ni1-K1	134.74
K1-C26	3.0891(18)	C10-O1-Ni1	128.96
K1-C25	3.3078(16)	Ni1-O1-K1	110.01
K1-S1	3.3683(6)	C12-O2-Ni1	128.78
K1-C13	3.4490(16)	Ni1-O2-K1	108.02

The Ni^{II} ion is square-planar coordinated by two carbene-C and two O atoms from the alcoholate group, with the angles formed between the metal centre and the donor atoms from the ligand, close to 90°. The bond distances between Ni and the two carbene-C of about 1.846-1.886 Å, are in line with reported values for such complexes.[67] The O atoms from the alcohol group are bridging the Ni^{II} core and a K ion, with binding angles of 110.01° and 108.08°. The K is coordinated in a distorted octahedral fashion to the O atoms from the O,O´chelating L^O, a triflate counteranion, a MeCN solvent molecule and also it has π-interactions with one of the phenyl groups in the backbone of the ligand. The ability of **4** to bind an alkali ion suggests that the [L^ONi] complex may serve as an O-O´-chelating which is of interest in view of a bimetallic [NiFe] complex. Other structural parameters are shown in appendix table 4.

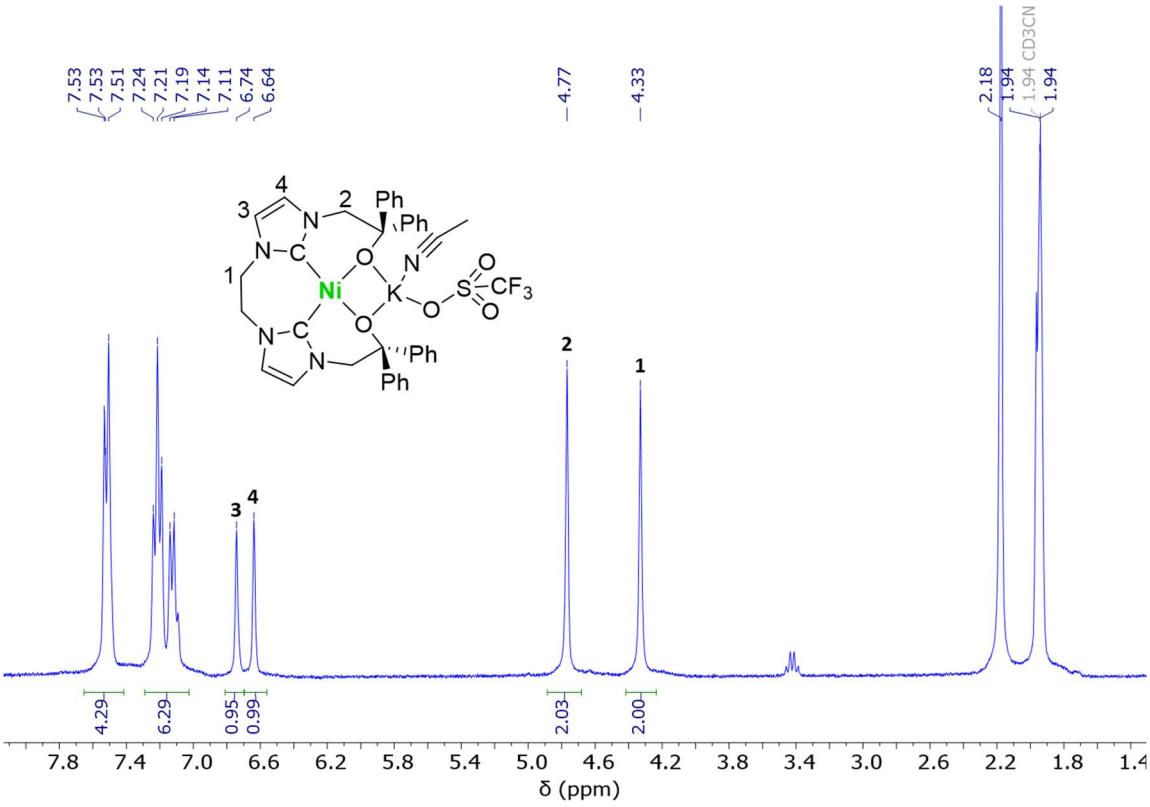

Figure 34 ^{1}H NMR of **5** in CD_3CN. MeCN residual signal at 1.94 ppm, water at 2.18 ppm.

The ^{1}H NMR spectrum of **5** shows two-fold symmetry in solution. In the spectrum, the signals assigned to the carbene protons and the alcohol protons are no longer present, confirming the de-protonation of the ligand. The signals of the two methylene groups are resonating at 4.33 ppm and 4.77 ppm, respectively, and in the aromatic region, the 10 protons from the phenyl substituents can be found, and identification of the two imidazole back-bone protons is possible. The singlets for the CH_2 groups indicate that the coordination at K is labile on NMR

time scale. This is supported by the structural data, reporting K1-O2 and K1-O1 bond distances of 2.60 and 2.63 Å.

The ESI(+) mass spectrum data shows a peak at 611.3 m/z, which is assigned to the $[L^{O}Ni]^{+}$ ion. The spectra are reported in the Appendix section (figure 18).

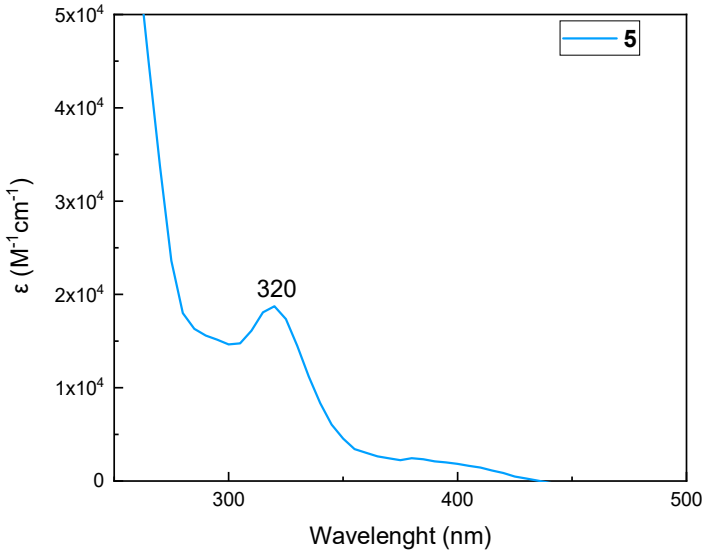

Figure 35 UV-Vis Spectrum of **5** in MeCN at $0.5 \cdot 10^{-5}$ M.

The UV-Vis spectrum of **5** shows an absorption band at λ_{max} = 320 nm, in accordance with bis-NHCs complexes reported in literature.[68] The λ_{max} value was tentatively assigned to ligand to metal charge transfer (LMCT) transition, based on the high molar extinction coefficient ($\varepsilon = 2 \cdot 10^4$ $M^{-1}cm^{-1}$).[69]

In order to investigate the redox properties of [L^{O}NiK](MeCN)(OTf) complex **5**, a complete analysis via cyclic voltammetry was performed in MeCN using Bu_4NPF_6 as electrolyte (0.1 M solution in MeCN).

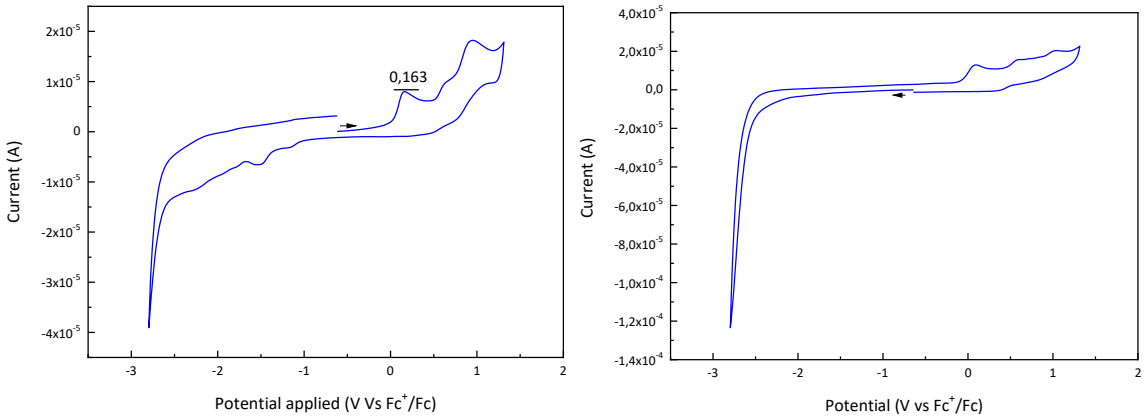

Figure 36 Cyclic voltammogram of **5** in MeCN in the anodic range (+1.2− -2.8) V at scan rate 100 mVs^{-1}. WE: GC; CE: Pt; Ref: Ag (left). Cyclic voltammogram of **5** in the cathodic range (-2.8 − +1.2) V in MeCN at scan rate 100 mVs^{-1}. WE: GC; CE: Pt; Ref: Ag (right).

In the CV in figure 36 (right), no relevant reductive process was observed, therefore the focus of the investigation of the electrochemical properties of complex **5** was given towards oxidative processes (CV in figure 38, left). A relevant oxidation process is noticed at $E_{\mathrm{p}}^{\mathrm{a}}$ = 0.163 V and in order to establish if this oxidation process is located at the metal center or on the backbone of the ligand, a CV of the ligand was recorded under the same conditions (see appendix figure 19). In the cyclic voltammogram of the ligand, this oxidation process was not observed, therefore it is reasonable to assign it to a metal-based process, namely an oxidation from Ni^{II} to Ni^{III}. To get more insight into the reversibility of this redox event, CVs were recorded at different scan rates.

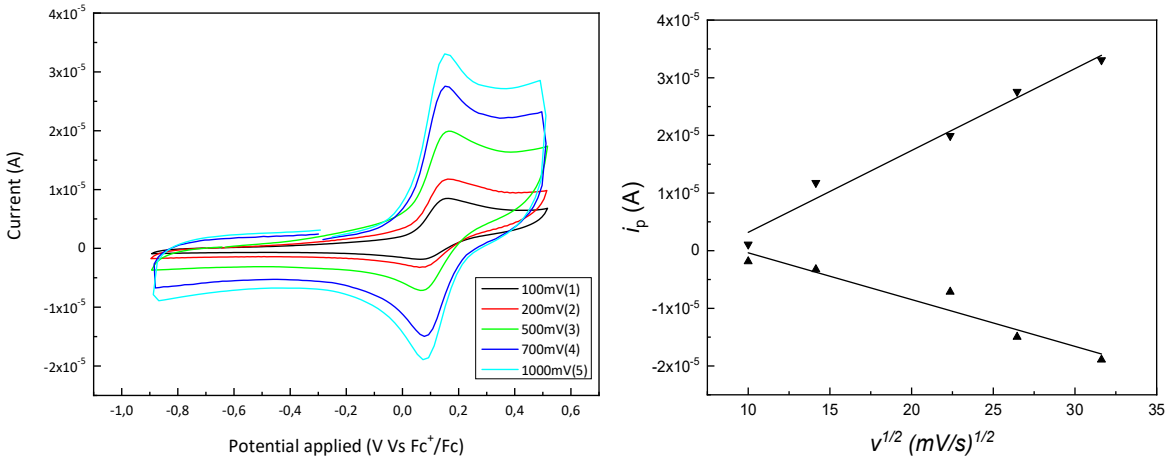

Figure 37 First oxidation process of **5** in MeCN in the oxidative range at different scan rates WE: GC; CE: Pt; Ref: Ag (left); linear fitting plot of peak currents vs square root of scan rates (right).

Figure 37 (left) shows the first oxidation process of complex **5**. To study the reversibility of this process, the peak currents were plotted against the square root of the scan rates (figure 39 right). The plot confirms that this oxidation process gains reversibility upon increasing the scan rate.

An attempt to chemically oxidize **5** was aimed at -30°C in a glovebox with Ar atmosphere in MeCN. $NOBF_4$ was used as oxidizing agent with an oxidation potential of 0.87 V in MeCN (Scheme 11).

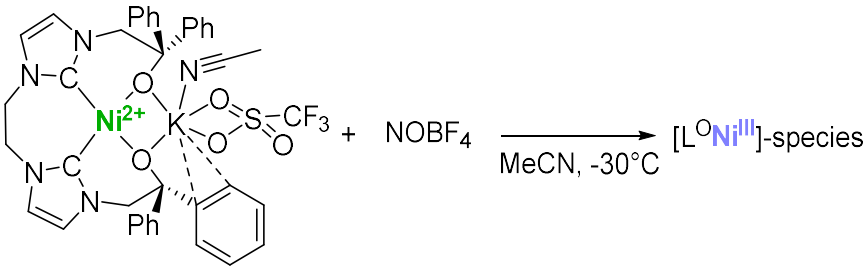

Scheme 11 Chemical Oxidation of [L^ONiK](MeCN)(OTf) complex **5**.

The reaction was monitored by EPR spectroscopy at -30°C and the experimental EPR spectrum as well as the simulated one are reported in figure 40.

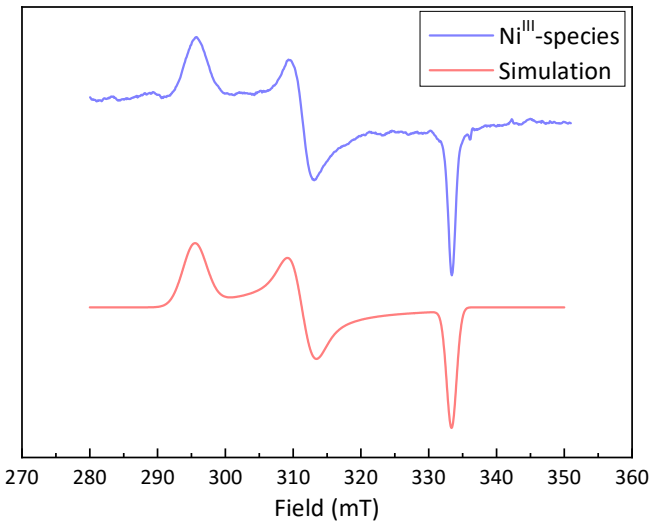

Figure 38 EPR spectrum of [$L^{O}Ni^{III}$]-species; experimental (top) and simulated (bottom) (g_1 = 2.28, g_2 = 2.16, g_3 = 2.02).

The rhombic EPR and relatively large *g* anisotropy (g_1 = 2.28, g_2 = 2.16, g_3 = 2.02) are indicative of a Ni^{III} complex. A comparison with published data from Meyer´s group, by Klawitter et al., confirmed that the *g* values are in line with a Ni^{III} carbene complex.[70]

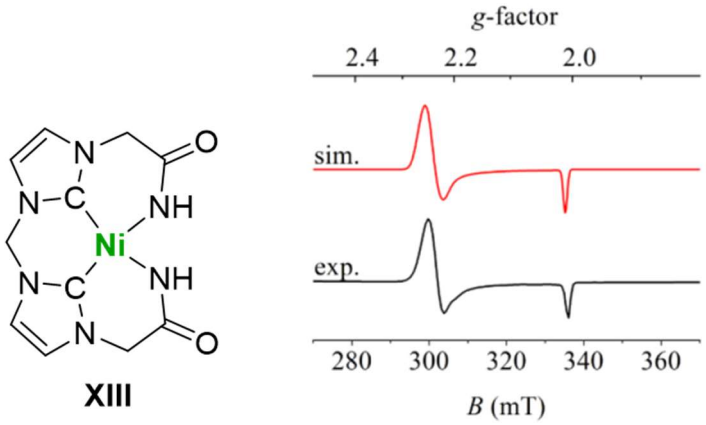

Figure 39 (Left) molecular structure of bis-NHC Ni^{II} complex **XIII**; (right) EPR spectrum of the one-electron-oxidized **XIII** in a frozen solution of water:glycerol (8:2), 0.1 M $NaClO_4$ at 140 K (black line) and simulated spectrum with g_1 = 2.247, g_2 = 2.245, g_3 = 2.011 (red line).

Such EPR signature with large anisotropy and $g_{\perp} > g_{||} \approx 2.0$ is typical for a d^7 Ni^{III} ion and this is also the case for the [$L^{O}Ni^{III}$]-species obtained.

Exploiting the quasi-reversible process shown in figure 37, an experiment for hydrogen oxidation was performed.[71] This experiment will be discussed in the next section.

4.4. Hydrogen Oxidation Reaction (HOR) Experiment with $L^{O}Ni$ complex

The hydrogen oxidation reaction (HOR) is one of the key processes in the direction of sustainable energy storage and conversion devices.[72] In an alkaline environment, HOR is given by:

$$H_2 + 2OH^- \rightarrow 2H_2O + 2e^-$$

Complex **5** has an interesting characteristic oxidation process, from Ni^{II} to Ni^{III} detected by cyclic voltammetry and assigned by EPR spectroscopy. In this section, the catalytic properties of [L^{O}NiK](MeCN)(OTf)complex **5** toward hydrogen oxidation are investigated, via electrochemistry. A suitable base has to be selected for the experiment, able to receive the proton produced in the oxidation, and having an oxidation potential higher than the potential of the first oxidation event in complex **5** (0.167 V vs Fc^+/Fc). For this experiment triethanolamine (TEOA) is selected, which has a first oxidation event occurring at $E_P^a = 0.455$ V vs Fc^+/Fc (CV in figure 40).

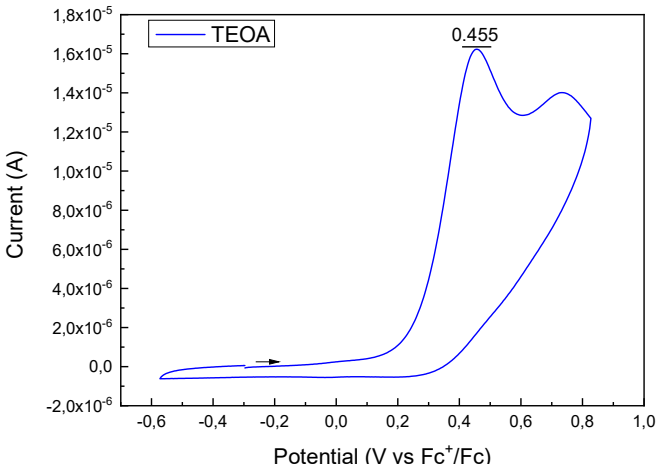

Figure 40 Cyclic Voltammogram of TEOA towards positive potentials (5 mM in MeCN) at scan rate 100 mVs^{-1}. WE: GC; CE: Pt; Ref: Ag. Potentials converted versus Fc^+/Fc.

The experiment is set up by having a 0.5 mM solution of **5** in electrolyte (Bu_4NPF_6 0.1 M in MeCN) in a tight-sealed CV cell, equipped with glassy carbon (Working Electrode), Pt wire (Counter Electrode) and Ag wire (Reference Electrode). H_2 gas is bubbled in the solution, saturating the mixture and the headspace, while also excluding traces of O_2. Using a Hamilton

gas-tight syringe, the equivalents of base were added subsequently. In figure 41, the voltammograms from addition of different equivalents of TEOA are shown.

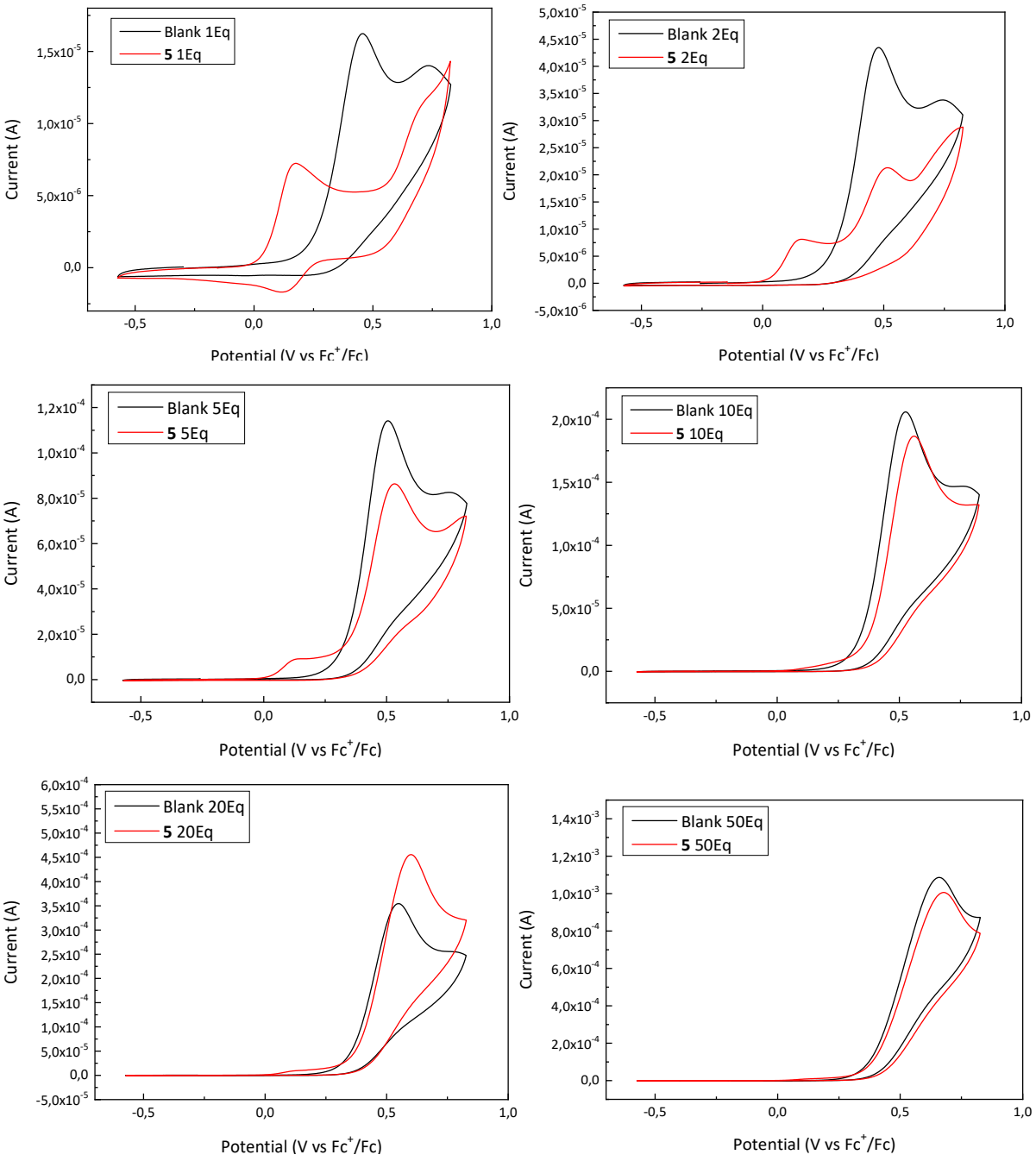

Figure 41 HOR experiment using **5** with 1 equivalent of TEOA (top-left); with 2 equivalents of TEOA (top-right); with 5 equivalents of TEOA (center-left); with 10 equivalents of TEOA (center-right); with 20 equivalents of TEOA (bottom-left); with 50 equivalents of TEOA (bottom-right) in MeCN at 100 mVs^{-1}.

Figure 41 shows the black curve corresponding to the blank electrolyte solution with the addition of different equivalents of TEOA, in order to compare them with the CVs of **5** in presence of TEOA (red curves). During the HOR experiment, no increase of the current along with the addition of more equivalents of base to the solution of complex **5** was achieved. Therefore, it can be stated that, compared to the CV time scale of events, there is no catalytic activity towards H_2 oxidation.

4.5. Synthesis of $[L^{O}NiFe](OTf)_2(acetone)_2$ complex

The Ni^{II} complex **5** was synthesized with in mind the possibility to use it as a starting building block for a [NiFe] model complex. In order to achieve a bimetallic system, a precursor Fe^{II} complex needed to be selected for the reaction with complex **5**. The first choice was $[FeCp(CO)(MeCN)_2]BF_4$, prepared following published work by Duboc et al. .[73] $[FeCp(CO)(MeCN)_2]BF_4$ had been used to synthesize complex **II** (see chapter 1.5), and it was expected to similarly provide the new complex **7**. The reaction was performed in a glovebox under Ar atmosphere, at room temperature.

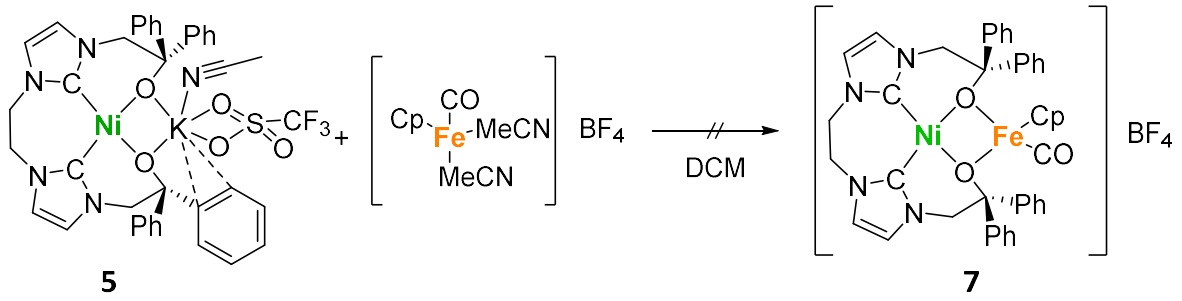

Scheme 12 Coupling reaction of **5** with Fe^{II} precursor complex.

The analysis of the crude of the reaction did not show the formation of **7**, so different synthetic pathways were explored. A second approach to obtain a [NiFe] bimetallic complex was conducted by reaction of compound **5** with one equivalent of $Fe(OTf)_2$, in a glovebox with Ar atmosphere at room temperature (Scheme 13).

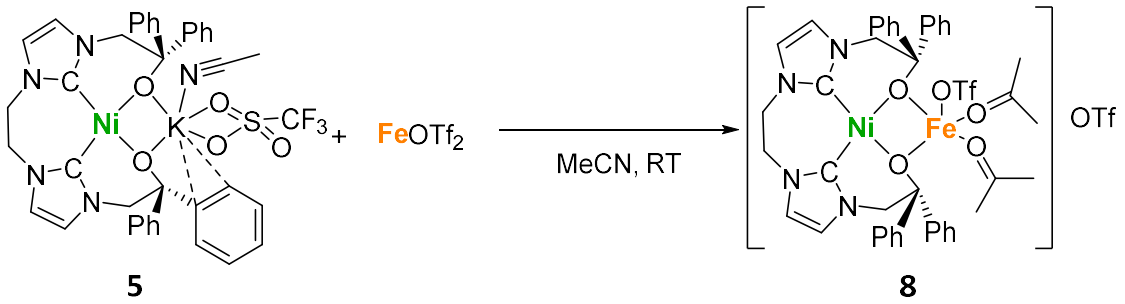

Scheme 13 Synthetic scheme for the formation of $[L^{O}NiFe](OTf)_2(acetone)_2$ complex **8**.

The K^+ ion in complex **5** was cleanly substituted with Fe^{II}, having as a byproduct of the reaction only potassium triflate, which was filtered off during the work-up. Diffusion of Et_2O in a solution of **8** in acetone afforded single crystals suitable for X-ray diffraction analysis.

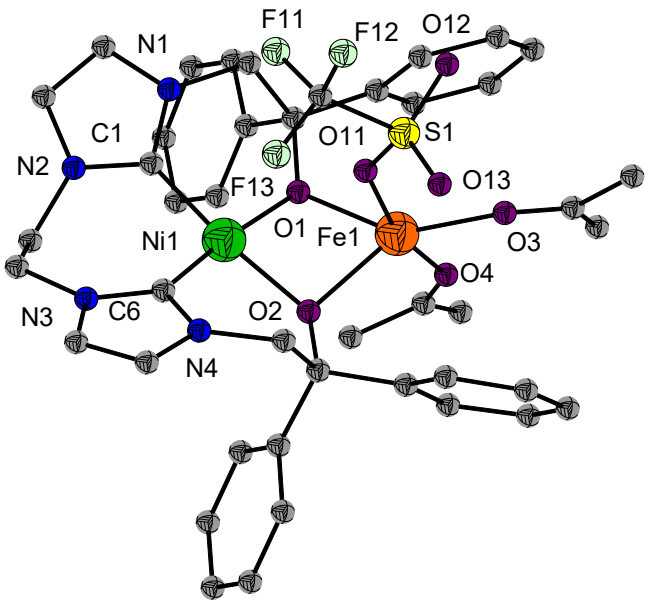

Figure 42 Molecular structure of **8**; hydrogen nuclei are omitted for clarity.

The X-ray diffraction data showed that complex $[L^{O}NiFe](OTf)_2(acetone)_2$ **8** crystallizes in the monoclinic group space $P2_1/n$, with 4 molecules per unit cell. Relevant bond lengths and angles are listed in table 7, focusing on the two metal nuclei.

Table 3 Selected bond lengths [Å] and bond angles [°] for **8**.

Atoms	Bond lengths [Å]	Atoms	Bond angles [°]
Ni1-C1	1.854(4)	C1-Ni1-C6	95.67(19)
Ni1-C6	1.881(4)	C1-Ni1-O1	91.14(16)
Ni1-O1	1.894(3)	C6-Ni1-O1	171.15(16)
Ni1-O2	1.911(3)	C1-Ni1-O2	169.83(17)
Fe1-O3	2.005(3)	C6-Ni1-O2	94.39(16)
Fe1-O1	2.036(3)	O1-Ni1-O2	79.00(12)
Fe1-O2	2.065(3)	C10-O1-Ni1	128.4(3)
Fe1-O4	2.128(4)	Ni1-O1-Fe1	99.06(13)
Fe1-O11	2.237(3)	C24-O2-Ni1	126.3(3)
Ni1-Fe1	2.9909(8)	Ni1-O2-Fe1	97.48(12)
		N1-C1-Ni1	124.3(3)
		N2-C1-Ni1	131.0(3)
		N4-C6-Ni1	119.2(3)
		N3-C6-Ni1	137.4(3)
		O3-Fe1-O1	148.38(13)
		O3-Fe1-O2	136.82(13)
		O1-Fe1-O2	72.33(11)

As previously witnessed with complex **5**, in complex **8** the Nickel core is square-planar coordinated by the two carbene-C and the two alcoholate-O donors of the ligand $[L^{O}]^{2-}$. The binding angles around Ni^{II} are about 90°, consistent with the square-planar configuration. The Fe^{II} ion is in a trigonal bipyramidal configuration, having O1, O2 and O3 as equatorial ligands, while O11 and O4 act as axial ligands. Interesting to notice are the binding angles Ni-O-Fe involving the bridging alcoholate-O, namely 99.06° for Ni1-O1-Fe1 and 97.48° for Ni1-O2-Fe1. The bond lengths Ni1-O1 and Ni1-O2 are comparable to each other, being respectively 1.89 Å and 1.91 Å. The distances Fe1-O1 and Fe1-O2 of 2.03 Å and 2.06 Å are longer compared to the Ni-bridging alcoholate-O distances.

To investigate the number of species obtained, as well as to confirm the oxidation and spin state of the Fe center, ^{57}Fe Mößbauer spectroscopy was used.

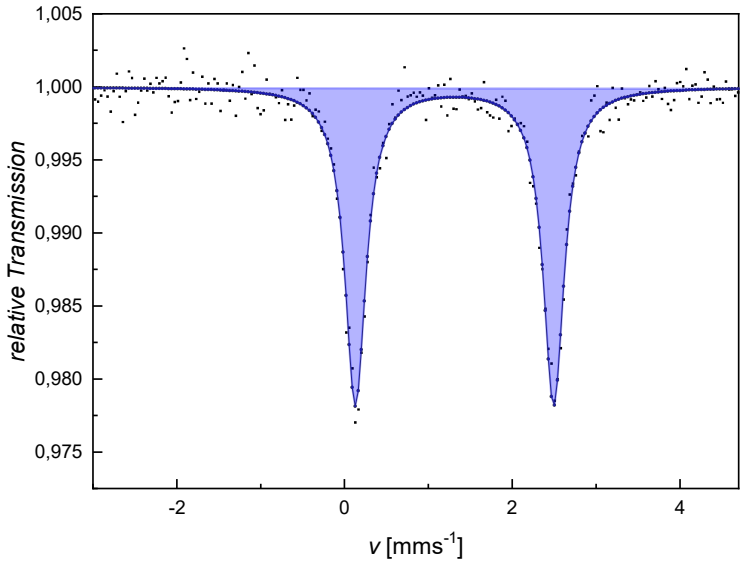

Figure 43 ^{57}Fe Mößbauer spectrum of $[L^{O}NiFe](OTf)_2(acetone)_2$ complex **8** in solid state.

In figure 43, the ^{57}Fe Mößbauer spectrum of solid **8** is shown. An isomer shift (IS) of 1.31 mms^{-1} and quadrupole splitting (QS) of 2.36 mms^{-1} are indicative of an Fe^{2+} ion in a high spin (HS) configuration.[74]

To test the behaviour in MeCN, a ^{57}Fe Mößbauer spectrum was also recorded in a frozen MeCN solution.

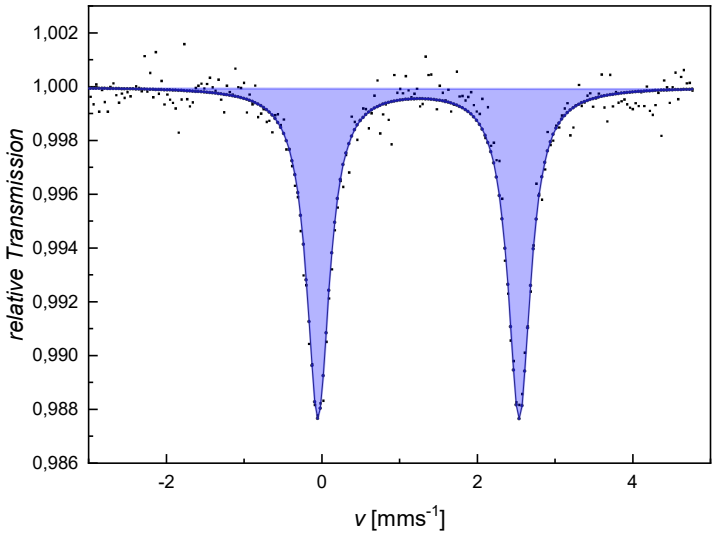

Figure 44 ^{57}Fe Mößbauer spectrum of **8** in a solution of MeCN.

From the data collected, only one doublet was observed, which means that also in solution is present only one Fe species. In this case, the IS is 1.25 mm/s and the QS is 2.59 mm/s, also assigned to an Fe^{2+} ion in a HS configuration, hence showing that the complex is unchanged in solution.[74] The small differences in values of IS and QS are attributable to a likely exchange of acetone by MeCN.

The magnetic properties of $[L^{O}NiFe](OTf)_2(acetone)_2$ complex **8** were probed with a Quantum Design MPMS3 SQUID magnetometer (figure 47).

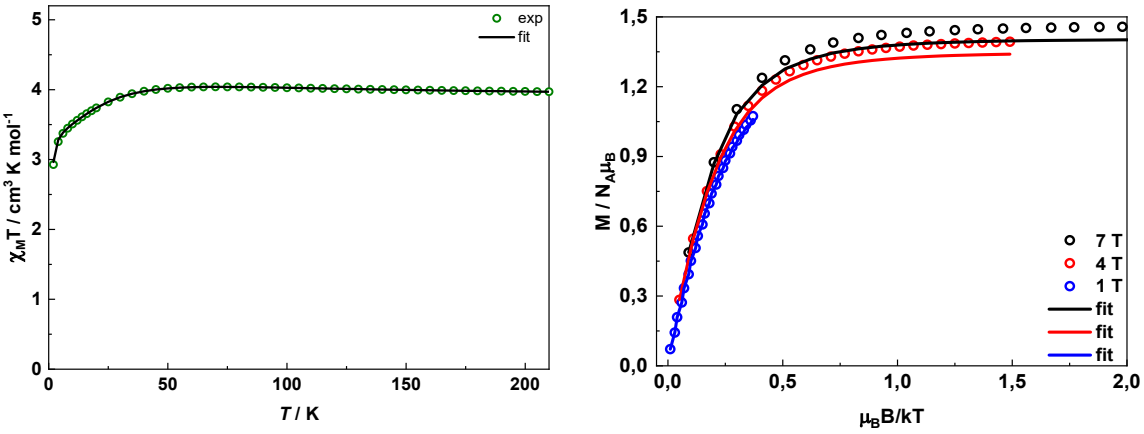

Figure 45 (Left) Temperature dependence of $\chi_M T$ or complex **8** at an applied dc field of 0.5 T. (Right) Variable-temperature variable-field magnetization for complex **8**. The solid lines are the best fit with D = – 21.5 cm^{-1}, $g_x = g_y = 2.12$, $g_z = 2.56$, 2zJ = 0.1 cm^{-1} and TIP = 9 ·10^{-6} cm^3mol^{-1} (subtracted).

The $\chi_M T$ value of 3.97 cm^3mol^{-1} K at 210 K indicates the presence of a low-spin Ni^{II} ion (d^8, $S = 0$) and a high-spin Fe^{II} ion (d^6, $S = 2.0$) (figure 45, left). The high-spin state of the Fe^{II} ion is in agreement with the Mößbauer spectroscopic results. The $\chi_M T$ value of 3.97 cm^3mol^{-1} K is higher than the expected value (3.0 cm^3mol^{-1} K) for an isolated non-interacting high-spin Fe(II) ion (d^6, $S = 2.0$, $g = 2.0$), indicating some orbital contribution to the magnetic moment.

$$\chi T = \frac{1}{8} g^2 S(S+1)$$

The $\chi_M T$ value remains almost constant until 50 K before gradually decreasing to 2.93 cm^3mol^{-1} K at 2.0 K. The magnetic susceptibility data were fitted along with the variable-field variable-temperature (VTVH) magnetization data (figure 45, right) to the spin Hamiltonian

$$\hat{H} = D\left[\hat{S}_z^2 - \frac{1}{3}S(S+1)\right] + E(\hat{S}_x^2 - \hat{S}_y^2) + \mu_B \vec{B} g \vec{S}$$

where *D and E* represent the axial and the rhombic zero-field splitting (ZFS) parameters, *S, S_x, S_y* and S_z represents the total spin and its corresponding x, y and z components, μ_B, *g*, *B* represents the electron Bohr's magneton, the Zeeman anisotropic interaction tensor and the magnetic field vector, respectively. The best fit with the program *julX*_2s[75] yields *D* = – 21.5 cm^{-1}, $g_x = g_y = 2.12$, $g_z = 2.56$, 2*zJ* = 0.1 cm^{-1} and *TIP* = 9 ·10^{-6} cm^3mol^{-1} (subtracted). Here, 2*zJ* represents the intermolecular magnetic exchange coupling.

Complex $[L^{O}NiFe](OTf)_2(Acetone)_2$ **8** was characterized also by ESI(+) mass spectrometry, showing a dominant peak around m/z = 815, which is assigned to the ion $[L^{O}NiFe](OTf)^{+}$.

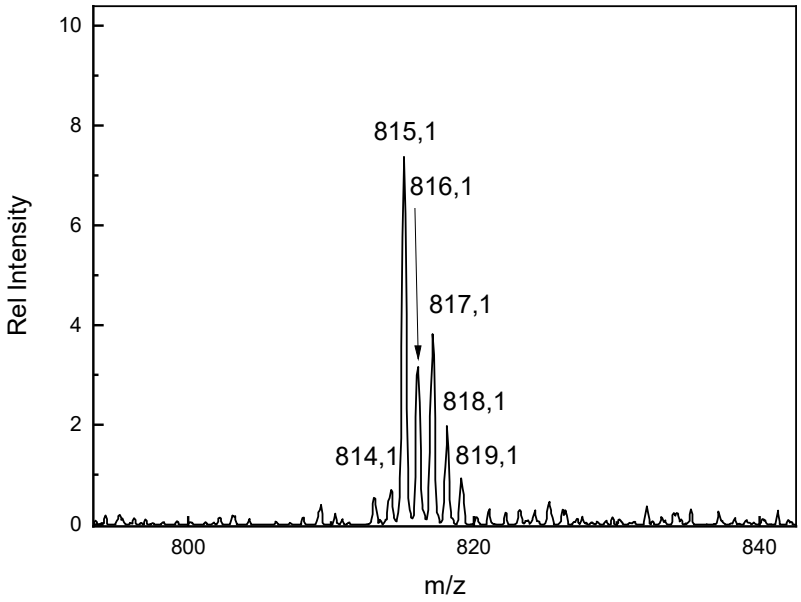

Figure 46. ESI(+) mass spectrum of **8** in MeCN.

The full mass spectrum is shown in the appendix section (appendix figure 23).

The IR spectrum of **8** confirms the presence of acetone also in the solid sample.

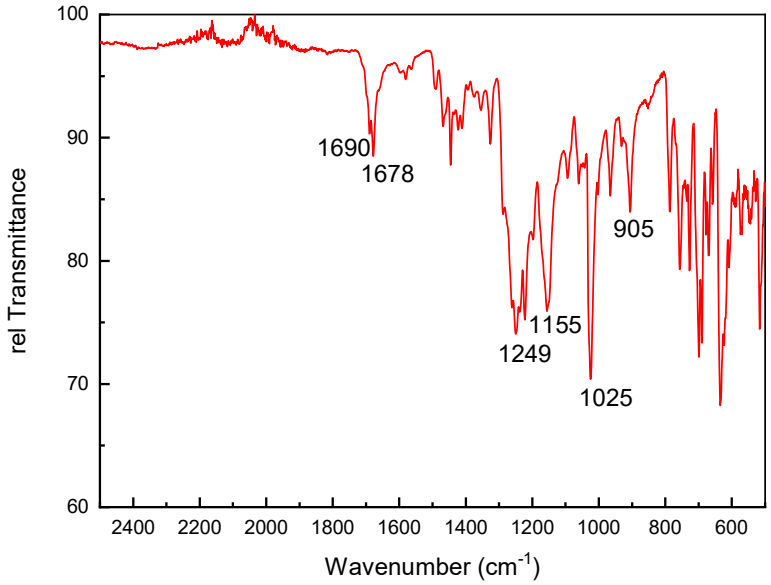

Figure 47. IR Spectrum of solid **8**.

The two bands at 1690 cm^{-1} and 1678 cm^{-1}, can be assigned to the C=O stretching vibrations of both acetone molecules, one coordinated equatorially and one axially.

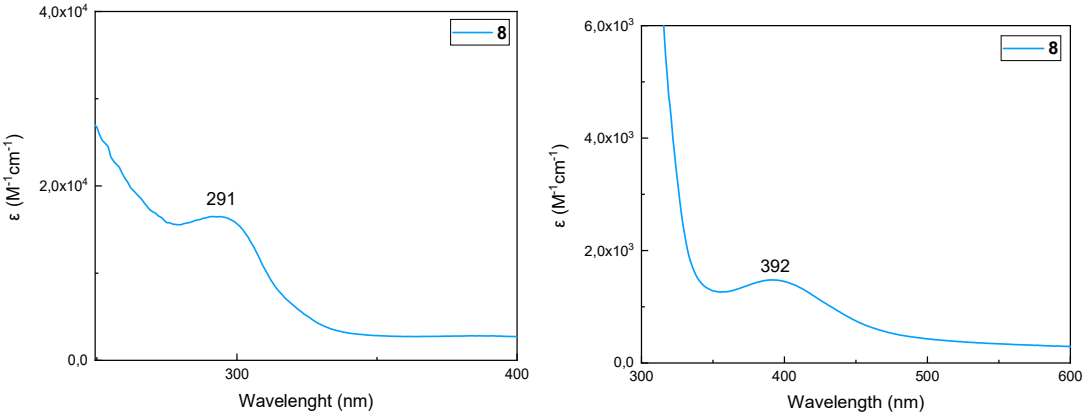

Figure 48 (Left) UV-Vis Spectrum of **8** in MeCN, at $5.5 \cdot 10^{-5}$ M; (right) UV-Vis Spectrum of **8** in MeCN, at $2.8 \cdot 10^{-4}$ M.

On the left side of figure 48 (left), the UV/Vis spectrum of **8** at $5.5 \cdot 10^{-5}$ M shows a maximum of the absorption at λ_{max} = 291 nm, significantly blue-shifted from the absorption of complex **5**, also tentatively assigned to a LMCT transition, based on the high molar extinction coefficient.[68-69] Therefore, this spectroscopic feature could rise from a O→Ni^{II} charge transfer transition. On the right side of figure 48, a UV/Vis spectrum was recorded at a higher concentration ($2.8 \cdot 10^{-4}$ M) to show a second absorption maximum at 392 nm. Based on the molar extinction coefficient, this band can be tentatively assigned to d-d transition.[76] Since this spectroscopic feature is not present in the UV/Vis spectrum of **5**, it can be attributable to the Fe^{II}.

Additionally, the electrochemical properties of complex **8** were investigated by cyclic voltammetry.

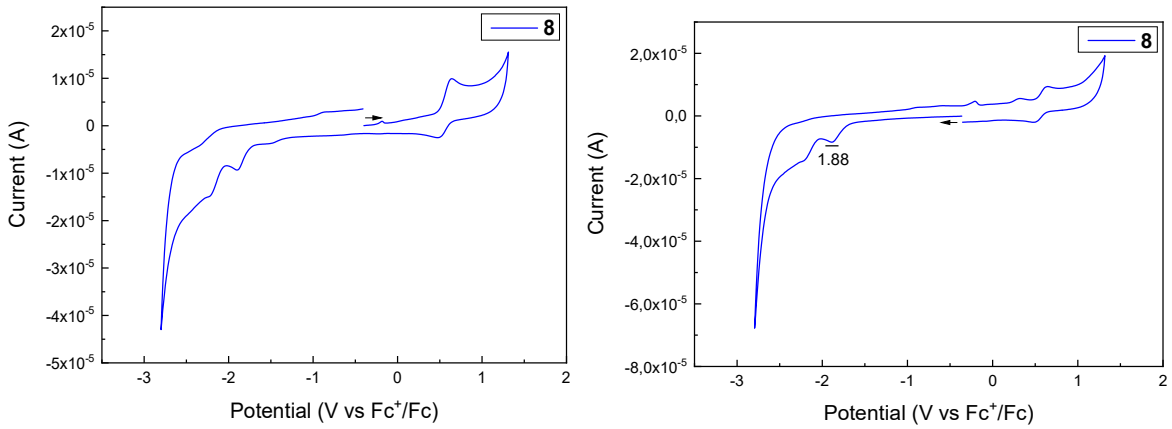

Figure 49 (Left) cyclic voltammogram of **8** in MeCN at 100 mVs^{-1} (anodic scan first). WE: GC; CE: Pt; Ref: Ag. (Right) cyclic voltammogram of **8** in MeCN at 100 mV s^{-1} (cathodic scan first). WE: GC; CE: Pt; Ref: Ag.

Similar to the redox behaviour of **5**, the CV of complex **8** towards anodic potential (figure 49, left) shows a quasi-reversible oxidation process occurring at $E_P^a = 0.55\ \mathrm{V}$ vs Fc^+/Fc is observed, likely corresponding to the oxidation from Ni^{2+} to Ni^{3+}. This process was analyzed at different scan rates (see figure 42).

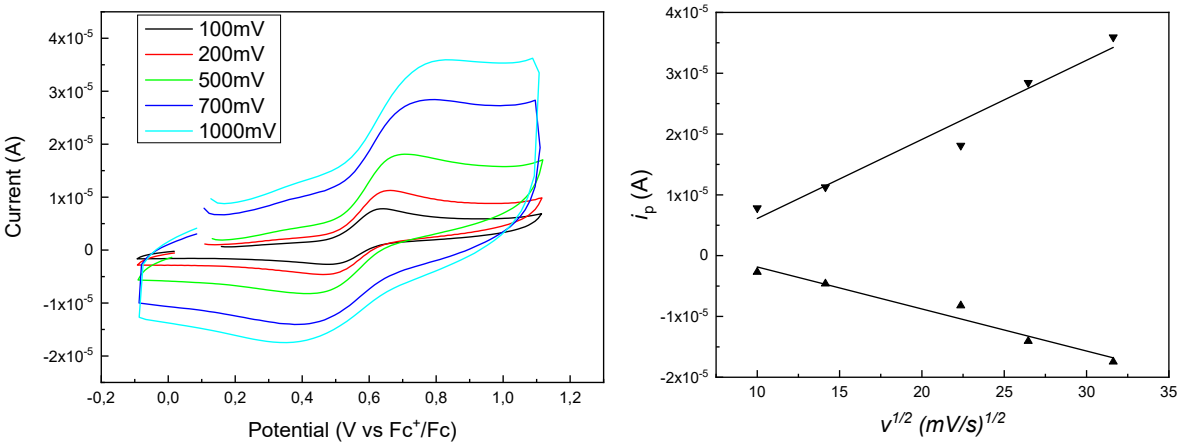

Figure 50 First Oxidation of complex **8** at different scan rates (left) in MeCN; Linear fitting of peak currents versus the square root of the scan rates (right). WE: GC; CE: Pt; Ref: Ag.

To gain insight into the oxidation process, the peak current was plotted against the square root of the scan rates and the resulting linear dependence shows a quasi-reversible behaviour.

As confirmation of this, the potential difference ΔE_p found for this process is 110 mV, which deviates slightly from the standard one-electron process value for Cp_2Fe in MeCN ($\Delta E_P = 90$ mV). The CV of **8** towards cathodic potentials (figure 51) was also recorded under the same conditions. Non-reversible processes were observed at $E_{P1}^{c} = -1.88$ V and $E_{P1}^{c} = -2.2$ V, vs Fc^+/Fc. The first reduction process has been studied at different scan rates, which confirms the non-reversibility of this redox process upon increasing the scan rate.

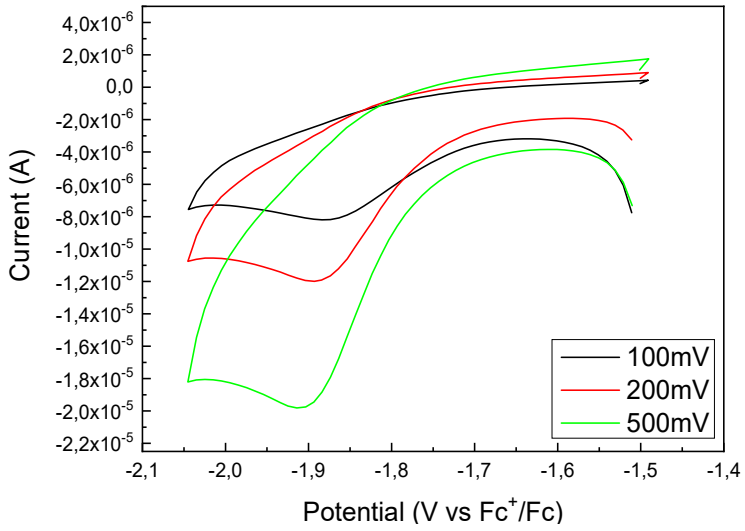

Figure 51. First reduction process of **8** at different scan rates in MeCN. WE: GC; CE: Pt; Ref: Ag.

Exploiting the first reduction process, a catalysis experiment for the Hydrogen Evolution Reaction (HER) can be set up, which will be fully described in the next chapter.

4.6. Hydrogen Evolution Reaction (HER) Experiment with $[L^{O}NiFe](OTf)_2(acetone)_2$ complex

The hydrogen evolution reaction (HER) is one of the most studied electrochemical processes due to the possibility to produce hydrogen by water electrolysis and it is non-polluting.[77] The reaction from a cathodic hydrogen evolution in an acidic environment is given by:

$$H^+ + e \rightarrow \frac{1}{2}H_2$$

Complex **8** shows an interesting reduction process at $E_P^c = -1.88$ V (figure 50), opening the possibility to investigate the catalytic properties toward hydrogen evolution. To perform the experiment, a suitable proton source is selected with a reduction potential lower than the reduction potential of complex **8**. For this reason, triethylammonium tetrafluoroborate ($TEA[BF_4]$) was selected as a proton source, having a first reduction event at $E_P^c = -1.93$ V vs Fc^+/Fc. In figure 52, the CV of $TEA[BF_4]$ in MeCN is reported.

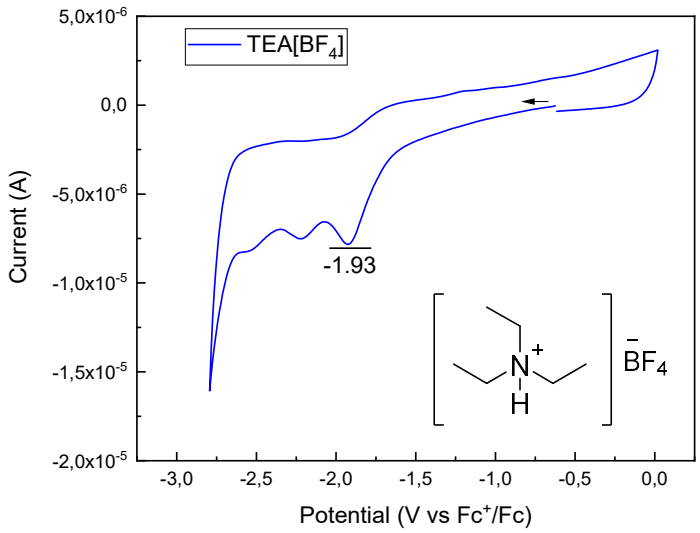

Figure 52. Chemical structure of $TEA[BF_4]$ and its cyclic voltammogram in MeCN towards cathodic potentials at 100 mVs^{-1}. WE: GC; CE: Pt; Ref: Ag.

The set-up of the experiment consists of a 0.5 mM solution of **8** in MeCN (Bu_4NPF_6 0.1 M) in a tight-sealed CV cell, equipped with glassy carbon (working electrode), Pt wire (counter electrode) and Ag wire (reference electrode). The analysis was performed under exclusion of O_2, and a Hamilton gas-tight syringe was used to inject $TEA[BF_4]$ during the experiment. The CV from -2.8 V to 0 V is plotted, with increasing equivalents of $TEA[BF_4]$.

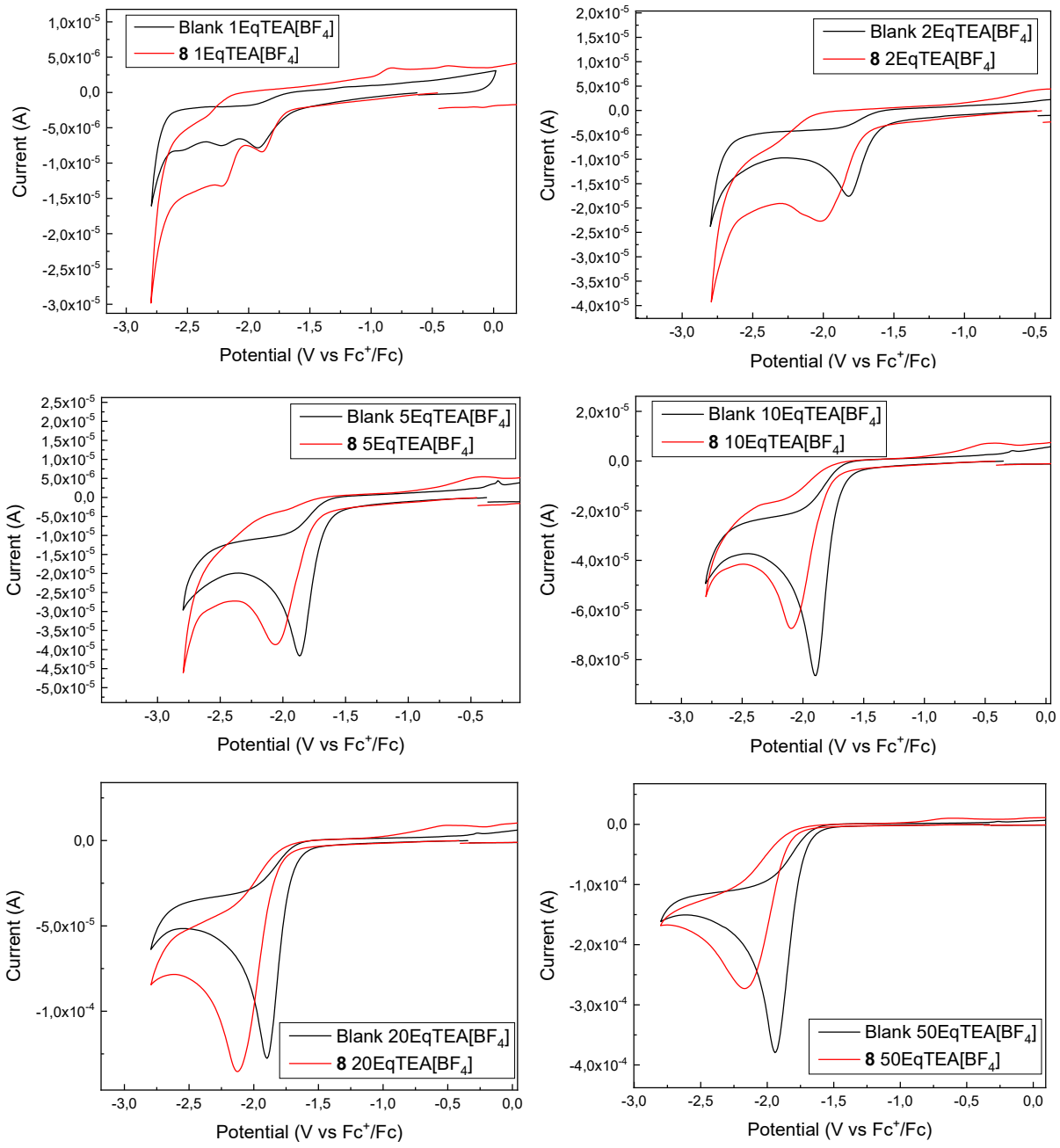

Figure 53. HER experiment using **8** with 1 equivalent of $TEA[BF_4]$ (top-left); with 2 equivalents of $TEA[BF_4]$ (top-right); with 5 equivalents of $TEA[BF_4]$ (center-left); with 10 equivalents of $TEA[BF_4]$ (center-right); with 20 equivalents of $TEA[BF_4]$ (bottom-left); with 50 equivalents of $TEA[BF_4]$ (bottom-right). (In MeCN at 100 mVs^{-1}).

In figure 53, the black curves represent the blank solution plus additions of different equivalents of the proton source. The black curves are used for comparison with the voltammogram of the solution of complex **8** (in red) with the addition of the same equivalents

of the proton source. Upon increasing the concentration of the proton source, no current enhancement indicative of an electrocatalytic process was observed.

4.7. Synthesis of $[L^{O}NiCo](MeCN)(I)_2$ complex

In the previews section, the ability of complex **5** to bind a second transition metal ion (Fe^{II}) was demonstrated. Following the approach already tested, a new bimetallic complex with Ni^{II} and Co^{II} was synthesized, using CoI_2 as a Co^{II} source, in an Ar atmosphere glovebox (Scheme 14).

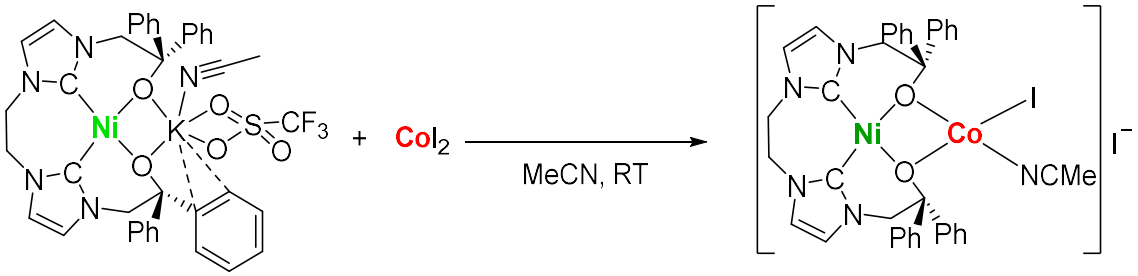

5 **9**

Scheme 14. Synthesis of bimetallic complex $L^{O}NiCo(MeCN)(I)_2$ **9**.

As for complex **8**, a substitution of the K^+ ion with the Co^{II} center occurred in 24h. Subsequently, the MeCN was removed in vacuo and the crude was dissolved in dry acetone. The potassium triflate precipitate was separated *via* filtration. The product appeared as a red solid, and by crystallization via diffusion of Et_2O in a MeCN solution, suitable single crystals for XRD were obtained. Furthermore, complex $[L^{O}NiCo](MeCN)(I)_2$ **9** is characterized by UV/Vis and X-ray diffraction.

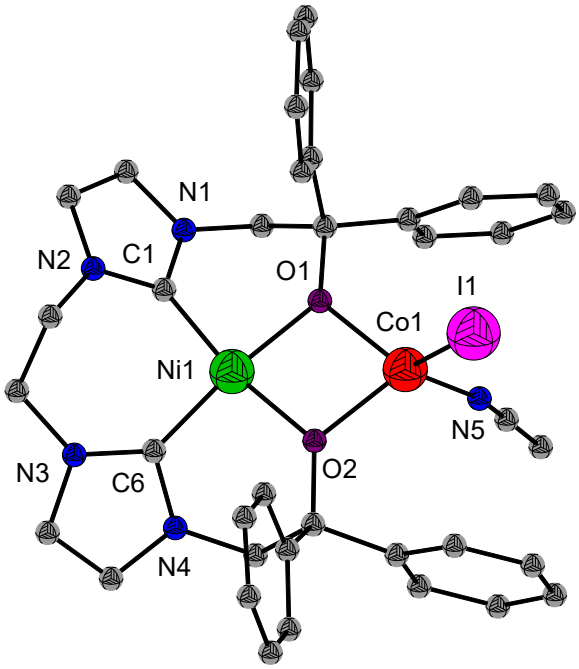

Figure 54 Molecular structure of [L^{O}NiCo](MeCN)$(I)_2$ complex **9**, hydrogen nuclei are omitted for clarity.

The crystallographic data show that complex **9** crystallizes in the triclinic P-1 space group, with 2 molecules per unit cell. Significant bond lengths and angles are shown in table 4.

Table 4 Selected bond lengths [Å] and bond angles [°] for L^{O}NiCo(MeCN)$(I)_2$ complex **9**.

Atoms	Bond lengths [Å]	Atoms	Bond angles
Ni1-C1	1.850(2)	C1-Ni1-C6	96.01(9)
Ni1-C6	1.885(2)	C1-Ni1-O2	169.27(7)
Ni1-O2	1.9086(15)	C6-Ni1-O2	93.83(7)
Ni1-O1	1.9133(15)	C1-Ni1-O1	90.19(8)
Ni1-Co1	2.9785(9)	C6-Ni1-O1	173.22(8)
Co1-O1	1.9511(15)	O2-Ni1-O1	80.20(6)
Co1-O2	1.9559(15)	C1-Ni1-Co1	129.98(7)
Co1-N5	2.0022(19)	C6-Ni1-Co1	133.96(6)
Co1-I1	2.5927(7)	O2-Ni1-Co1	40.16(4)
		O1-Ni1-Co1	40.04(4)
		O1-Co1-Ni1	39.12(4)
		O2-Co1-Ni1	39.01(4)
		N5-Co1-Ni1	119.33(6)
		I1-Co1-Ni1	126.187(19)
		O2-Co1-I1	118.09(4)
		N5-Co1-I1	114.48(6)

Similarly to previously described complexes, in compound **9** the Ni^{II} ion is bound in a square-planar geometry to carbene-C1, carbene-C6, O1 and O2. The bond distances d(Ni1-C1) and d(Ni1-C6) are comparable with the distances d(Ni1-O1) and d(Ni1-O6, having the carbene-C-Ni bonds length 0.02 Å shorter than the Ni-O bond, in line with the stronger σ-donor character of the carbenes. Binding angles C1-Ni1-O1 and C6-Ni1-O2 are the closest to 90°, but the angles C1-Ni1-C6 (96°) and, especially, O2-Ni1-O1 (80°) show that the square-planar geometry is indeed slightly distorted. The Co^{II} ion is coordinated in a distorted tetrahedron geometry by the two bridging O atoms, an iodide ion, and a molecule of MeCN. This is confirmed by the angles O2-Co1-I2 and N5-Co1-I1, of 114° to 118°. The distances d(Ni1-O1) and d(Ni1-O2) of 1.91 Å, are comparable with d(Co1-O1) and d(Co1-O2) of 1.95 Å. Finally, the distance d(Ni-Co) in complex **9** of 2.98 Å is very similar to the distance d(Ni-fe) in complex **8** of 2.99 Å.

Complex **9** was further characterized by UV/Vis spectroscopy. Given the difference in the intensity of the bands, the spectrum was recorded at two different concentrations.

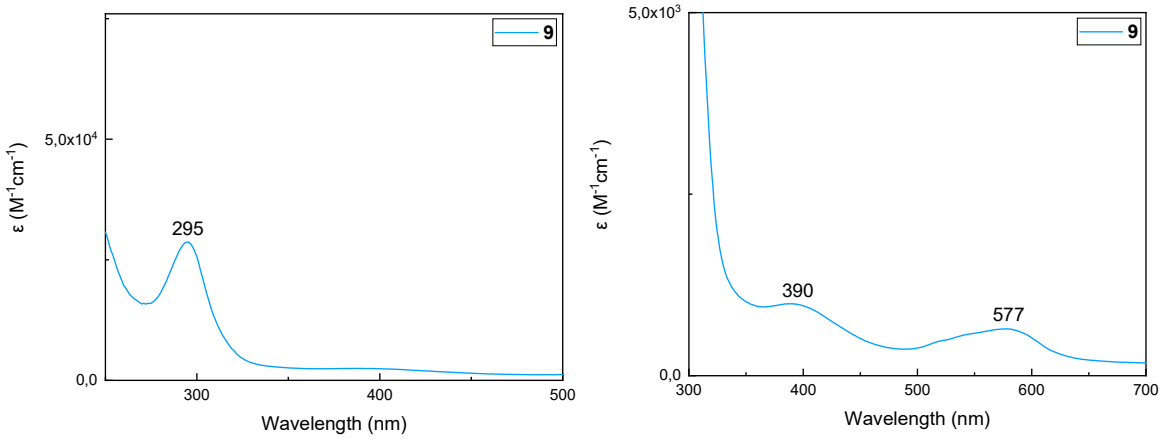

Figure 55 (Left) UV/Vis spectrum of **9** $5.5 \cdot 10^{-5}$ M in MeCN. (Right) UV/Vis spectrum of **9** $2.8 \cdot 10^{-4}$ M in MeCN.

The UV/Vis Spectrum recorded at $5.5 \cdot 10^{-5}$ M (figure 55, left) shows a maximum absorption at λ_{max} = 295 nm, and similarly to complex **8**, based on the high molar extinction coefficient, it is possible to tentatively assign this band to a LMCT transition (O→Ni).[68,69] Figure 55 (right) shows the UV/vis spectrum at higher concentration ($2.8 \cdot 10^{-4}$ M) so that the absorption bands at 390 nm and 577 nm are well visible. Based on the value of the molar extinction coefficient, these bands are tentatively assigned to d-d transition of a high spin Co^{II} center.[76,78]

4.8. Synthesis of $[L^O(L^OH)Fe_2](OTf)$ complex

In a similar fashion as for synthesizing complex **5**, proligand **4** was used to attempt the synthesis of an Fe^{II} complex $[L^OFe]$. Since the synthesis of complex **5** required a soluble Ni source in organic media to obtain a stable complex, the same approach was taken for this synthesis, and $FeBr_2(THF)_2$ was used as a metal source with potassium tert-butoxide as a base (Scheme 15). The product was crystallized via diffusion of Et_2O in a MeCN solution.

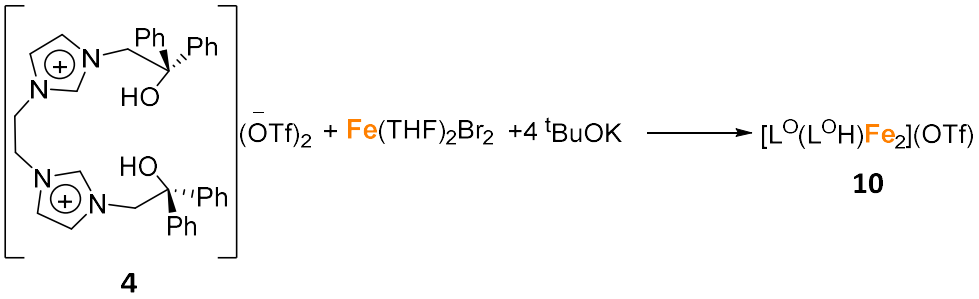

Scheme 15 Synthesis of $[L^O(L^OH)Fe_2](OTf)$ complex **10**.

Interestingly, the synthesis did not lead to the expected $[L^OFe]$ complex, instead, after crystallization, a dimer $[L^O(L^OH)Fe_2](OTf)$ complex (**10**) was obtained, where two units of the ligand bind two Fe centers. The XRD data is shown in figure 58.

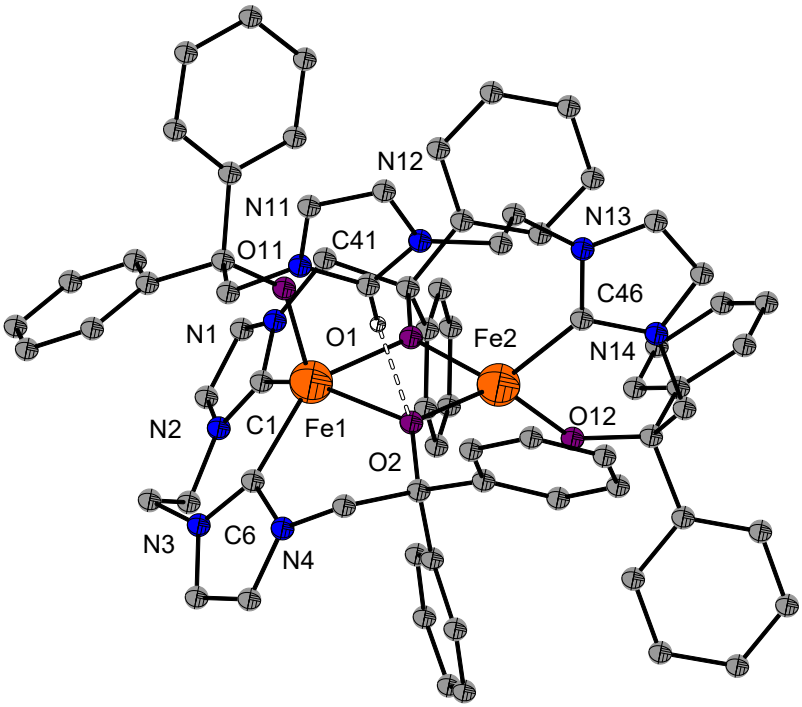

Figure 56 Molecular structure of $[L^O(L^OH)Fe_2](OTf)$ complex **10**.

The X-ray data showed that $[L^{O}(L^{O}H)Fe_2](OTf)$ complex crystallizes in the monoclinic group space $P2_1/n$, with 4 molecules per unit cell. The structural image shows that one of the imidazolinium units is not deprotonated, so it does not bind any of the Fe^{II} ions. Instead, the formation of a hydrogen bond between the hydrogen bound to carbene-C41 and the O2 atom of one of the bridging alcoholates occurs. Below, a table with bond lengths and angles is reported.

Table 5 Selected bond lengths [Å] and bond angles [°] for $[L^{O}(L^{O}H)Fe_2](OTf)$ complex **10**.

Atoms	Bond lengths [Å]	Atoms	Bond angles [°]
Fe1-O11	1.9161(18)	O11-Fe1-C1	107.80(9)
Fe1-C1	2.124(3)	O11-Fe1-C6	115.06(10)
Fe1-C6	2.151(3)	C1-Fe1-C6	96.93(10)
Fe1-O2	2.1687(17)	O11-Fe1-O2	105.38(7)
Fe1-O1	2.2046(17)	C1-Fe1-O2	140.72(9)
Fe2-O12	1.9119(19)	C6-Fe1-O2	87.46(8)
Fe2-O1	1.9971(17)	O11-Fe1-O1	96.24(7)
Fe2-O2	2.0394(17)	C1-Fe1-O1	82.97(8)
Fe2-C46	2.088(3)	C6-Fe1-O1	146.78(9)
		O2-Fe1-O1	73.03(6)
		O12-Fe2-O1	118.15(8)
		O12-Fe2-O2	131.57(8)
		O1-Fe2-O2	80.29(7)
		O12-Fe2-C46	92.30(10)
		O1-Fe2-C46	121.52(9)
		O2-Fe2-C46	116.62(9)
		C10-O1-Fe2	131.58(15)
		C10-O1-Fe1	125.18(14)
		Fe2-O1-Fe1	103.23(7)
		C24-O2-Fe2	120.46(15)
		C24-O2-Fe1	127.19(15)
		Fe2-O2-Fe1	103.08(7)
		C50-O11-Fe1	136.80(16)
		C64-O12-Fe2	133.03(18)
		N2-C1-Fe1	138.74(19)
		N1-C1-Fe1	117.81(18)
		N4-C6-Fe1	123.37(19)
		N3-C6-Fe1	129.93(19)
		N13-C46-Fe2	134.31(19)
		N14-C46-Fe2	119.5(2)

The Fe1 center is bound in a distorted pyramidal geometry, with the metal ion slightly out of the plane of the base. It is bound by two carbene-C and two alcoholate-O from one molecule

of the fully deprotonated ligand $[L^O]^{2-}$, that form the base of the pyramid, and one alcoholate-O of the $[L^OH]^{1-}$ ligand, as the apex of the pyramid. The two O of the base of the pyramid are bridging the two Fe^{II} ions. The Fe2 center is in a distorted tetrahedral geometry, bound by the bridging O atom from $[L^O]^{2-}$, and a carbene-C and an alcoholate-O from the $[L^OH]^{1-}$ ligand. The angles formed by O1-Fe2-O2 and C46-Fe2-O12 are 80° and 92°, significantly lower than the other two angles formed by O1-Fe2-C46 and O2-Fe2-O12, which are 121° and 117°, hence the distortion from the classic tetrahedral geometry. Interesting to notice is that the bridging oxygen atoms O1 and O2 are more closely bound to the Fe2 center, by a value of ca. 0.2 Å. Comparison of the bond distances of the Fe1 ion with the carbene C1 and C6 to the previously described metal complexes **8** and **9** (ca. 1.9 Å), highlights a longer bond carbene-Fe of ca. 0.25 Å, likely because of the lower coordination number of Fe2 (CN = 4) compared to Fe1 (CN = 5). On the other hand, Fe2 ion binds the carbene-C46 of the $[L^OH]^{1-}$ ligand more closely, with a 2.08 Å bond length, which is still higher than the one observed for the other complexes. The bond distances d(Fe1-O11) and d(Fe1-O12) of 1.91 Å are significantly shorter than the d(Fe1-O1) and d(Fe1-O2) of 2.20 Å and 2.17 Å respectively, involving the bridging O-atoms.

Further investigations by NMR spectroscopy and ESI-mass spectrometry did not lead to the characterization of the product, due to the fact that Fe^{II} in this complex may be in high-spin configuration and, probably also not stable in solution. Overall, the formation of the $[L^O(L^OH)Fe_2](OTf)$ complex likely occurred because of improper stoichiometry of base added.

4.9. Summary

The novel proligand $[L^{O}H_4](OTf)_2$ (**4**) was successfully synthesized and characterized. The $[L^{O}NiK(MeCN)(OTf)]$ complex **5** was isolated and fully characterized by different spectroscopic techniques. The electrochemical properties were investigated and the catalysis towards the hydrogen oxidation reaction (HOR) was attempted.

Making use of the ability of the $[L^{O}Ni]$ unit to bind multiple metal centers in close proximity, a series of bi-metallic complexes was prepared. The $L^{O}NiFe(OTf)_2(Acetone)_2$ complex **8** was fully characterized and the electrochemical properties were investigated. Exploiting the first reduction process of complex **8**, the catalysis towards hydrogen evolution reaction (HER) was probed and the results were discussed. The $L^{O}NiCo(MeCN)(I)_2$ complex **9** was prepared and the spectroscopic features, as well as the structural parameters, were discussed. Finally, the $[L^{O}(L^{O}H)Fe_2](OTf)$ complex **10** was synthesized and characterized by X-ray diffractometry.

In the next chapter, the properties of the $[L^{O}Ni]$ unit as a neutral metalloligand are further described and discussed.

5. [$L^{O}Ni$] unit as metalloligand for the synthesis and characterization of trimetallic $L^{O}NiMNiL^{O}$ (M = Fe^{II}, Co^{II}) complexes

5.1. Introduction

In chapter 4, the novel proligand **4** was proposed and the [$L^{O}NiK(MeCN)(OTf)$] complex **5** was isolated, characterized and used for the synthesis of bi-metallic complexes and their characterization. In this chapter, the ability of [$L^{O}Ni$] to act as a neutral {O-O´}metalloligand moiety will be discussed and exploited. A series of tri-metallic complexes containing 3d metals such as Fe^{II} and Co^{II} will be described.

The first trimetallic [$L^{O}NiFeNiL^{O}$]$(OTf)_2$ complex will be presented with its full characterization. Of particular interest are its structural and electrochemical properties which will be thoroughly discussed. Given its redox features, an experiment for possible catalysis towards the HER will be set up and the data analyzed.

A second trimetallic complex [$L^{O}NiCoNiL^{O}$]$(OTf)_2$ will be also synthesized and characterized by different spectroscopic techniques. Particular interest will be put into the investigation of the magnetic properties of this complex and the correlation between them and their peculiar structural features.

5.2. Synthesis of $[L^{O}NiFeNiL^{O}](OTf)_2$ complex

The synthesis of the trimetallic $[L^{O}NiFeNiL^{O}](OTf)_2$ complex **11** can be achieved via two routes. The first approach consists of reacting already formed bimetallic $L^{O}NiFe(OTf)_2(acetone)_2$ complex **8** with one equivalent of $[L^{O}NiK(MeCN)(OTf)]$ complex **5**, leaving the reaction stirring for 48h, then removing the solvent (Scheme 16). The product is obtained as yellow crystals from diffusion of Et_2O in a MeCN solution.

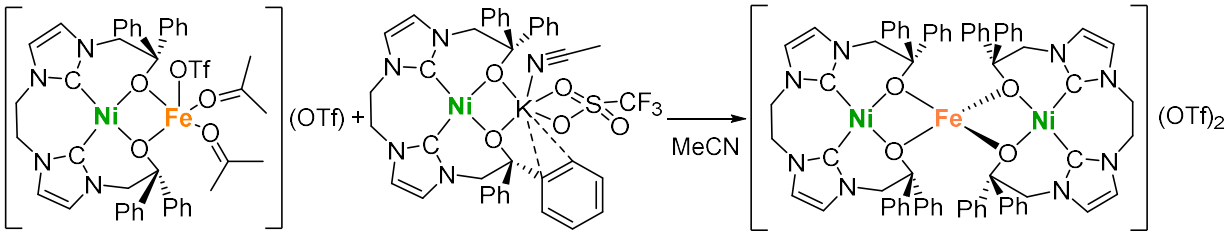

8 **5** **11**

Scheme 16 First synthetic route for $[L^{O}NiFeNiL^{O}](OTf)_2$ complex **11**.

As a second route, the starting point is complex **5** which reacts with $Fe(OTf)_2$ in a 2:1 ratio, and after 48h of stirring and subsequent removal of the solvent, the product can be obtained via crystallization by diffusion of Et_2O in a MeCN solution (Scheme 17).

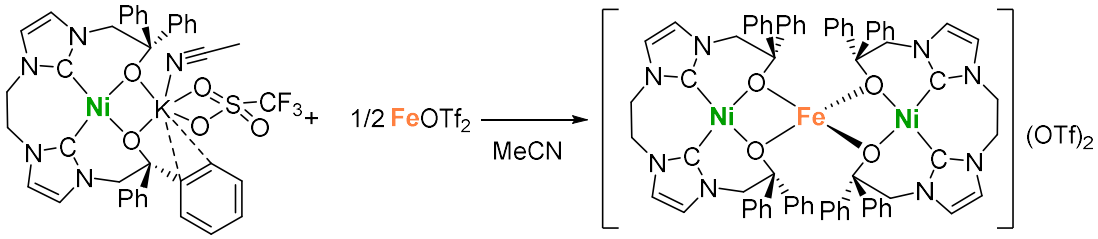

5 **11**

Scheme 17 Second synthetic route for $[L^{O}NiFeNiL^{O}](OTf)_2$ complex **11**.

Both routes are reproducible and the product was obtained with the same high purity. Compound **11** was characterized by ^1H NMR spectroscopy, ESI(+) mass spectrometry, X-ray diffraction, Mößbauer spectroscopy, SQUID and UV/Vis spectroscopy. Furthermore, the possible activity of complex **11** towards electrocatalytic proton reduction was investigated.

The X-ray diffraction results are discussed below.

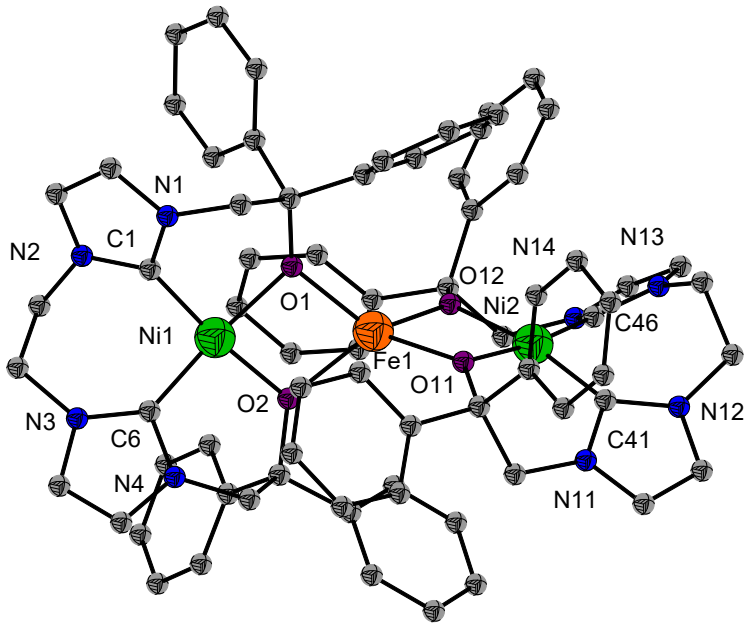

Figure 57 Molecular structure of **11**; Hydrogen atoms are omitted for clarity.

From the structural data, it is possible to see that complex **11** crystallizes in the monoclinic space group $P2_1/c$, with 4 molecules per unit cell. The complex presents itself as having two [L^{O}Ni] acting as a {O-O´}metalloligand in the complexation of the central Fe^{II} ion. Significant bond lengths and angles are reported in table 6.

Table 6 Selected bond lengths [Å] and bond angles [°] for [L^{O}NiFeNiL^{O}](OTf)$_2$ complex **11.**

Atoms	Bond lengths [Å]	Atoms	Bond angles [°]
Ni1-C1	1.843(6)	C1-Ni1-C6	91.2(3)
Ni1-C6	1.870(6)	C6-Ni1-O2	95.5(2)
Ni1-O2	1.914(4)	C1-Ni1-O1	91.4(2)
Ni1-O1	1.953(4)	O2-Ni1-O1	82.43(16)
Ni2-C46	1.837(6)	Ni1-O1-Fe1	98.74(17)
Ni2-C41	1.867(6)	Ni1-O2-Fe1	100.24(17)
Ni2-O11	1.922(4)	C46-Ni2-C41	91.0(3)
Ni2-O12	1.955(4)	C41-Ni2-O11	95.4(2)
Fe1-O2	2.019(4)	C46-Ni2-O12	91.2(2)
Fe1-O11	2.020(4)	O11-Ni2-O12	83.16(16)
Fe1-O1	2.025(4)	Ni1-O1-Fe1	98.74(17)
Fe1-O12	2.028(4)	Ni1-O2-Fe1	100.24(17)
		O2-Fe1-O11	119.14(16)
		O2-Fe1-O1	78.11(16)
		O11-Fe1-O12	78.93(16)
		O1-Fe1-O12	124.43(15)

The two [L^{O}Ni] units have comparable bond lengths and angles. Both Ni^{II} ions are in a square-planar configuration with binding angles close to 90°, as already reported for complex **5**. Interestingly, in complex **11** the four alcoholate-O are bridging to a single Fe ion, in a distorted tetrahedral geometry. The Fe^{II} center is thus found in a rather unusual $\{O_4\}$ environment and all Fe-O bonds have very comparable lengths of ca. 2.02 Å. The angles O2-Fe-O1 and O11-Fe1-O12 are 78°. On the other hand, the angles formed by O2-Fe1-O11 and O1-Fe1-O12 are significantly wider (119° and 124° respectively), causing the distortion in the tetrahedral geometry around the central Fe^{II}.

The ^{1}H NMR spectrum of [L^{O}NiFeNiL^{O}]$(OTf)_2$ in CD_3CN is shown in figure 58.

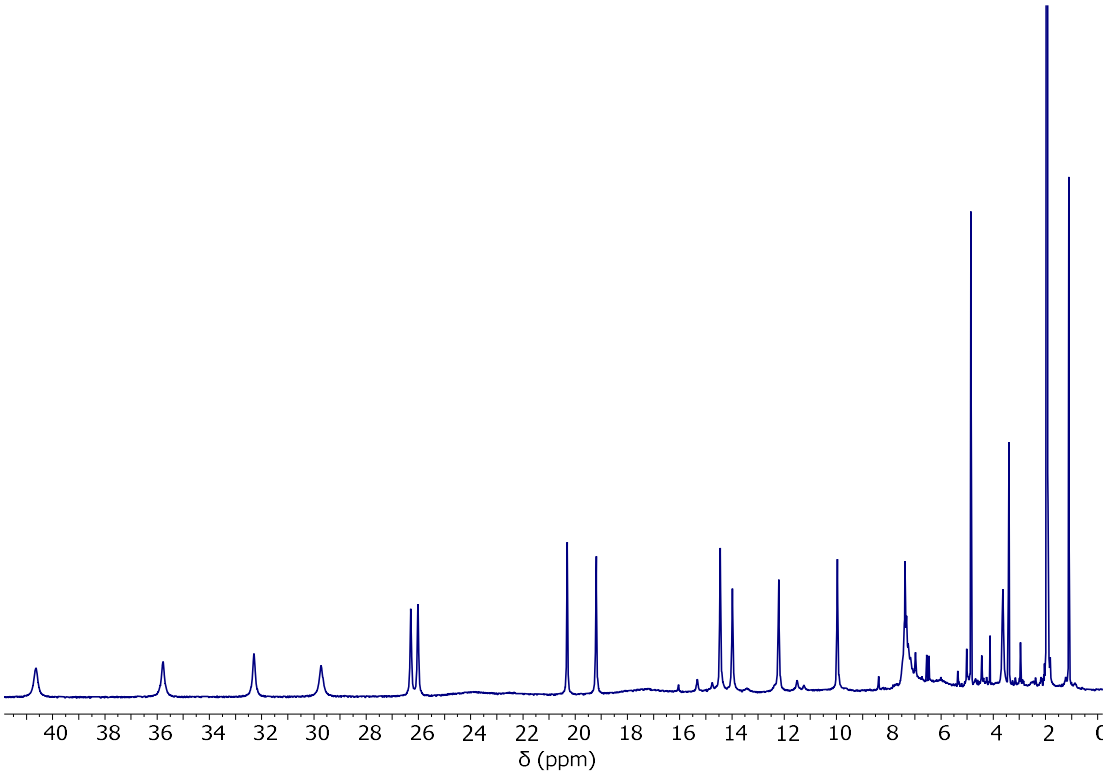

Figure 58 ^{1}H NMR of **11** in CD_3CN.

Given the paramagnetic nature of complex **11**, signals span a wide chemical shift range. However, the assignment of those peaks has been proved challenging, despite the full 2D-characterization experiments run. The 2D spectra are reported in the appendix section.

Complex **11** was analyzed by ESI(+) mass spectrometry, and the spectrum recorded for a MeCN solution shows a signal for the doubly charged ion $[L^{O}NiFeNiL^{O}]^{2+}$, indicating that the trinuclear NiFeNi core remains intact in MeCN solution.

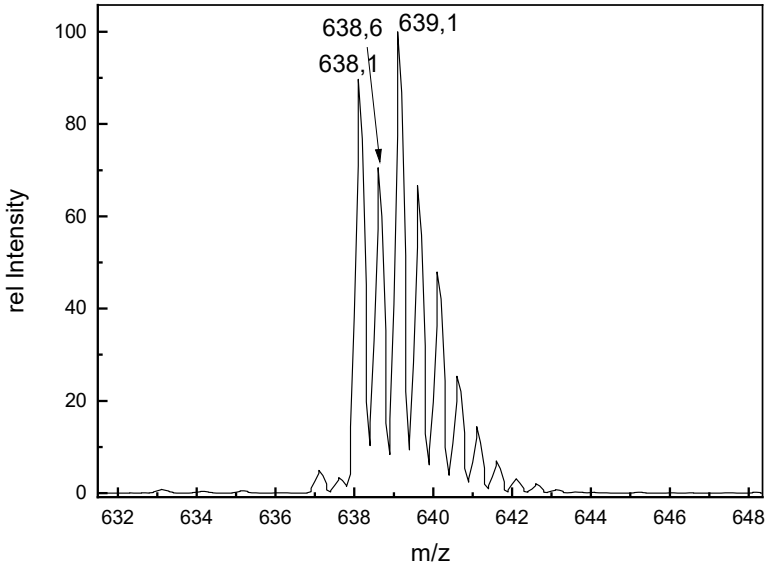

Figure 59 ESI(+) mass spectrum of $[L^{O}NiFeNiL^{O}](OTf)_2$ **11** in MeCN.

Complex **11** was further characterized by UV/Vis spectroscopy at two different concentrations, $5.5 \cdot 10^{-5}$ mM and $2.8 \cdot 10^{-4}$ mM, given the difference in intensity of the absorption bands.

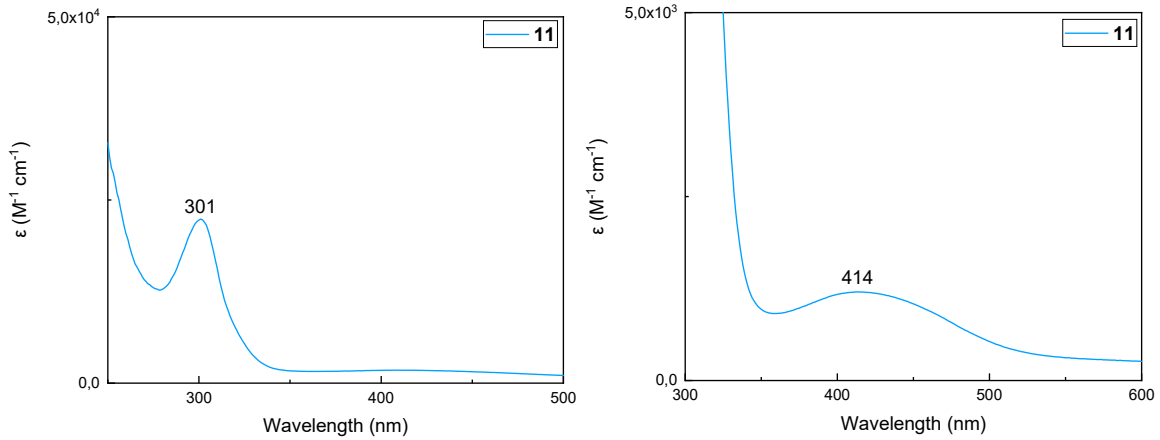

Figure 60 (Left) UV/Vis spectrum of **11** in MeCN at $5.5 \cdot 10^{-5}$ M; (right) UV/Vis Spectrum of **11** in MeCN at $2.8 \cdot 10^{-4}$ M.

The UV/Vis spectrum of **11** recorded at $5.5 \cdot 10^{-5}$ M (figure 60, left) shows an absorption maximum at λ_{max} = 301 nm, slightly red-shifted compared to the spectra of the bimetallic

complexes **8** and **9**, but still at lower values compared to literature reported bis-NHCs nickel complexes (see also chapter 4.3).[68] This red-shift is likely caused by the presence of the Fe^{II} ion, bound to the two bridging O-atoms of the two units of [L^{O}Ni]. Having a high molar extinction coefficient, this band is tentatively assigned to MLCT transitions (O→Ni^{II}).[69] A spectrum recorded at higher concentration of $2.8 \cdot 10^{-4}$ M (figure 60, right) reveals an absorption maximum at λ_{max} = 414 nm. Based on the lower molar extinction coefficient, this band is tentatively assigned to d-d transition processes for high spin Fe^{II}.[76]

To investigate the oxidation state and spin configuration of the Fe center, complex **11** was further characterized by ^{57}Fe Mößbauer spectroscopy and SQUID magnetometry.

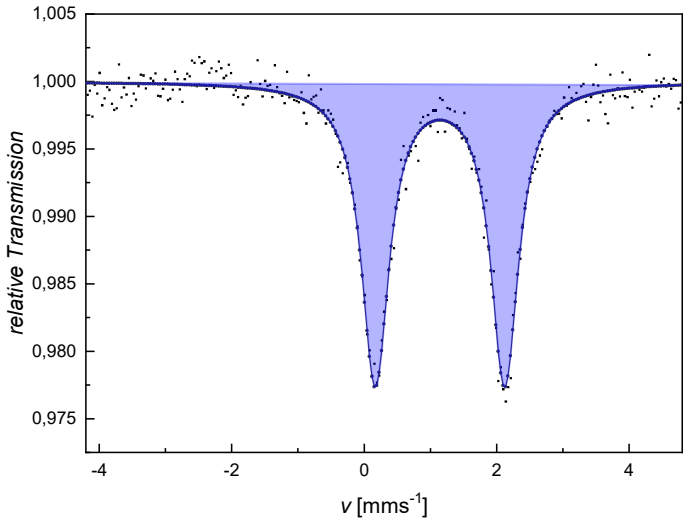

Figure 61 Solid state ^{57}Fe Mößbauer Spectrum of **11**, recorded at 80K.

In figure 61 the ^{57}Fe Mößbauer spectrum of solid **11** shows a single quadrupole doublet with an isomer shift of 1.14 mms^{-1} and quadrupole splitting of 1.95 mms^{-1}, and with this, it is possible to assign the spectrum to a HS-Fe^{2+} species.[74]

The magnetic properties of the trimetallic [L^{O}NiFeNiL^{O}]$(OTf)_2$ complex **11** were investigated with a Quantum Design MPMS3 SQUID magnetometer using a polycrystalline powder sample.

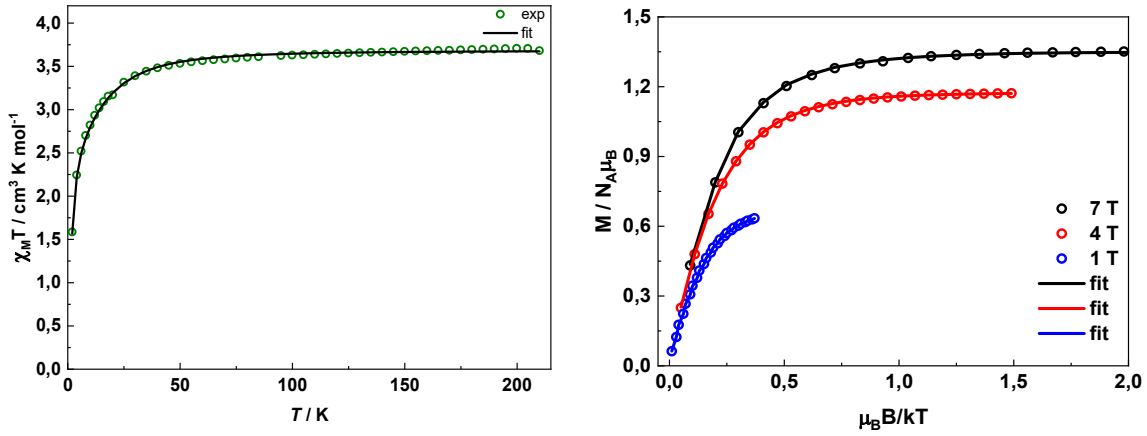

Figure 62 (Left) Temperature dependence of χ_MT for complex **11** at an applied dc field of 0.5 T. (Right) Variable-temperature variable-field magnetization for complex **11**. The solid lines are the best fit with D = – 12.8 cm^{-1}, E/D = 0.31, g_{iso} = 2.21 and TIP = 800 · 10-6 cm^{3}mol^{-1} (subtracted).

The $\chi_M T$ value of 3.68 cm^{3}mol^{-1} K at 210 K is in accordance with the presence of a two diamagnetic low-spin Ni^{II} ions (d^8, S = 0) and a high-spin Fe^{II} ion (d^6, S = 2.0) (figure 62, left) as observed previously in case of complex **8**. The high-spin state of the Fe^{II} ion, in this case, was also established by Mößbauer spectroscopy. Complex **11** displays similar temperature-dependent magnetic behaviour as the bimetallic complex **8**. The $\chi_M T$ value remains almost constant until 50 K before gradually decreasing to 1.59 cm^{3}mol^{-1} K at 2.0 K. The experimental magnetic susceptibility data along with the variable-field variable-temperature (VTVH) magnetization data was modelled with the respective spin Hamiltonian as described in chapter 4.5. The best fit with the program *julX*_2s[75] yields D = – 12.8 cm^{-1}, E/D = 0.31, g_{iso} = 2.21 and TIP = 800 · 10-6 cm^{3}mol^{-1} (subtracted).

The electrochemical properties of complex **11** were investigated by cyclic voltammetry. Figure 63 shows the CV of **11** in MeCN, scanning towards positive potentials first.

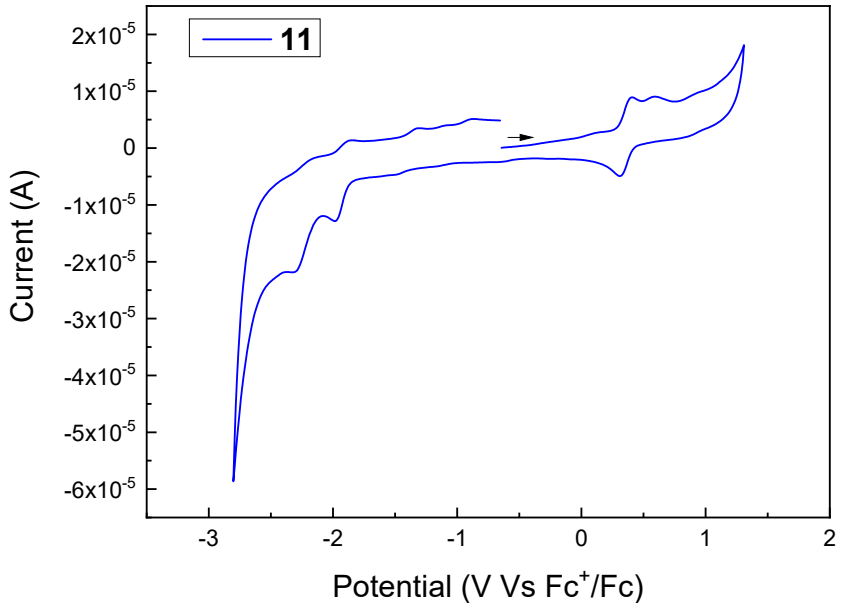

Figure 63 Cyclic voltammogram of **11**, scanning towards positive potentials first in MeCN at scan rate 100 mVs^{-1}. WE: GC; CE: Pt; Ref: Ag.

Similar to the redox behaviour of complexes **5** and **8**, complex **11** exhibits a quasi-reversible oxidation event, this time at 0.35 V vs Fc^{+}/Fc, tentatively assigned to Ni^{II} to Ni^{III} oxidation, based on comparison with the CV data for [L^{O}NiK(MeCN)(OTf)]. The CV at all scan rates is shown in the Appendix section (appendix figure 36) and will not be discussed further.

The CV scanning towards negative potentials first was also recorded under the same conditions and it is reported in figure 64.

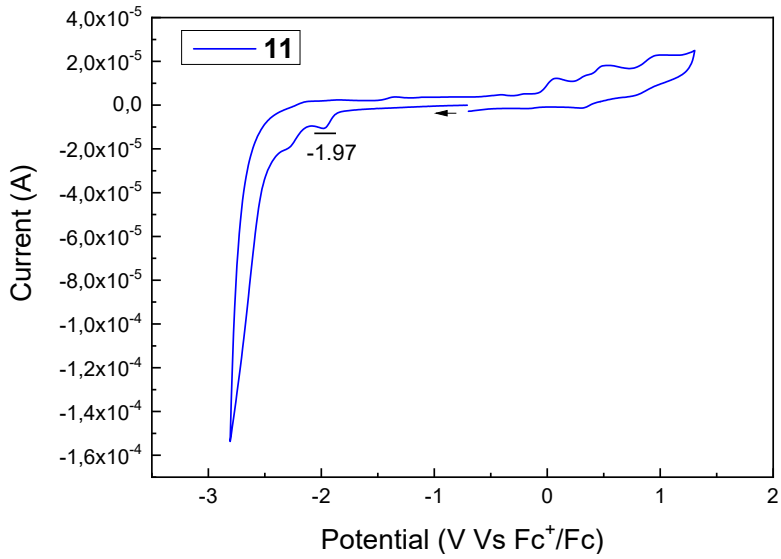

Figure 64 Cyclic voltammogram of **11**, scanning towards cathodic potentials first in MeCN at scan rate 100 mVs^{-1}. WE: GC; CE: Pt; Ref: Ag.

A non-reversible reduction process takes place at $E_P^c = -1.97$ V vs Fc^+/Fc and this was also recorded at different scan rates.

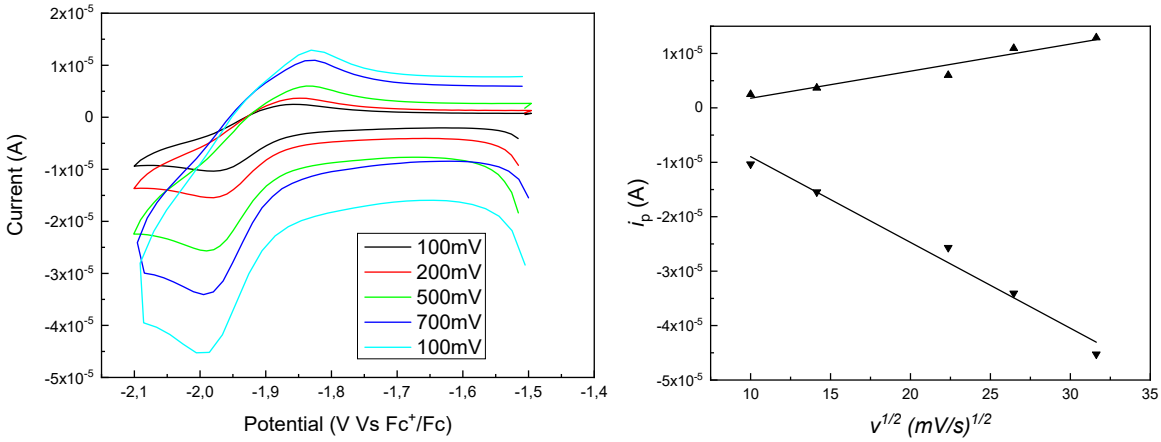

Figure 65 First reduction process of **11**, recorded at different scan rates (left) in MeCN; peak currents versus square-root of the scan rates plot (right). WE: GC; CE: Pt; Ref: Ag.

Capitalizing on the first reduction process, an experiment for Hydrogen Evolution Reaction (HER) can be also set up using complex **11**. The experimental procedure and data will be described in the next section.

5.3. Hydrogen Evolution Reaction (HER) Experiment with $[L^{O}NiFeNiL^{O}](OTf)_2$ complex

In this section, the activity of complex **11** with respect to HER catalysis is investigated by CV. As with complex **8**, it is crucial to provide H^+ from an appropriate source, which must have a reduction potential lower than the first reduction process of complex **11** ($E_P^c = -1.97$ V vs Fc^+/Fc). For this reason, benzoic acid (BZA) was selected, with a reduction potential of $E_P^c = 2.2$ V vs Fc^+/Fc (CV of BZA in figure 66).

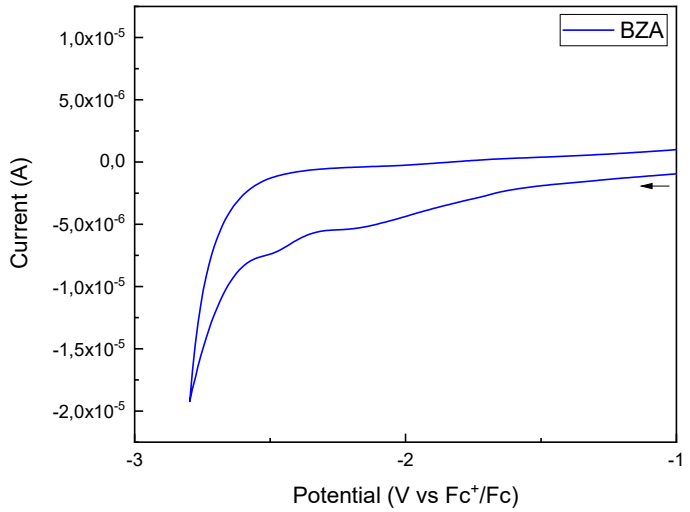

Figure 66 CV of BZA recorded scanning towards negative potentials first, in MeCN at scan rate 100 mVs^{-1}. WE: GC; CE: Pt; Ref: Ag.

The set-up of the experiment consists in having a 0.5 mM solution of **11** in MeCN (Bu_4NPF_6 0.1 M) in a tight-sealed CV cell at room temperature, equipped with glassy carbon (working electrode), Pt wire (counter electrode) and Ag wire (reference electrode). The analysis is run in a N_2 atmosphere glovebox, under exclusion of O_2. A Hamilton gas-tight syringe was used to inject the appropriate amount of BZA during the experiment. Below, the CVs given by increasing equivalents of proton source are plotted, in a range from -2.8 V to 0 V.

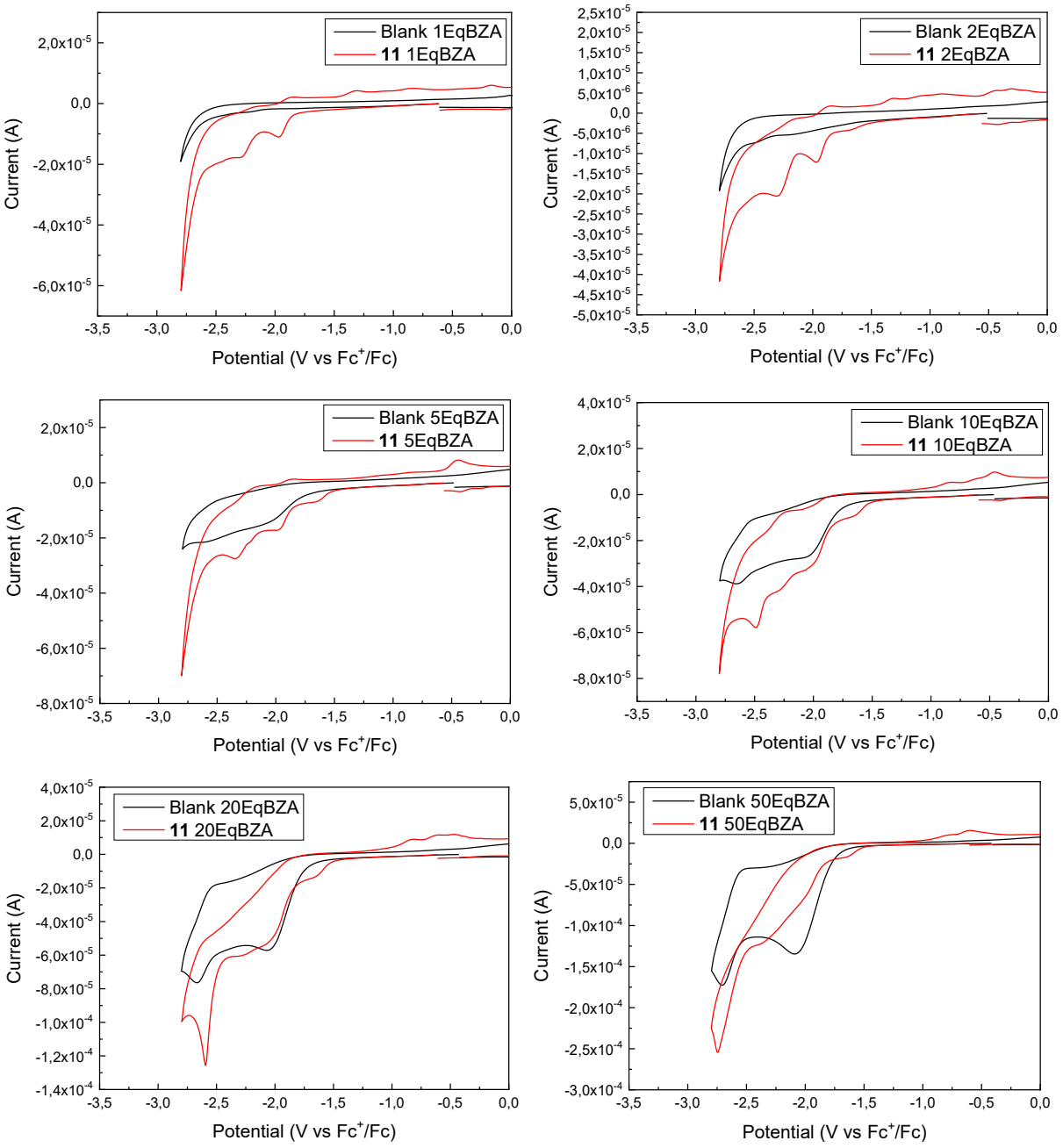

Figure 67 HER experiment of **11** with 1 equivalent of BZA (top-left); with 2 equivalents of BZA (top-right); with 5 equivalents of BZA (center-left); with 10 equivalents of BZA (center-right); with 20 equivalents of BZA (bottom-left); with 50 equivalents of BZA (bottom-right). (in MeCN at 100 mVs^{-1}).

In Figure 67, the black curves represent the blank solution plus additions of different equivalents of BZA. The black curves are used for comparison with the CVs of the solution of complex **11** (in red) upon addition of the same equivalents of the proton source. Upon increasing the concentration of the proton source, no enhancement in the catalytic current of complex **11** was observed.

5.4. Synthesis of $[L^{O}NiCoNiL^{O}](OTf)_2$ complex

The synthesis of the trinuclear complex $[L^{O}NiCoNiL^{O}](OTf)_2$ **12** can be achieved by following the strategy used for the preparation of complex **11**. $Co(OTf)_2$ is dissolved in MeCN and stirred for a minute at room temperature, then complex **5** is added solid, in a 1:2 ratio (Scheme 18). After stirring for 48h the product is obtained via crystallization by diffusion of Et_2O in a solution of MeCN, affording red crystals.

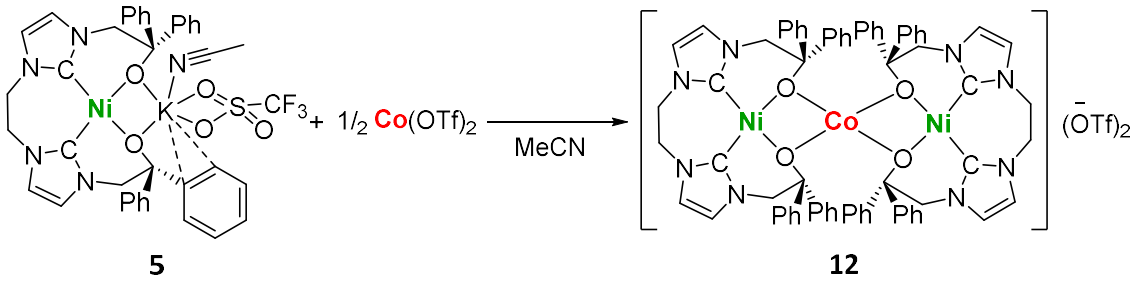

Scheme 18 Synthetic scheme of $[L^{O}NiCoNiL^{O}](OTf)_2$ complex **12**.

$[L^{O}NiCoNiL^{O}](OTf)_2$ complex **12** was characterized by means of X-ray diffraction, UV/Vis spectroscopy, ESI(+) mass spectrometry and Elemental Analysis. Magnetic properties were investigated in detail by SQUID magnetometry.

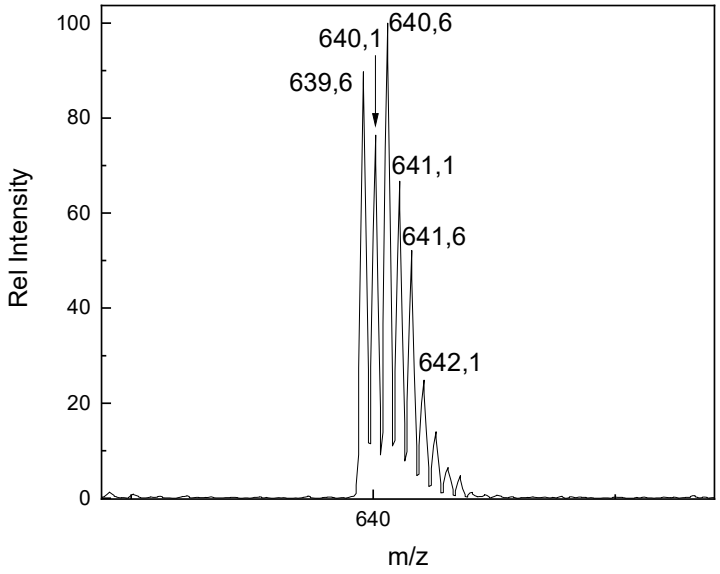

Figure 68 ESI(+) mass spectrum of $[L^{O}NiCoNiL^{O}](OTf)_2$ complex **12** recorded in MeCN.

As already witnessed with complex **11**, the mass spectrum shows the signal of the doubly-charged ion $[L^{O}NiCoNiL^{O}]^{2+}$ at 639 m/z, indicating that the NiCoNi core remains intact in solution of MeCN.

The UV/Vis characterization was also performed and the spectra were recorded at two different concentrations, $5.5 \cdot 10^{-5}$ mM and $2.8 \cdot 10^{-4}$ mM, given the difference in intensity of the absorption bands, shown in figure 71 (left and right).

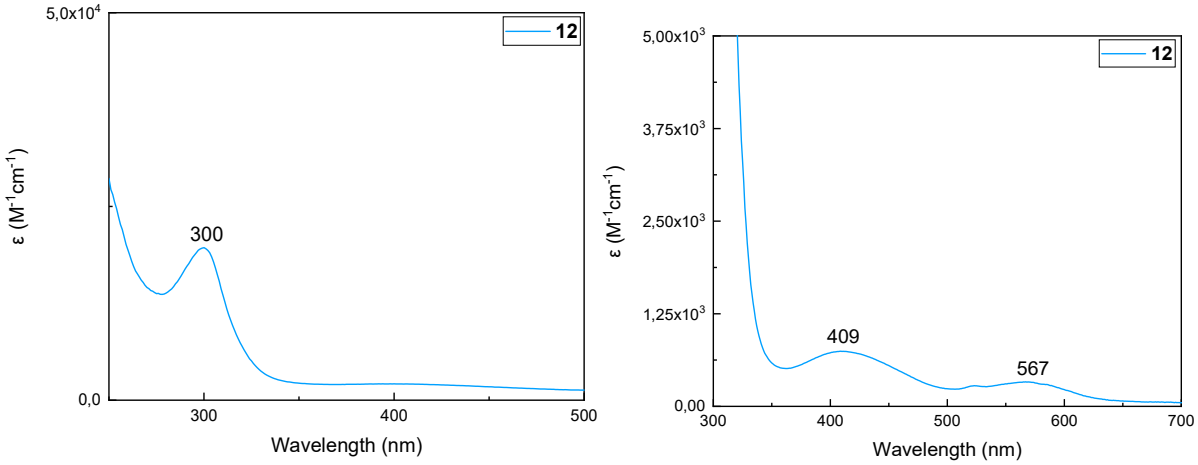

Figure 69 (Left) UV/Vis spectrum of $[L^{O}NiCoNiL^{O}](OTf)_2$ complex **12** in MeCN at $5.5 \cdot 10^{-5}$ M. (Right) UV/Vis Spectrum of **12** in MeCN at $2.8 \cdot 10^{-4}$ M.

Similarly to complex **11**, the UV/vis spectrum of complex **12** at $5.5 \cdot 10^{-5}$ M (figure 69, left) shows an absorption maximum at λ_{max} = 300 nm, slightly red-shifted compared to the bi-metallic complexes **8** and **9**, likely caused by the presence of a Co^{II} bound to the bridging O-atoms of the two $[L^{O}Ni]$ units.[68] Based on the high molar extinction coefficient, the λ_{max} is tentatively assigned to a MLCT transition ($O \rightarrow Ni^{II}$).[69] The spectrum recorded at higher concentration ($2.8 \cdot 10^{-4}$ M) (figure 69, right) shows maxima absorptions at λ_{max} = 409 nm and λ_{max} = 567 nm. As already stated in chapter 4.7. for the bimetallic $[L^{O}NiCo](MeCN)(I)_2$ complex **9**, and based on their lower molar extinction coefficients, these bands are tentatively assigned to d-d transitions for high spin Co^{II} ions.[78,76] For better comparison, table 7 reports the UV/Vis absorptions for all complexes discussed.

Table 7 UV/Vis absorption features of complexes **5**, **8**, **9**, **11** and **12**.

Complexes	λ_{max} 1 (nm)	λ_{max} 2 (nm)	λ_{max} 3 (nm)
$[L^{O}NiK](MeCN)(OTf)$ **5**	320		
$[L^{O}NiFe](OTf)_2(Acetone)_2$ **8**	291	392	
$[L^{O}NiCo](MeCN)(I)_2$ **9**	295	390	577
$[L^{O}NiFeNiL^{O}](OTf)_2$ **11**	301	414	
$[L^{O}NiCoNiL^{O}](OTf)_2$ **12**	300	409	567

The structure of complex **12**, with selected parameters, is reported in figure 70 and Table 8.

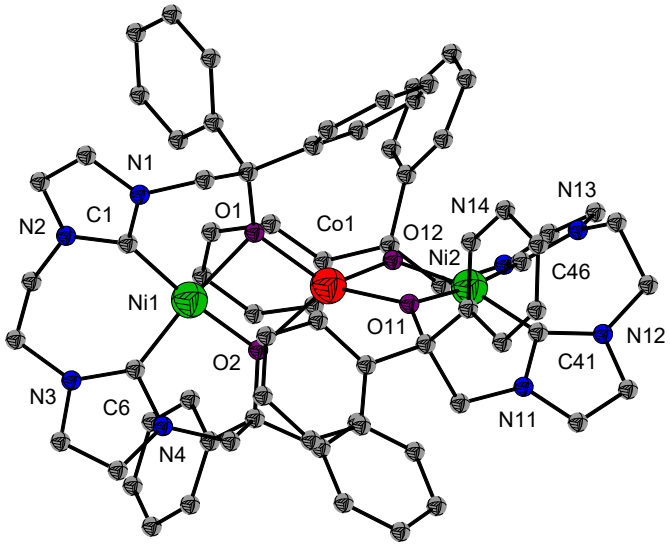

Figure 70 Molecular structure of $[L^{O}NiCoNiL^{O}](OTf)_2$ complex **12** (H-atoms were omitted for clarity).

Complex **12** crystallizes in the monoclinic space group $P2_1/c$, with 4 molecules per unit cell. As in the case of complex **11**, complex **12** builds upon two units of $[L^{O}Ni]$ acting as a metalloligand towards a single central Co^{II} ion.

Table 8 Selected bond lengths [Å] and bond angles [°] for $[L^{O}NiCoNiL^{O}](OTf)_2$ complex **12**.

Atoms	Bond lengths [Å]	Atoms	Bond angles [°]
Ni1-C1	1.840(4)	C1-Ni1-C6	90.56(17)
Ni1-C6	1.882(4)	C1-Ni1-O2	172.51(14)
Ni1-O2	1.923(3)	C6-Ni1-O2	96.01(14)
Ni1-O1	1.953(3)	C1-Ni1-O1	92.04(15)
Ni1-Co1	2.9838(7)	C6-Ni1-O1	168.90(16)
Ni2-C46	1.846(4)	O2-Ni1-O1	82.18(11)
Ni2-C41	1.875(4)	C46-Ni2-C41	90.40(17)
Ni2-O11	1.923(3)	C46-Ni2-O11	172.45(14)
Ni2-O12	1.947(3)	C41-Ni2-O11	96.03(15)
Ni2-Co1	2.9773(7)	C46-Ni2-O12	91.89(15)
Ni1-Co1	2.9838(7)	C41-Ni2-O12	167.05(17)
Ni2-Co1	2.9773(7)	O11-Ni2-O12	82.72(11)
Co1-O2	1.989(3)	O2-Co1-O1	79.58(11)
Co1-O1	1.992(3)	O2-Co1-O12	130.02(13)
Co1-O12	1.996(3)	O1-Co1-O12	125.02(11)
Co1-O11	1.996(3)	O2-Co1-O11	121.62(11)
		O1-Co1-O11	128.09(12)
		O12-Co1-O11	79.69(11)

As already reported for complex **11**, also in complex **12** the two [L^{O}Ni] units have comparable bond lengths and angles. The Ni^{II} ions are coordinating in a square-planar configuration with binding angles very close to 90° (see table 8). The central Co^{II} ion is bound to the four oxygen from the two {O-O´}-chelating [L^{O}Ni] metalloligands. All four Co-O distances are around 1.99 Å. The O-Co-O´ angles involving the {O-O´}-chelating [L^{O}Ni] units are small (ca. 80°) while all the other O-Co-O angles are much wider (121-130°). These, as well as other structural features, will be further discussed in the next section.

5.5. $[L^{O}NiCoNiL^{O}](OTf)_2$ complex as zero-field Single Ion Magnet (SIM)

The magnetic properties of the trimetallic complex **12** were probed with a Quantum Design MPMS3 SQUID magnetometer on a powder polycrystalline sample covered with low viscosity perfluoropolyether-based inert oil Fomblin Y45 to prevent any torquing of the microcrystals. The $\chi_M T$ value of 3.09 cm^3mol^{-1} K at 210 K is in agreement with the presence of two low-spin Ni^{II} ions (d^8, S = 0) and a high-spin Co^{II} ion (d^7, S = 3/2) (figure 71, left). The $\chi_M T$ value of 3.09 cm^3mol^{-1} K is higher than the expected value (1.875 cm^3mol^{-1} K) for an isolated non-interacting high-spin Co(II) ion (d^7, S = 3/2, g = 2.0), indicating considerable orbital contributions to the magnetic moment. The $\chi_M T$ value remains almost constant until 100 K before gradually decreasing on cooling to 2.16 cm^3mol^{-1} K at 2.0 K. As the nearest Co^{II}-Co^{II} distance in the crystal lattice is rather large (12.184 Å), intermolecular interactions can be assumed to be negligible and the decrease of $\chi_M T$ can be ascribed to the presence of large zero-field splitting (ZFS) and significant magnetic anisotropy. The magnetic susceptibility data of complex **12** were fitted along with the variable-field variable-temperature (VTVH) magnetization data (figure 71, right) to the spin Hamiltonian

$$\widehat{H} = D\left[\hat{S}_z^2 - \frac{1}{3}S(S+1)\right] + E(\hat{S}_x^2 - \hat{S}_y^2) + \mu_B \vec{B} g \vec{S}$$

where the terms represent their meaning as described in chapter 4.5. The best fit with the program *julX*_2s[75] yields D = -74.3cm^{-1}, E/D = 0, g_x = g_y = 2.33, g_z = 2.89 and *TIP* =178 · 10^{-6} cm^3mol^{-1} (subtracted).

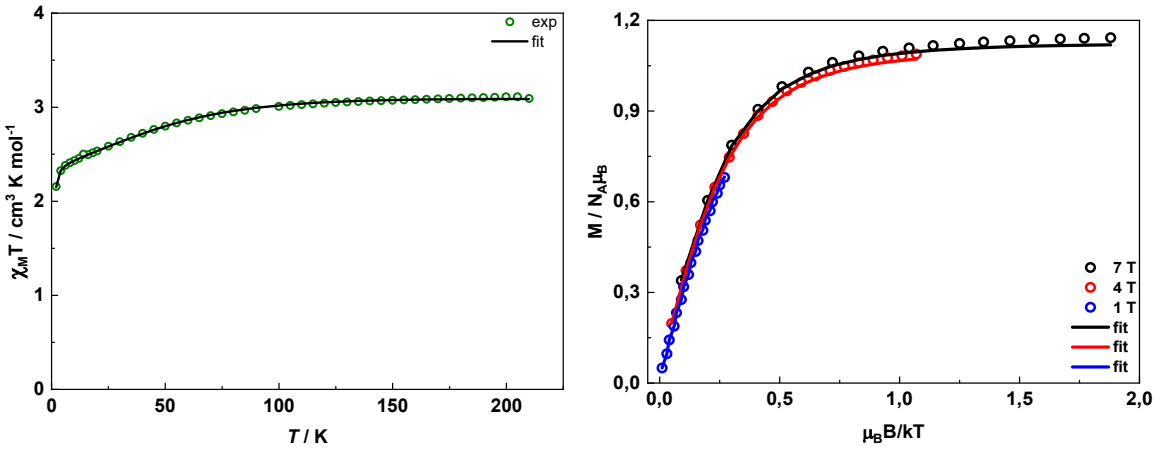

Figure 71 (Left) Temperature dependence of $\chi_M T$ for complex **12** at an applied dc field of 0.5 T. (Right) Variable-temperature variable-field magnetization for complex **12**. The solid lines are the best fit with D = -74.3cm^{-1}, E/D = 0, $g_x = g_y$ = 2.33, g_z = 2.89 and TIP = 178 · 10^{-6} cm^{3}mol^{-1} (subtracted).

The large negative D indicates a significant separation between the ground state m_S = ±3/2 Kramers doublet (KD) and the excited state m_S = ±1/2 KD. To investigate the slow relaxation dynamics of magnetization, ac susceptibility measurements were performed on polycrystalline samples of **12** in the frequency range of 0.1 – 1000 Hz in an oscillating ac field of 3.0 Oe without the application of any external dc field. Temperature-dependent and temperature-independent regimes were observed in the frequency-dependent out-of-phase (χ_M'') component of ac susceptibilities with clear maxima up to 12.2 K (figure 72).

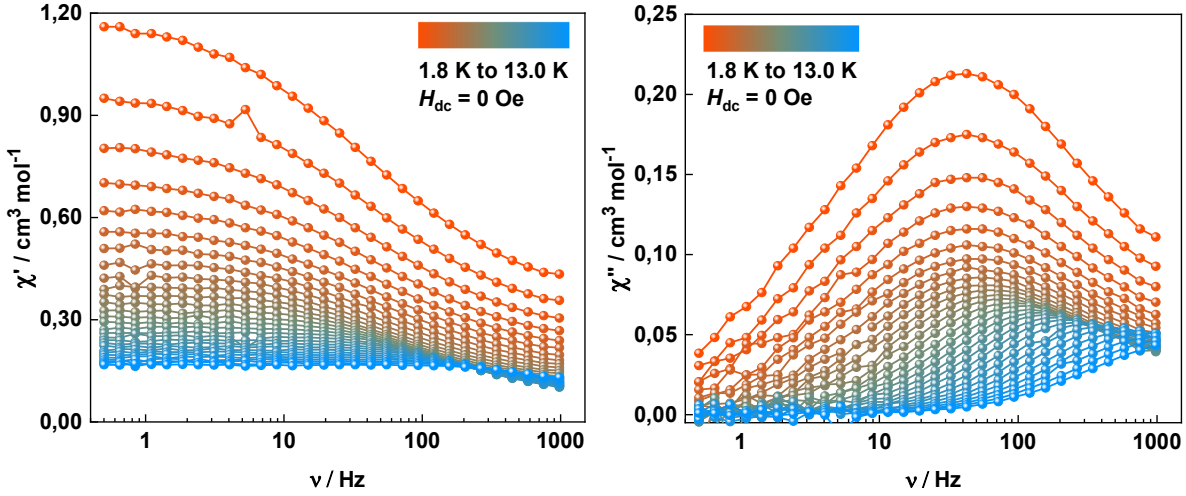

Figure 72 In-phase (χ_M') (left) and out-of-phase (χ_M'') (right) component of the frequency-dependent (0.1–1000 Hz) ac susceptibility measured for **12** in the indicated temperature range under zero applied dc field for **12**.

The Cole-Cole plots of the out-of-phase (χ_M'') versus in-phase (χ_M') component of the ac susceptibilities display a distorted semi-circular curve (Figure 73, top). The χ_M'' versus χ_M' curves were fitted with the generalized Debye function to extract the relaxation times (τ). Analysis reveals the α parameter to lie in the 0.13-0.43 range indicating a wide distribution of relaxation times. At low temperatures, QTM dominates the relaxation mechanism, whereas the Orbach and Raman processes seem to be favourable pathways for relaxation at higher temperatures. A linear fit to the relaxation rates at higher temperatures yields U_{eff} = 66.7 K and $\tau_0 = 7.37 \times 10^{-7}$ s. To gain further insight into the dynamics of magnetic relaxation, the relaxation rates (τ) over the entire temperature range were treated with the following function (figure 73, bottom),

$$1/\tau = 1/\tau_{QTM} + AH^4T + CT^n + \tau_o^{-1} \exp(-U_{eff}/k_BT)$$

where the first term represents magnetic relaxation through QTM, the second and third terms correspond to relaxation via a direct and Raman process, and the last term represents relaxation through the Orbach mechanism, respectively. The best fit yields: U_{eff} = 125 K, $\tau_0 = 1.32 \times 10^{-8}$ s; C = 0.403 $s^{-1} K^{-n}$, n = 3.54; τ_{QTM} = 0.00349 s. To the best of our knowledge, this is the highest energy barrier reported for any 3d-SIMs based solely on oxo-donor ligand scaffolds. A survey of the literature also reveals that this is indeed the first example of any zero-field SIM based solely on an oxo-donor ligand scaffold.

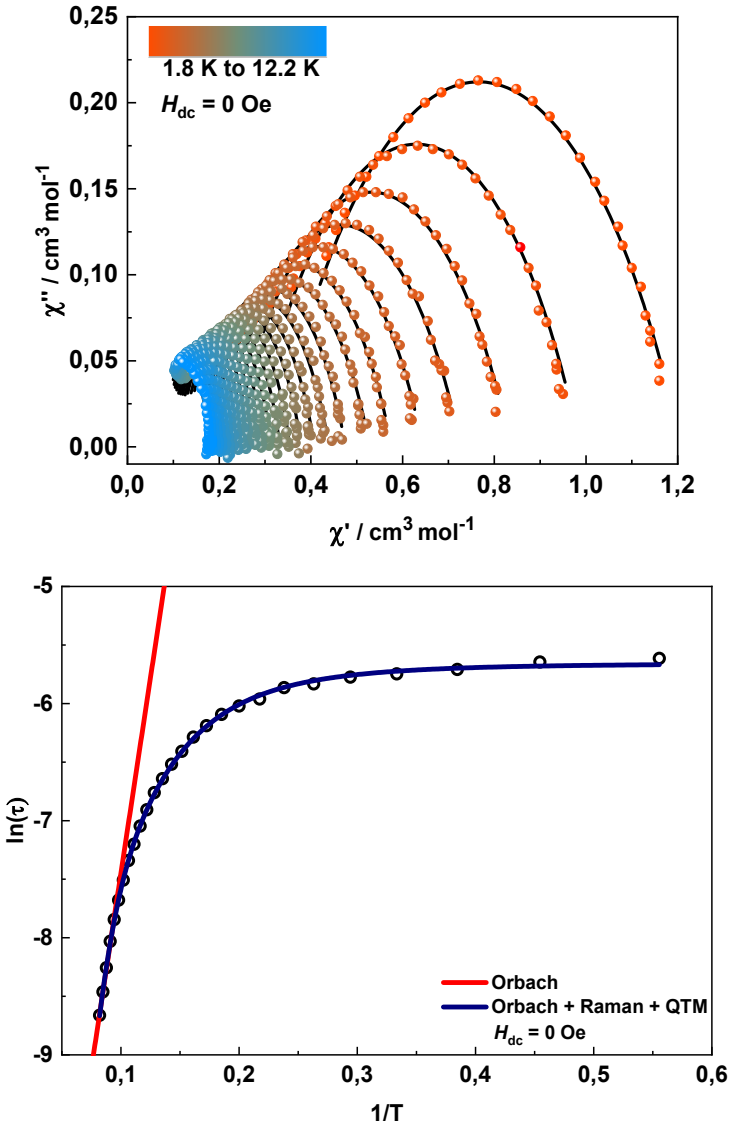

Figure 73 (Top) Cole–Cole plots for **12** under zero dc field. (Bottom) The plot of the relaxation time τ (logarithmic scale) versus T^{-1} for **12** under zero dc field; the solid red line corresponds to the fitting of the Orbach relaxation process and the solid blue line represents the best fitting to the combination of Orbach, QTM and Raman mechanism.

In order to get further insights into the relaxation dynamics, ac susceptibility measurements were also carried out under the application of an external dc field (figure 74). Application of an optimum dc field of 2000 Oe quenches the fast relaxation process via QTM operating at a lower temperature range (figure 73, bottom). Analysis of the Cole-Cole plots reveals a parameter in the 0.10-0.19 range indicating a narrower distribution of relaxation times (figure 75, top).

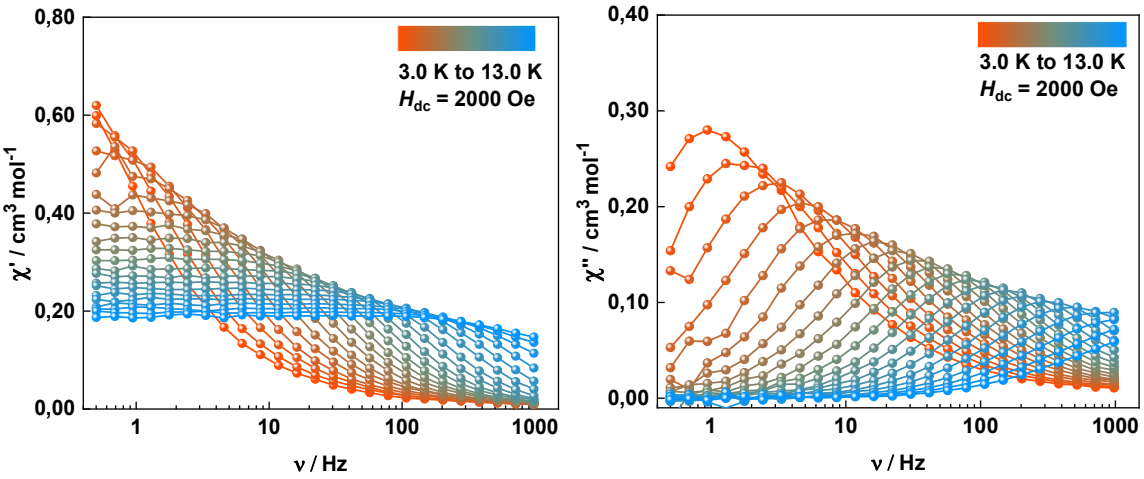

Figure 74 (Left) In-phase (χ_M') and (Right) out-of-phase (χ_M'') component of the frequency-dependent (0.1–1000 Hz) ac susceptibility measured for complex **12** in the indicated temperature range under an applied dc field of 2000 Oe.

Linear fitting of the high-temperature relaxation rates with an Arrhenius law estimates an energy barrier for magnetization reversal of U_{eff} = 94.5 K with $\tau_0 = 6.16 \times 10^{-8}$ s. As in the previous case, fitting the relaxation times over the entire temperature range indicates the relaxation to mainly proceed via the Orbach and Raman relaxation mechanisms (figure 75, bottom). The best fit parameters are U_{eff} = 134 K, $\tau_0 = 3.40 \times 10^{-9}$ s; C = 0.088 s^{-1} K^{-n}, n = 4.05.

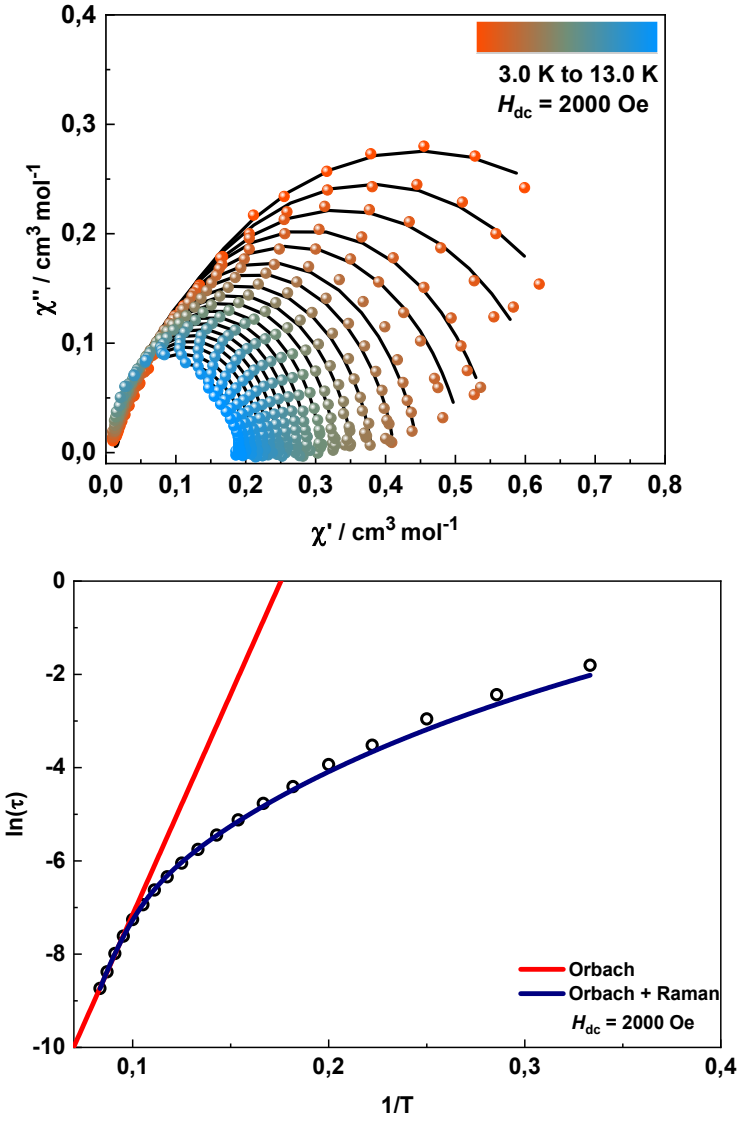

Figure 75 (Top) Cole–Cole plots for **12** under an applied dc field of 2000 Oe. (Bottom) The plot of the relaxation time τ (logarithmic scale) versus T^{-1} for **12** under an applied dc field of 2000 Oe; the solid red line corresponds to the fitting of the Orbach relaxation process, and the solid blue line represents the best fitting to the combination of Orbach and Raman mechanism.

In figure 75 (bottom), the red line follows the relaxation time in the Orbach process, which has a linear dependency on the temperature. The U_{eff} found for the Orbach process is 94.5 K, and τ_0 is $6.16 \cdot 10^{-8}$ s. The solid blue line takes into account both the Orbach and Raman processes. Since the experiment is conducted in an applied dc Field of 2000 Oe, QTM is quenched. Taking into account these two relaxation processes, we can obtain these parameters: U_{eff} = 134 K, $\tau_0 = 3.40 \times 10^{-9}$ s; C = 0.088 s^{-1} K^{-n}, n = 4.05.

Variable field magnetization measurement conducted at 1.8 K at a sweep rate of 100 Oe/s, however, does not reveal any opening of a hysteresis loop, indicating the blocking temperature of the SIM to be below 1.8 K, the minimum temperature accessible by our SQUID magnetometer (figure 76).

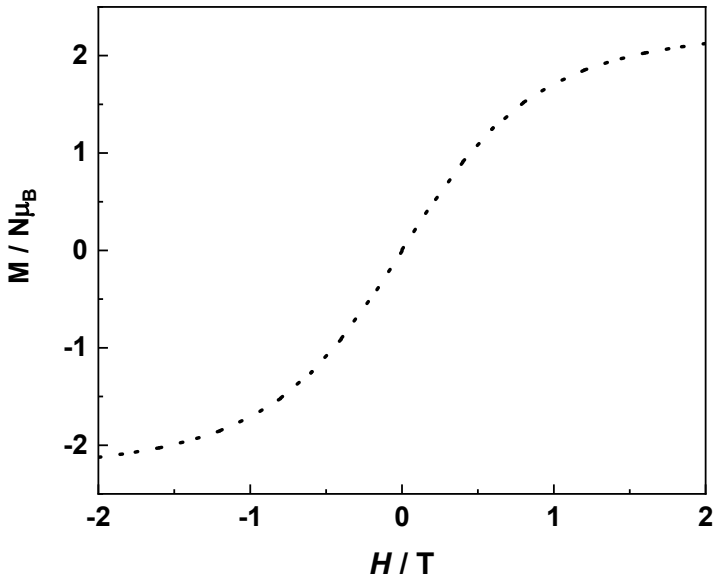

Figure 76 Variable-field magnetization for complex **12** at 1.8 K at a sweep rate of 100 Oe/s.

The unprecedented zero-field SIM behaviour of **12** can be ascribed to the following facts:

a) As stated above, to the best of our knowledge, there are no reports of any zero-field 3d SIM with the metal ion being ligated solely by O-donors. It is now an established fact that if the first coordination sphere in a compressed or elongated tetrahedral (D_{2d} symmetry) Co^{II} complex is of soft donor atoms, the $m_s = \pm 3/2$ KD is stabilized and ZFS is enhanced.[58,79–81] In the present case, the presence of the diamagnetic Ni^{II} ions in the metalloligands significantly reduces the hard nature of the oxo-donors.

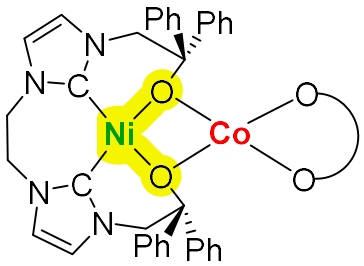

Figure 77 Structure of complex **12**, highlighting the softer character of the oxo-donors towards the Co^{II} center.

b) Various magneto-structural correlation studies have further established that a bite angle of 71-81° in the case of a bidentate ligand system is optimal for enhancing the magnetic anisotropy in a tetrahedral [CoN_4] system.[82] In our present case, the bite angle of the {O-O´}-metalloligand (79.58° and 79.69°) falls within the range. However, one has to consider that the optimal bite angle would differ depending on the nature of the ligand system and other structural parameters.

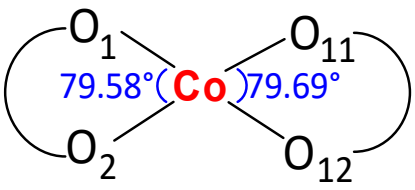

Atoms	Bond angles [°]
O2-Co1-O1	79.58(11)
O12-Co1-O11	79.69(11)

Figure 78 Chelating bond angles for **12**.

c) Further, we have shown from the recent research in our group that the optimal dihedral angle for maximizing the magnetic anisotropy of a [CoN_4] D_{2d} system is 90°.[83] The dihedral angle of 84.32° in complex **12** is very close to the optimal dihedral angle

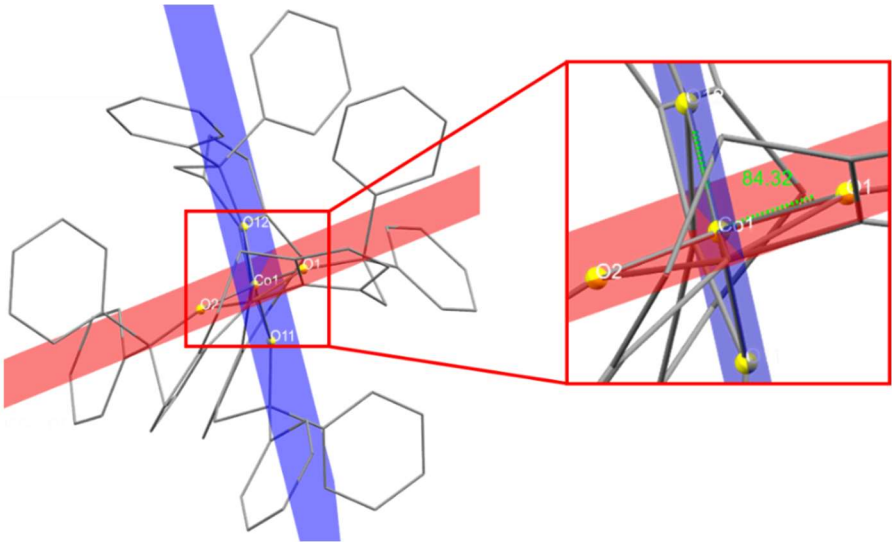

Figure 79 Dihedral angle in **12** formed by the planes containing the two [L^ONi] units (figure obtained from the software Mercury).

A compilation of Co^{II} SIM complexes is shown in table 9, displaying D and U_{eff} values in presence/absence of an applied magnetic field. At the bottom, data for **12** is reported for comparison. A full description of the table can be found in the appendix section.

Table 9 Compilation of tetracoordinate Co^{II} SIM complexes.[58]

Compound	D Value (cm^{-1})	Applied magnetic field (H/Oe)	Ueff (cm^{-1})
$(Ph_4P)_2[Co(SPh)_4]$ (**A**)[58]	-70	1000	21
$(Ph_4P)_2$ $[Co(C_3S_5)_2]$ (**B**)[84]	161	0	33.9
$(HNEt_3)_2[Co(pdms)_2]$ (**C**)[56]	-115	0	118
$(HNEt_3)_2[Co(L^1)_2](H_2O)$ ($\mathbf{D_I}$)[85]	-144.1	0	46.02
$(Bu_4N)_2[Co(L^2)_2](H_2O)$ ($\mathbf{D_{II}}$)[85]	-130.8	0	58.41
$[Co(L^3)_2](ClO_4)_2$ (**E**)[86]	-45.9	1000	46.9
$[Co(salbim)_2]$ (**F**)[87]	67	-	-
$[Co(acac)_2(H_2O)_2]$ (**G**)[88]	57	-	-
$[Co(OPh)_4](CH_3CN)$ ($\mathbf{H_I}$)[79]	-11.3	1400	21
$[K(Ph_4P)][Co(OPh)_4]$ ($\mathbf{H_{II}}$)[79]	-23.8	0	34
$(Ph_4P)_2[Co(SPh)_4]$ ($\mathbf{H_{III}}$)[79]	-62	0	21
$(Ph_4P)_2[Co(SePh)_4]$ ($\mathbf{H_{IV}}$)[79]	-83	0	19.1
$Co(quinoline)_2I_2$ ($\mathbf{I_I}$)[89]	9.2	-	-
$Co(PPh_3)_2I_2$ ($\mathbf{I_{II}}$)[89]	-36.9	1000	21.2
$[Co(AsPh_3)_2I_2]$ ($\mathbf{I_{III}}$)[89]	-74.7	1000	22.6
$(HNEt_3)_2[Co(bmsab)_2]$ ($\mathbf{J_I}$)[90]	-115	-	-
$K_2[Co(bmsab)_2]$ ($\mathbf{J_{II}}$)[90]	-118	-	-
$(HNEt_3)_2[Co(btsab)_2]$ ($\mathbf{J_{III}}$)[90]	-110	-	-
$[Co(L^{Br})_2]$ ($\mathbf{K_I}$)[91]	-36.7	400	36
$[Co(L^{Ph})_2](CH_2Cl_2)$ ($\mathbf{K_{II}}$)[91]	-39.8	400	43
$[Co(L^{Sal,2\text{-}Ph})_2]$ ($\mathbf{L_I}$)[92]	-25.1	1000	49
$[Co(L^{Nph,2\text{-}Ph})_2]$ ($\mathbf{L_{II}}$)[92]	-31.4	1000	78
$[Co(Himl)_2](CH_3OH)$ ($\mathbf{M_I}$)[93]	-42	1400	-
$[Co(Himn)_2]$ ($\mathbf{M_{II}}$)[93]	-38	0	-
$[Co(Hthp)_2]$ ($\mathbf{M_{III}}$)[93]	-35	800	61.9
$[CoL^4(NCS)_2]$ ($\mathbf{N_I}$)[94]	-16.2	1000	20.9
$[CoL^4(Cl)_2]$ ($\mathbf{N_{II}}$)[94]	-15.1	1000	17.7
$[CoL^4(Br)_2]$ ($\mathbf{N_{III}}$)[94]	-11.6	1000	12.9
$[CoL^4(I)_2]$ ($\mathbf{N_{IV}}$)[94]	-7.3	1000	6.3
$C_{16}H_{52}B_{20}CoN_2S_4$ ($\mathbf{O_I}$)[95]	-71.6	1000	26.8
$[NEt_4][Co(PPh_3)Cl_3]$ ($\mathbf{P_I}$)[96]	42.8	1200	-
$[NEt_4][Co(PPh_3)Br_3]$ ($\mathbf{P_{II}}$)[96]	41.2	1500	-
$[L^ONiCoNiL^O](OTf)_2$ (**12**)	-74.3	0	125
$[L^ONiCoNiL^O](OTf)_2$ (**12**)	-74.3	2000	134

5.6. Summary and outlook

There have been intense efforts in the design and development of suitable SIMs in the last decade to harness the maximum magnetic anisotropy of 3d ions. In this work a bimetallic [L^{O}NiK(MeCN)(OTf)] system **5** was developed, where the K^{+} ion can be suitably replaced by divalent 3d metal ions, such as Fe^{II} and Co^{II}, to produce trimetallic systems, having the [L^{O}Ni] unit acting as a metalloligand. The [L^{O}NiMNiL^{O}]$^{2+}$ (M = Fe, Co) systems were synthesized and characterized with the aid of both spectroscopic and analytical techniques.

The electrochemical redox processes with [L^{O}NiFeNiL^{O}](OTf)$_2$ **11** prompted us to investigate the Hydrogen Evolution Reaction (HER) activity.

The most interesting part of the project was the isolation of complex [L^{O}NiCoNiL^{O}](OTf)$_2$, which shows an unprecedented zero-field SIM behaviour for a Co^{II} complex with exclusive oxo-donors; in this case, the [L^{O}Ni] subunits act as a neutral oxo-donor metalloligand. The reduced hardness or increased softness of the oxo-donor ligand sites helps in maximizing the magnetic anisotropy of the system leading to a zero-field with an effective energy barrier of over 125 K. The zero-field SIM behaviour of complex **12** stems from the manifestation of the close to optimal bite angle and close to optimal dihedral angle around the central paramagnetic Co^{II} ion in D_{2d} symmetry. These findings suggest the future development of modified metalloligand systems to maximize the magnetic anisotropy of 3d-SIMs. Complex **12** serves as the starting point to further the understanding in the field of designing new SIMs based on 3d ions.

6. Overall Summary

The new bis-imidazolinium proligands $[L^{S}H_4](OTf)_2$ (**2**) and $[L^{O}H_4](OTf)_2$ (**4**) were designed and synthesized to serve as tetradentate bis(NHC)-dithiolato and bis(NHC)-dialcoholato ligands for the complexation of Ni^{II}. The proligands and the complexes obtained were characterized by different spectroscopic techniques.

In case of **2**, multiple attempts with different metal ions were made. Despite this, has been proven impossible to synthesize any complex with it so far.

Aiming to compare the role of the potential O-bridging atoms in a bimetallic NiFe complex to the role of the S-bridging atom in complex $\mathbf{II_A}$ during electrocatalytic H_2 production, proligand $[L^{O}H_4](OTf)_2$ (**4**) was prepared. The Ni^{II} complex $[L^{O}NiK(MeCN)(OTf)]$ (**5**) was isolated and characterized, and electrocatalysis towards the hydrogen oxidation reaction (HOR) was attempted.

Making use of the ability of the $[L^{O}Ni]$ unit to bind multiple metal centers in close proximity, a series of bimetallic and trimetallic complexes with 3d metals, such as Fe^{II} and Co^{II}, was synthesized. The complex $L^{O}NiFe(OTf)_2(acetone)_2$ (**8**) was isolated and exploiting its first reduction process, the potential electrocatalysis towards hydrogen evolution reaction (HER) was probed.

The trimetallic $[L^{O}NiML^{O}]^{2+}$ (M = Fe, Co) systems were synthesized and characterized. Electrocatalytic hydrogen evolution was tested using $[L^{O}NiFeNiL^{O}](OTf)_2$ complex (**11**), and the results were discussed.

Complex $[L^{O}NiCoNiL^{O}](OTf)_2$ (**12**) showed an unprecedented zero-field SIM behaviour for a Co^{II} complex with exclusive oxo-donors. At zero-field **12** exhibits an effective energy barrier of over 125 K. The correlation between the structural feature of **12**, such as the close to optimal bite angle and the close to optimal dihedral angle around the central Co^{II} ion, may lead to the development of modified metalloligand systems to maximize the magnetic anisotropy of 3d-SIMs.

7. Experimental Part

7.1. General remarks and collaboration

The research and synthesis of all the complexes described build upon prior collaborative work with Dr. Carole Duboc´s group at the Université Grenoble Alpes in Grenoble, France. All the electrochemical characterizations of the complexes and experiments described were carried out in Grenoble.

7.2. Materials and Methods

7.2.1. Materials

Compounds **XVII** and **XVIII**, Bis(trifluoromethylsulfonyloxyl)ethane, Ni(DME)Br_2 were prepared following literature procedures. Chemicals and other reagents were purchased from commercial suppliers (MERCK, TCI, ChemPur, ABCR and BDL) and used without further purification. The proligands, precursors and complexes were synthesised under dried Ar atmosphere (dried by passing over P_2O_5 on solid support [Silicapent®, MERCK]) using Schlenk techniques. Syntheses of all Fe and Co complexes were performed in Ar atmosphere glovebox with levels of H_2O and O_2 below 0.5 ppm. All glassware was dried prior to synthesis in a 120°C oven, overnight. The solvents were HPLC or p.a. grade, were dried following standard procedures as necessary, stored under molecular sieves (3Å) and degassed with Ar. All deuterated solvents were treated as the non-deuterated analogous. Carbon Monoxide gas (CO) was purchased from MERCK and used without further purification. Hydrogen gas (H_2) was purchased from LINDE and used without further purification.

7.2.2. NMR Spectroscopy

^{1}H, ^{13}C, and ^{19}F NMR spectra were recorded on a spectrometer BRUKER AVANCE 300 or 400 MHz at 298 K, unless mentioned otherwise. All chemical shifts are reported in ppm and referenced to the corresponding signal of the residual solvent. ^{13}C NMR spectra were recorded in proton decoupled mode. Peaks are labelled according to their multiplicity and abbreviated as follows: s (singlet), d (doublet), t (triplet), q (quadruplet) and m (multiplet). The coupling constants were given in Hz and the analysis of the spectra was carried out with MestReNova 14.1.1.

7.2.3. Mass Spectrometry (MS)

ESI MS measurements were performed on a Thermo Finnigan Trace LCQ spectrometer or a Bruker HTCultra instrument. The air-sensitive samples were prepared in a glovebox under Ar atmosphere and injected in the machine via a direct Peek^{TM} capillary connection.

7.2.4. Ultraviolett/visible Spectroscopy (UV/Vis) and Infrared Spectroscopy (IR)

UV/Vis spectra were recorded on a Varian Cary 5000 or Varian Cary 60 machine, using quartz cells (1 cm) in the solvent indicated.

Solid state and solution IR spectra were recorded with a Cary 630 FTIR spectrometer with Dial Path Technilogy and analyzed by FTIR Microlab software. The peaks are labelled according to their corresponding intensity.

7.2.5. Mößbauer Spectroscopy (MB)

MB spectra were recorded at the indicated temperature with a ^{57}Co source in a Rh matrix using an alternating constant-acceleration *WissEl* Mößbauer spectrometer operated in the transmission mode and equipped with a *Janis* closed-cycle helium cryostat. All measurement were performed and have been analyzed by Dr. Serhiy Demeshko. Isomer Shifts (IS) and Quadrupole Splitting (QS) are given in mms^{-1} relative to iron metal at ambient temperature. For simulation of the experimental data, the Mfit program was used. Air-sensitive samples were prepared in a glovebox under Ar, and immediately frozen in liquid nitrogen. Solids samples were prepared in sealable PEEK tablets, mounted in a sample holder. Solution samples were placed in a PEEK cup, requiring ca. 30 mg of solid material dissolved in 1 mL of appropriate solvent. Data were collected for one day in order to have a satisfactory signal/noise ratio.

7.2.6. Electron Paramagnetic Resonance Spectroscopy (EPR)

X-band EPR spectra were recorded with a Bruker E500 ELEXSYS spectrometer equipped with a standard cavity (ER4102ST, 9.45 GHz). The measurements were performed by Dr. Claudia A. Sctückl and have been analyzed with the help of Dr. Yang Liu. The temperature was regulated with an Oxford Instrument Helium flow cryostat (ESP910) and an Oxford temperature controller (ITC-4). Microwave frequency was recorded with the built-in frequency counter and

the calibration of the magnetic field was done with an NMR field probe (Bruker ER035M). The simulated spectra were obtained by using Easy Spin or XSophe software.

7.2.7. Magnetic Susceptibility Measurements (SQUID)

For the measurement of temperature-dependent magnetic susceptibilities, a SQUID magnetometer (Quantum Design MPMS3) was used. Measurements were performed by Dr. Sandeep K. Gupta. Solid samples were placed in a capsule inside a glovebox under Ar atmosphere. To avoid orientation of the crystalline material, all solids were fixed with low viscosity perfluoroether based inert oil *Fomblin Y45*. The capsule was placed in a diamagnetic sample holder (PTFE straw). A correction for the diamagnetic contribution of the gelatin capsule was applied to each raw data file, according to the formula $M_{dia}(caps) = \chi_g \cdot m \cdot H$. Using Pascal constants and the increment method, the molar susceptibility data were corrected for the diamagnetic contribution. According to $\chi_{calc} = (1 - PI) \cdot \chi + PI \cdot \chi_{mono} + TIP$, temperature-independent paramagnetism (*TIP*) and paramagnetic impurities (*PI*) were included in the calculations. Intermolecular interactions were included in a mean-field approach by using a Weiß temperature Θ. The Weiß temperature Θ (defined as $\Theta = z\, J_{inter}\, S(S+1)/3k$) relates to intermolecular interactions $z\, J_{inter}$, where J_{inter} represents the interaction parameter between two nearest neighbour magnetic centres, k is the Boltzmann constant (0.695 $cm^{-1}\, K^{-1}$) and z is the number of the nearest neighbour centres.

7.2.8. X-Ray Crystallography

X-ray data were obtained from a BRUKER D8-QUEST (graphite monochromated Mo-Kα radiation, λ = 0.71073 Å) or from an STOE IPDS II diffractometer by the use of w scans at low temperature. All measurements were performed and have been analyzed by Dr. Sebastian Dechert. Structures measured were resolved with the SHELXT software and refined on F^2 using all reflections with SHELXL. Non-Hydrogen atoms were anisotropically refined unless otherwise noted. Hydrogen atoms were placed in calculated positions and assigned to an isotropic displacement of 1.2/1.5 Ueq(C). Face-indexed absorption corrections were performed by the program X-RED.

7.2.9. Electrochemistry

Cyclic voltammetry (CV) was performed under inert conditions with a Gamry Interface 1000b potentiostat controlled by Gamry software, or a PGSTAT100N potentiostat controlled by

NOVA 2.5.1 or also IVIUM software. CV in Grenoble was recorded and analyzed with the help of Dr. Marcello Gennari and Dr. Carole Duboc. Samples were measured in MeCN solution at a concentration of 0.5 mM of complex and 0.1 M of Bu_4NPF_6 as conductive salt. Glassy carbon electrode was used as a working electrode, platinum wire as a counter electrode and silver wire in a 0.1 M solution of $AgNO_3$ in MeCN as a reference electrode. Ferrocene was added as an internal standard and all spectra were referenced to the ferrocene/ferrocenium redox couple (Fc/Fc^+). The electrochemical analysis was carried out with Gamry EChem Analyst software or NOVA 2.5.1 software.

7.3. Syntheses of proligands

7.3.1. Synthesis of ligand precursor 1

1

In a 3-neck 500 mL Schlenk flask, equipped with a reflux condenser and a dropping funnel, imidazole (9 g, 0.13 mol, 1 eq) was dissolved in 80 mL of dry toluene at 80°C. In a separate flask, isobutylene sulfide (3.84 g, 0.04 mol, 0.33 eq) was dissolved in 50 mL of dry toluene and then transferred in the dropping funnel. The solution of the sulfide was added dropwise to the initial solution and then the reaction was stirred at reflux overnight. The solution was allowed to cool to room temperature, then 100 mL of Et_2O were poured into the flask and the mixture was kept in the freezer overnight, allowing the precipitation of the excess imidazole. The solution was filtered and the organics were washed with a 1 M solution of $NaHCO_3$, brine and finally dried over Na_2SO_4. The solution was filtered and the solvent was removed via rotary evaporator, to give a yellow oil as a product (3.74 g, 0.02 mol, Yield = 55%).

^{1}H NMR (300 MHz, $CDCl_3$): δ[ppm] = 1.34 (s, 6 H, 5-H), 3.97 (s, 2 H, 4-H), 6.95 (d, 1 H, 3-H), 7.00 (d, 1 H, 2-H), 7.50 (s, 1 H, 1-H).

ESI-MS(+): m/z = 157.1 [**1**+H]$^+$

7.3.2. Synthesis of [L^SH_4] proligand

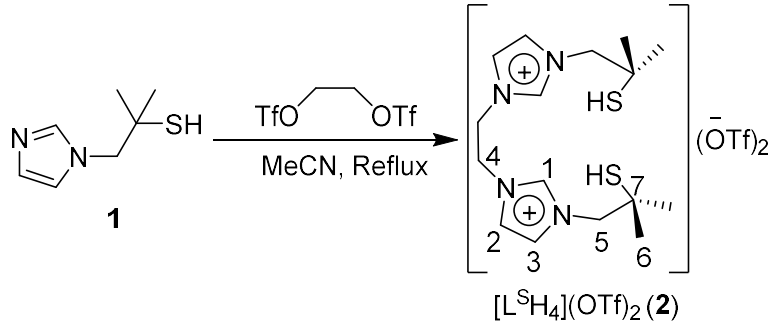

1 $[L^SH_4](OTf)_2$ (**2**)

In a two-necked 100 mL flask, equipped with a condenser, **1** (4.00 g, 0.026 mol, 2 eq) was dissolved in MeCN at 80°C, then 1,2-bis(trifluoromethylsulfonyloxyl) ethane (4.18 g, 0.013 mol, 1 eq) was added and the reaction was stirred at reflux overnight. The solvent was evaporated via rotary evaporator and the crude was dissolved in the minimum quantity of MeCN. 200 mL of pentane were added to the flask and the solution was cooled at -27°C overnight allowing precipitation. The product was obtained as a white powder (5.00 g, 0.01 mol, Yield = 79%).

^{1}H NMR (300 MHz, DMSO-d^6): δ[ppm] = 1.30 (s, 12 H, 6-H), 4.26 (s, 4 H, 4-H), 4.76 (s, 4 H, 5-H), 7.72 (d, 2 H, 3-H), 7.77 (d, 2 H, 2-H), 9.08 (s, 2 H, 1-H).

^{13}C NMR (75 MHz, DMSO-d^6): δ[ppm] = 29.18 (6-C), 43.48 (7-C), 48.47 (5-C), 60.71 (4-C), 121.81 (3-C), 124.62 (2-C), 137.38 (1-C).

ESI-MS(+): m/z = 489.13 $[L^SH_4(OTf)]^+$

7.3.3. Synthesis of [L^OH_4] proligand

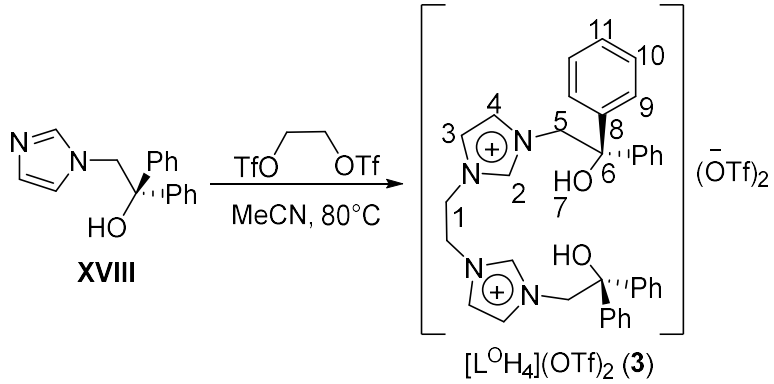

Precursor **XVIII** (7.41 g, 0,028 mol, 2 eq) was dissolved in MeCN and the solution was heated to reflux temperature (80°C) overnight. After that, 1,2-Bis(trifluoromethylsulfonyloxyl)ethane (4.8 g, 1.8 mL, 0.01 mol, 1 eq) was introduced into the reaction flask and the reaction was stirred at reflux overnight. The solvent was removed in vacuo, giving an oil. Dissolving in the minimum quantity of THF and layering with Et_2O, caused the crystallization of the product as a white powder (9.1 g, 0.01 mol, Yield = 78%).

^{1}H NMR (300 MHz, DMSO-d^6): δ[ppm] = 4.56 (s, 4 H, 1-H), 5.07 (s, 4 H, 5-H), 6.62 (s, 2 H, 7-H), 7.17 (s, 2 H, 3-H), 7.22 (s, 2 H, 4-H), 7.25-7.45 (m, 20 H, Ph-H, aromatic), 8.78 (s, 2 H, 2-H).

^{13}C NMR (75 MHz, DMSO-d^6): δ[ppm] = 48.26 (1-C), 57.99 (5-C), 76.27 (6-C), 121.20 (4-C), 124.33 (3-C), 126.07 (9-C), 127.66 (11-C), 128.48 (10-C), 137.29 (2-C), 143.79 (8-C).

ESI-MS(+): m/z = 278.1 [$L^OH_4^{2+}$], 705.2 [L^OH_4(OTf)]$^+$.

UV/Vis (MeCN): λ [nm] (ε [L M^{-1} cm^{-1}]) = 260 ($1.13x10^3$).

IR : ṽ [cm^{-1}] = 1026 (strong, sharp), 1153 (strong, sharp), 1250 (strong sharp), 1449 (strong, sharp), 1559 (strong, sharp) C=N, C-N, C=C stretching/bending fingerprints, 3138 (medium, broad, C-H stretching), 3406 (medium, broad O-H stretching).

7.4. Syntheses of Complexes

7.4.1. Synthesis of [L^{O}NiK(MeCN)(OTf)]

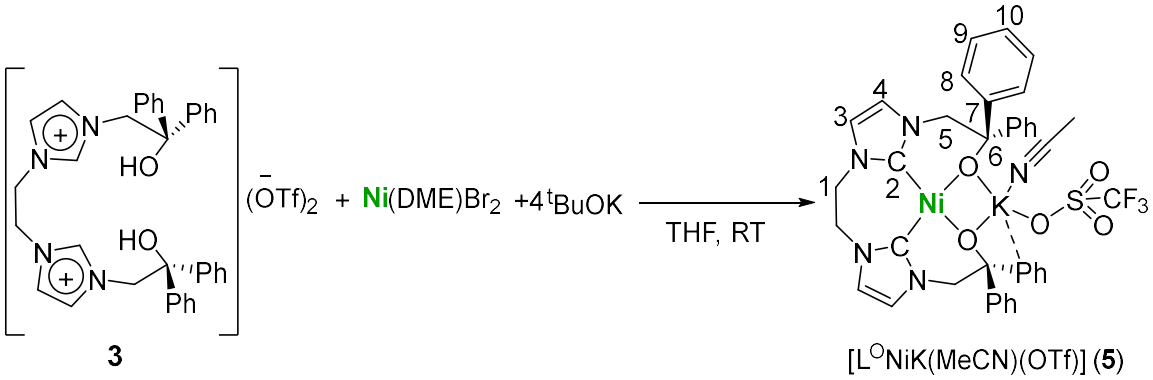

3 [L^{O}NiK(MeCN)(OTf)] (**5**)

[L^{O}H$_4$] proligand (0.5 g, 0.6 mmol, 1 eq) was dissolved in in 20 mL of THF, then Ni(DME)Br$_2$ (0.12 g, 0.6 mmol, 1 eq) was introduced into the reaction mixture. Separately, ^{t}BuOK (0.3 g, 2.3 mmol, 4 eq) was dissolved in 10 mL of THF, then the solution of the base was added dropwise to the solution of ligand and metal. The reaction was stirred at room temperature overnight, then the solvent was removed via rotary evaporator. DCM was used to wash the crude, and the solution was filtered. After removal of the solvent, the solid was dissolved in the minimum quantity of MeCN and put in diffusion of Et$_2$O in the fridge. After 48h the product was obtained as yellow-green crystals (0.200 g, 0.238 mmol, Yield = 40%).

^{1}H NMR (300 MHz, CD$_3$CN): δ[ppm] = 4.33 (s, 4 H, 1-H), 4.78 (s, 4 H, 5-H), 6.66 (s, 2 H, 4-H), 6.78 (s, 2 H, 3-C), 7.10-7.55 (m, 20 H, 8-9-10-H, aromatic).

^{13}C NMR (75 MHz, CD$_3$CN): δ[ppm] = 48.75 (1-C), 62.98 (5-C), 76.78 (6-C), 121.91 (3-C), 123.24 (4-C), 126.81 (10-C), 127.86 (8-C), 128.51 (9-C), 149.93 (7-C), 162.24 (2-C).

ESI-MS(+): m/z = 611.2 [L^{O}Ni]$^{+}$.

Elemental Analysis (C, H, N): Calculated % = 55.7, 4.2, 8.3

Measured % = 55.3, 4.2, 8.3

UV/Vis (MeCN): λ [nm] (ε [M^{-1} cm^{-1}]) = 320 (6.3 x 10^3).

7.4.2. Synthesis of $[L^{O}NiFe](OTf)_2(Acetone)_2$

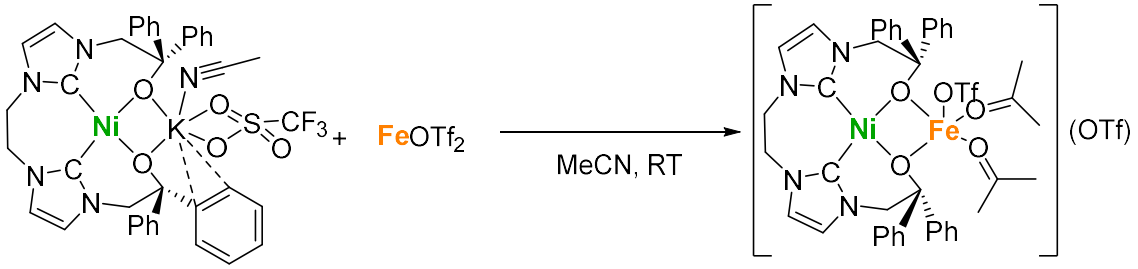

$[L^{O}NiK(MeCN)(OTf)]$ (**5**) $[L^{O}NiFe](OTf)_2(Acetone)_2$ (**8**)

$Fe(OTf)_2$ (40 mg, 0.12 mmol 1 eq) was dissolved in 8 mL of MeCN, then solid **5** (100 mg, 0.12 mmol, 1 eq) was added. The reaction mixture was stirred for 2 hours at room temperature, then the solvent was removed via rotary evaporator. The crude was treated with acetone and then the solution was filtered, allowing the removal of the triflate salts. Single crystals were obtained via diffusion of Et_2O overnight (66 mg, 0.07 mmol, Yield = 60%).

Elemental Analysis (C, H, N): Calculated % = 48.1, 3.7, 5.7

Measured % = 47.9, 3.9, 5.5

ESI-MS(+): m/z = 815.1 $[L^{O}NiFe(OTf)]^{-}$, 473.7 $[L^{O}NiFe]^{2+}$.

MB: *IS* = 1.31 mms^{-1}; *QS* = 2.36 mms^{-1}.

UV/Vis (MeCN): λ [nm] (ε [M^{-1} cm^{-1}]) = 291 (1.6 x 10^4); 392 (1.4 x 10^3).

7.4.3. Synthesis of $[L^{O}NiCo](MeCN)(I)_2$

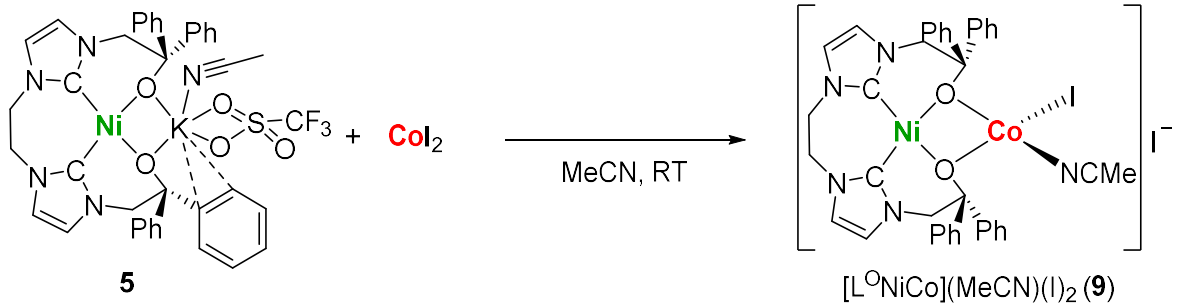

5 $[L^{O}NiCo](MeCN)(I)_2$ (**9**)

CoI_2 (37 mg, 0.12 mmol, 1 eq) was dissolved in ca. 10 mL of MeCN, then solid **5** (100 mg, 0.12 mmol, 1 eq) was added and the solution was stirred overnight. The mixture was filtered and the solvent was removed in vacuo. The crude was treated with acetone and the solution was filtered. Single crystals grew from the diffusion of Et_2O in a solution of the crude product in MeCN, at -27°C (80 mg, 0.09 mmol, Yield = 69%).

UV/Vis (MeCN): λ [nm] (ε [M^{-1} cm^{-1}]) = 295 (2.8 x 10^4); 390 (9.9 x 10^2); 577 (6.5 x 10^2).

7.4.4. Synthesis of $[L^O(L^OH)Fe_2](OTf)$

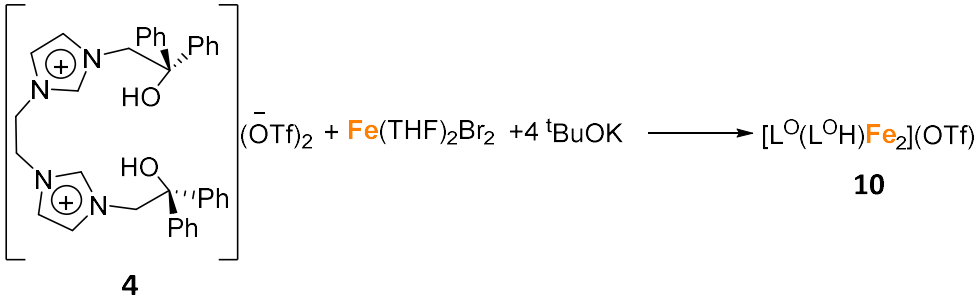

4 **10**

In the glovebox, proligand **4** (100 mg, 0.12 mmol, 1 eq) was dissolved in THF, then $FeBr_2(THF)_2$ (42 mg, 0.12 mmol, 1 eq) was added. In a separate flask, ^{t}BuOK (53 mg, 0.47 mmol, 4 eq) was dissolved in THF and this solution was added dropwise to the solution of **4** and $Fe(THF)_2Br_2$. The reaction mixture was stirred overnight, filtrated and the solvent was removed in vacuo. The solid was dissolved in MeCN and Et_2O was allowed to diffuse slowly, to produce single crystals suitable for XRD measurement.

7.4.5. Synthesis of $[L^{O}NiFeNiL^{O}](OTf)_2$

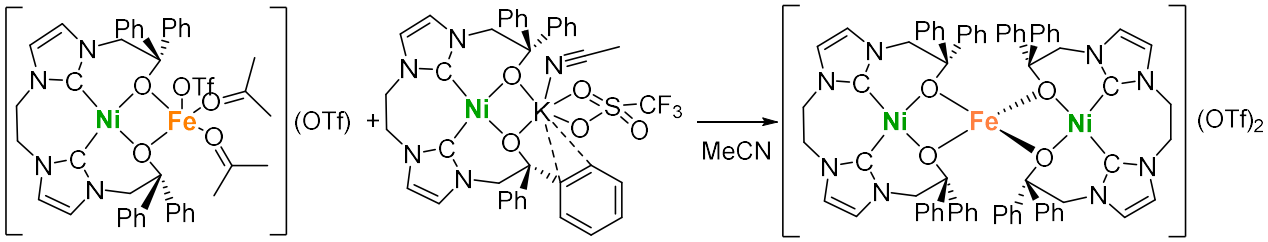

8 **5** **11**

8 (12 mg, 0.01 mmol, 1 eq) was dissolved in MeCN. Solid **5** (10 mg, 0.01 mmol, 1 eq) was added and the reaction was stirred for 48 hours. The solvent was removed in vacuo and single crystals were obtained by diffusion of Et_2O into a MeCN solution of the crude product (12 mg, 0.01 mmol, Yield = 73%).

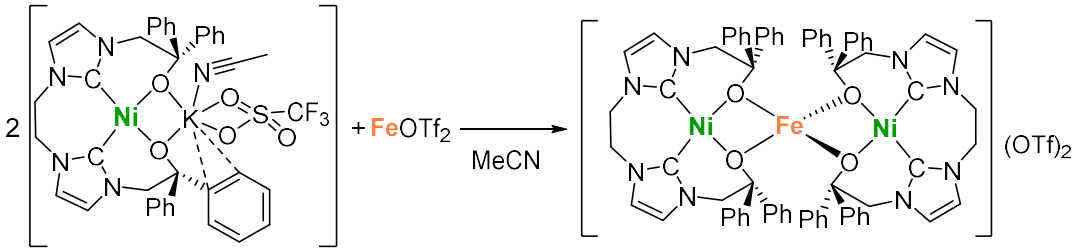

5 $[L^{O}NiFeNiL^{O}](OTf)_2$ **11**

$Fe(OTf)_2$ (6.0 mg, 0.02 mmol, 0.5 eq) was dissolved in 6.0 mL of MeCN, then solid **5** (30 mg, 0.046 mmol, 1 eq) was added and the solution was stirred for 48 hours. The solvent was then removed in vacuo and the crude was dissolved in the minimum quantity of acetone. The resulting solution was filtered. Crystallization by slow diffusion of Et_2O at -27°C allows single crystals to grow (41 mg, 0.03 mmol, Yield = 71%).

ESI-MS(+): m/z = 639.1 $[L^{O}NiFeNiL^{O}]^{2+}$.

MB: *IS* = 1.14 mms^{-1}; *QS* = 1.95 mms^{-1}.

UV/Vis (MeCN): λ [nm] (ε [M^{-1} cm^{-1}]) = 301 (2.2 x 10^4); 414 (1.2 x 10^3).

Elemental Analysis (C, H, N): Calculated % = 50.53, 3.73, 6.29

Measured % = 49.75, 3.72, 6.16

7.4.6. Synthesis of $[L^{O}NiCoNiL^{O}](OTf)_2$

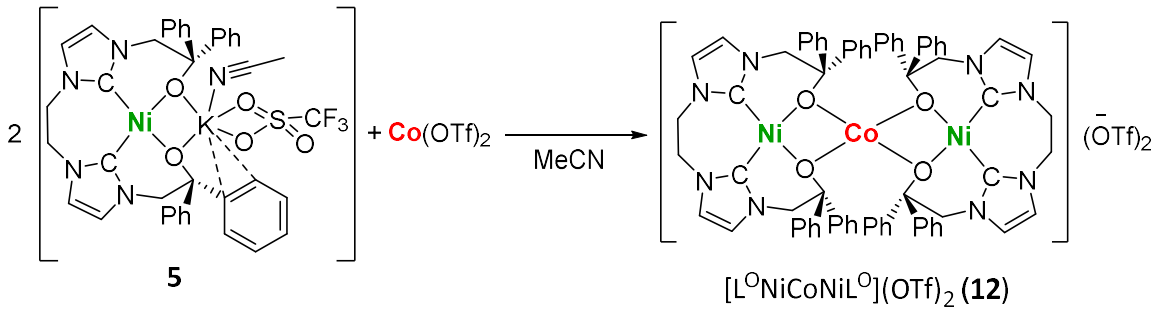

5 $[L^{O}NiCoNiL^{O}](OTf)_2$ (**12**)

$Co(OTf)_2$ (6.4 mg, 0.02 mmol, 0.5 eq) was dissolved in 6.0 mL of MeCN, then solid $C2O2^{Ph}$ NiK (30 mg, 0.04 mmol, 1 eq) was added and the solution was stirred for 48 hours. The solvent was then removed in vacuo and the crude was dissolved in the minimum quantity of acetone. The resulting solution was filtered. Crystallization by slow diffusion of Et_2O at -27°C allows single crystals to grow (40 mg, 0.03 mmol, Yield = 70%).

ESI-MS(+): m/z = 639.6 $[L^{O}NiCoNiL^{O}]^{2+}$.

Elemental analysis (C, H, N): Calculated % = 56.26, 4.08, 7.09

Measured % = 56.18, 4.06, 7.09

UV/Vis (MeCN): λ [nm] (ε [M^{-1} cm^{-1}]) = 300 (1,9 x 10^4); 409 (7,4 x 10^2); 567 (3,3 x 10^2).

8. Appendix

8.1. Further Analytical Data

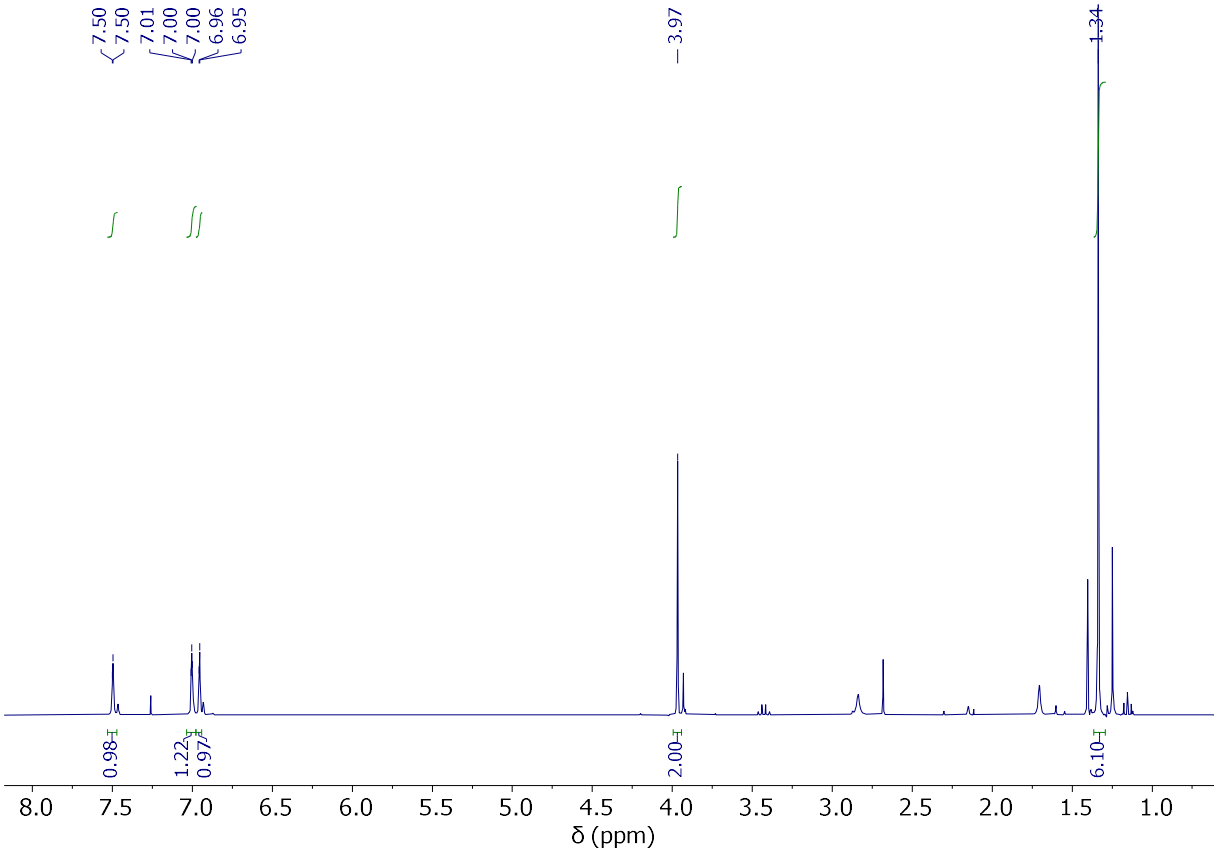

Appendix Figure 1 ^{1}H NMR spectrum of **1** in DMSO-d_6.

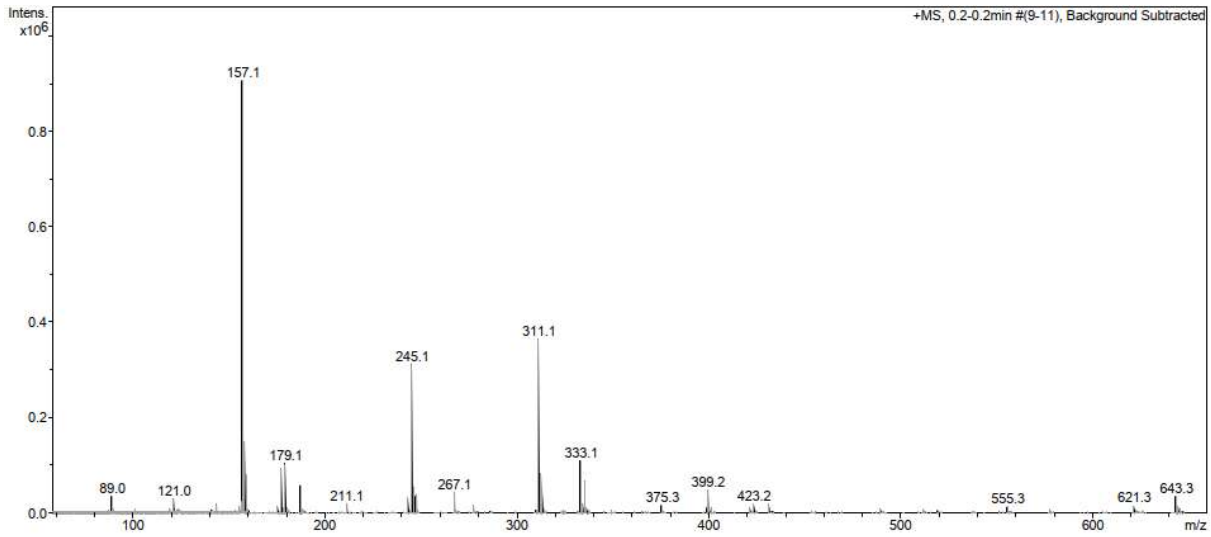

Appendix Figure 2 ESI(+) mass spectrum of **1**.

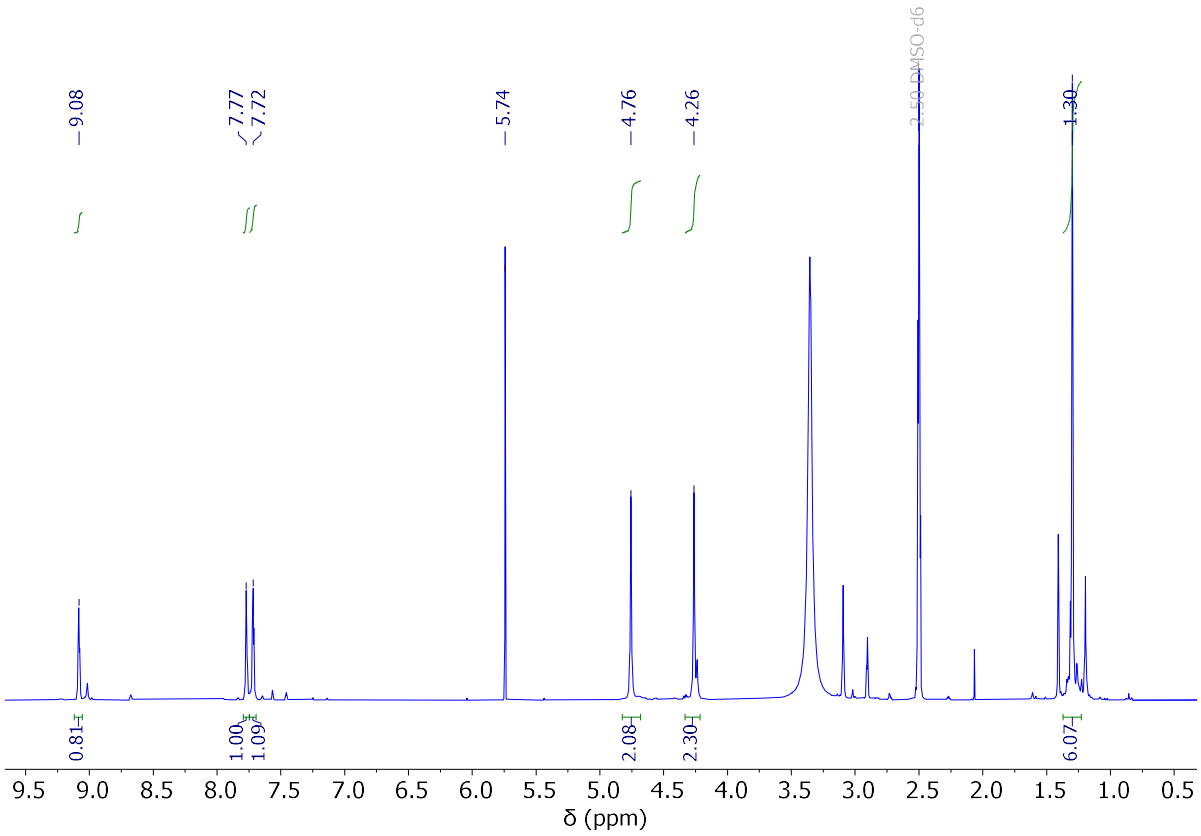

Appendix Figure 3. ^{1}H NMR spectrum of **2** in DMSO-d_6.

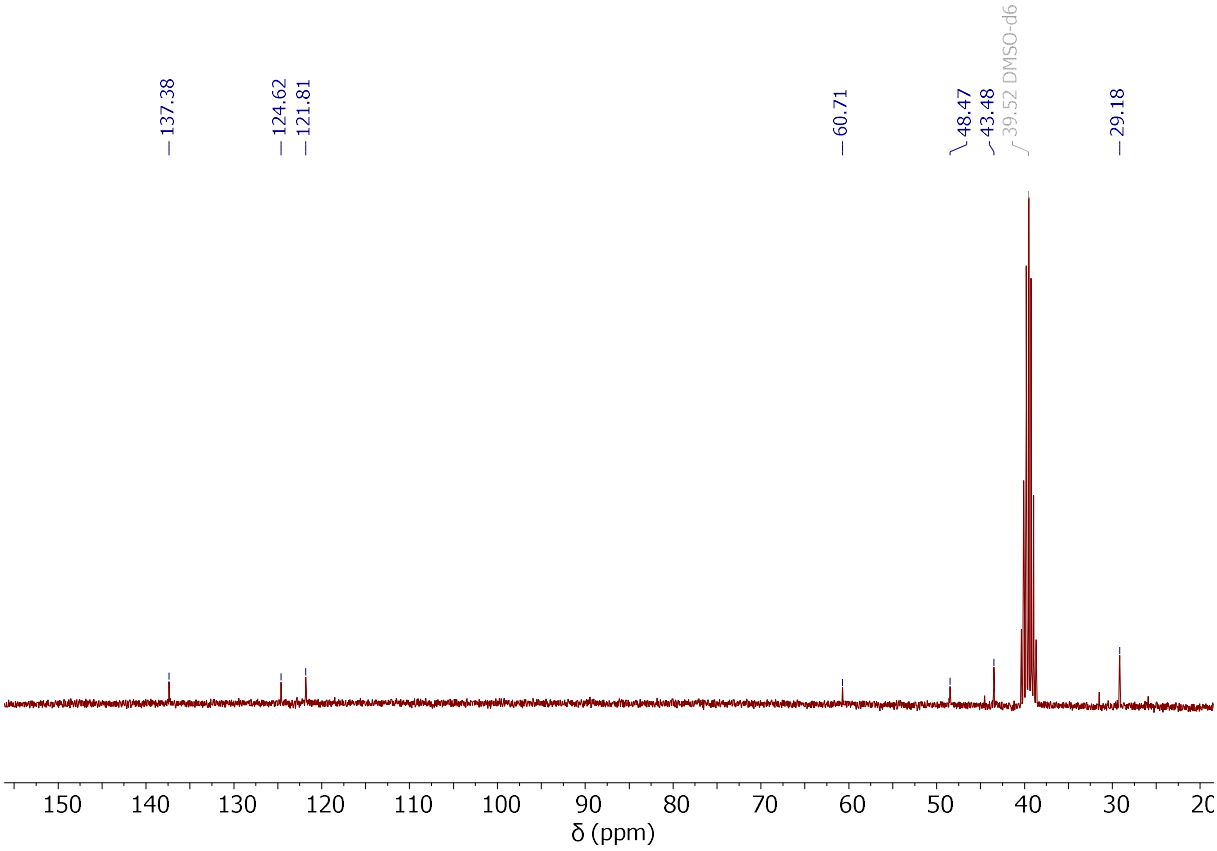

Appendix Figure 4. ^{13}C NMR spectrum of **2** in DMSO-d_6.

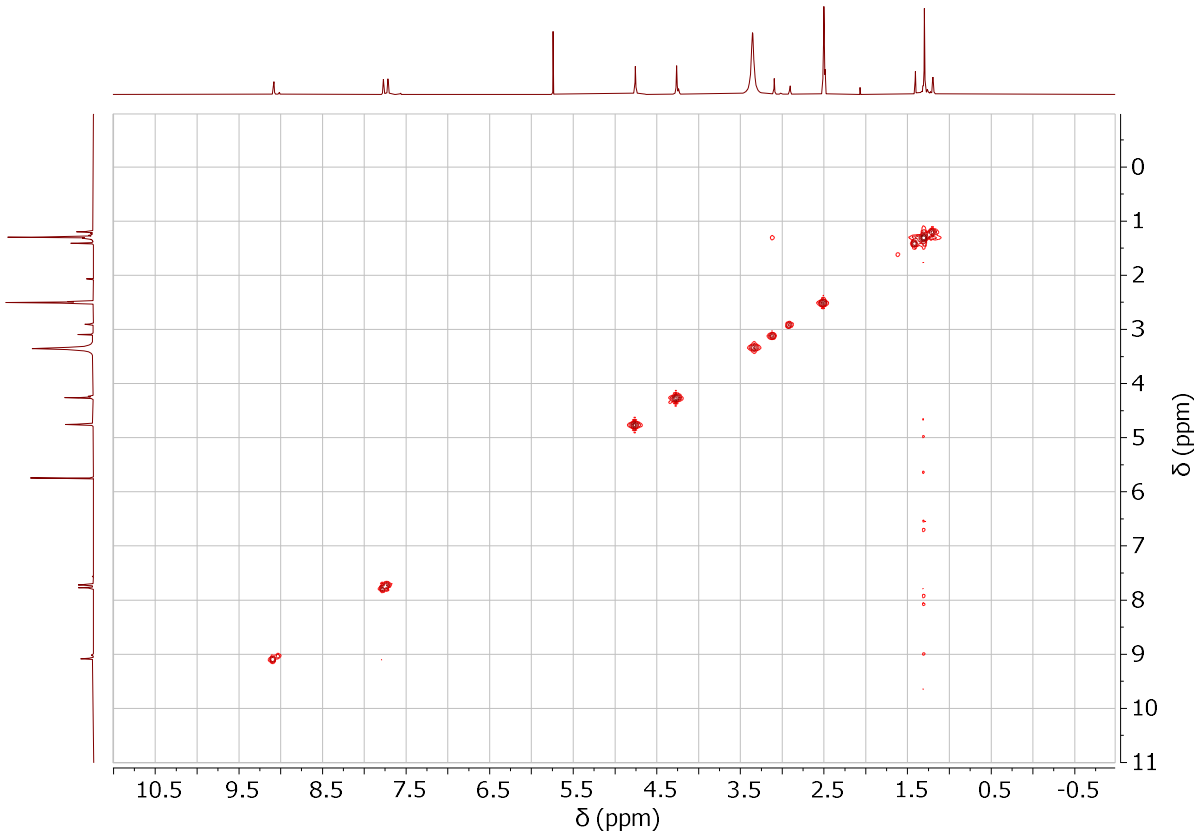

Appendix Figure 5. COSY spectrum of **2** in DMSO-d_6.

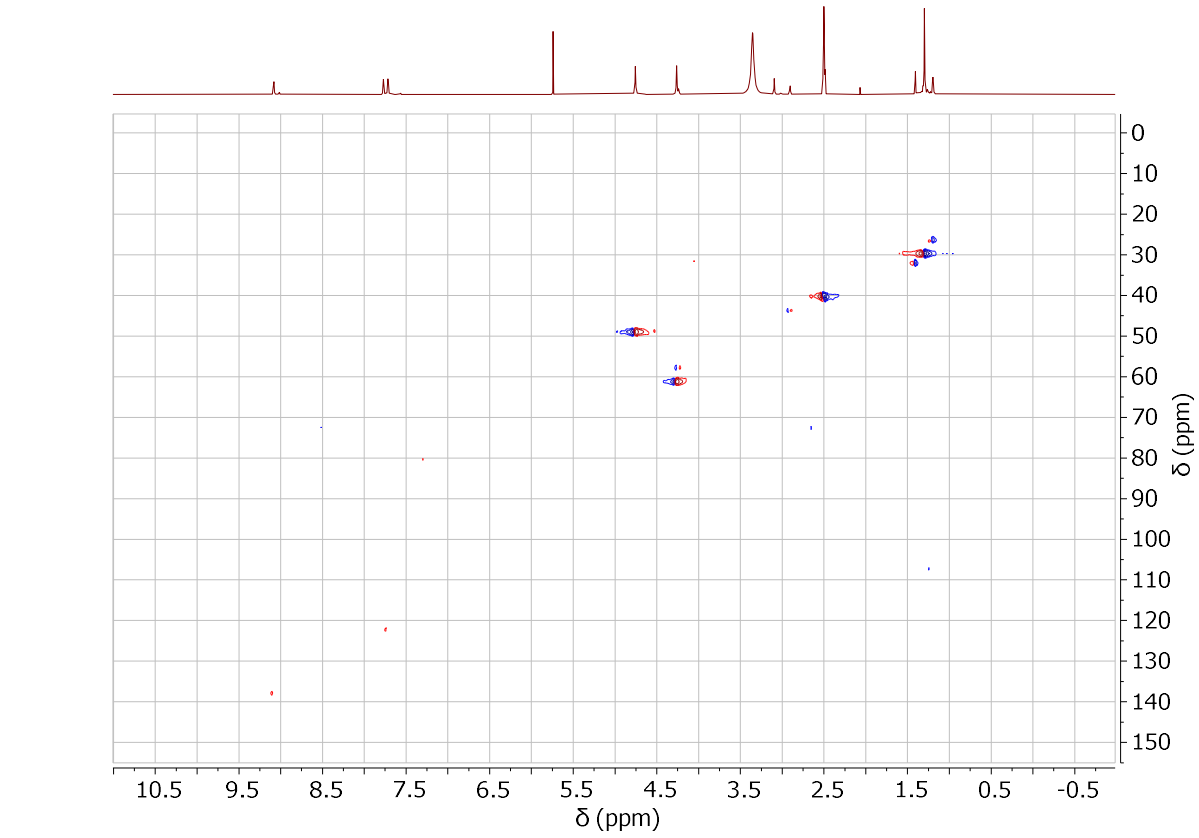

Appendix Figure 6. HSQC spectrum of **2** in DMSO-d_6.

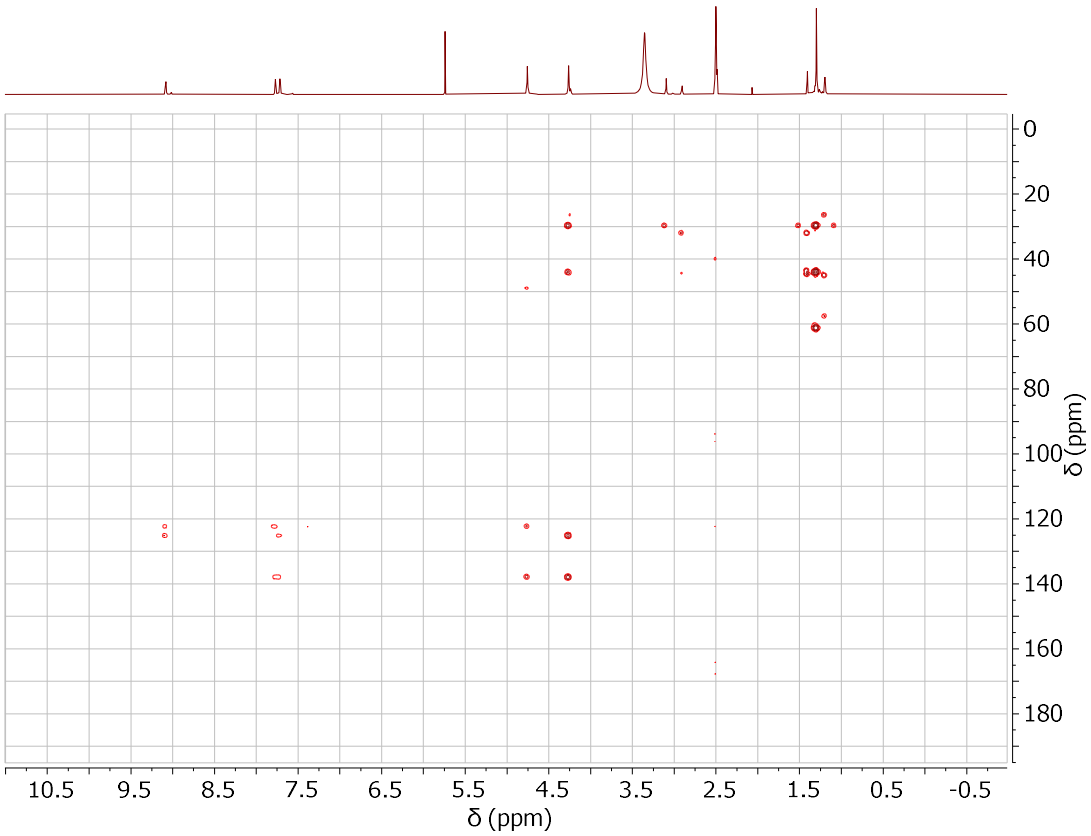

Appendix Figure 7 HMBC spectrum of **2** in DMSO-d_6.

Appendix Table 1. Selected bond lengths [Å] for **3**.

Atoms	Bond lengths
S1-C10	1.813(12)
S2-C14	1.810(12)
N1-C1	1.327(13)
N1-C2	1.422(13)
N1-C9	1.448(13)
N2-C1	1.327(12)
N2-C3	1.391(13)
N2-C4	1.459(13)
N3-C6	1.336(12)
N3-C7	1.360(13)
N3-C5	1.492(13)
N4-C6	1.315(13)
N4-C8	1.366(13)
N4-C13	1.488(12)
C2-C3	1.340(16)
C4-C5	1.510(15)
C7-C8	1.381(15)
C9-C10	1.535(15)
C10-C11	1.527(16)
C10-C12	1.629(14)
C13-C14	1.515(14)

C14-C15	1.530(15)
C14-C16	1.664(13)
B1-C21	1.629(16)
B1-C27	1.638(14)
B1-C39	1.645(13)
B1-C33	1.662(14)
C21-C22	1.396(14)
C21-C26	1.402(14)
C22-C23	1.384(16)
C23-C24	1.341(16)
C24-C25	1.402(17)
C25-C26	1.363(16)
C27-C28	1.404(13)
C27-C32	1.426(13)
C28-C29	1.361(13)
C29-C30	1.388(15)
C30-C31	1.390(15)
C31-C32	1.374(14)
C33-C38	1.388(14)
C33-C34	1.397(14)
C34-C35	1.388(15)
C35-C36	1.387(16)
C36-C37	1.344(15)
C37-C38	1.408(14)
C39-C44	1.396(14)
C39-C40	1.425(14)
C40-C41	1.375(15)
C41-C42	1.383(17)
C42-C43	1.389(16)
C43-C44	1.380(14)
B2-C69	1.621(14)
B2-C57	1.650(13)
B2-C51	1.653(14)
B2-C63	1.658(14)
C51-C52	1.400(13)
C51-C56	1.408(13)
C53-C54	1.431(15)
C54-C55	1.380(15)
C55-C56	1.428(14)
C57-C62	1.401(13)
C57-C58	1.408(14)
C58-C59	1.400(15)
C59-C60	1.366(17)
C61-C62	1.386(14)
C63-C64	1.392(13)
C63-C68	1.401(14)
C64-C65	1.413(14)
C65-C66	1.368(15)

C66-C67	1.377(15)
C67-C68	1.405(14)
C69-C70	1.400(14)
C69-C74	1.414(14)
C70-C71	1.396(14)
C71-C72	1.362(16)
C72-C73	1.375(16)
C73-C74	1.393(14)

Appendix Table 2. Selected bond angles [°] for **3.**

Atoms	**Bond angles**
C1-N1-C2	108.5(8)
C1-N1-C9	126.0(8)
C2-N1-C9	125.5(8)
C1-N2-C3	108.1(8)
C1-N2-C4	126.4(9)
C3-N2-C4	125.5(8)
C6-N3-C7	109.9(8)
C6-N3-C5	125.7(8)
C7-N3-C5	124.4(8)
C6-N4-C8	109.5(8)
C6-N4-C13	125.1(8)
C8-N4-C13	125.2(9)
N2-C1-N1	109.3(9)
C3-C2-N1	105.4(9)
C2-C3-N2	108.7(9)
N2-C4-C5	113.2(8)
N3-C5-C4	112.9(8)
N4-C6-N3	108.0(9)
N3-C7-C8	105.7(9)
N4-C8-C7	106.9(9)
N1-C9-C10	113.1(9)
C11-C10-C9	107.2(10)
C11-C10-C12	107.8(9)
C9-C10-C12	113.3(8)
C11-C10-S1	111.9(8)
C9-C10-S1	111.5(8)
C12-C10-S1	105.1(8)
N4-C13-C14	113.9(8)
C13-C14-C15	107.6(9)
C13-C14-C16	113.3(8)
C15-C14-C16	109.0(8)
C13-C14-S2	111.6(7)
C15-C14-S2	109.8(8)
C16-C14-S2	105.4(6)
C21-B1-C27	108.9(8)

C21-B1-C39	111.6(8)
C27-B1-C39	109.5(8)
C21-B1-C33	109.7(8)
C27-B1-C33	106.2(8)
C39-B1-C33	110.8(8)
C22-C21-C26	113.1(9)
C22-C21-B1	124.2(9)
C26-C21-B1	122.7(9)
C23-C22-C21	122.9(10)
C24-C23-C22	121.9(11)
C23-C24-C25	118.0(10)
C26-C25-C24	119.4(10)
C25-C26-C21	124.7(10)
C28-C27-C32	114.1(8)
C28-C27-B1	123.9(8)
C32-C27-B1	121.9(8)
C29-C28-C27	123.7(9)
C28-C29-C30	121.0(10)
C29-C30-C31	117.7(9)
C32-C31-C30	121.2(9)
C31-C32-C27	122.3(10)
C38-C33-C34	114.3(9)
C38-C33-B1	122.4(9)
C34-C33-B1	122.7(9)
C35-C34-C33	123.4(10)
C36-C35-C34	119.8(10)
C37-C36-C35	119.0(10)
C36-C37-C38	120.5(10)
C33-C38-C37	122.9(10)
C44-C39-C40	113.8(9)
C44-C39-B1	122.1(9)
C40-C39-B1	124.0(9)
C41-C40-C39	122.4(10)
C40-C41-C42	121.7(11)
C41-C42-C43	117.7(10)
C44-C43-C42	120.3(10)
C43-C44-C39	124.1(10)
C69-B2-C57	111.1(8)
C69-B2-C51	109.0(8)
C57-B2-C51	112.9(8)
C69-B2-C63	107.6(8)
C57-B2-C63	108.1(8)
C51-B2-C63	108.0(7)
C52-C51-C56	114.9(9)
C52-C51-B2	122.2(8)
C56-C51-B2	122.8(8)
C53-C52-C51	124.7(9)
C52-C53-C54	119.1(9)

C55-C54-C53	118.9(10)
C54-C55-C56	119.8(9)
C51-C56-C55	122.7(9)
C62-C57-C58	115.1(9)
C62-C57-B2	124.2(8)
C58-C57-B2	120.7(8)
C59-C58-C57	121.6(10)
C60-C59-C58	121.5(11)
C59-C60-C61	118.4(9)
C62-C61-C60	120.3(10)
C61-C62-C57	123.1(10)
C64-C63-C68	116.6(9)
C64-C63-B2	122.3(8)
C68-C63-B2	120.9(8)
C63-C64-C65	121.9(9)
C66-C65-C64	119.6(9)
C65-C66-C67	120.5(9)
C66-C67-C68	119.6(10)
C63-C68-C67	121.8(9)
C70-C69-C74	113.8(9)
C70-C69-B2	125.7(9)
C74-C69-B2	120.5(9)
C71-C70-C69	123.7(10)
C72-C71-C70	119.9(10)
C71-C72-C73	119.4(9)
C72-C73-C74	120.4(10)
C73-C74-C69	122.7(10)

Appendix Table 3. Crystal data and refinement details for **3**.

empirical formula	$C_{64}H_{68}B_2N_4S_2$
formula weight	978.96
T [K]	133(2)
crystal size [mm³]	0.460×0.220×0.160
crystal system	monoclinic
space group	*Cc*
a [Å]	18.8311(18)
b [Å]	10.8093(13)
c [Å]	27.071(3)
a [°]	90
b [°]	104.048(9)
g [°]	90
V [Å³]	5345.6(11)
Z	4
r [g/cm³]	1.216
F(000)	2088
μ [mm^{-1}]	0.145
T_{min} / T_{max}	0.6730 / 0.9319
q-range [°]	1.551 - 26.306
hkl-range	±23, ±13, ±33
measured refl.	30732
unique refl. [R_{int}]	30732
observed refl. ($I > 2s(I)$)	19337
data / restraints / param.	30732 / 2 / 655
goodness-of-fit (F^2)	1.086
*R*1, *wR*2 ($I > 2s(I)$)	0.0776, 0.2290
*R*1, *wR*2 (all data)	0.1185, 0.2655
resid. el. dens. [e/Å³]	-0.507 / 0.503

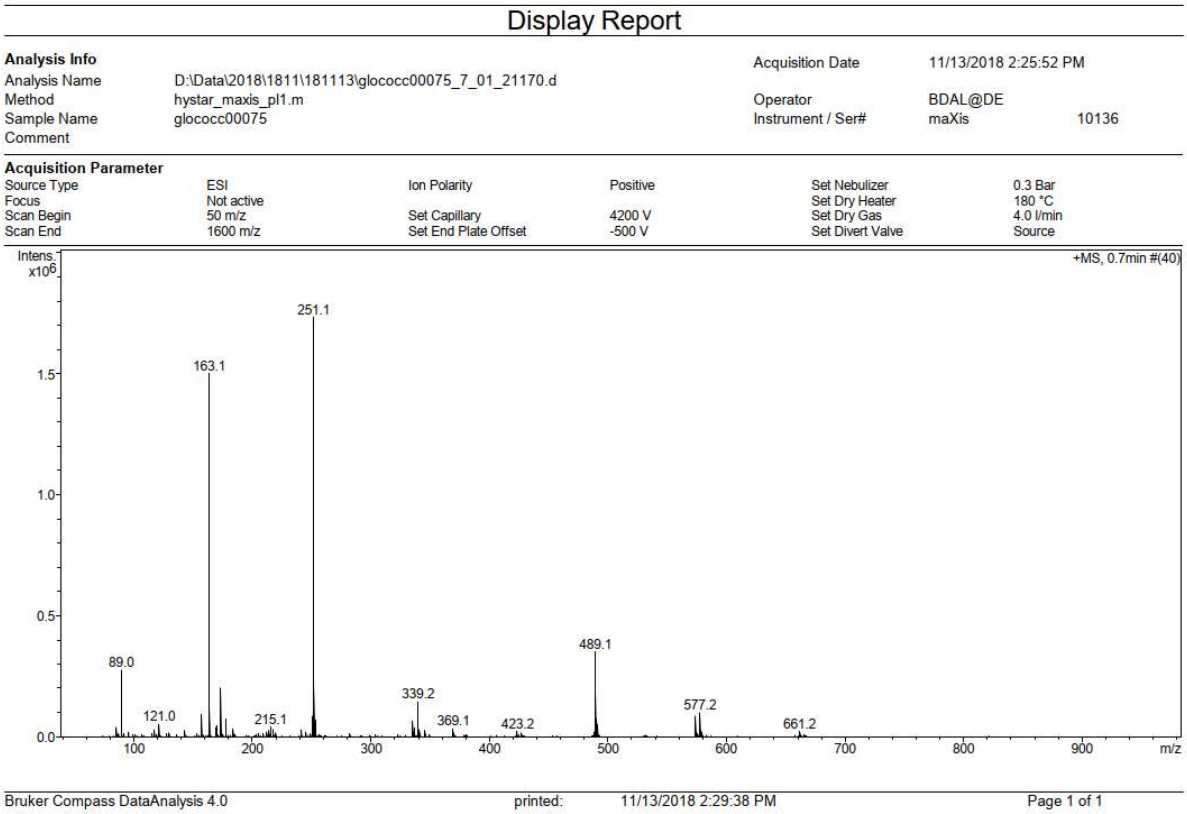

Appendix Figure 8. ESI-MS data of **3** in THF.

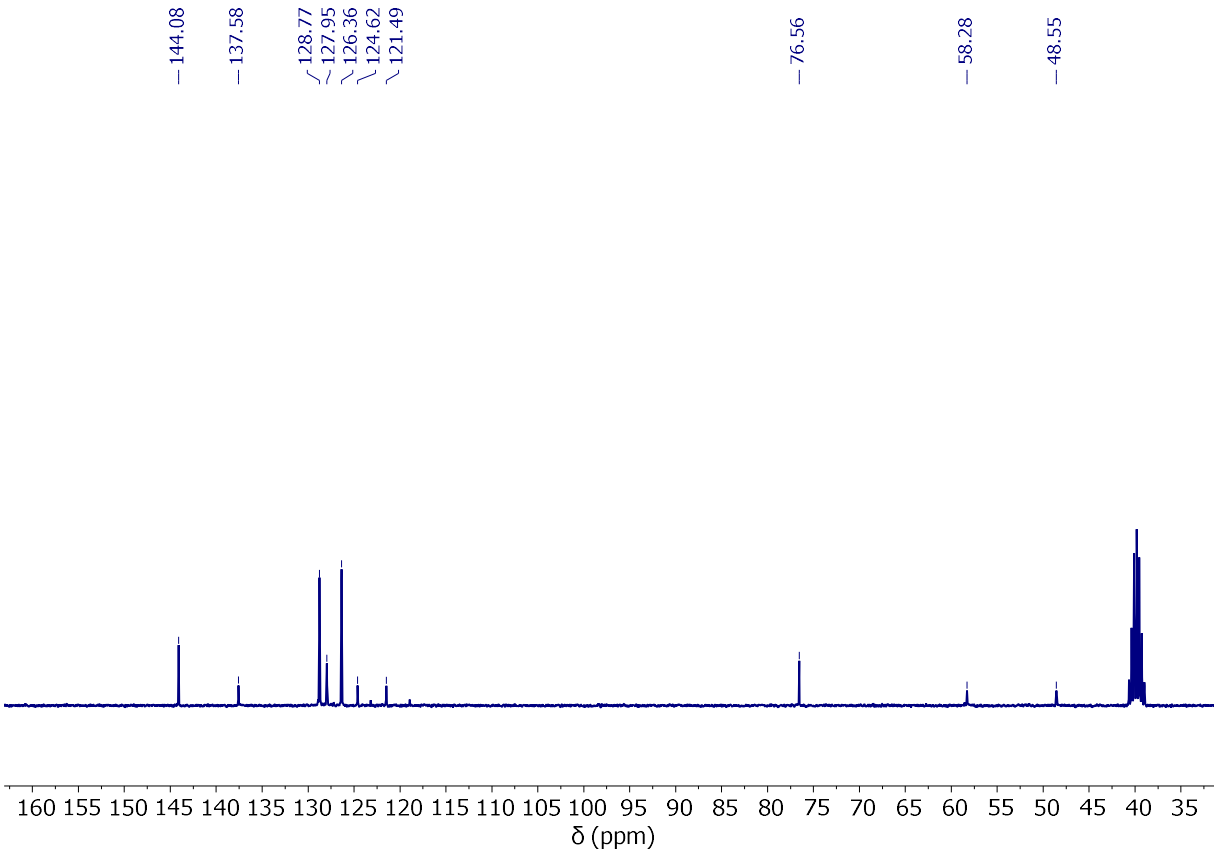

Appendix Figure 9. ^{1}H NMR spectrum of **4** in DMSO-d_6.

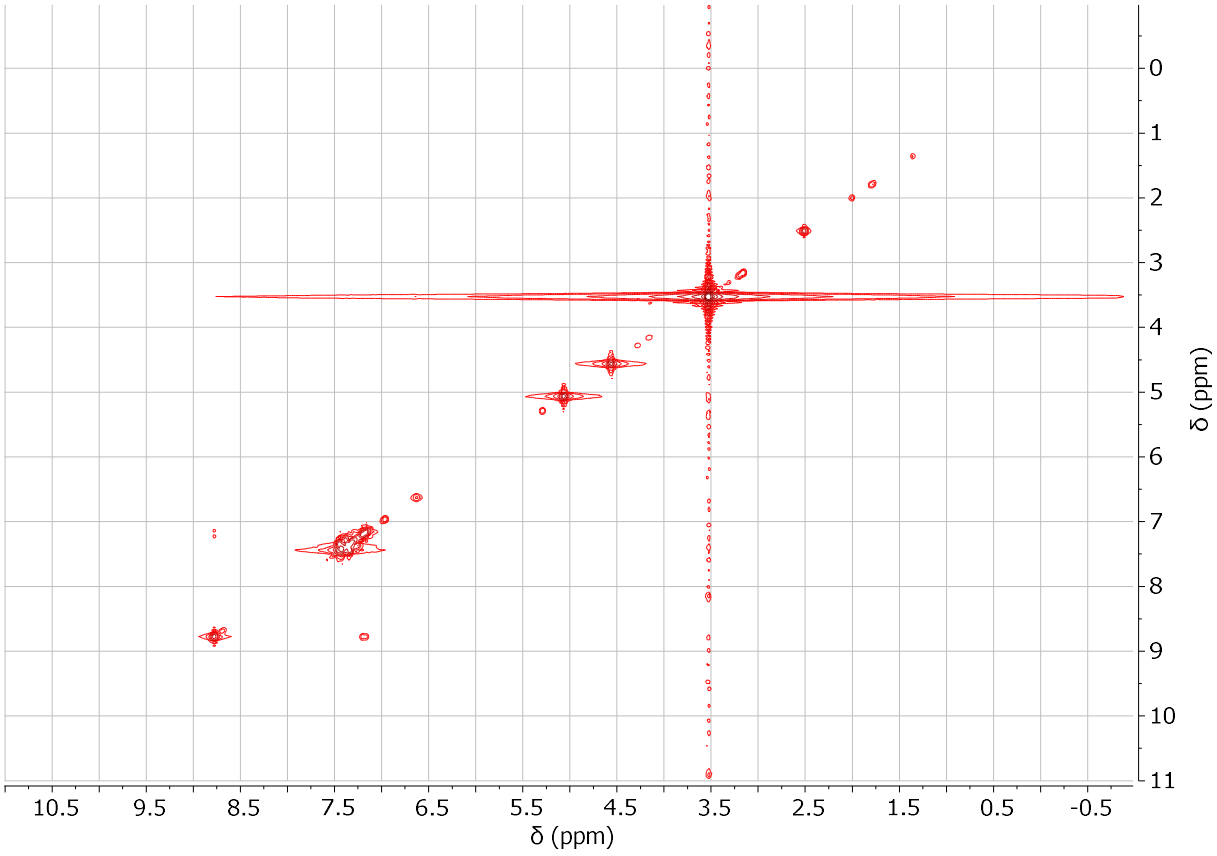

Appendix Figure 10. COSY spectrum of **4**.

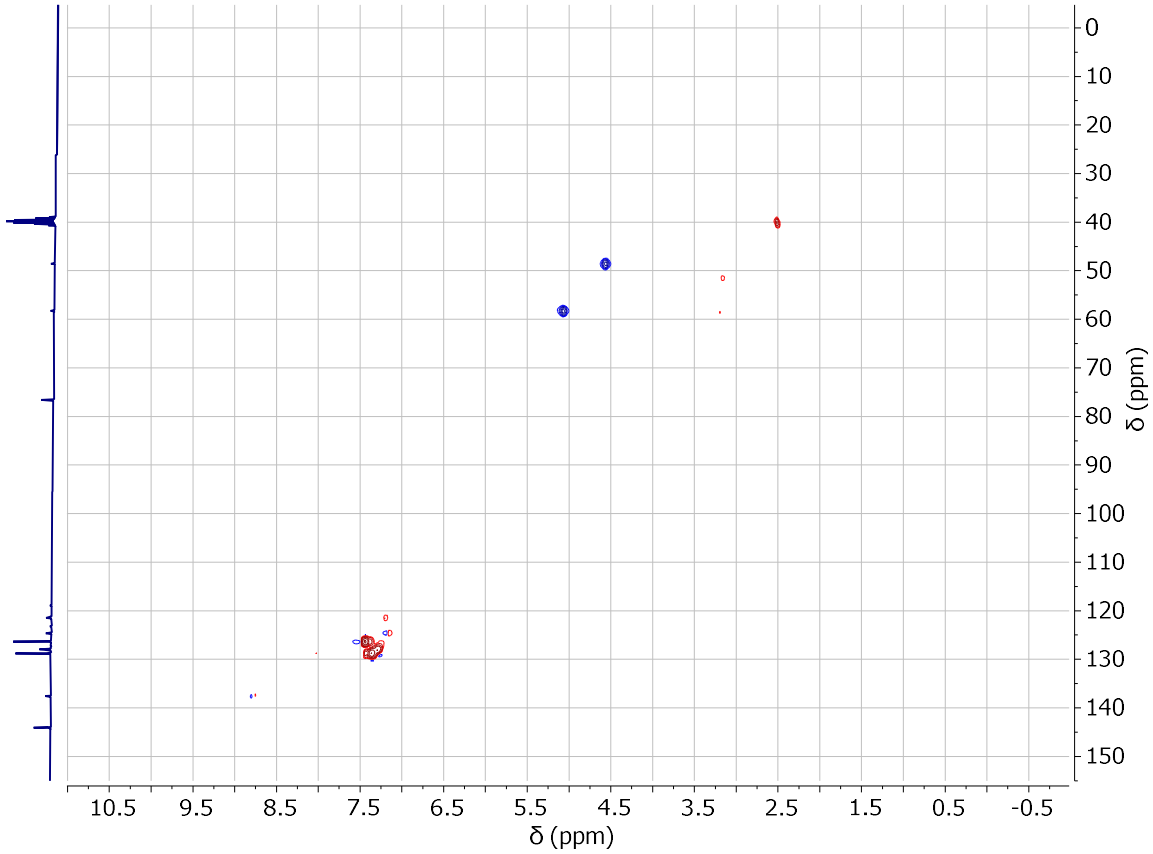

Appendix Figure 11 HSQC spectrum of **4**.

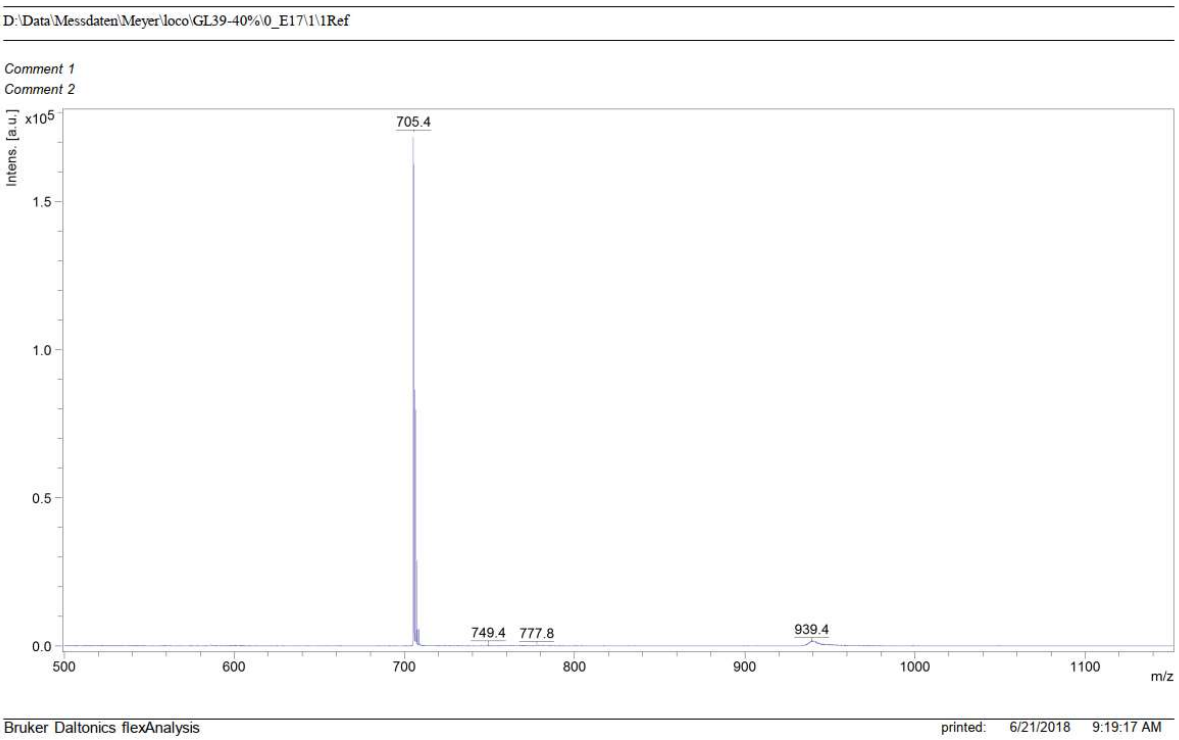

Appendix Figure **12**. MALDI-MS data of **4**.

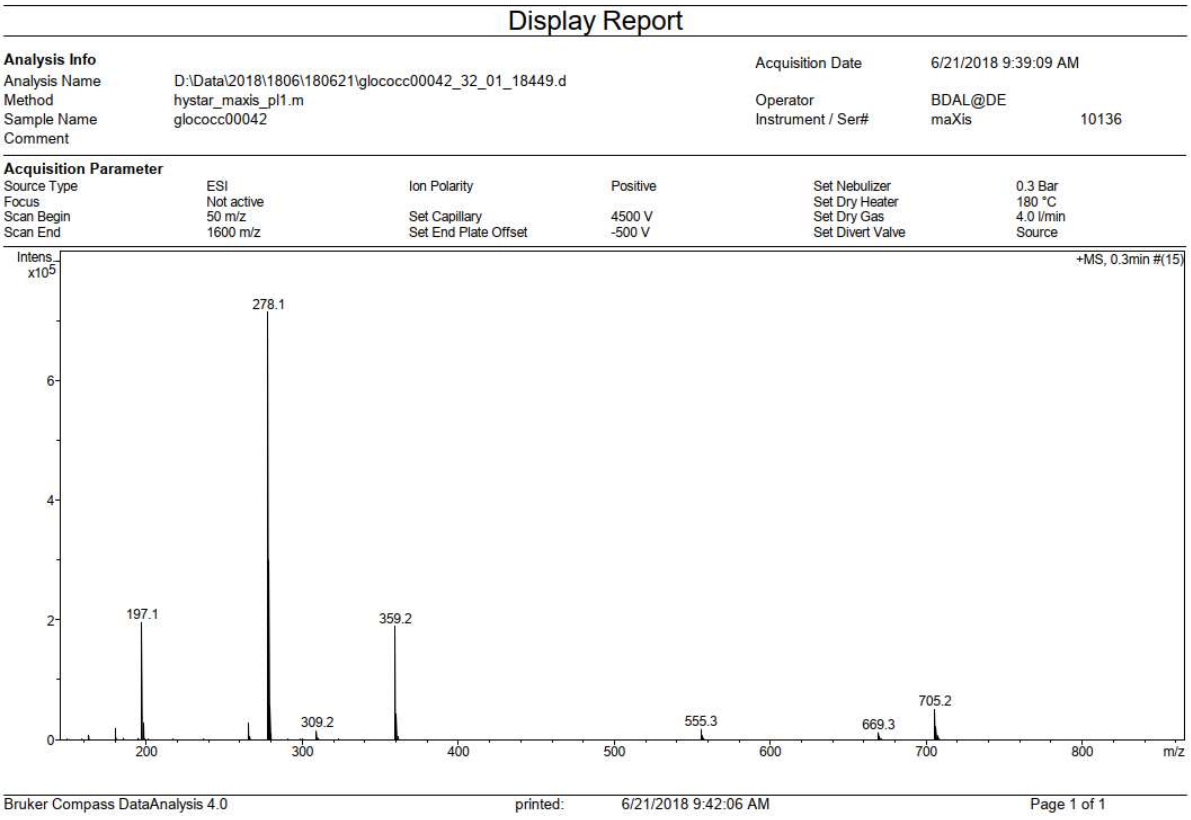

Appendix Figure **13**. ESI-MS data for **4**.

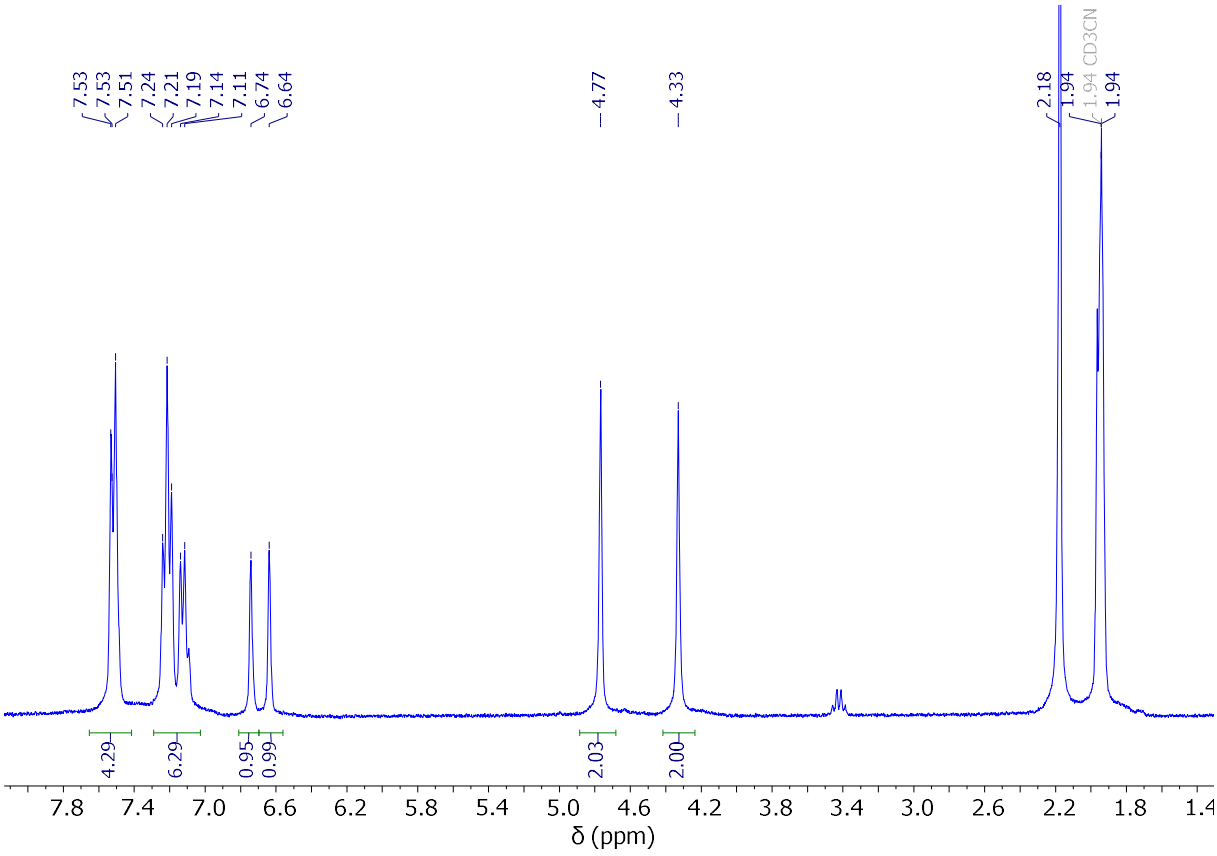

Appendix Figure 14. ^{1}H NMR spectrum of **5** in MeCN-d_3.

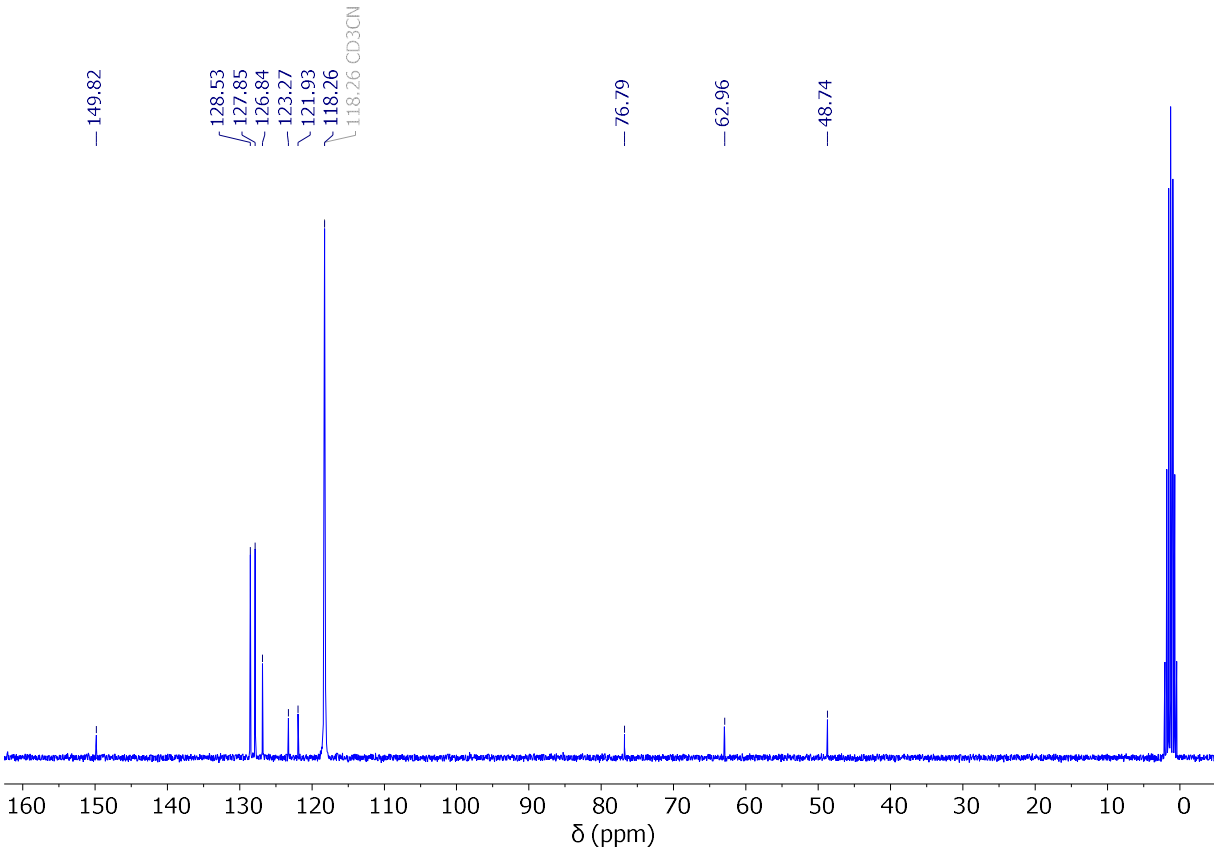

Appendix Figure 15. ^{13}C NMR spectrum of **5** in MeCN-d_3.

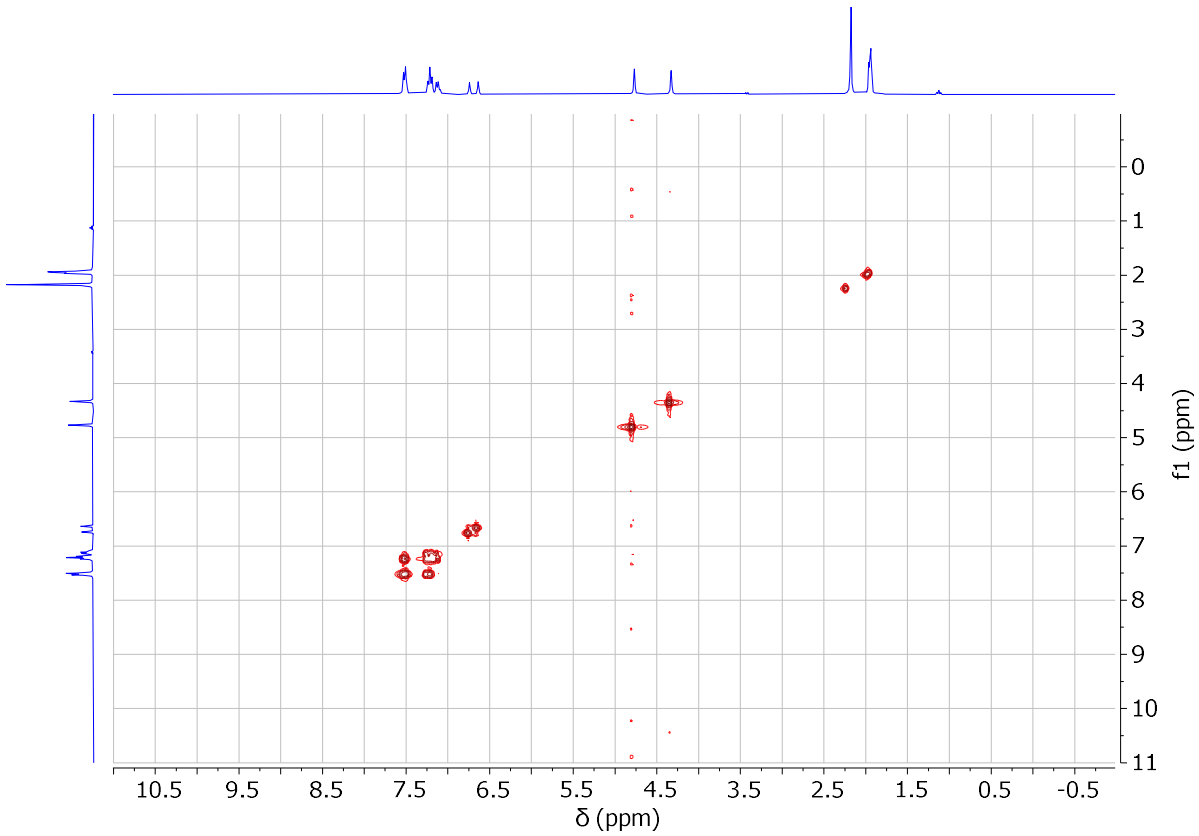

Appendix Figure 16. COSY spectrum of **5** .

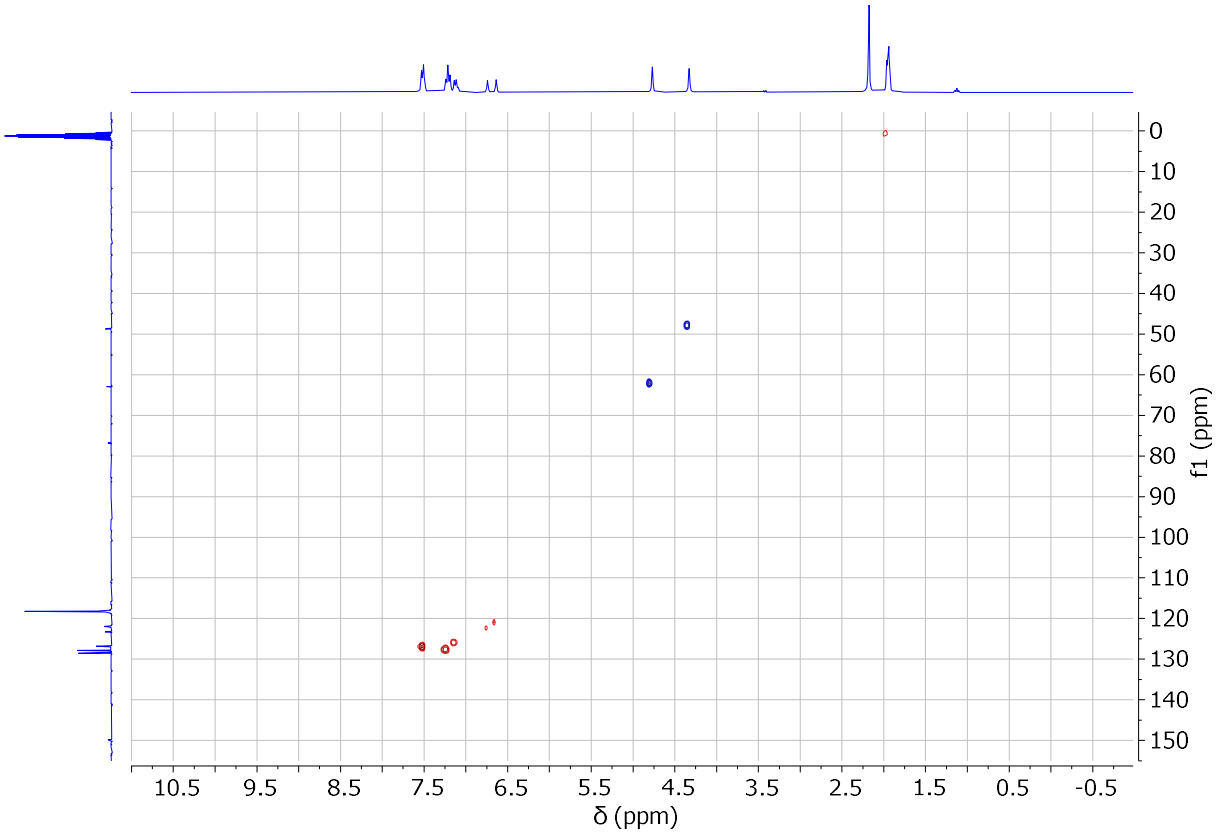

Appendix Figure 17. HSQC spectrum of **5**.

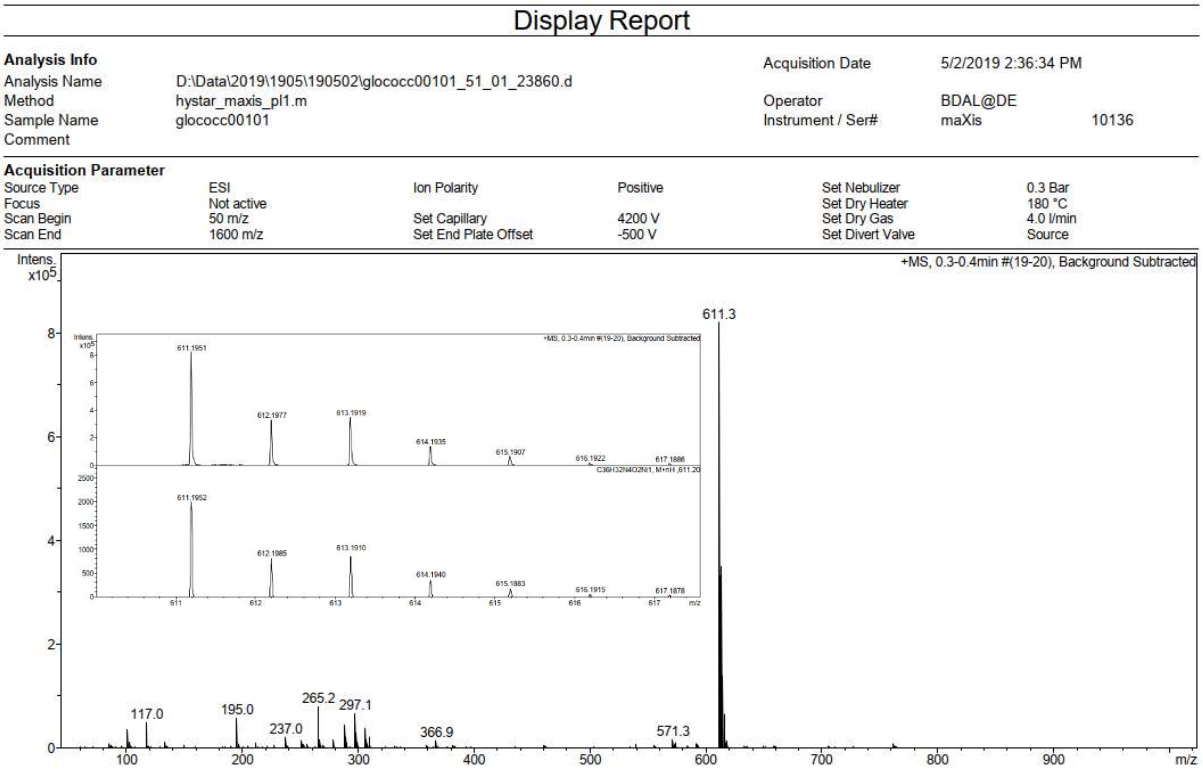

Appendix Figure 18. ESI-MS data of **5** with simulated data.

Atoms	Bond lengths [Å]	Atoms	Bond angles [°]
Ni1-C1	1.8462(15)	C1-Ni1-O1	90.85
Ni1-O1	1.8733(11)	C1-Ni1-O2	170.56
Ni1-O2	1.8843(11)	O1-Ni1-O2	82.92
Ni1-C6	1.8862(16)	C1-Ni1-C6	95.38
Ni1-K1	3.6852(4)	O1-Ni1-C6	169.03
K1-O1	2.5967(11)	O2-Ni1-C6	91.93
K1-O2	2.6373(11)	C1-Ni1-K1	129.27
K1-N11	2.812(2)	O1-Ni1-K1	41.46
K1-O12	2.8306(14)	O2-Ni1-K1	42.89
K1-O11	2.9083(15)	C6-Ni1-K1	134.74
K1-C26	3.0891(18)	C10-O1-Ni1	128.96
K1-C25	3.3078(16)	Ni1-O1-K1	110.01
K1-S1	3.3683(6)	C12-O2-Ni1	128.78
K1-C13	3.4490(16)	Ni1-O2-K1	108.02

Appendix Table 4. Crystal data and refinement details for **5**.

empirical formula	$C_{39}H_{35}F_3KN_5NiO_5S$
formula weight	840.59
T [K]	133(2)
crystal size [mm³]	0.500×0.360×0.340
crystal system	monoclinic
space group	$P2_1/c$
a [Å]	11.4622(3)
b [Å]	18.2636(6)
c [Å]	17.9294(4)
α [°]	90
β [°]	93.256(2)
γ [°]	90
V [Å³]	3747.30(18)
Z	4
ρ [g/cm³]	1.490
F(000)	1736
μ [mm^{-1}]	0.751
T_{min} / T_{max}	0.7314 / 0.8486
θ-range [°]	1.593 - 26.851
hkl-range	±14, ±23, -21 - 22
measured refl.	51539
unique refl. [R_{int}]	7965 [0.0203]
observed refl. ($I > 2\sigma(I)$)	7258
data / restraints / param.	7965 / 0 / 497
goodness-of-fit (F^2)	1.042
$R1$, $wR2$ ($I > 2\sigma(I)$)	0.0297, 0.0789
$R1$, $wR2$ (all data)	0.0336, 0.0817
resid. el. dens. [e/Å³]	-0.503 / 0.566

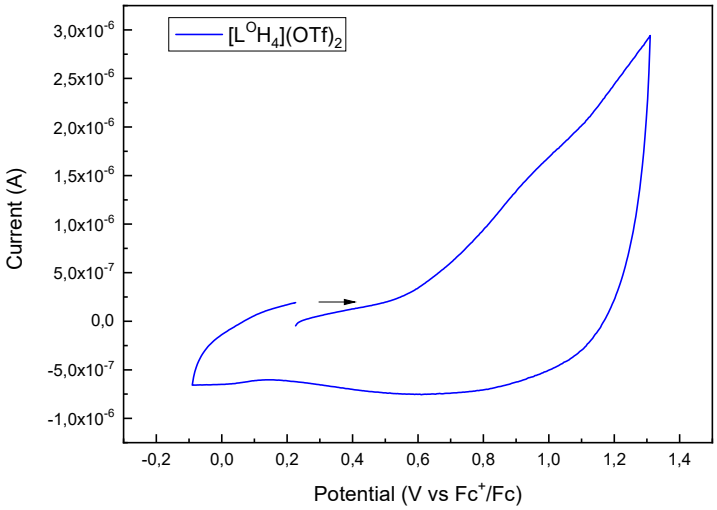

Appendix Figure 19. Cyclic voltammogram of **4** scanning anodicly first at scan rate 100 mVs^{-1}. WE: GC; CE: Pt; Ref: Ag (left).

Appendix Table 5. Crystal data and refinement details for **8**.

empirical formula	$C_{44}H_{44}F_6FeN_4NiO_{10}S_2$
formula weight	1081.51
T [K]	133(2)
crystal size [mm³]	0.210×0.160×0.120
crystal system	monoclinic
space group	$P2_1/n$
a [Å]	15.4160(7)
b [Å]	15.5938(4)
c [Å]	18.5273(8)
α [°]	90
β [°]	98.174(3)
γ [°]	90
V [Å³]	4408.6(3)
Z	4
ρ [g/cm³]	1.629
F(000)	2224
μ [mm^{-1}]	0.941
T_{min} / T_{max}	0.5897 / 0.8632
θ-range [°]	1.610 - 26.952
hkl-range	±19, -19 - 18, ±23
measured refl.	59528
unique refl. [R_{int}]	9400 [0.1203]
observed refl. ($I > 2\sigma(I)$)	5577
data / restraints / param.	9400 / 0 / 617
goodness-of-fit (F^2)	1.087
$R1$, $wR2$ ($I > 2\sigma(I)$)	0.0559, 0.1096
$R1$, $wR2$ (all data)	0.1228, 0.1384
resid. el. dens. [e/Å³]	-0.423 / 0.653

I.S.	Q.S.	fwhm	w_R/L	I_R/L	d[%]	rel_I.[%]
1.31	2.36	0.31			2.18	100.00

fsumsq: 0.2118E+01 (n: not optimized, c: correlated)

Int.: 0.5596E+00 theo_Int.: 0.5585E+00 (99.80 %)

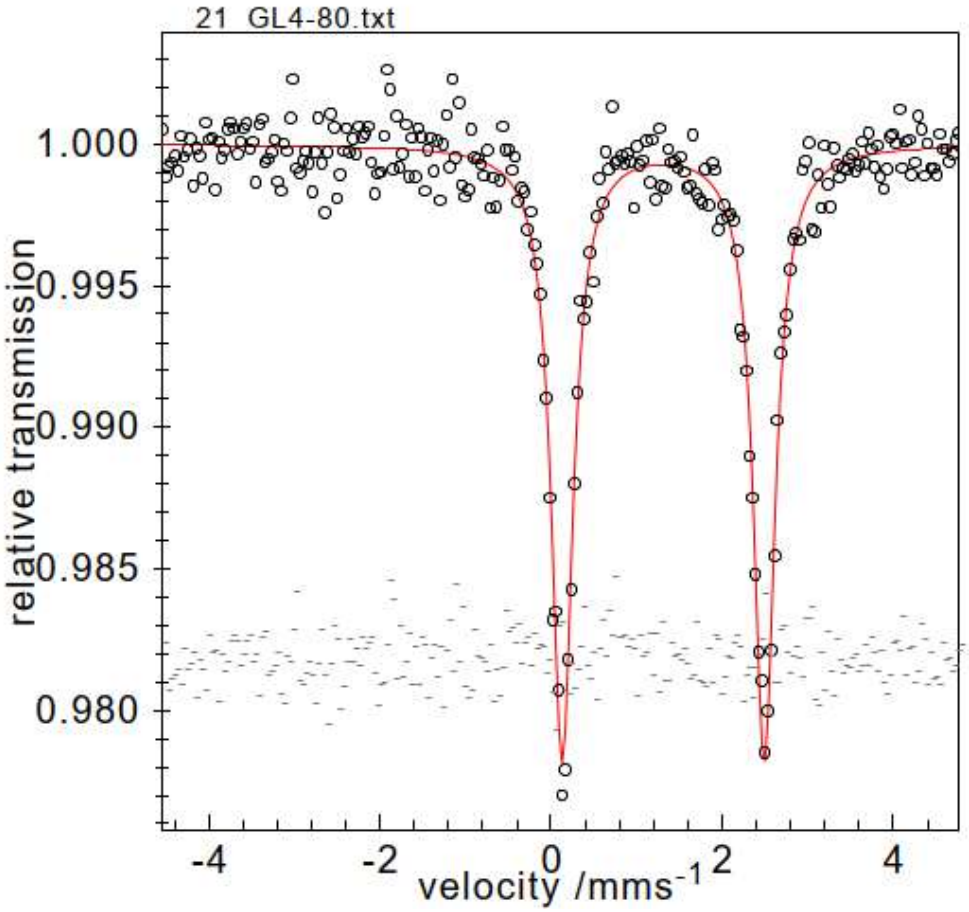

Appendix Figure 20. Mößbauer spectrum of solid **8** recorded at 80 K and parameters.

I.S.	Q.S.	fwhm	w_R/L	I_R/L	d[%]	rel_I.[%]
1.25	2.59	0.35			1.23	100.00 -gr

fsumsq: 0.7871E+00 (n: not optimized, c: correlated)

Int.: 0.3647E+00 theo_Int.: 0.3641E+00 (99.84 %)

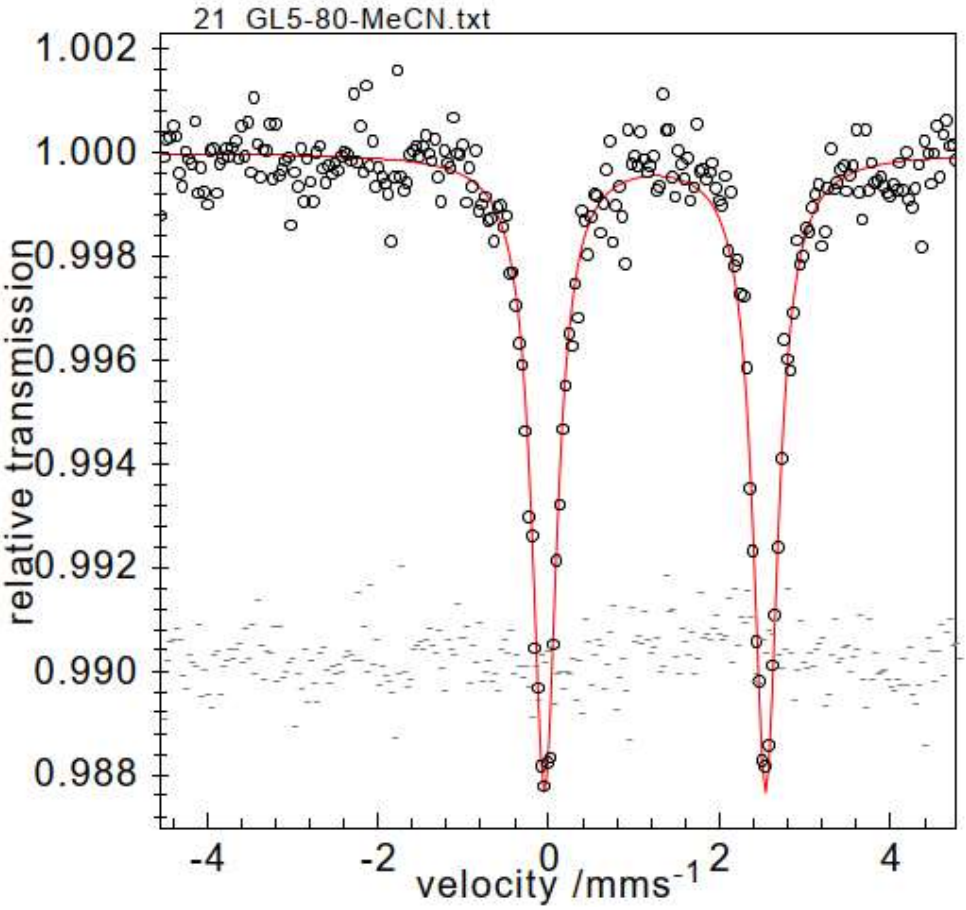

Appendix Figure 21. Mößbauer spectrum of **8** in a frozen solution of MeCN recorded at 80 K and parameters.

```
Spin 1 =   2.0
_var_____________value__ifit_________
   D1                -21.483   f
E/D1                   0.000
  gx1                  2.117   f
  gy1                  2.117   c
  gz1                  2.558   f
-----------------------------------------
TIP [1e-6 emu]          9.4   (subtracted)
2zJ [cm-1]             0.10
PI   [%] (S= 0.0        0.0
TW_for_PI   [K]        0.00
Error_Sum    0.79886E-02     R_Val.:     0.106E-04
-----------------------------------------
efile:        21_GL251_heat.txt     (fsum:  0.984E-01)
molar mass/g   :  1081.50        chi_dia:  -0.5420E+03
sample/mg      :     7.75
B-fields[T]    :    0.500  0.500
-----------------------------------------
efile:        21_GL251_VTVH.txt     (fsum:  0.539E+00)
molar mass/g   :  1081.50        chi_dia:  -0.5420E+03
sample/mg      :     7.75
B-fields[T]    :    7.000  7.000  4.000  4.000  0.000  1.000
-----------------------------------------
Lebedev grid:   16 pts
PC Y(45)  48.45mg,  d:-0.237E-03,  s:  0.000E+00,  p:  0.163E-03
```

Appendix Figure 22. SQUID data for **8**.

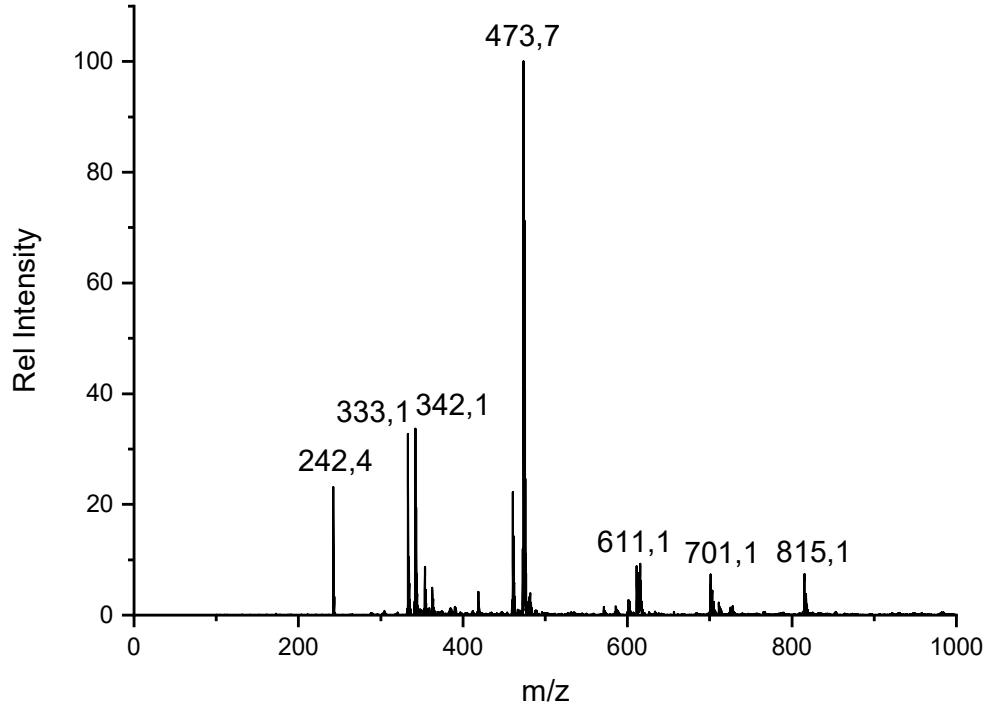

Appendix Figure 23. ESI-MS analysis of **8** in MeCN.

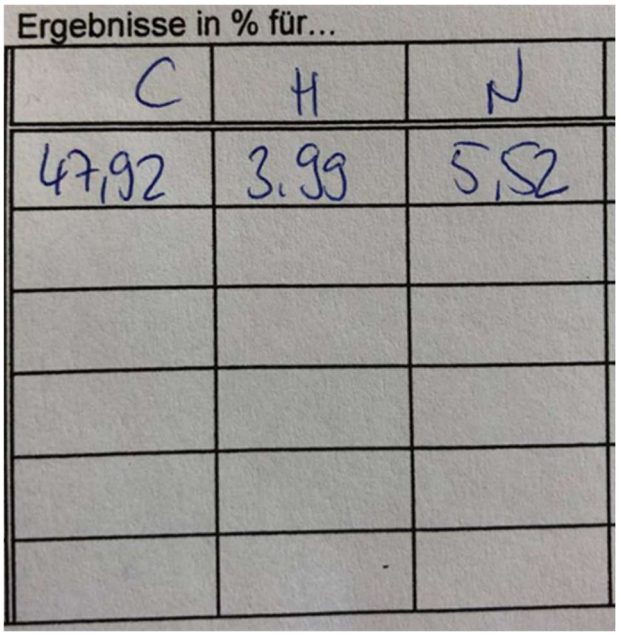

Appendix Figure 24. Elemental Analysis of **8**, C H and N percentages.

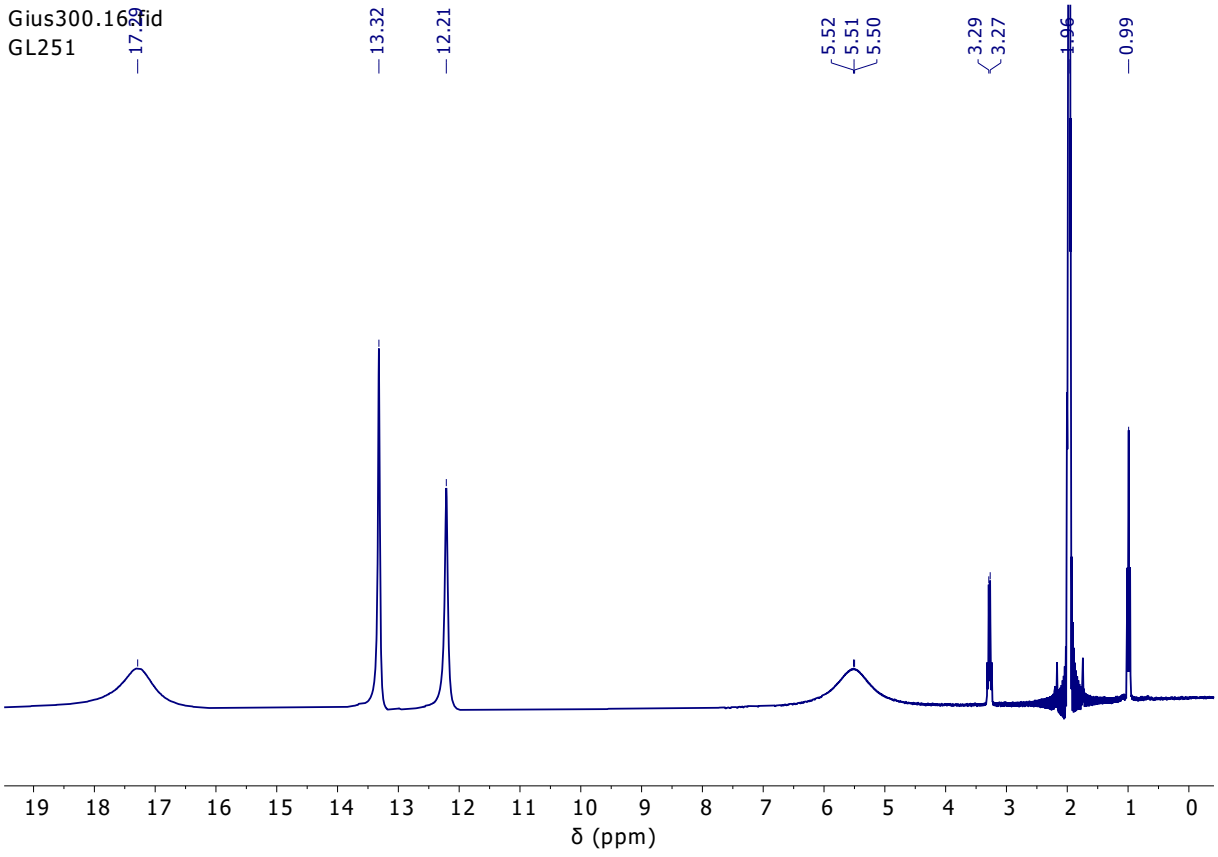

Appendix Figure 25. ^{1}H NMR spectrum of **8** in MeCN-d_3.

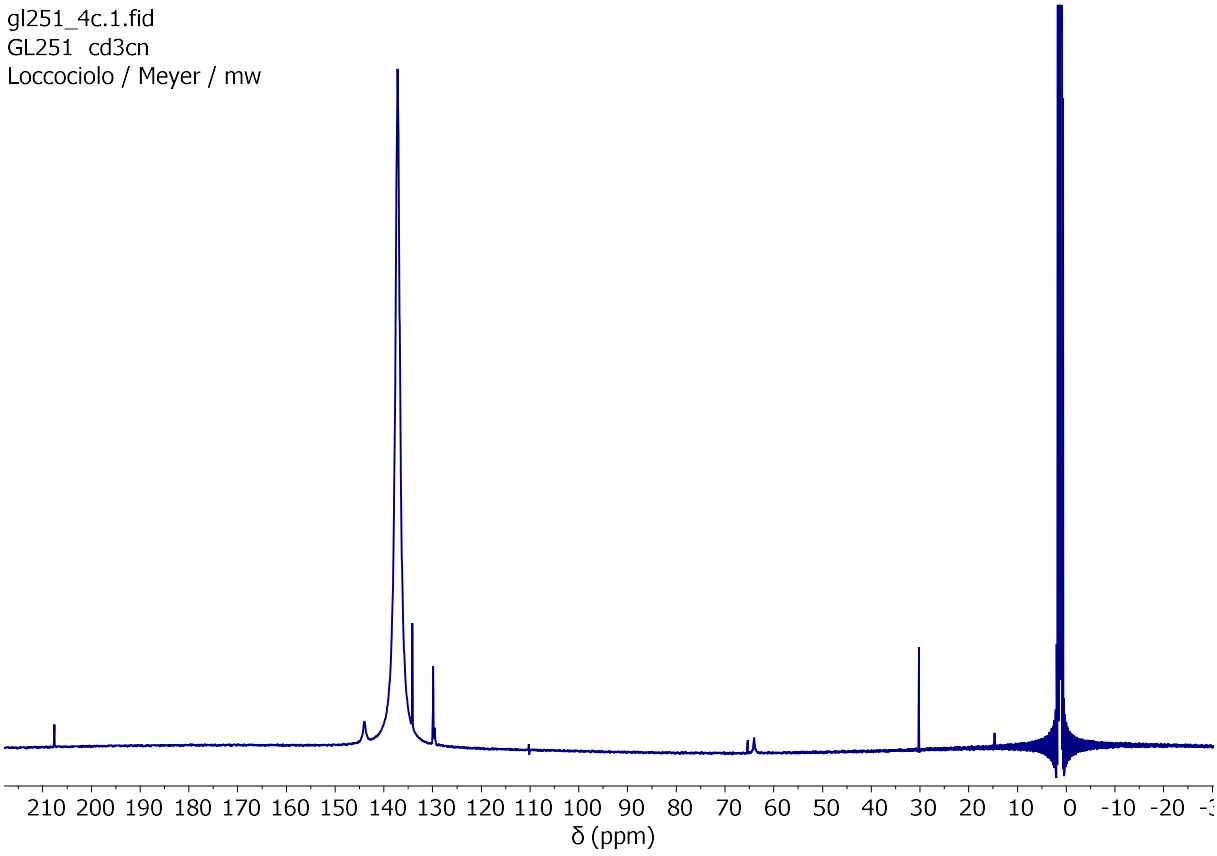

Appendix Figure 26. ^{13}C NMR spectrum of **8** in MeCN-d_3.

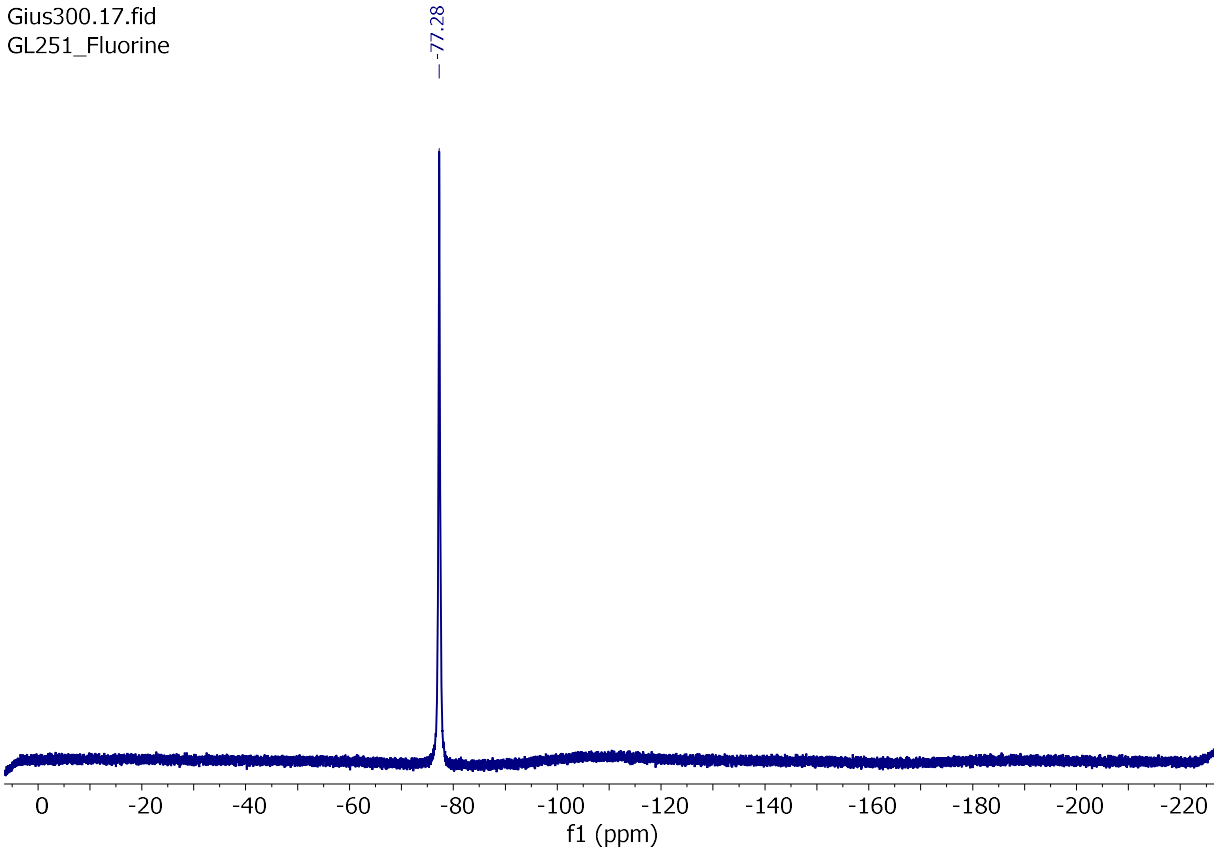

Appendix Figure 27. ^{19}F NMR spectrum of **8** in MeCN-d_3.

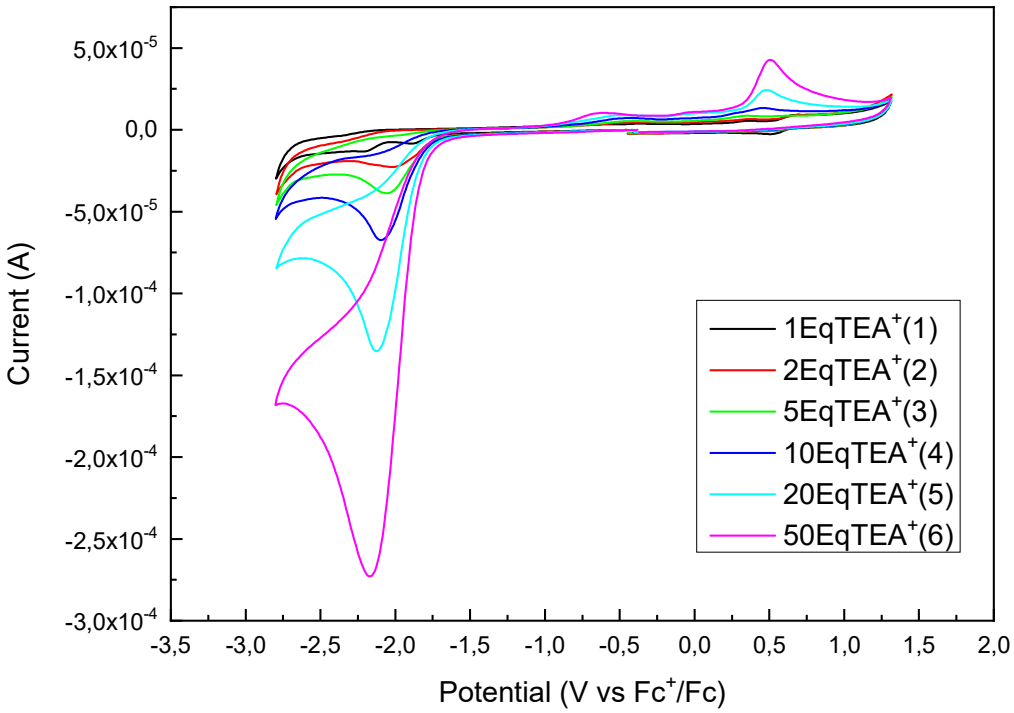

Appendix Figure 28. Full cyclic voltammogram for the HER experiments using complex **8**, at scan rate 100 mVs^{-1}. WE: GC; CE: Pt; Ref: Ag.

Appendix Table 6 Crystal data and refinement details for **9**.

empirical formula	$C_{43}H_{42.50}CoI_2N_{7.50}NiO_2$
formula weight	1067.78
T [K]	100(2)
crystal size [mm^3]	0.433×0.187×0.092
crystal system	triclinic
space group	*P*-1
a [Å]	12.164(4)
b [Å]	12.880(4)
c [Å]	15.301(5)
α [°]	83.571(11)
β [°]	79.560(10)
γ [°]	67.055(10)
V [$Å^3$]	2168.8(12)
Z	2
ρ [g/cm^3]	1.635
F(000)	1060
μ [mm^{-1}]	2.285
T_{min} / T_{max}	0.65 / 0.82
θ-range [°]	2.140 - 27.918
hkl-range	±15, ±16, ±20
measured refl.	105348
unique refl. [R_{int}]	10311 [0.0472]
observed refl. ($I > 2\sigma(I)$)	9106

data / restraints / param.	10311 / 27 / 527
goodness-of-fit (F^2)	1.034
$R1$, $wR2$ ($I > 2\sigma(I)$)	0.0229, 0.0488
$R1$, $wR2$ (all data)	0.0292, 0.0518
resid. el. dens. [e/Å³]	-0.827 / 1.242

Appendix Table 7 Crystal data and refinement details for **10**.

empirical formula	$C_{77}H_{71}F_3Fe_2N_{10}O_7S$
formula weight	1449.19
T [K]	143(2)
crystal size [mm³]	0.430×0.200×0.159
crystal system	monoclinic
space group	$P2_1/n$
a [Å]	11.6551(4)
b [Å]	19.1572(7)
c [Å]	37.8125(12)
α [°]	90
β [°]	97.8390(10)
γ [°]	90
V [Å³]	8363.8(5)
Z	4
ρ [g/cm³]	1.151
F(000)	3016
μ [mm^{-1}]	0.431
T_{min} / T_{max}	0.83 / 0.93
θ-range [°]	2.059 - 27.910
hkl-range	±15, ±25, ±49
measured refl.	187163
unique refl. [R_{int}]	20002 [0.0640]
observed refl. ($I > 2\sigma(I)$)	16021
data / restraints / param.	20002 / 106 / 976
goodness-of-fit (F^2)	1.098
$R1$, $wR2$ ($I > 2\sigma(I)$)	0.0628, 0.1430
$R1$, $wR2$ (all data)	0.0795, 0.1503
resid. el. dens. [e/Å³]	-0.644 / 0.434

Appendix Table 8 Crystal data and refinement details for **11**.

empirical formula	$C_{84}H_{79}F_6FeN_{13}Ni_2O_{11}S_2$
formula weight	1797.99
T [K]	133(2)
crystal size [mm³]	0.220×0.190×0.100
crystal system	monoclinic
space group	$P2_1/c$
a [Å]	15.7679(4)
b [Å]	16.1461(4)
c [Å]	32.9734(8)
α [°]	90
β [°]	103.117(2)
γ [°]	90
V [Å³]	8175.7(4)
Z	4
ρ [g/cm³]	1.461
F(000)	3720
μ [mm^{-1}]	0.765
T_{min} / T_{max}	0.6479 / 0.8957
θ-range [°]	1.261 - 25.815
hkl-range	-18 - 19, ±19, ±40
measured refl.	86101
unique refl. [R_{int}]	15769 [0.1048]
observed refl. ($I > 2\sigma(I)$)	10070
data / restraints / param.	15769 / 28 / 1093
goodness-of-fit (F^2)	1.043
$R1$, $wR2$ ($I > 2\sigma(I)$)	0.0659, 0.1463
$R1$, $wR2$ (all data)	0.1234, 0.1761
resid. el. dens. [e/Å³]	-0.442 / 0.804

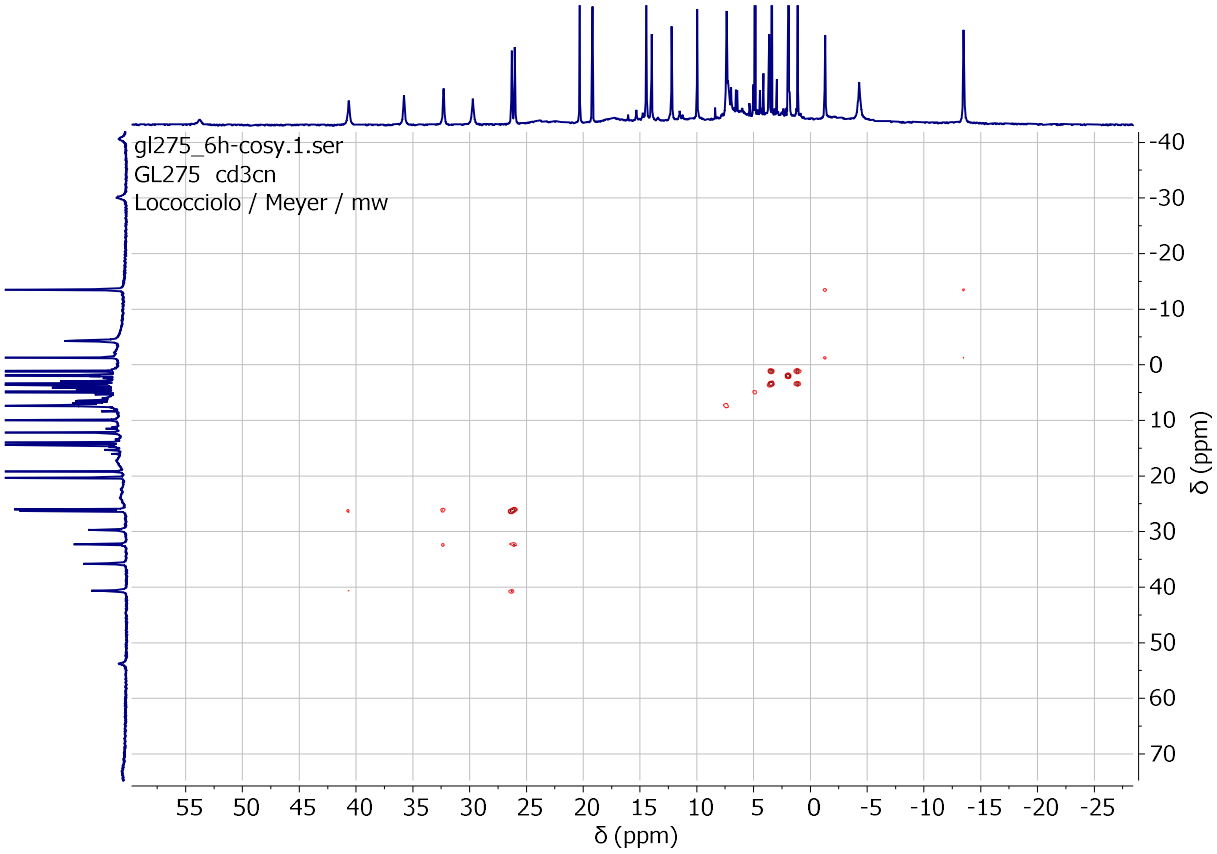

Appendix Figure 29 COSY spectrum of **11** in CD_3CN.

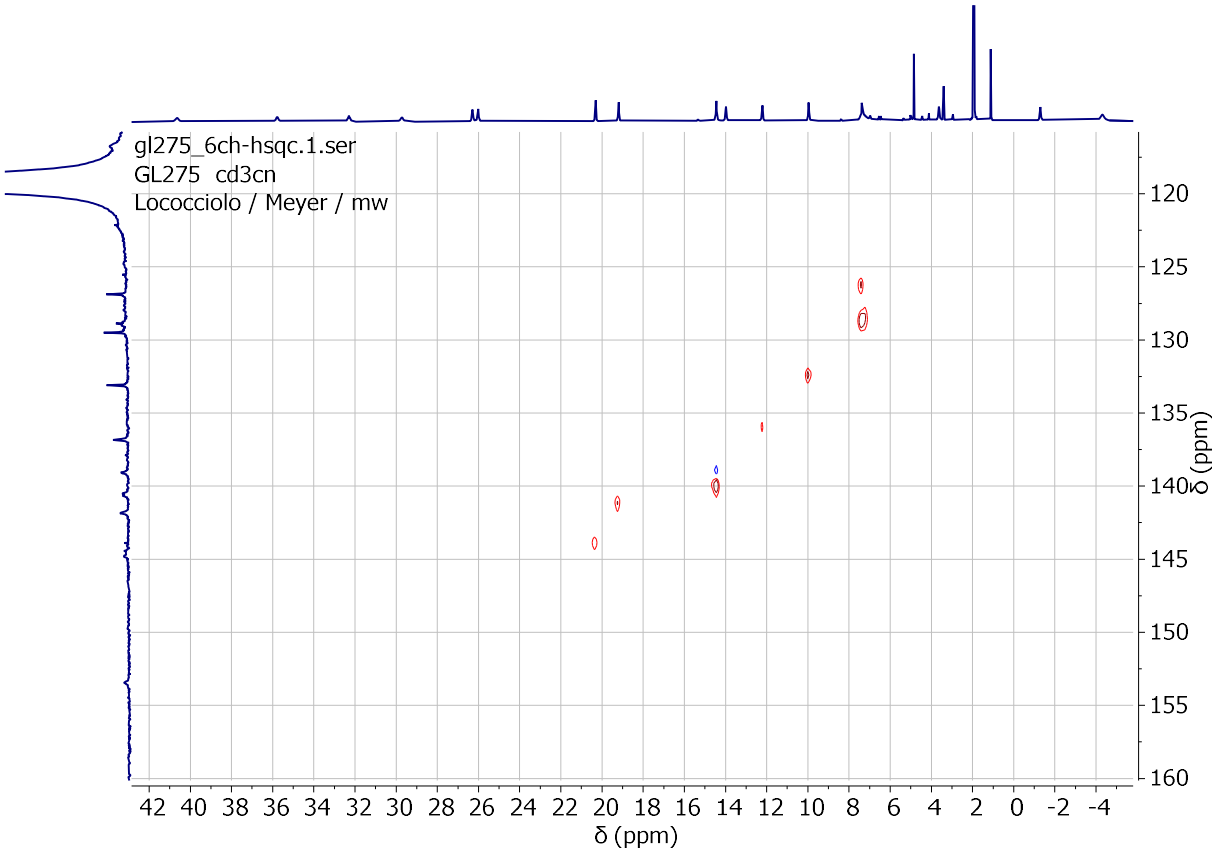

Appendix Figure 30 HSQC spectrum of **11** in CD_3CN.

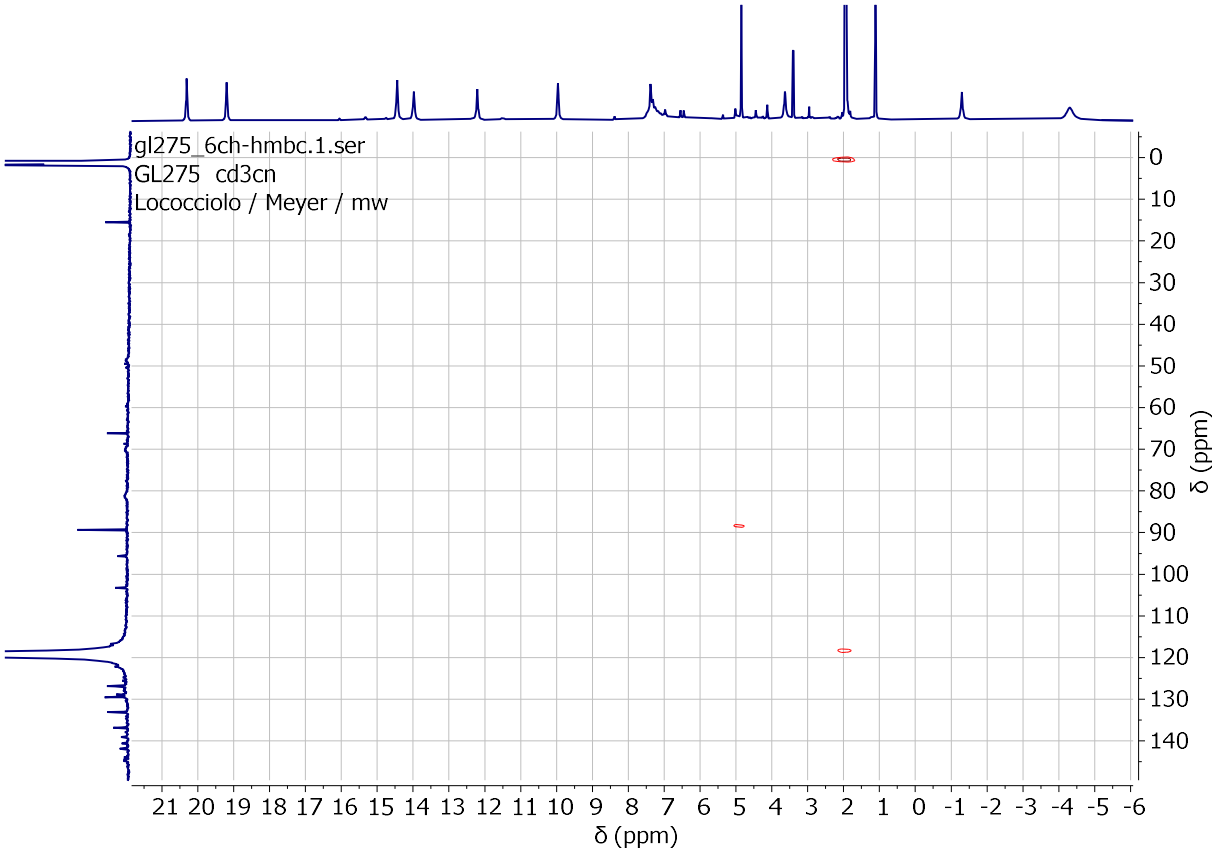

Appendix Figure 31 HMBC spectrum of **11** in CD_3CN.

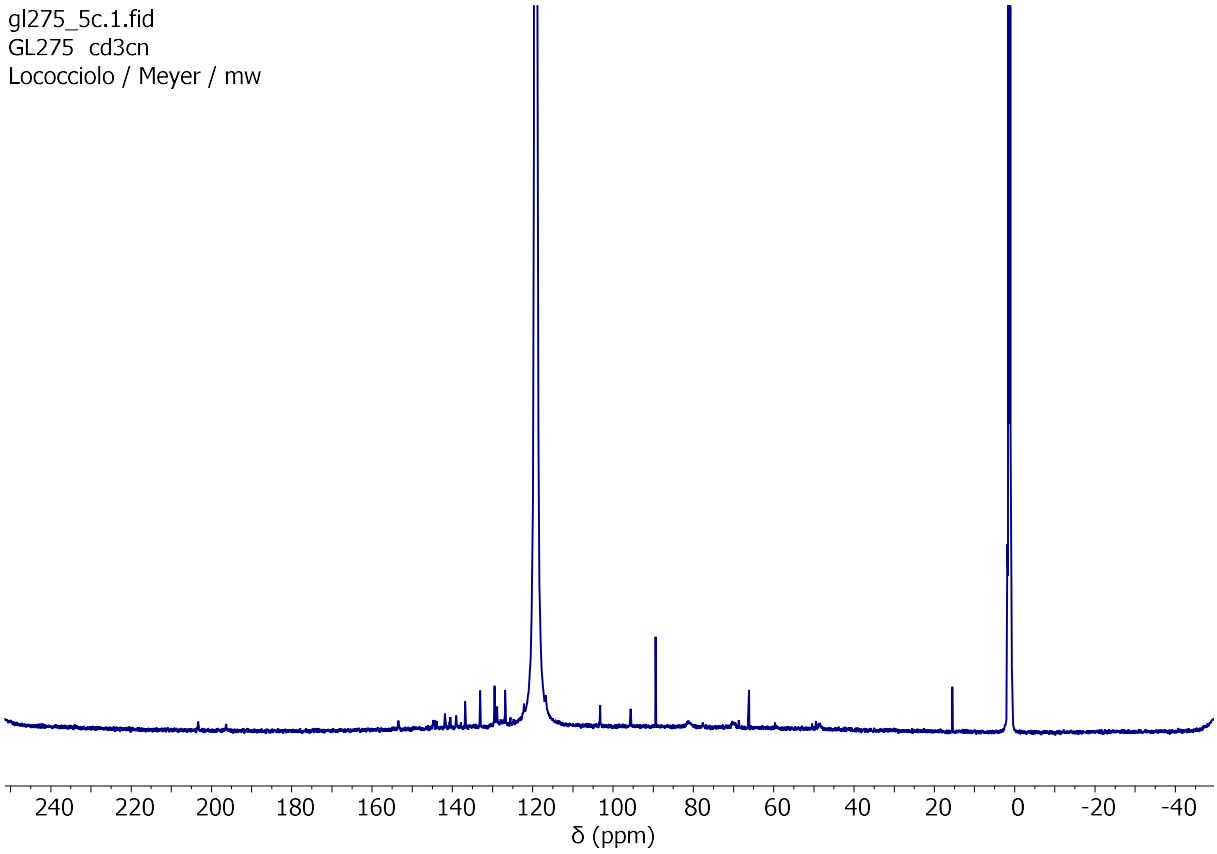

Appendix Figure 32 ^{13}C NMR spectrum of **11** in CD_3CN.

I.S.	Q.S.	fwhm	w_R/L	I_R/L	d[%]	rel_I.[%]
1.14	1.95	0.51			2.23	100.00 - gr

fsumsq: 0.2364E+01 (n: not optimized, c: correlated)

Int.: 0.9429E+00 theo_Int.: 0.9412E+00 (99.82 %)

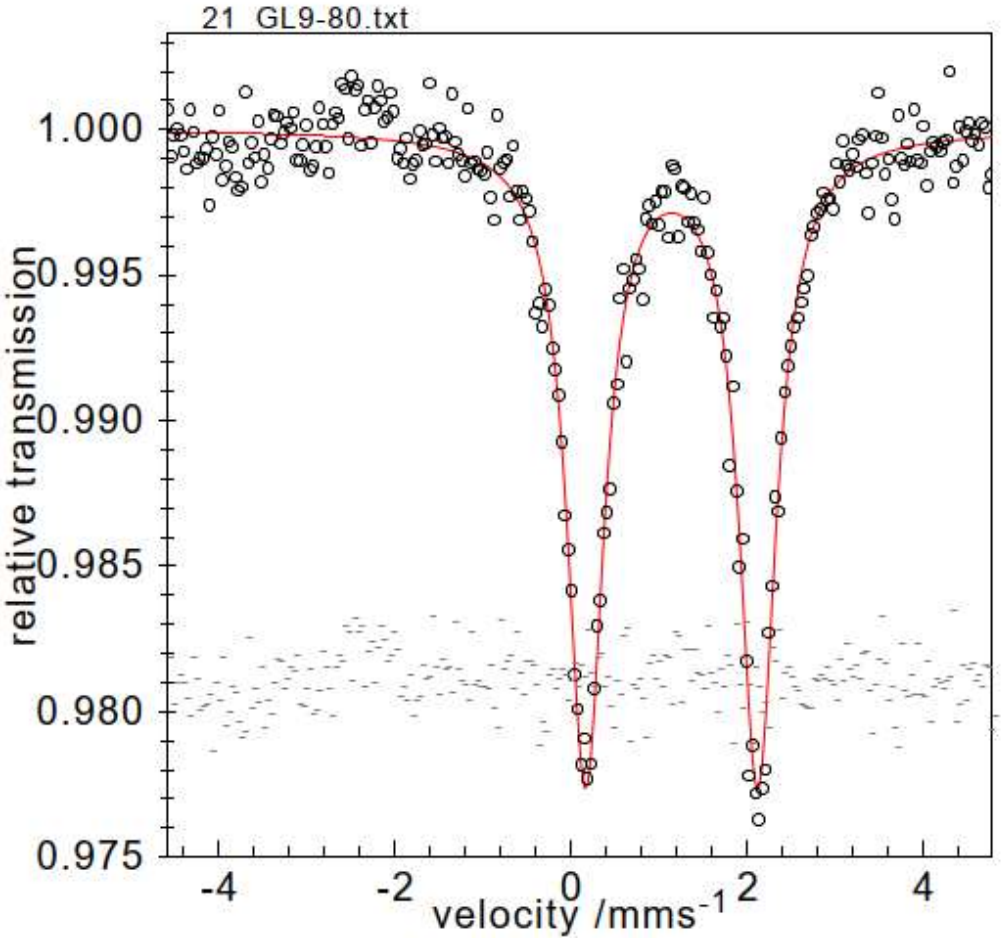

Appendix Figure 33 Mößbauer spectrum of solid **11** recorded at 80 K and parameters.

```
Spin 1 =   2.0
_var_____________value__ifit_________
   D1                -12.778   f
E/D1                   0.318   f
  gx1                  2.215   f
  gy1                  2.215   c
  gz1                  2.215   c
-------------------------------------
TIP [1e-6 emu]       800.0   (subtracted)
2zJ [cm-1]             0.00
PI   [%]  (S= 0.0      0.0
TW_for_PI    [K]       0.00
Error_Sum    0.32351E+00     R_Val.:     0.532E-03
-------------------------------------
efile:       2022_GL275.txt     (fsum: 0.138E+01)
molar mass/g   :  1782.89       chi_dia: -0.8965E+03
sample/mg      :     8.00
B-fields[T]    :    0.500 0.500
-------------------------------------
efile:       2022_GL275_VTVH.txt     (fsum: 0.466E-01)
molar mass/g   :  1782.89       chi_dia: -0.8965E+03
sample/mg      :     8.00
B-fields[T]    :    7.000 7.000 4.000 4.000 0.000 1.000
-------------------------------------
Lebedev grid:   16 pts
PC Y45 48.30mg, d:-0.240E-03, s: 0.000E+00, p: 0.000E+00
```

Appendix Figure 34 SQUID parameters found for **11**.

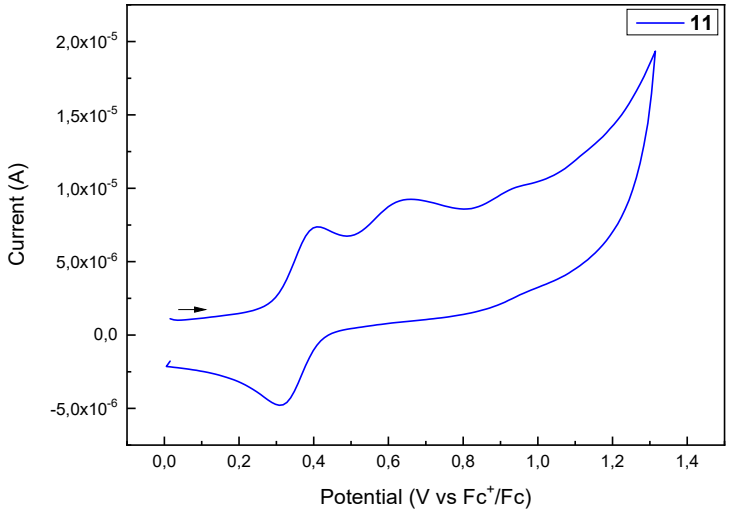

Appendix Figure 35 Cyclic voltammogram of **11**, in the anodic range at scan rate 100 mVs^{-1}. WE: GC; CE: Pt; Ref: Ag.

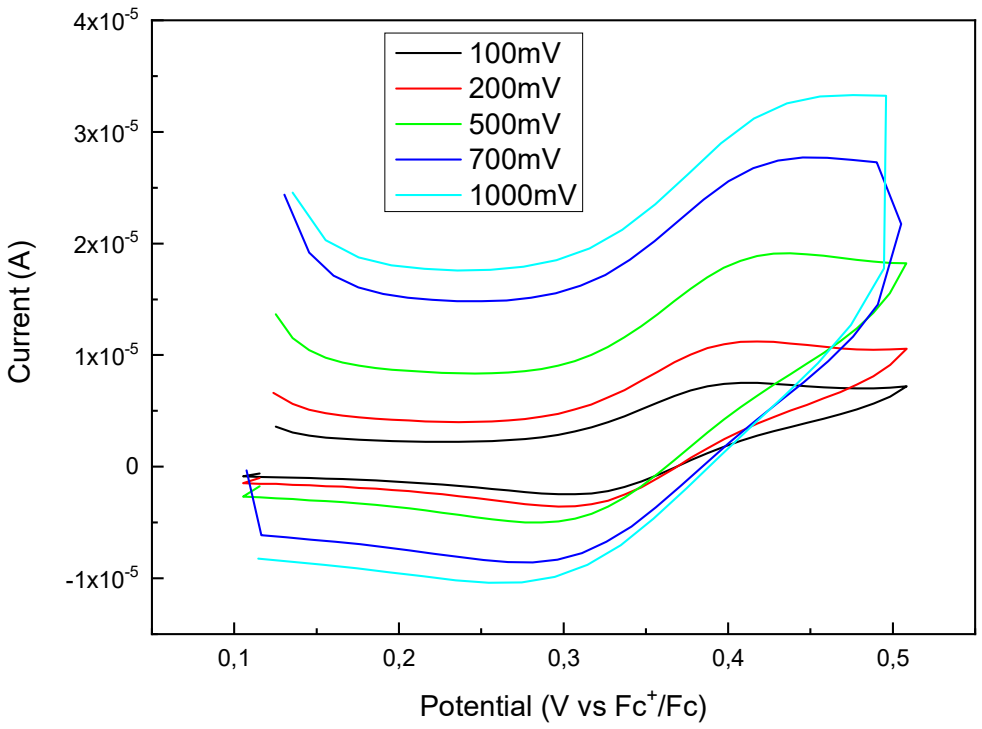

Appendix Figure 36 First oxidation process of **11** at different scan rates. WE: GC; CE: Pt; Ref: Ag.

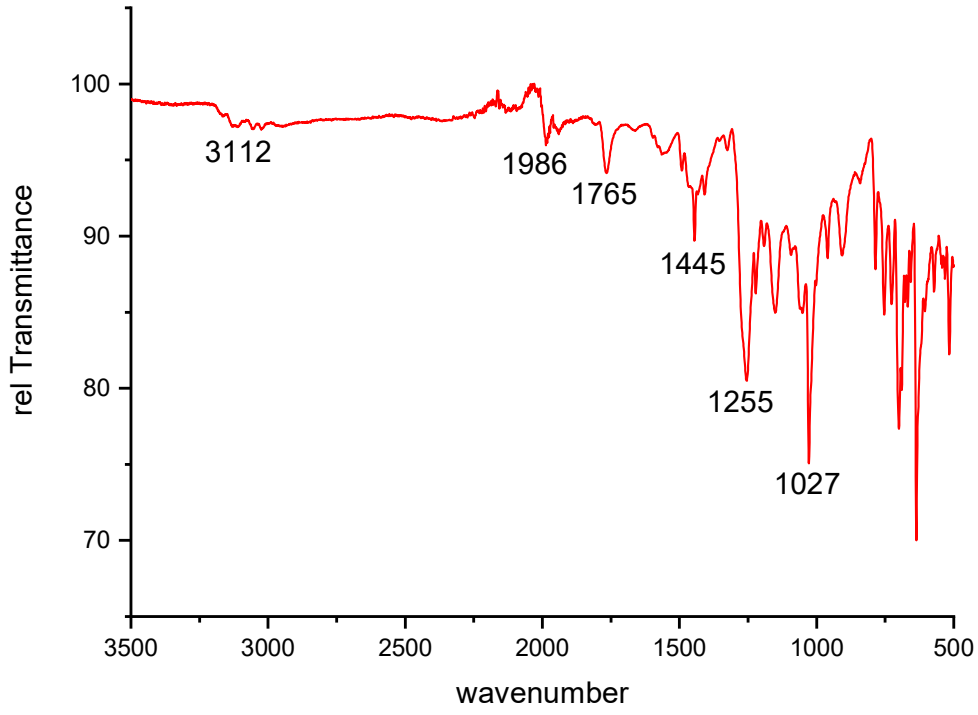

Appendix Figure 37 IR Spectrum of **11**.

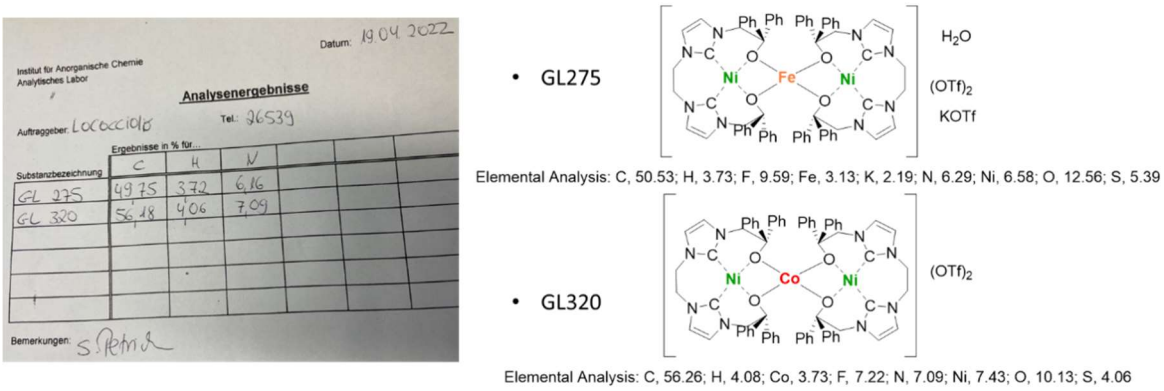

Appendix Figure 38 Elemental Analysis data for **11** and **12**.

Appendix Table 9 Crystal data and refinement details for **12.**

empirical formula	$C_{78}H_{70}CoF_6N_{10}Ni_2O_{10}S_2$
formula weight	1661.91
T [K]	100(2)
crystal size [mm³]	0.490×0.340×0.120
crystal system	monoclinic
space group	$P2_1/c$
a [Å]	15.7445(17)
b [Å]	16.2910(19)
c [Å]	32.842(4)
a [°]	90
b [°]	103.091(3)
g [°]	90
V [Å³]	8204.9(16)
Z	4
r [g/cm³]	1.345
F(000)	3428
μ [mm^{-1}]	0.779
T_{min} / T_{max}	0.50 / 0.58
q-range [°]	2.028 - 28.130
hkl-range	-19 - 20, ±21, ±43
measured refl.	224074
unique refl. [R_{int}]	19861 [0.0882]
observed refl. ($I > 2s(I)$)	14041
data / restraints / param.	19861 / 68 / 1015
goodness-of-fit (F^2)	1.026
*R*1, *wR*2 ($I > 2s(I)$)	0.0728, 0.1798
*R*1, *wR*2 (all data)	0.1056, 0.2023
resid. el. dens. [e/Å³]	-1.329 / 2.351

Appendix Table 10 Magnetic properties of complex **12**.

Complex	g_x	g_y	g_z	D (cm^{-1})	E/D	U_{eff} (K) @ H_{dc} = 0 Oe	U_{eff} (K) @ H_{dc} = 2000 Oe
12	2.32	2.32	2.88	-74.3	0.0	125 K	134 K

Description of table 9, chapter 5.5: pdms = 1,2-bis(methanesulfonamido)benzene;

Hsalbim = 2-(1H-benzimidazol-2-yl)phenol; acac = acetylacetonate;

bmsab = 1,2-bis(methanesulfonamido)benzene;

btsab = 1,2-bis(toluenesulfonamido)benzene];

$Himl^-$ = 2-(2-imidazolyl)phenolate;

$Himn^-$ = 2-(2-imidazolinyl)phenolate;

$Hthp^-$= 2-(1,4,5,6-tetrahydropyrimidin-2-yl)phenolate; $TpPh_2$ = hydrotris(3,5-diphenyl-pyrazolyl)borate;

HL^{Br} = 1-[N-(4-Bromophenyl)carboximidoyl]naphthalen-2-ol;

HL^{Ph} = 1-[N-(2 Phenylphenyl)carboximidoyl]naphthalen-2-ol;

HL^{Sal},2-Ph = (2-(([1,10-biphenyl]-2-ylimino)methyl)phenol);

HL^{Nph},2-Ph = (1-(([1,10-biphenyl]-2-ylimino)methyl)naphthalen-2-ol);

bcpp = bis(1-chloroimidazo[1,5–a]pyridin-3-yl)pyridine;

terpy = terpyridine;

phen = 1,100-phenanthroline;

TMC =1,4,7,10-tetramethyl-1,4,7,10-tetraazacyclododecane;

tpa = tris(2-methylpyridyl)amine;

$TpPh_2$ = hydrotris(3,5-diphenyl-pyrazolyl)borate;

H_2L^1 = N,N'-bis(p-toluenesulfonyl)oxamide;

H_2L^2 = N,N'-diphenyloxamide;

L^3 = 2,9-diphenyl-1,10-phenanthroline;

L^4 = 9,9-dimethyl-4,5-bis(diphenylphosphino) xanthene

9. List of abbreviations

AC	alternate current
ATP	adenosine triphosphate
Bu	butyl
BZA	benzoic acid
CE	counter electrode
CN	coordination number
COD	cyclooctadiene
COSY	correlation spectroscopy
Cp	cyclopentadiene
CV	cyclic voltammetry
D	doublet (NMR)
DC	direct current
DiPP	2,6-di-iso-propylphenyl
DMSO	dimethylsulfoxide
eq	equivalent
ESI	electrospray ionization
ET	electron transport
Et	ethyl
Et al.	et alii
Et_2O	diethyil ether
EtOH	ethanol
Fc/Fc^+	ferrocene/ferrocenium
GC	glassy carbon
H_2ases	hydrogenases
HER	hydrogen evolution reaction
HMBC	heteronuclear multiple-bond correlation spectroscopy
HOR	hydrogen oxydation reaction
HS	high spin
HSQC	heteronuclear single quantum coherance
IR	infrared
IS	isomer shift
K^tObu	potassium tert-butoxide
LMCT	ligand to metal charge transfer
LS	low spin
m	multiplet (NMR)
m/z	mass over charge (mass spectrometry)
Me	methyl
MeCN	acetonitrile, CH_3CN
MO	molecular orbitals
MS	mass spectrometry
NAD(P)H	nicotinamide adenine dinucleotide phosphate
NHC	N-heterocyclic carbene
NMR	nuclear magnetic resonance
ORTEP	oak ridge thermal-ellipsoid plot program
OS	open shell

PEM	proton exchange membrane
ppm	part per milion
QS	quadrupole splitting
QTM	quantum tunneling magnetization
Ref	reference
s	singlet (NMR)
SIM	single ion magnet
SMM	single molecule magnet
SRM	slow relaxation of the magnetization
TEA	triethylamine
TEOA	triethanolamine
TOF	turnover frequency
TON	turnover number
UV/Vis	ultraviolet and visible
WE	working electrode

10. References

(1) Armaroli, N.; Balzani, V. *Chemistry (Weinheim an der Bergstrasse, Germany)* **2016**, *22*, 32–57.

(2) D'Amato, G.; Holgate, S. T.; Pawankar, R.; Ledford, D. K.; Cecchi, L.; Al-Ahmad, M.; Al-Enezi, F.; Al-Muhsen, S.; Ansotegui, I.; Baena-Cagnani, C. E.; Baker, D. J.; Bayram, H.; Bergmann, K. C.; Boulet, L.-P.; Buters, J. T. M.; D'Amato, M.; Dorsano, S.; Douwes, J.; Finlay, S. E.; Garrasi, D.; Gómez, M.; Haahtela, T.; Halwani, R.; Hassani, Y.; Mahboub, B.; Marks, G.; Michelozzi, P.; Montagni, M.; Nunes, C.; Oh, J. J.-W.; Popov, T. A.; Portnoy, J.; Ridolo, E.; Rosário, N.; Rottem, M.; Sánchez-Borges, M.; Sibanda, E.; Sienra-Monge, J. J.; Vitale, C.; Annesi-Maesano, I. *The World Allergy Organization journal* **2015**, *8*, 25.

(3) Haines, A.; Ebi, K. *The New England journal of medicine* **2019**, *380*, 263–273.

(4) Langen, P.; Hucho, F. *Angw. Chem.*, **2008**, 47, 1824-1827.

(5) Spaans, S. K.; Weusthuis, R. A.; van der Oost, J.; Kengen, S. W. M. *Frontiers in microbiology* **2015**, *6*, 742.

(6) Loyselle P., Prokopius, K. *Teledyne Energy Systems, Inc., Proton Exchange Member (PEM) Fuel Cell Engineering Model Powerplant*, thesis report, **2013**.

(7) Yang, C.-J. *Energy Policy* **2009**, *37*, 1805–1808.

(8) Davydova, E. S.; Mukerjee, S.; Jaouen, F.; Dekel, D. R. *ACS Catal.* **2018**, *8*, 6665–6690.

(9) Tafel, J. *Zeitschrift für Physikalische Chemie* **1905**, *50U*, 641–712.

(10) Heyrovský, J. *Recl. Trav. Chim. Pays-Bas* **1927**, *46*, 582–585.

(11) Volmer, M. *Zeitschrift für Physikalische Chemie* **5020**, 203–213.

(12) Zhao, G.; Rui, K.; Dou, S. X.; Sun, W. *Adv. Funct. Mater.* **2018**, 28, 1803291.

(13) Grimes, C.A., Varghese, O.K., Ranjan, S. *Light, water, hydrogen: the solar generation of hydrogen by water photoelectrolysis*, **2008**, Springer.

(14) Turner, J.A., *Science* **2004***, 305, 972− 974*.

(15) Konieczny, A.; Mondal, K.; Wiltowski, T.; Dydo, P. *International Journal of Hydrogen Energy* **2008**, *33*, 264–272.

(16) Vesborg, P. C. K.; Jaramillo, T. F. *RSC Adv.* **2012**, *2*, 7933.

(17) Frey, M. *ChemBioChem* **2002**, *3*, 153–160.

(18) Higuchi, Y.; Ogata, H.; Miki, K.; Yasuoka, N.; Yagi, T. *Structure* **1999**, *7* , 549–556.

(19) Adams, M. W. *BBA - Bioenergetics* **1990**, *1020*, 115–145.

(20) Fauque, G.; Peck, H. D.; Moura, J. J.; Huynh, B. H.; Berlier, Y.; DerVartanian, D. V.; Teixeira, M.; Przybyla, A. E.; Lespinat, P. A.; Moura, I. *FEMS Microbiol Rev* **1988**, *4*, 299–344.

(21) Przybyla, A. E.; Robbins, J.; Menon, N.; Peck, H. D. *FEMS Microbiol Rev* **1992**, *8*, 109–135.

(22) Lubitz, W.; Ogata, H.; Rüdiger, O.; Reijerse, E. *Chem. Rev.* **2014**, *114*, 4081–4148.

(23) Volbeda, A.; Charon, M. H.; Piras, C.; Hatchikian, E. C.; Frey, M.; Fontecilla-Camps, J. C. *Nature* **1995**, *373*, 580–587.

(24) Higuchi, Y.; Yagi, T.; Yasuoka, N. *Structure* **1997**, *5*, 1671–1680.

(25) Hatchikian, E. C.; Bruschi, M.; Le Gall, J. *Biochem. and Biophys. Research Comm.s* **1978**, *82*, 451–461.

(26) Huynh, B. H.; Patil, D. S.; Moura, I.; Teixeira, M.; Moura, J. J.; DerVartanian, D. V.; Czechowski, M. H.; Prickril, B. C.; Peck, H. D.; LeGall, J. *J. of Biol. Chem.* **1987**, *262*, 795–800.

(27) Happe, R. P.; Roseboom, W.; Pierik, A. J.; Albracht, S. P.; Bagley, K. A. *Nature* **1997**, *385*, 126.

(28) Hidalgo, R.; Ash, P. A.; Healy, A. J.; Vincent, K. A. *Angew. Chem. (International ed. in English)* **2015**, *54*, 7110–7113.

(29) Fritsch, J.; Scheerer, P.; Frielingsdorf, S.; Kroschinsky, S.; Friedrich, B.; Lenz, O.; Spahn, C. M. T. *Nature* **2011**, *479*, 249–252.

(30) Kampa, M.; Lubitz, W.; van Gastel, M.; Neese, F. *J. of Biol. inorganic Chem.* **2012**, *17*, 1269–1281.

(31) Saggu, M.; Zebger, I.; Ludwig, M.; Lenz, O.; Friedrich, B.; Hildebrandt, P.; Lendzian, F. *Journal of Biological Chemistry* **2009**, *284*, 16264–16276.

(32) Murphy, B. J.; Hidalgo, R.; Roessler, M. M.; Evans, R. M.; Ash, P. A.; Myers, W. K.; Vincent, K. A.; Armstrong, F. A. *J. Am. Chem. Soc.* **2015**, *137*, 8484–8489.

(33) Kaur-Ghumaan, S.; Stein, M. *Dal. Trans.* **2014**, *43*, 9392–9405.

(34) Brazzolotto, D.; Gennari, M.; Queyriaux, N.; Simmons, T.R.; Pécaut, J.; Demeshko, S.; Meyer, F.; Orio, M.; Artero, V.; Duboc, C. *Nat. Chem.,* **2016**, 8, 1054.

(35) Canaguier, S.; Field, M.; Oudart, Y.; Pécaut, J.; Fontecave, M.; Artero, V. *Chem. Comm.* **2010**, *46*, 5876–5878.

(36) Brazzolotto, D.; Wang, L.; Tang, H.; Gennari, M.; Queyriaux, N.; Philouze, C.; Demeshko, S.; Meyer, F.; Orio, M.; Artero, V.; Hall, M. B.; Duboc, C. *ACS Catal.* **2018**, *8*, 10658–10667.

(37) Sun, L.; Adam, S. M.; Mokdad, W.; David, R.; Milet, A.; Artero, V.; Duboc, C. *Faraday discussions* **2022**, *234*, 34–41.

(38) Fillman, K. L.; Przyojski, J. A.; Al-Afyouni, M. H.; Tonzetich, Z. J.; Neidig, M. L. *Chem. science* **2015**, *6*, 1178–1188.

(39) Przyojski, J. A.; Veggeberg, K. P.; Arman, H. D.; Tonzetich, Z. J. *ACS Catal.* **2015**, *5*, 5938–5946.

(40) Lee, H. M.; Jiang, T.; Stevens, E. D.; Nolan, S. P. *Organom.* **2001**, *20*, 1255–1258.

(41) Stauffer, S. R.; Lee, S.; Stambuli, J. P.; Hauck, S. I.; Hartwig, J. F. *Org. letters* **2000**, *2*, 1423–1426.

(42) Huang, J.; Stevens, E. D.; Nolan, S. P.; Petersen, J. L. *J. Am. Chem. Soc.* **1999**, *121*, 2674–2678.

(43) Zhang, Y.; Ngeow, K. C.; Ying, J. Y. *Org. letters* **2007**, *9*, 3495–3498.

(44) Vijaykumar, G.; Jose, A.; Vardhanapu, P. K.; P, S.; Mandal, S. K. *Organom.* **2017**, *36*, 4753–4758.

(45) Hameury, S.; Frémont, P. de; Braunstein, P. *Chem. Soc. Rev.* **2017**, *46*, 632–733.

(46) Lee, C.-C.; Ke, W.-C.; Chan, K.-T.; Lai, C.-L.; Hu, C.-H.; Lee, H. M. *Chem. (Weinheim an der Bergstrasse, Germany)* **2007**, *13*, 582–591.

(47) O, W. W. N.; Lough, A. J.; Morris, R. H. *Organom.* **2009**, *28*, 6755–6761.

(48) Liddle, S. T.; Edworthy, I. S.; Arnold, P. L. *Chem. Soc. Rev.* **2007**, *36*, 1732–1744.

(49) Bullock, R. M. *Catalysis without precious metals*; Wiley-VCH, **2011**.

(50) Kühl, O. *Chem. Soc. Rev.* **2007**, *36*, 592–607.

(51) Bertini, S.; Albrecht, M. *Chimia* **2020**, *74*, 483–488.

(52) Hameury, S.; Frémont, P. de; Breuil, P.-A. R.; Olivier-Bourbigou, H.; Braunstein, P. *Inorg. chem.* **2014**, *53*, 5189–5200.

(53) Juráková, J.; Šalitroš, I. *Monatshefte fur chemie* **2022**, 1–36.

(54) Magnani, N.; Caciuffo, R. *Inorganics* **2018**, *6*, 26.

(55) Gomes, C. S. B.; Costa, S. I.; Silva, L. C.; Jiménez-Tenorio, M.; Valerga, P.; Puerta, M. C.; Gomes, P. T. *Eur. J. Inorg. Chem.* **2018**, *2018*, 597–607.

(56) Rechkemmer, Y.; Breitgoff, F. D.; van der Meer, M.; Atanasov, M.; Hakl, M.; Orlita, M.; Neugebauer, P.; Neese, F.; Sarkar, B.; van Slageren, J. *Nat. Comm.* **2016**, *7*, 10467.

(57) Vaidya, S.; Tewary, S.; Singh, S. K.; Langley, S. K.; Murray, K. S.; Lan, Y.; Wernsdorfer, W.; Rajaraman, G.; Shanmugam, M. *Inorg. Chem.* **2016**, *55*, 9564–9578.

(58) Zadrozny, J. M.; Long, J. R. *J. of the Am. Chem. Soc.* **2011**, *133*, 20732–20734.

(59) Ohki, Y.; Tatsumi, K. *Eur. J. Inorg. Chem.* **2011**, *2011*, 973–985.

(60) Reger, D. L.; Coleman, C. *J. of Organom. Chem.* **1977**, *131*, 153–162.

(61) Yue, Z.; Dunya, H.; Aryal, S.; Segre, C. U.; Mandal, B. *J. of Power Sources* **2018**, *401*, 271–277.

(62) Kuchitsu, K.; Fukuyama, T.; Tamaru, Y.; Yoshida, Z.; Tabushi, I. *J. Am. Chem. Soc.* **1971**, *93*, 2799–2800.

(63) *CRC Handbook of Chemistry and Physics*, **2010**.

(64) Allen, F. H.; Kennard, O.; Watson, D. G.; Brammer, L.; Orpen, A. G.; Taylor, R. *J. Chem. Soc., Perkin Trans. 2* **1987**, S1.

(65) Shimizu, S.; Ogata, M. *J. Org. Chem.* **1986**, *51*, 3897–3900.

(66) Kaestner, P.; Strehmel, V. *J. of Polymer Science* **2020**, *58*, 977–987.

(67) Da Menezes Silva, V. H.; Braga, A. A. C.; Cundari, T. R. *Organom.* **2016**, *35*, 3170–3181.

(68) Huynh, H. V.; Koh, C. H. M.; van Nguyen, H. *Dal. Trans.* **2017**, *46*, 11318–11326.

(69) Choi, M.-Y.; Chan, M. C.-W.; Zhang, S.; Cheung, K.-K.; Che, C.-M.; Wong, K.-Y. *Organom.* **1999**, *18*, 2074–2080.

(70) Reineke, M. H.; Porter, T. M.; Ostericher, A. L.; Kubiak, C. P. *Organom.* **2018**, *37*, 448–453.

(71) Klawitter, I.; Meyer, S.; Demeshko, S.; Meyer, F. *Zeitschrift für Naturforschung B* **2013**, *68*, 458–466.

(72) *Comprehensive Renewable Energy*; Elsevier, **2022**.

(73) Dekel, D. R. *Current Opinion in Electrochemistry* **2018**, *12*, 182–188.

(74) Cutler, A. R.; Todaro, A. B. *Organom.* **1988**, *7*, 1782–1787.

(75) Gütlich, P. *Z. anorg. allg. Chem.* **2012**, *638*, 15–43.

(76) E. Bill. *Max-Planck Institute for Chemical Energy Conversion, Mülheim/Ruhr, Germany*.

(77) Garbowski, E.; Praliaud, H. Electronic Spectroscopy. In *Catalyst Characterization : Physical Techniques for Solid Materials*; Imelik, B., Védrine, J., Eds.; Fundamental and Applied Catalysis; Springer US, Plenum Press, **1994**;.

(78) Kibler, L. A. *Chemphyschem : a Eur. J. of Chem. phys. and Phys. chem.* **2006**, *7*, 985–991.

(79) McMillin, D. R.; Rosenberg, R. C.; Gray, H. B. *Proceedings of the National Academy of Sciences of the United States of America* **1974**, *71*, 4760–4762.

(80) Zadrozny, J. M.; Telser, J.; Long, J. R. *Polyhedron* **2013**, *64*, 209–217.

(81) Suturina, E. A.; Maganas, D.; Bill, E.; Atanasov, M.; Neese, F. *Inorg. Chem.* **2015**, *54*, 9948–9961.

(82) Vaidya, S.; Upadhyay, A.; Singh, S. K.; Gupta, T.; Tewary, S.; Langley, S. K.; Walsh, J. P. S.; Murray, K. S.; Rajaraman, G.; Shanmugam, M. *Chem. comm.* **2015**, *51*, 3739–3742.

(83) Legendre, C. M.; Damgaard-Møller, E.; Overgaard, J.; Stalke, D. *Eur. J. Inorg. Chem.* **2021**, *2021*, 3108–3114.

(84) Gupta S. K., Rao, S. V., Demeshko, S., Dechert, S., Bill, E., Atanasov, M., Neese, F. Meyer, F., unpublished work.

(84) Fataftah, M. S.; Zadrozny, J. M.; Rogers, D. M.; Freedman, D. E. *Inorg. Chem.* **2014**, *53*, 10716–10721.

(85) Cui, H.-H.; Lu, F.; Chen, X.-T.; Zhang, Y.-Q.; Tong, W.; Xue, Z.-L. *Inorg. Chem.* **2019**, *58*, 12555–12564.

(86) Wu, C.-M.; Tsai, J.-E.; Lee, G.-H.; Yang, E.-C. *Dalt. Trans.* **2020**, *49*, 16813–16820.

(87) Šebová, M.; Jorík, V.; Moncoľ, J.; Kožíšek, J.; Boča, R. *Polyhedron* **2011**, *30*, 1163–1170.

(88) Gómez-Coca, S.; Urtizberea, A.; Cremades, E.; Alonso, P. J.; Camón, A.; Ruiz, E.; Luis, F. *Nat. Commun.* **2014**, *5*, 4300.

(89) Saber, M. R.; Dunbar, K. R. *Chem. Comm.* **2014**, *50*, 12266–12269.

(90) Bamberger, H.; Albold, U.; Dubnická Midlíková, J.; Su, C.-Y.; Deibel, N.; Hunger, D.; Hallmen, P. P.; Neugebauer, P.; Beerhues, J.; Demeshko, S.; Meyer, F.; Sarkar, B.; van Slageren, J. *Inorg. Chem.* **2021**, *60*, 2953–2963.

(91) Ziegenbalg, S.; Hornig, D.; Görls, H.; Plass, W. *Inorg. Chem.* **2016**, *55*, 4047–4058.

(92) Böhme, M.; Ziegenbalg, S.; Aliabadi, A.; Schnegg, A.; Görls, H.; Plass, W. *Dalt. Trans.* **2018**, *47*, 10861–10873.

(93) Mitsuhashi, R.; Hosoya, S.; Suzuki, T.; Sunatsuki, Y.; Sakiyama, H.; Mikuriya, M. *Dalt. Trans.,* **2019**, *48*, 395–399.

(94) Mondal, A. K.; Sundararajan, M.; Konar, S. *Dalt. Trans.,* **2018**, *47*, 3745–3754.

(95) Tu, D.; Shao, D.; Yan, H.; Lu, C. *Chem. Comm.* **2016**, *52*, 14326–14329.

(96) Lv, W.; Cui, H.-H.; Chen, L.; Zhang, Y.-Q.; Chen, X.-T.; Wang, Z.; Ouyang, Z.-W.; Xue, Z.-L. *Dalt. Trans.,* **2022**, *51*, 7530–7538.

11. Acknowledgements

I have to thank many people, from many parts of the world, who were part of my journey. My PhD time and my thesis would have not been possible without your support.

First of all, I have to thank Prof. Dr. Franc Meyer for giving me the opportunity to conduct my PhD work in his group. I am very grateful for his support, expertise, guidance, academic freedom and endless optimism. I want to thank him also for the abundance of the resources available in the lab. All of this made me grow as a scientist and allowed me to expand my knowledge and abilities in different fields of research. I would further like to address a special thank to Prof. Dr. Inke Siewert for her precious comments on my research and for overtaking the position of the second supervisor. My thanks go to Dr. Carole Duboc, for her guidance and pieces of advice, as well as for hosting me in her laboratories in Grenoble.

I would like to express my gratitude to all colleagues and collaborators who contributed to this thesis work: Dr. Sebastian Dechert for X-ray diffraction measurements and refinement of the obtained molecular structures, Dr. Serhiy Demeshko and Lanxia Hu for Mößbauer spectroscopy measurements, Dr. Claudia Stückl for EPR measurements, Dr. Sandeep K. Gupta for the magnetic measurements, Dr. Marcello Gennari for the help in the electrochemistry work done in Grenoble and Andreas Schwarz and Jörg Teichgräber for the distribution of chemicals and laboratory equipment. I am grateful to Dr. Claudia Stückl and Britta Müller-Wollmann and the rest of the staff for their invaluable help with all the administrative tasks. I am in dept with Dr. Serhiy Demeshko, Dr. Sandeep K. Gupta, Dr. Sheida Rajabi and Sara Ida Mozzi for proofreading this thesis. I also have to thank my bachelor students Desirée Bothe and Daniel Trzewik for their scientific contribution to this thesis work and for the nice time working together.

Then thanks to all my labmates: to Thomas, for being my big brother in the lab, showing me the best time and being a scientist to look up to; to Hendrik, that made my first year unforgettable; to Allyssa, that guided me through the rough times of research with all her optimism; to Moritz, for being simply the best and for all the smashing; to Alisa, for being the coolest master student and friend; and to Jörg, for being the supervillain in all the stories and calling me “Diana, goddess of hunting”. Special thanks also to Dr. Lisa Vondung and her group for spicing up the last months of my PhD.

Big thanks to the AK Meyer current and past group members for the amazing working environment, Ajdin, Disha, Guillermo (papi), Isabel, Kenny, Kevin, Lanxia, Leili, Mike (and Nora), Sandeep (chekcheck), Simin, Valeria, Xian, Yang, Yue and all the rest.

A very special mention goes to these important people: to Munmun, for being a kind and reliable “mum”; to Anna, for being an angel (but still very tough); to Joanne, for always being supportive and for appreciating my “Alone again again” playlist like nobody else; to Ele, for always putting everything in the right perspective and sharing the love for queen Mary with me; to Nils, Nellox, Polatotti, for experiencing with me “the best week of our PhD” and teaching me how to surf; to ShaoAn, for his incredible scientific knowledge and support, as big as his incompetence to everyday life tasks, and for the multiple happy memories made together; to Sheida (Janedelam) for always taking care of me, filling my spirit with joy and laughter and being a companion for many adventures (and for Nafasaaaaam); to Sara (Sendra), for being an accomplice in all my best ideas, shopping, gin-nights, games and most importantly, for failing at life together with me.

Thanks to Angelica and Giuliana. Even if they are far away, they are always close to me.

I have to thank my fairy-sister Matteo, for appearing at the very right time and accompanying me on all the best adventures. The world is ours.

Thank you to my twin-soul Marta, that makes everything better, especially me. Thank you for the critics, the evolution, the love. We are one and the same.

A big thank you to my parents, my sister and all my huge family, that make me who I am and always support me, watching my back from afar.

Finally, thanks to myself, for being able to navigate through all the pain and still being able to collect the best memories.